University of California
Santa Barbara

Search for supersymmetry at CMS in proton-proton collisions with center-of-mass energy of 13 TeV in the single-lepton final state using the sum of masses of large-radius jets

A dissertation submitted in partial satisfaction
of the requirements for the degree

Doctor of Philosophy
in
Physics

by

Adam Leo Dishaw

Committee in charge:

Professor Jeffrey D. Richman, Chair
Professor Claudio Campagnari
Professor Nathaniel Craig

June 2017

The Dissertation of Adam Leo Dishaw is approved.

Professor Claudio Campagnari

Professor Nathaniel Craig

Professor Jeffrey D. Richman, Committee Chair

June 2017

Search for supersymmetry at CMS in proton-proton collisions with center-of-mass energy of 13 TeV in the single-lepton final state using the sum of masses of large-radius jets

by

Adam Leo Dishaw

To all those who have helped and encouraged me along the way.

Acknowledgements

The search for supersymmetry described in this thesis is the result of a team effort and would not have been possible without the input and effort of many other people. My biggest contributions were to the development and implementation of the statistical methods for the search, and to the creation of the plotting tools used to make many of the figures in this document. However, most of the analysis would still be incomplete or non-existent, without the rest of the "RA4-M_J" team.

First, I must thank my advisor, Jeffrey Richman, who has been a fantastic mentor over the last five years at the University of California, Santa Barbara (UCSB). I am grateful for his extraordinary commitment to teaching all of his students and for providing me with a variety of opportunities to work on interesting projects throughout graduate school. I would also like to thank David Stuart, who has been like a second advisor to me. I must also thank all of my colleagues who did much of the work that made this search possible: Manuel Franco Sevilla, Ana Ovcharova, Jae Hyeok Yoo, Ryan Heller, and Rohan Bhandari. While he worked on a different project, I would also like to thank Jack Bradmiller-Feld for his useful feedback throughout the development of the analysis.

I also want to thank my friends and roommates Jack Bradmiller-Feld (again), Alex Walter, Shankari Rajagopal, and Dave Sutherland for reminding me to occasionally take a break and making my time in California so much more enjoyable.

During the first three years of my time at UCSB, I received generous financial support from the Department of Energy, Office of Science Graduate Fellowship Program (DOE SCGF). I would like to thank all those who administered and funded this program.

My pursuit of physics did not begin in California. I would like to thank the many people at Cornell University who helped me make it to graduate school, particularly my undergraduate research advisor, Jim Alexander, who gave me my first opportunity

to do research at the Large Hadron Collider. During my time at Cornell, I had the opportunity to work with two great friends and colleagues, Ben Nachman and Nathan Mirman. I could not have asked for better people with whom to learn about particle physics.

As in graduate school, I did need some reminders to take time away from physics while at Cornell. Thanks to my friends and roommates Andrew Livingstone, Ryan Santo, and Jeremy Mantell for the many rounds of Wiffle Ball, scoop hockey, and other apartment games. You were all good yarmisches.

I am also grateful to my high school physics teacher, Michael Lillis, whose class encouraged me to major in physics in college.

Of course, none of this would have occurred without the support of my parents, Mary and Donald Dishaw; my brother, Ryan Dishaw; and all of my extended family. I would like to thank my mom and dad not just for being fantastic parents, but for sparking my initial interest in physics with their Christmas gift to me in eighth grade: a copy of Brian Greene's "The Elegant Universe."

Finally, I would like to thank my wonderful girlfriend, Evelyn Bing, for her support and encouragement as I wrote this dissertation, and for her endless patience while I lived 3000 miles away. I cannot wait to join you in New York!

Thank you all!

Curriculum Vitæ

Adam Leo Dishaw

Education

2017	Ph.D. in Physics (expected), University of California, Santa Barbara
2015	M.A. in Physics, University of California, Santa Barbara
2012	B.A. in Mathematics and Physics, *magna cum laude*, Cornell University

Selected Publications

CMS Collaboration, "Search for supersymmetry in pp collisions at $\sqrt{s} = 13\,\text{TeV}$ in the single-lepton final state using the sum of masses of large-radius jets", arXiv:1705.04673. Submitted to Physical Review Letters.

CMS Collaboration, "Search for supersymmetry in pp collisions at $\sqrt{s} = 13\,\text{TeV}$ in the single-lepton final state using the sum of masses of large-radius jets", *Journal of High Energy Physics* **2016** (2016), no. 8, 122, doi:10.1007/JHEP08(2016)122, arXiv:1605.04608.

CMS Collaboration, "Searches for electroweak neutralino and chargino production in channels with Higgs, Z, and W bosons in pp collisions at 8 TeV", *Physical Review D*, **90** (November, 2014) 092007, doi:10.1103/PhysRevD.90.092007, arXiv:1409.3168.

CMS Collaboration, "Measurement of masses in the $\text{t}\bar{\text{t}}$ system by kinematic endpoints in pp collisions at $\sqrt{s} = 7\,\text{TeV}$", *The European Physical Journal C* **73** (2013), no. 7, 2494, doi:10.1140/epjc/s10052-013-2494-7, arXiv:1304.5783.

Abstract

Search for supersymmetry at CMS in proton-proton collisions with center-of-mass energy of 13 TeV in the single-lepton final state using the sum of masses of large-radius jets

by

Adam Leo Dishaw

This dissertation describes a search for supersymmetry in $35.9\,\mathrm{fb}^{-1}$ of proton-proton collisions with $\sqrt{s} = 13\,\mathrm{TeV}$ produced by the LHC and recorded by the CMS experiment. The search targets events having a final state with a single lepton, high jet multiplicity, at least one b-tagged jet, and missing transverse momentum. Standard model background yields are estimated using the sum of the masses of large-radius jets in each event. The observed yields are consistent with the estimated background yields. This consistency is interpreted in term of simplified models of supersymmetry in which gluinos are pair produced and each subsequently decay into a top quark, anti-top quark, and neutralino via an intermediate on- or off-shell stop squark. Assuming a 100% branching fraction for this decay chain, gluino masses up to approximately 1.9 TeV are excluded at a 95% confidence level for neutralino masses below 1 TeV. Similarly, neutralino masses up to approximately 1175 GeV are excluded when the gluino mass is 1.7 TeV.

Contents

Curriculum Vitae **vii**

Abstract **viii**

List of Figures **xi**

List of Tables **xxiii**

1 Introduction **1**
1.1 Standard Model 3
1.2 Supersymmetry 10

2 Experimental Apparatus **18**
2.1 Large Hadron Collider 18
2.2 Compact Muon Solenoid 22

3 Object and Event Reconstruction **38**
3.1 Tracks 38
3.2 Calorimeter Clustering 41
3.3 Particle Flow 41
3.4 Leptons 44
3.5 Jets 50
3.6 $E_{\mathrm{T}}^{\mathrm{miss}}$ 59

4 Real and Simulated Data Samples **60**
4.1 Real Data 60
4.2 Monte Carlo Simulation 64

5 Event Selection **69**
5.1 The Baseline Selection, M_J, and m_{T} 69
5.2 ISR and M_J 73
5.3 Removing Single Lepton Events with m_{T} 78

6 Background Estimation **80**
6.1 Extrapolating from Low m_{T} to High m_{T} . . . 80
6.2 The "ABCD" Method . . . 83
6.3 Sensitivity of the ABCD Method . . . 86
6.4 Adding Bins . . . 89
6.5 Adding Systematic Uncertainties . . . 95
6.6 Maximum Likelihood Parameter Estimation . . . 97

7 Systematic Uncertainty in Background Estimates **101**
7.1 Effects of Mismodeling in Simulation . . . 103
7.2 Categorizing High-m_{T} Events . . . 109
7.3 Dilepton and $N_{\mathrm{jets}} = 5$ Control Samples . . . 117
7.4 Validation of Control Samples . . . 127
7.5 Checking for Mismodeling in Control Samples . . . 128

8 Systematic Uncertainty in Signal Model **140**

9 Results and Interpretations **145**
9.1 Estimated Backgrounds . . . 145
9.2 Simple Interpretation of Results . . . 154
9.3 Statistical Methods . . . 159
9.4 T1tttt and T5tttt Limits . . . 167
9.5 Aggregate Bins . . . 170

10 Summary and Conclusions **173**

Bibliography **176**

List of Figures

1.1 Particles of the standard model and several of their key properties, arranged in the commonly used "periodic table" of particles. Figure from Reference [1]. 8
1.2 Cross section for production of selected standard model particles at the LHC. Figure from Reference [2]. 9
1.3 Left: correction to the Higgs propagator from a fermion loop. Right: hypothetical correction to the Higgs propagator from the fermion's scalar superpartner. Theoretical particles introduced by supersymmetry are drawn with red lines. 11
1.4 Qualitative example of a natural SUSY spectrum from Reference [3]. . . 14
1.5 Comparison of gluino and squark production cross sections at a center-of-momentum collision energy of 13 TeV. The squark cross sections assume a ten-fold degeneracy among the squark flavors, not including the stop squark. Figure from Reference [4]. 15
1.6 T1tttt (left) and T5tttt (right) Feynman diagrams. Note that the details of the underlying interaction are not shown, including the presence of additional final state particles produced from the proton remnants after the underlying parton-parton interaction, which are needed for charge conservation. Theoretical particles added by supersymmetry are drawn with red lines. 16

2.1 Diagram of the various accelerators connected to the LHC. Figure from Reference [5] 20
2.2 Integrated luminosity as a function of time for 2016 proton-proton collision. Figure from Reference [6] 22
2.3 Number of vertices per event for events passing the baseline selection of this search. Due to pileup, events have an average of nearly 23 vertices each. 23
2.4 Exploded three-dimensional view of the CMS detector. Figure from Reference [7]. 24

2.5 Cross sectional wedge of the CMS detector in the r-ϕ plane, showing the detector layers and the interaction of several types of particles with the various layers. Figure from Reference [8]. 25
2.6 Layout of the pixel and silicon strip trackers. Figure from Reference [9]. . 28
2.7 Diagram of one quarter of the CMS detector, veiwed in the r-η plane. The diagram highlights the location of the HCAL subdetector components, positioned outside the tracking detector and inside the muon chambers. Figure from Reference [9]. 30
2.8 Cross-sectional view of a drift cell. Figure from Reference [9] 32
2.9 Schematic showing a portion of the data path for the ME1/1 stations, including the Optical Data Acquisition Motherboard (ODMB). Image from Reference [10]. 34
2.10 Schematic diagram showing how an L1A is generated from trigger primitives from the calorimeter and muon systems [9]. 36

3.1 Overall efficiency of the reconstruction, identification, isolation, and vertexing requirements for both muons (left) and electrons (right) as a function of p_{T} and η. Plots from supplementary material for Reference [11] and published online in Reference [12]. 46
3.2 Distribution of $m_{\mathrm{T2}}(l, \mathrm{track}, \vec{E}_{\mathrm{T}}^{\mathrm{miss}})$ for leptonic tracks (left) and hadronic tracks(right) in simulated events. Only tracks from events passing the baseline selection of Chapter 5 and satisfying $m_{\mathrm{T}}(l, \vec{E}_{\mathrm{T}}^{\mathrm{miss}}) > 140\,\mathrm{GeV}$ and $M_J > 250\,\mathrm{GeV}$ are included, where M_J is as defined in Section 3.5.5. Dilepton $\mathrm{t\bar{t}}$ events are shown in blue, while T1tttt events are shown in red for mass parameters $m_{\tilde{\mathrm{g}}} = 1500\,\mathrm{GeV}$ and $m_{\tilde{\chi}^0_1} = 100\,\mathrm{GeV}$ (solid) and for $m_{\tilde{\mathrm{g}}} = 1200\,\mathrm{GeV}$ and $m_{\tilde{\chi}^0_1} = 800\,\mathrm{GeV}$ (dashed). Nearly all tracks in dilepton $\mathrm{t\bar{t}}$ events satisfy the expected $m_{\mathrm{T2}}(l, \mathrm{track}, \vec{E}_{\mathrm{T}}^{\mathrm{miss}}) < m_{\mathrm{W}^{\pm}}$, while the majority of tracks in T1tttt events have $m_{\mathrm{T2}}(l, \mathrm{track}, \vec{E}_{\mathrm{T}}^{\mathrm{miss}}) > m_{\mathrm{W}^{\pm}}$. Only about 30% of T1tttt events produce an isolated track, and so most events will not appear in these plots. This also means that only about 10% of T1tttt events will contain a veto track satisfying the m_{T2} and other requirements listed in Table 3.3. Figure from Reference [13]. 51
3.3 Efficiency of the CSVv2 and DeepCSV b-tagging efficiencies, computed in simulated $\mathrm{t\bar{t}}$+jets events. The medium working point of CSVv2 is used in this analysis. Figure from Reference [12]. 58

4.1 Efficiency of the $E_{\mathrm{T}}^{\mathrm{miss}}$- and $H_{\mathrm{T}}^{\mathrm{miss}}$-based triggers (left), leptonic triggers (center), and the logical OR of all triggers (right) as a function of offline $E_{\mathrm{T}}^{\mathrm{miss}}$ in events with an offline muon. The sample consists of events passing the HLT_PFJet450 trigger and an offline selection requiring three or more jets and $S_{\mathrm{T}} > 500\,\mathrm{GeV}$. Figure from Reference [13]. 63

4.2 Efficiency of the $E_{\mathrm{T}}^{\mathrm{miss}}$- and $H_{\mathrm{T}}^{\mathrm{miss}}$-based triggers (left), leptonic triggers (center), and the logical OR of all triggers (right) as a function of offline $E_{\mathrm{T}}^{\mathrm{miss}}$ in events with an offline electron. The sample consists of events passing the HLT_PFJet450 trigger and an offline selection requiring three or more jets and $S_{\mathrm{T}} > 500\,\mathrm{GeV}$. Figure from Reference [13]. 63
4.3 Combined efficiency of all triggers used in this analysis as a function of offline N_{jets}, N_{b}, and M_J for events containing an offline muon. The sample consists of events passing the HLT_PFJet450 trigger and an offline selection requiring three or more jets, $E_{\mathrm{T}}^{\mathrm{miss}} > 200\,\mathrm{GeV}$, and $S_{\mathrm{T}} > 500\,\mathrm{GeV}$. Figure from Reference [13]. 64
4.4 Combined efficiency of all triggers used in this analysis as a function of offline N_{jets}, N_{b}, and M_J for events containing an offline electron. The sample consists of events passing the HLT_PFJet450 trigger and an offline selection requiring three or more jets, $E_{\mathrm{T}}^{\mathrm{miss}} > 200\,\mathrm{GeV}$, and $S_{\mathrm{T}} > 500\,\mathrm{GeV}$. Figure from Reference [13]. 65

5.1 Distribution of baseline selection variables S_{T} (top left), $E_{\mathrm{T}}^{\mathrm{miss}}$ (top right), N_{jets} (bottom left), and N_{b} (bottom right). Distributions are shown in an "$N-1$" fashion with all requirements of the baseline selection applied, except for any pertaining to the variable whose distribution is shown. The blue shaded region in the ratio plots (bottom panels) indicates statistical uncertainty from the limited sample size of the Monte Carlo simulation. Plots from Reference [13]. 72
5.2 Distribution of M_J and m_{T} after the baseline selection. The blue shaded region in the ratio plots (bottom panels) indicates statistical uncertainty from the limited sample size of the Monte Carlo simulation. Left plot from Reference [13]. Right plot from supplementary technical material of Reference [11]. 73
5.3 Distribution of M_J for events with $p_{\mathrm{T,ISR}} < 10\,\mathrm{GeV}$ and events with $p_{\mathrm{T,ISR}} > 100\,\mathrm{GeV}$. The distribution is shown for $\mathrm{t\bar{t}}$ events with either one or two true leptons (dark and light blue, respectively) and for an example T1tttt model (red). When large amounts of ISR are present, the high-M_J tails become similar for two $\mathrm{t\bar{t}}$ components. The events shown have at least one reconstructed lepton and satisfy $E_{\mathrm{T}}^{\mathrm{miss}} > 200\,\mathrm{GeV}$ and $H_{\mathrm{T}} > 500\,\mathrm{GeV}$. Figure from Reference [13]. 74
5.4 Simple diagram showing how objects are clustered into large-R jets in a $\mathrm{t\bar{t}}$ + jets event without ISR (left) or with ISR (right). Here, the ISR is shown overlapping with the ISR jets. High ISR may also result from the two top quarks recoiling against the ISR and overlapping with each other. 75

5.5 Reconstruction of a 2015 event (run number 256843, lumi block 282, event 408328426) with $M_J = 1173\,\text{GeV}$. The event has an electron and nine jets (yellow circles), two of which are b-tagged (bold yellow circle). It appears to be a $\text{t}\bar{\text{t}}$ + jets event in which the two top quarks recoiled off of an ISR jet with $p_\text{T} = 1468\,\text{GeV}$, causing their decay producets to overlap. Many of the decay products are clustered into a single large-R jet with mass 897 GeV, causing the large M_J. Note that the large-R jets shown in green circles were clustered with $R = 1.2$ rather than the $R = 1.4$ used for the 2016 version of the search described in this dissertation [14, 11]. The left image shows a two-dimensional projection in η-ϕ space. The event is displayed using the Fireworks software from CMS.[15] 76

5.6 Distribution of M_J when large-R jets are clustered with radius parameters $R = 1.2$ (left) and $R = 1.4$ (right). The distributions are shown for $\text{t}\bar{\text{t}}$ (blue) events and two selected T1tttt mass points (red). The solid red line corresponds to the non-compressed benchmark with mass parameters $m_{\tilde{\text{g}}} = 1800\,\text{GeV}$ and $m_{\tilde{\chi}1}^{0} = 100\,\text{GeV}$, while the dashed red line corresponds to the compressed benchmark with $m_{\tilde{\text{g}}} = 1400\,\text{GeV}$ and $m_{\tilde{\chi}1}^{0} = 1000\,\text{GeV}$. In all cases, a selection of $N_\text{leps} = 1$, $H_\text{T} > 500\,\text{GeV}$, $E_\text{T}^\text{miss} > 200\,\text{GeV}$, $N_\text{jets} \geq 6$, and $N_\text{b} \geq 1$ is applied. Figure from Reference [13]. 77

5.7 "Receiver Operating Characteristic," or ROC, curves showing the efficiency with which background $\text{t}\bar{\text{t}}$ + jets events pass an M_J-requirement (y-axis) as a function of the efficiency for signal events (x-axis). Each curve corresponds to a particular choice of clustering radius R for the large-R jets, while points along a single curve correspond to varying M_J selection thresholds. The largest M_J requirements are in the bottom-left corner. Points near the bottom-right corner are the most desirable since they simultaneously have high signal efficiency and strong background rejection. The left plot uses the non-compressed T1tttt benchmark point, while the right right uses the compressed benchmark. The clustering radius makes little difference in the performance of the M_J requirement for non-compressed models. For compressed models, increasing the radius improves performance up until approximately $R = 1.4$, after which further increases do not produce significant improvement, motivating the choice of $R = 1.4$ in this search. Figure from Reference [13]. 78

6.1 Scatter plot of m_{T} versus M_J. Dark blue, downward pointing triangles represent $\mathrm{t\bar{t}}$ events with a single true charged lepton. Light blue, upward pointing triangles represent $\mathrm{t\bar{t}}$ events with two true charged leptons. The red squares represent T1tttt events for the NC mass point. The scatter plot is normalized such that one point represent one expected event at an integrated luminosity of $35.9\,\mathrm{fb}^{-1}$. The correlation coefficients for the two $\mathrm{t\bar{t}}$ components, indicated in the legend, are both small. If all $\mathrm{t\bar{t}}$ events are considered together, the overall correlation coefficient is $\rho \approx 0.01$. Figure from supplementary technical material for Reference [11]. 82
6.2 Comparison of normalized M_J and N_{jets} distributions for two categories of simulated $\mathrm{t\bar{t}}$ events: those with a single true lepton and reconstructed $m_{\mathrm{T}} \leq 140\,\mathrm{GeV}$ and those with two true leptons and reconstructed $m_{\mathrm{T}} > 140\,\mathrm{GeV}$. These samples constitute the dominant source of background events in their respective m_{T} ranges. For both M_J and N_{jets}, the distributions are similar for the low- and high-m_{T} samples. Figure from Reference [13]. 83
6.3 Expected number of signal events in R4 needed for a "5σ" discovery (solid lines) or exclusion at a 95% confidence level, as a function of the expected number of background events in R4 (along x-axis) and the signal-to-background ratio $R = R(M_J) = R(m_{\mathrm{T}})$ (along the y-axis). Note that sensitivity is computed using an asymptotic approximation which may not be fully accurate in the limit of very small yields. 88
6.4 Schematic representation of an unbinned ABCD plane in M_J and m_{T}. . . 89
6.5 Schematic representation of an ABCD background estimation method split into three bins by using separate planes. 90
6.6 Diagram showing an $m \times n$ (in this case, 2×4) "ABCD" plane using M_J and m_{T}. The ABCD method can be generalized to an $m \times n$ plane as long as the x-axis and y-axis variables are either independent or simulation can be trusted to correctly model any correlations between them. 91
6.7 Schematic representation of the ABCD binning used in this search. The separate planes represent the three $E_{\mathrm{T}}^{\mathrm{miss}}$ bins $200\,\mathrm{GeV} < MET \leq 350\,\mathrm{GeV}$, $350\,\mathrm{GeV} < E_{\mathrm{T}}^{\mathrm{miss}} \leq 500\,\mathrm{GeV}$, and $E_{\mathrm{T}}^{\mathrm{miss}} > 500\,\mathrm{GeV}$. 93
6.8 Measured value of $R(m_{\mathrm{T}})$ in simulation as a function of N_{jets} and N_{b} for the low-M_J (left half) and high-M_J (right half) regions. If the $R(m_{\mathrm{T}})$ value at low-M_J matches the corresponding value at high-M_J, then no κ correction is needed. If the differences are small, simulation can be generally be trusted to provide an appropriate correction. $R(m_{\mathrm{T}})$ is only mildly dependent on N_{jets} and N_{b}, particularly for $M_J \leq 400\,\mathrm{GeV}$. The lack of complex kinematic dependencies makes it more likely that the simulation will accurately model the behavior. Figure from supplementary technical material of Reference [11]. 94

6.9 Measured values of κ in simulation with their associated uncertainties. The κ values are typically close to unity and do not show any strong dependence on N_{jets} and N_{b}. This adds confidence in the ability of the simulation to accurately model κ. Figure from Reference [13]. 94

7.1 Values of κ for an extended $E_{\text{T}}^{\text{miss}}$ range, including the $E_{\text{T}}^{\text{miss}} > 200\,\text{GeV}$ analysis regions and $100\,\text{GeV} < E_{\text{T}}^{\text{miss}} \leq 200\,\text{GeV}$ validation region. Figure from supplementary technical material for Reference [11]. 102
7.2 Changes in κ caused by doubling the weight of events satisfying $[E_{\text{T}}^{\text{miss}}(\text{reco}) - E_{\text{T}}^{\text{miss}}(\text{true})]/E_{\text{T}}^{\text{miss}}(\text{true}) > 0.5$. The effect is largest in low $E_{\text{T}}^{\text{miss}}$ bins where events with fake $E_{\text{T}}^{\text{miss}}$ are relatively more common. Figure from Reference [13]. 106
7.3 Shift in κ caused by modifying the b-tagging scale factors by three times their measured uncertainties. Figure from Reference [13]. 108
7.4 Physics processes contributing to the high-m_{T} background in five $E_{\text{T}}^{\text{miss}}$ bins. From left to right, the top row shows the composition of the $100\,\text{GeV} < E_{\text{T}}^{\text{miss}} \leq 150\,\text{GeV}$ and $150\,\text{GeV} < E_{\text{T}}^{\text{miss}} \leq 200\,\text{GeV}$ bins, while the bottom row shows the composition of the $200\,\text{GeV} < E_{\text{T}}^{\text{miss}} \leq 350\,\text{GeV}$, $350\,\text{GeV} < E_{\text{T}}^{\text{miss}} \leq 500\,\text{GeV}$, and $E_{\text{T}}^{\text{miss}} > 500\,\text{GeV}$ bins. Figure from Reference [13]. 110
7.5 M_J distributions for several categories of events passing the baseline selection with relaxed $E_{\text{T}}^{\text{miss}} > 100\,\text{GeV}$ requirement. Only events from $\text{t}\bar{\text{t}}+\text{jets}$ processes are included. High-m_{T} events with either two prompt light leptons (light blue) or a single prompt light lepton and a hadronically decaying τ lepton (purple) are able to reproduce the M_J distribution of the low-m_{T} background in the $M_J > 250\,\text{GeV}$ region. The single lepton backgrounds with well-measured (green) or mismeasured (red) m_{T} have a different M_J distribution, potentially causing κ to deviate from unity. Figure from supplementary technical material for Reference [11]. 112
7.6 $E_{\text{T}}^{\text{miss}}$ mismeasurement and maximum b-quark p_{T} distributions for $\text{t}\bar{\text{t}}+\text{jets}$ events at low and high m_{T}. The baseline selection is applied with a relaxed $E_{\text{T}}^{\text{miss}} > 100\,\text{GeV}$ requirement. Figure from Reference [13]. 113
7.7 κ values as measured in simulated events from $\text{t}\bar{\text{t}}+\text{jets}$ processes. For the multi-neutrino component (cyan circles), $\kappa \approx 1$ independent of $E_{\text{T}}^{\text{miss}}$. For the mismeasured $E_{\text{T}}^{\text{miss}}$ (red triangle) and non-prompt neutrino (green squares) components, κ has a strong $E_{\text{T}}^{\text{miss}}$ dependence and can be far from unity. The presence of these components is responsible for causing κ to deviate from unity. Fortunately, events in the latter two categories are less common than the multi-neutrino events, so the overall κ in simulated $\text{t}\bar{\text{t}}+\text{jets}$ events (black square) remains near unity. The simulated $\text{t}\bar{\text{t}}+\text{jets}$ events never contain an off-shell $\text{W}^{\pm}$. Figure from Reference [13]. 115

7.8 κ values as measured in simulated events from $W^{\pm}$ + jets processes. For the mismeasured E_T^{miss} (red square) and non-prompt neutrino (green circle) components, κ has a strong E_T^{miss} dependence and can be far from unity, but shows similar E_T^{miss} dependency as the κ values for the simulated $t\bar{t}$ + jets events shown in Figure 7.7. The events containing an off-shell $W^{\pm}$ (yellow triangle) typically have κ closer to unity and have a milder E_T^{miss} dependence. No multi-neutrino events are include in the simulation of $W^{\pm}$ + jets events, and so the overall κ (black square) is not necessarily close to unity. Figure from Reference [13]. 116

7.9 κ values measured in simulation (all processes) for the $N_{jets} = 5$ control sample (top left), analysis region (top right), and $150\,GeV \leq E_T^{miss} < 200\,GeV$ validation sample (bottom). $\kappa \approx 1$ in all bins for the multi-neutrino component (blue circles). At high-E_T^{miss}, these events make up a higher fraction of the background, making the overall $\kappa \approx 1$ (black squares). The values for the non-prompt neutrino (green square), mismeasured E_T^{miss} (red upward-pointing triangle), and off-shell $W^{\pm}$ (yellow downward-pointing triangle) components have more complicated E_T^{miss}-dependencies. Within each category, κ does not have clear N_{jets} dependence. Figure from Reference [13]. 118

7.10 Composition of high-m_T background in bins of E_T^{miss} (left to right: $100\,GeV < E_T^{miss} \leq 150\,GeV$, $150\,GeV < E_T^{miss} \leq 200\,GeV$, $200\,GeV < E_T^{miss} \leq 350\,GeV$, and $E_T^{miss} > 500\,GeV$) and N_{jets} (top to bottom: $N_{jets} = 5$, $6 \leq N_{jets} \leq 8$, and $N_{jets} \geq 9$). Multi-neutrino events dominate at high E_T^{miss}, but events with mismeasured E_T^{miss} are more common at low E_T^{miss}. The composition is nearly constant with respect to N_{jets}. Figure from supplementary technical material for Reference [11]. 119

7.11 Composition of the events satisfying $N_{leps} = 2$ in the dilepton control sample, split into $M_J \leq 400\,GeV$ (left) and $M_J > 400\,GeV$ (right) events. The compositions of the two M_J ranges are similar, with most events containing two prompt light leptons and originating from $t\bar{t}$ + jets processes. Events with $N_{leps} = 2$ are roughly six times as common as events with $N_{leps} = N_{veto} = 1$, so these pie charts approximate the overall composition of the dilepton control sample well. Figure from Reference [13]. 121

7.12 Composition of the events satisfying $N_{leps} = N_{veto} = 1$ in the dilepton control sample, split into $M_J \leq 400\,GeV$ (left) and $M_J > 400\,GeV$ (right) events. The compositions of the two M_J ranges are similar. In both cases, events from $t\bar{t}$ + jets process and containing either two prompt light leptons, or one prompt light lepton and a hadronically decaying τ lepton are the most common. Figure from Reference [13]. 122

7.13 Shift in κ in the dilepton sample caused by doubling the weight of events in R4 with a single lepton and mismeasured $E_{\mathrm{T}}^{\mathrm{miss}}$. Changes are measured in bins of $E_{\mathrm{T}}^{\mathrm{miss}}$ (top) and N_{jets} (bottom). Red points show unmodified κ from simulation with a two-part error bar. The inner red part shows statistical uncertainty due to the number of simulated events available. The outer black part represents the expected size of fluctuations about the underlying κ in $35\,\mathrm{fb}^{-1}$ of real data. Black points shows the modified simulation with added mismodeling, treated as real data. Negligible change is observed for all $E_{\mathrm{T}}^{\mathrm{miss}}$ and N_{jets} bins. Figure from Reference [13]. 129
7.14 Shift in κ caused by doubling the weight of events in R4 with a single lepton and mismeasured $E_{\mathrm{T}}^{\mathrm{miss}}$, as measured in the $N_{\mathrm{jets}} = 5$ control sample (top) and analysis regions (bottom). Both samples are binned in $E_{\mathrm{T}}^{\mathrm{miss}}$, and changes in κ in the analysis region are mirrored by similar changes in the $N_{\mathrm{jets}} = 5$ control sample. The largest shifts in κ for this scenario occur at low $E_{\mathrm{T}}^{\mathrm{miss}}$, where events with mismeasured $E_{\mathrm{T}}^{\mathrm{miss}}$ make up a larger fraction of the background composition. Figure from Reference [13] 130
7.15 Shifts in κ caused by doubling the weight of events in R4 with a single lepton and mismeasured $E_{\mathrm{T}}^{\mathrm{miss}}$ are approximately independent of N_{jets} (top) and N_{b} (bottom), shown here in the analysis region and $N_{\mathrm{jets}} = 5$ control samples. Figure from Reference [13]. 131
7.16 Shift in κ caused by changing the ISR corrections by twice their uncertainty in $\mathrm{t\bar{t}}$ + jets events with a single lepton, as seen in the dilepton (top) and $N_{\mathrm{jets}} = 5$ (middle) control samples and analysis region (bottom). In all cases, changes in κ are approximately independent of $E_{\mathrm{T}}^{\mathrm{miss}}$. Figure from Reference [13]. 132
7.17 Shifts in κ caused by changing the $\mathrm{t\bar{t}}$ + jets ISR corrections by twice their uncertainty in events with a single lepton are largest in the high-N_{jets} bins. The -11% shift observed in the $N_{\mathrm{jets}} \geq 9$ bin of the analysis region (bottom) is matched by similar changes in the $N_{\mathrm{jets}} \geq 9$ bins of the dilepton control sample (top). Figure from Reference [13]. 133
7.18 Shifts in κ caused by changing the ISR corrections by twice their uncertainty in $\mathrm{t\bar{t}}$ + jets events with a single lepton are approximately independent of N_{b}, as shown here for the $N_{\mathrm{jets}} = 5$ control sample and $N_{\mathrm{jets}} \geq 6$ analysis region. Figure from Reference [13]. 134

7.19 Differences in the observed and simulated κ for the dilepton (top) and $N_{\text{jets}} = 5$ (bottom) control samples. Observed values are consistent with those predicted by simulation. Systematic uncertainties assigned from the control regions are taken from the σ_{stat} reported in these plots. The dilepton control sample yields 6% and 16% $= \frac{14\%}{100\%-14\%}$ uncertainties for the $6 \leq N_{\text{jets}} \leq 8$ and $N_{\text{jets}} \geq 9$ bins, respectively. The $N_{\text{jets}} = 5$ control samples yields 16% $= \frac{14\%}{100\%-14\%}$ and 41% $= \frac{29\%}{100\%-29\%}$ uncertainties for the $200\,\text{GeV} < E_{\text{T}}^{\text{miss}} \leq 350\,\text{GeV}$ and $E_{\text{T}}^{\text{miss}} > 350\,\text{GeV}$ bins, respectively. The remaining low $E_{\text{T}}^{\text{miss}}$ bins shown here are not used to assign uncertainties, but provide confidence in the accuracy of the simulation. Figure from Reference [13]. 135

7.20 Additional checks for mismodeling in simulation performed before unblinding the signal region. No significant differences between simulated and observed κ values are seen in the $N_{\text{leps}} = N_{\text{veto}} = 1$ subset of the dilepton control sample (top left), the full dilepton control sample binned in N_{jets} (top right), the low $E_{\text{T}}^{\text{miss}}$ validation region (bottom left), or the $N_{\text{jets}} = 5$ control sample and analysis region binned in N_{b} (bottom right). Note that the bottom right plot shown here does show κ values obtained by unblinding the signal region. In practice, these are initially hidden until the other values have been checked. Figure from Reference [13]. 137

7.21 Comparison of κ values measured in simulation and real data for the analysis regions. There is a modest (between two and three standard deviations) upward fluctuation in κ relative to the simulated value in the $E_{\text{T}}^{\text{miss}} > 500\,\text{GeV}$ bin. Having at least one such fluctuation of this size is expected considering the number of bins tested in this section. Figure from Reference [13]. 139

9.1 M_J distribution in bins of $E_{\text{T}}^{\text{miss}}$ (left-to-right: $200\,\text{GeV} < E_{\text{T}}^{\text{miss}} \leq 350\,\text{GeV}$, $350\,\text{GeV} < E_{\text{T}}^{\text{miss}} \leq 500\,\text{GeV}$, $E_{\text{T}}^{\text{miss}} > 500\,\text{GeV}$) and N_{b} ($N_{\text{b}} = 1$ in top row, $N_{\text{b}} \geq 2$ in bottom row). The black points show the M_J distribution for events with $m_{\text{T}} > 140\,\text{GeV}$. The blue line shows the corresponding distribution for events with $m_{\text{T}} \leq 140\,\text{GeV}$, normalized to have the same integral as the low-m_{T} distribution. In all $E_{\text{T}}^{\text{miss}}$ and N_{b} bins, the distributions are similar. Figure from Reference [13]. 147

9.2 Two-dimensional scatter plot showing M_J and m_{T} for the observed events satisfying $200\,\text{GeV} < E_{\text{T}}^{\text{miss}} \leq 350\,\text{GeV}$ (top left), $350\,\text{GeV} < E_{\text{T}}^{\text{miss}} \leq 500\,\text{GeV}$ (top right), and $E_{\text{T}}^{\text{miss}} > 500\,\text{GeV}$ (bottom). The underlying color map indicates the weighted density of events in simulation. The red squares show a representative sample of points from a selected signal model, T1tttt(1800,100), normalized such that each square corresponds to one event at an integrated luminosity of $35.9\,\text{fb}^{-1}$. Figure from supplementary technical material for Reference [11]. 148

9.3 Graphical representation of the global fit results shown in Table 9.1. The observed yields are shown as black dots, while the fitted background is shown as a filled histogram. The partitioning of the fitted background into two components ($t\bar{t}$ + jets in blue and other background in green) is done by taking the fraction of events coming from $t\bar{t}$ + jets processes from simulation, and is meant only to give a rough sense of the background composition rather than to convey any particular knowledge obtained from the fit. Although the fit used to produce the plot has fixed $r = 0$, the expected signal yield for the T1tttt(1800,100) process is shown stacked on top of the background as a dashed red line. Figure from Reference [13]. . 152
9.4 Correlation matrix for the background estimates produced by the predictive fit. The covariance matrix can be obtained using the uncertainties listed in the "Pred. Fit" background column of Table 9.1. Figure from supplementary material for Reference [11]. 153
9.5 Correlation matrix for the background estimates produced by the global fit. The covariance matrix can be obtained using the uncertainties listed in the "Glob. Fit" background column of Table 9.1. Figure from supplementary material for Reference [11]. 155
9.6 Contributions of the 42 bins (and one systematic uncertainty factor) to the approximately χ^2-distributed test-statistic q from Equation (9.1). The null hypothesis is the usual background-only fit with fixed $r = 0$. The alternative hypothesis used for comparison is a saturated model in which each bin is allowed to have an independent Poisson mean parameter. The horizontal line shows the median expected significance per bin in the absence of signal. If the significance contribution from each bin were set to this value, one would obtain $p = 0.5$. 157
9.7 Contributions of the 42 bins (and one systematic uncertainty factor) to the approximately chi-square distributed test-statistic q from Equation (9.1). The null hypothesis is the usual background-only fit with fixed $r = 0$. The alternative hypothesis used for comparison has a floating r and uses T1tttt(1800,100) for the signal shape. 159
9.8 Contributions of the 42 bins (and one systematic uncertainty factor) to the approximately chi-square distributed test-statistic q from Equation (9.1). The null hypothesis is the usual background-only fit with fixed $r = 0$. The alternative hypothesis used for comparison has a floating r and uses T1tttt(1400,1000) for the signal shape. 160
9.9 Contributions of the 42 bins (and one systematic uncertainty factor) to the approximately chi-square distributed test-statistic q from Equation (9.1). The null hypothesis is the usual background-only fit with fixed $r = 0$. The alternative hypothesis used for comparison has a floating r and uses T1tttt(1300,1075) for the signal shape. 161

9.10 Left: The unbounded test statistic q_r from Equation (9.2) as a function of the observed yield N_{obs} for a single bin counting experiment model with a mean expected background yield of 10^6, a mean expected signal yield of 3×10^3, and no systematic uncertainties. The test statistic is shown for $r = 0$ and $r = 1$. Right: The distribution of the test statistics ($r = 0$ in black, $r = 1$ in red) for a background-only scenario (solid) and signal-plus-background scenario (dashed). 161
9.11 Left: The test statistic $q_{r,\text{sig}}$ from Equation (9.3) as a function of the observed yield N_{obs} for a single bin counting experiment model with a mean expected background yield of 10^6, a mean expected signal yield of 3×10^3, and no systematic uncertainties. The test statistic is shown for $r = 0$ and $r = 1$. Right: The distribution of the test statistics ($r = 0$ in black, $r = 1$ in red) for a background-only scenario (solid) and signal-plus-background scenario (dashed). The test statistic $q_{0,\text{sig}}$ has a known distribution in the absence of signal and is used to compute discovery significance. 162
9.12 Left: The test statistic $q_{r,\text{lim}}$ from Equation (9.4) as a function of the observed yield N_{obs} for a single bin counting experiment model with a mean expected background yield of 10^6, a mean expected signal yield of 3×10^3, and no systematic uncertainties. The test statistic is shown for $r = 0$ and $r = 1$. Right: The distribution of the test statistics ($r = 0$ in black, $r = 1$ in red) for a background-only scenario (solid) and signal-plus-background scenario (dashed). The $q_{r,\text{lim}}$ are used to compute CL_s upper limits. Note that $q_{0,\text{lim}}$ is identically zero. 163
9.13 Illustration of how $q_{r,\text{lim}}$ is used to compute CL_s upper limits on the signal strength parameter r for a single bin counting experiment model with a mean expected background yield of 10^6, a mean expected signal yield of 3×10^3, and no systematic uncertainties. The vertical line represents the observed $q_{r,\text{lim}}$ when the observed yield is equal to the expected background. CL_b, the probability of obtaining a higher $q_{r,\text{lim}}$ than the observed value given a background-only scenario (solid line), does not change with r. CL_{s+b}, the probability of obtaining a higher $q_{r,\text{lim}}$ given a signal-plus-background scenario (dashed line) decreases with increasing r. The upper limit at 95% confidence corresponds to $r \approx 0.665$ where $CL_s = CL_{s+b}/CL_b = 0.05$ (center right panel). 166
9.14 Observed significance in the T1tttt (left) and T5tttt (right) mass planes. Figure from supplementary material for Reference [11]. 168

9.15 CL_s upper limits at a 95% confidence limit for T1tttt (left) and T5tttt (right). The color map shows the cross section upper limits. The black lines shows the excluded range of mass parameters (solid). The dashed black lines indicate uncertainty originating in the signal cross section. Points below and left of this line have a theoretical cross section above the excluded cross section. Similarly, the region of expected exclusion is shown by red lines, with the dashed red lines indicating experimental uncertainty. Left plot from Reference [13]. Right plot from supplementary material for Reference [11]. 169
9.16 Comparison of the excluded regions for T1tttt and T5tttt models, showing their similarity. T5tttt limits are worse than T1tttt limits at low $\widetilde{\chi}_1^0$mass because the $\widetilde{\chi}_1^0$carries less momentum, reducing the average $E_{\mathrm{T}}^{\mathrm{miss}}$ of T5tttt events. Figure from Reference [11]. 170

List of Tables

1.1 Particles of the standard model and their properties. Antiparticles are not listed in this table, but would have identical mass and opposite charges as their corresponding particle. In cases where the left- and right-handed particles differ, the values for the left-handed version are shown without parentheses, while the values for the right-handed particle are shown with parenthesis. Particle masses m are those reported by Reference [16]. Although the standard model assumes neutrinos are massless, they are known to have a small non-zero mass. This deficiency can be fixed by, for example, adding right-handed neutrinos to the standard model. Note that the choice of renormalization scheme can affect the quark masses; the scheme chosen for each quark is listed in Reference [16]. J is the spin of each particle. The $SU_c(3)$ representations indicate the number of possible color charges for each particle and their transformation properties, with **8** denoting the adjoint representation, **3** the fundamental representation, $\bar{\mathbf{3}}$ the anti-fundamental representation (only relevant for anti-quarks and thus not present in this table), and **1** the trivial representation. T_3 is the third component of weak isospin and Y the weak hypercharge, the two of which are summed to find the conserved electric charge $Q = T_3 + \frac{Y}{2}$. . . . 7

1.2 Counting the degrees of freedom for the guage and Higgs bosons of the standard model and their superpartners. The left super-column shows the standard model particles; the center shows their superpartners; the right column shows the mass eigenstates of the superpartners, obtained by mixing the superpartners listed in the center super-column. The table assumes two complex Higgs doublets. Table reproduced from Reference [17]. 12

2.1 Typical values of LHC beam parameters for several run years. Maximum number of bunches and peak luminosity are reported for Point 1 (ATLAS) and Point 5 (CMS), which have the highest luminosity [18]. 21

3.1 Kinematic and quality requirements applied to muons. d_{xy} and d_z are the transverse and longitudinal impact parameters of the tracks associated to the muon. The "Is global or tracker muon" excludes standalone muons. . 45
3.2 Kinematic and quality requirements applied to electrons. Different requirements are applied to electrons in the barrel ($\left|\eta_{\text{supercluster}}\right| \leq 1.479$) and endcap ($\left|\eta_{\text{supercluster}}\right| > 1.479$). d_{xy} and d_z are the transverse and longitudinal impact parameters of the tracks associated to the electron. $\sigma_{i\eta i\eta}$ is a shower shape variable which measures the width of the ECAL energy deposits in the η direction. 45
3.3 Selection requirements for veto tracks. In all cases, it is assumed the track has not already been identified as an electron or muon. m_{T2} requires an identified electron or muon to compute. If an event does not contain any leptons, the m_{T2} and charge requirements are omitted. For charged hadron tracks, the definition of mini-isolation is modified to exclude photons and neutral hadron candidates, retaining only the first term in Equation (3.1). 49
3.4 Kinematic and quality requirements applied to the jets after removing those matched to leptons. The "fraction" requirements refer to the fraction of the energy of the jet coming from a particular source as identified by the PF algorithm. 55

4.1 Integrated luminosity of the data eras used in this analysis, including only those passing the Golden JSON requirement in which all subdetectors are functioning properly. The uncertainty on the total integrated luminosity is 2.6%. 61
4.2 List of all triggers used in this analysis. The final trigger decision is the logical OR of the individual triggers. 62
4.3 Simulated background processes and their equivalent integrated luminosities. 67
4.4 Weights to correct the ISR multiplicity distribution in simulated event samples. For $\mathrm{t\bar{t}}$ events, $C = 1.071$. For signal events, $C = 1.143$. The correction is not applied to other samples. 68

5.1 Expected yields from simulated standard model background and SUSY signal process after sequential application of event selection criteria. Yields are normalized to an integrated luminosity of $35.9\,\text{fb}^{-1}$. The "Other" category includes Drell-Yan processes and production of $\text{t}\bar{\text{t}}\text{t}\bar{\text{t}}$, Z + jets, ZZ, $\text{W}^{\pm}\text{Z}$, $\text{W}^{\pm}\text{W}^{\pm}$, $\text{t}\bar{\text{t}}\text{H}$, $\text{W}^{\pm}\text{H}$, ZH, and ggZH. In cases where a Higgs boson is produced, it is assumed to decay to $\text{b}\bar{\text{b}}$. The "$\text{t}\bar{\text{t}}\,V$" category includes $\text{t}\bar{\text{t}}\text{W}^{\pm}$, $\text{t}\bar{\text{t}}\text{Z}$, and $\text{t}\bar{\text{t}}\gamma$. The "NC" and "C" T1tttt signal models correspond to the ($m_{\tilde{\text{g}}} = 1800\,\text{GeV}$, $m_{\tilde{\chi}1}^{0} = 100\,\text{GeV}$) and ($m_{\tilde{\text{g}}} = 1400\,\text{GeV}$, $m_{\tilde{\chi}1}^{0} = 1000\,\text{GeV}$) mass points, respectively, as described in Section 4.2. Rows above the horizontal line correspond to requirements included in the baseline selection. For entries with an expected yield of 0, statistical uncertainties are at most 0.15 events. The precision is limited by the number of simulated events available. Table from Reference [13]. 71

7.1 Summary of the effect of various intentionally applied mismodeling scenarios on κ. Note that these values are intended to represent the potential size of changes in κ caused by various mismodeling scenarios. They are not assigned as systematic uncertainties. 104

7.2 Yields and maximum likelihood ABCD predictions for the dilepton control region, including a $100\,\text{GeV} < E_{\text{T}}^{\text{miss}} \leq 200\,\text{GeV}$ validation sample. The observed yields are consistent with the predictions for both $E_{\text{T}}^{\text{miss}}$ ranges and for both the low- and high-N_{jets} bins. Were the simulation to have significant inaccuracies in its modeling of κ for this sample, it would bias the predictions, causing an inconsistency that would appear in this table. The T1tttt yields shown are not used in the background-only fit, but are provided to show that the dilepton control sample does not suffer from significant signal contamination. The significances reported in the rightmost column are Z-scores, sometimes quoted in "σ" or standard deviations. Note that the "Pred." column contains true predictions. The R4 bins are excluded from the likelihood to create a "predictive fit." The procedure for doing this is described in Section 9.1. While the systematic uncertainties derived from the dilepton control sample are typically obtained from Figure 7.19, they can in principle be computed from the predictions in the bottom two rows. Table from Reference [13]. 123

7.3 Yields and maximum likelihood ABCD predictions for the $N_{\text{jets}} = 5$ control sample, binned in $E_{\text{T}}^{\text{miss}}$ and including low-$E_{\text{T}}^{\text{miss}}$ validation regions. As in Table 7.2, inaccuracies in the modeling of κ in simulation would appear here. We would typically read off the systematic uncertainties derived from the $N_{\text{jets}} = 5$ control samples from Figure 7.19, but we can in principle compute them from the uncertainties in the background predictions for the R4 rows in the $E_{\text{T}}^{\text{miss}}$ ranges $200\,\text{GeV} < E_{\text{T}}^{\text{miss}} \leq 350\,\text{GeV}$ and $350\,\text{GeV} < E_{\text{T}}^{\text{miss}} \leq 500\,\text{GeV}$. Table from Reference [13]. 125

7.4 Fractional systematic uncertainties, expressed in percentages, for the signal bins. Uncertainties combine those from the dilepton and $N_{\text{jets}} = 5$ control samples by treating them as independent, as in Equation (7.3). . 126

8.1 Sizes of systematic uncertainties assigned to the R4 bins for two selected signal models. Systematic uncertainties in different rows are treated as uncorrelated. Uncertainties within a row are treated as fully correlated if they have the same sign, and fully anti-correlated if they have opposite signs. Table from Reference [13]. 142

9.1 Estimated backgrounds with fixed $r = 0$. Results are independent of signal model, but two T1tttt columns give a sense of which bins would be sensitive to the presence of signal. The $\hat{\kappa}$ columns include systematic uncertainty. The two values are from the predictive fit (R4 bins not included in the likelihood) and global fit (all bins included). Predictive and global background estimates are shown along with expected yields from simulation. Observed yields are consistent with background estimates. Table in part from supplementary material for Reference [11]. 149

9.2 Results from the background-only predictive fit in four aggregate bin options. The fit is independent of any signal model, but T1tttt yields from simulation are provided to give a sense of potential sensitivity. Note that each row is a separate fit, unlike in Table 9.1 where the rows are all produced by a single fit. Observed yields are consistent with the estimated backgrounds. 171

9.3 Expected limits and significance for each of the four aggregate bin options and the full, finely binned analysis. The aggregate bin names correspond to those defined in Table 9.2. Note that the background systematic uncertainties are simply taken from the most similar bin in the full analysis rather than recomputing them from scratch. A 25% systematic uncertainty is assumed for the signal yield in all bins. 172

Chapter 1

Introduction

In particle physics, one calls a particle "elementary" or "fundamental" if it has no known substructure. After the discovery of atoms in the nineteenth century, they were the most fundamental particles known to science. The 1897 discovery of the electron by Sir Joseph John Thomson and the early twentieth century discovery of the nucleus by Hans Geiger, Ernest Marsden, and Ernest Rutherford showed that, in fact, atoms were divisible and made of yet smaller entities. Later experiments by Rutherford and James Chadwick revealed that the nucleus contained yet smaller particles now known as protons and neutrons. The quark model proposed by Murray Gell-Mann and George Zweig in 1964 hypothesized that protons and neutrons (and a host of other hadrons then thought to be elementary) were composed of quarks; this was confirmed at the Stanford Linear Accelerator Center (SLAC). To this day, quarks are still thought to be elementary.

Rather than looking at this sequence of discoveries as moving towards smaller and smaller sizes, it is useful to think of them as progressing to higher and higher energy scales. Separating electrons from atoms generally requires approximately 10^0 to 10^1 eV of energy; this scale is typical of chemical reactions. Removing neutrons and protons from the nucleus requires far more energy, typically on the order of 10^7 eV, a scale characteristic

of nuclear physics. The binding energy holding quarks together inside of a proton is even larger and responsible for almost all of the proton's mass, approximately 10^9 eV. Today, we have the standard model (SM) of particle physics, a theory which incorporates all the currently known fundamental particles and their interactions. In 2012, the CMS and ATLAS experiments observed the Higgs boson with a mass of approximately 125 GeV [19, 20, 21, 22, 23, 24]. This was the last particle of the standard model to be observed, and confirmed ability of the standard model to make accurate predictions at the electroweak scale of 10^{11} eV.

While the standard model has been able to make remarkably accurate and precise predictions that agree with nearly all experiments to date, it is known to have several shortcomings, such as its inability to explain dark matter and dark energy, its omission of gravity, and the unusually low mass of the Higgs boson. Supersymmetry is one theory that has the potential to address several of these issues and, depending on the choice of parameters in the theory, may be testable at the 10^{12} eV scale now accessible with the Large Hadron Collider (LHC) operated by the European Organization for Nuclear Research (CERN). This chapter will discuss the motivation for supersymmetry and some of its key properties relevant to searches at the LHC.

The remaining chapters will explain how the search operates, starting with how the LHC and CMS detector produce and record events in Chapter 2. Chapter 3 describes the recontruction of events within CMS and requirements for the identification of various physics objects used in this search. The data and simulated event samples used are described briefly in Chapter 4.

With this preliminary information out of the way, we will then proceed to describe the search itself, beginning with the "ABCD" background estimation procedure in Chapter 6. We then assess the systematic uncertainties associated with this procedure and with the simulated signal samples in Chapters 7 and 8, respectively.

Finally, Chapters 9 and 10 will provide the results and summarize the search.

The search described in this document has been submitted for publication in Reference [11], with some supplementary material in Reference [12]. A superseded version of the paper is available in Reference [25]. Private documentation intended for distribution only within the CMS experiment is available in Reference [13]. The methods are similar to those of the earlier search documented in Reference [14].

1.1 Standard Model

Before attempting to search for supersymmetry, we must understand the current state of particle physics and, in particular, the standard model. Informally, the standard model is a theory describing the known fundamental particles, their properties, and the rules governing their interactions, excluding gravity. More formally, it is a relativistic quantum field theory. Since it does not include gravitational effects, the standard model assumes that the fields exist within Minkowski space, providing a set of global symmetries described by the Poincaré group. The standard model also postulates that there is a local, internal gauge symmetry described by the group $\mathrm{SU}_c(3) \times \mathrm{SU}_L(2) \times \mathrm{U}_Y(1)$. The Lagrangian of the standard model,

$$\begin{aligned}\mathcal{L} = &-\frac{1}{4}F^a_{\mu\nu}F_a^{\mu\nu} + i\bar{\psi}_i \not{D}\psi_i + i\psi_i \not{D}\bar{\psi}_i + y_{ij}(\psi_i\psi_j + \bar{\psi}_i\bar{\psi}_j)\phi \\ &+ (D_\mu\phi)^\dagger(D^\mu\phi) + \mu^2\phi^\dagger\phi - \lambda(\phi^\dagger\phi)^2, \end{aligned} \tag{1.1}$$

obeys this symmetry. Here, $F^a_{\mu\nu} = \partial_\mu A^a_\nu - \partial_\nu A^a_\mu + g f^{abc} A^b_\mu A^c_\nu$ is the field strength tensor for the gauge field A with coupling constant g and structure constants f^{abc}. The gauge covariant derivatives are $D_\mu = \partial_\mu - ig\lambda_a A^a_\mu$, where the λ_a are the appropriate representation matrices, the choice of representation depending on the field D_μ is acting on. Using

Feynman slash notation, $\not{D} = \gamma^\mu D_\mu$. The fermion fields are denoted by ψ_i, the scalar Higgs field by ϕ, and their Yukawa couplings by y_{ij}. Note that Equation (1.1) has been written in an extremely condensed form and should be interpreted as having an implicit sum over the gauge boson and fermion fields.

The generators of the gauge symmetry groups are identified with gauge bosons, the force mediating particles of the standard model. The group $\mathrm{SU}_c(3)$ has eight generators corresponding to the eight possible gluon color charges. $\mathrm{SU}_L(2)$ has three generators, corresponding to the fields W_1, W_2, and W_3. $\mathrm{U}_Y(1)$ has just one generator, corresponding to the gauge field B. The more familiar $\mathrm{W}^\pm$ bosons are linear combinations of the W_1 and W_2, $\mathrm{W}^\pm = \frac{\mathrm{W}_1 \mp \mathrm{W}_2}{\sqrt{2}}$. The Z and γ are linear combinations of the B and W_3,

$$\begin{pmatrix} \gamma \\ \mathrm{Z} \end{pmatrix} = \begin{pmatrix} \cos\theta_\mathrm{W} & \sin\theta_\mathrm{W} \\ -\sin\theta_\mathrm{W} & \cos\theta_\mathrm{W} \end{pmatrix} \begin{pmatrix} \mathrm{B} \\ \mathrm{W}_3 \end{pmatrix}, \tag{1.2}$$

where θ_W is known as the Weinberg angle.

The matter content of the standard model comprises three generations of fermions. Within each generation, there is an $\mathrm{SU}_L(2)$ doublet of left-handed quarks, a doublet of left-handed leptons (one electrically charged lepton and one neutrino), a right-handed up-type quark singlet, a right-handed down-type quark singlet, and a right-handed charged lepton singlet. The standard model does not contain right-handed neutrinos, though it is possible to add such particles. For each of the above particles, there is additionally a corresponding anti-particle with identical mass, but all charges negated.

The quarks carry color charge and therefore interact with gluons. This results in a property called color confinement: particles with color charge cannot be isolated and are only found in bound color-singlet states, such as hadrons. The exception is the top quark, whose short lifetime of only $5 \times 10^{-25}\,\mathrm{s}$ means that it decays before it is able to

hadronize. Only left-handed quarks interact via the weak force, while all quarks carry electric charge and interact electromagnetically.

Leptons, on the other hand, are colorless and do not interact via the strong force. Similar to the quarks, the left-handed charged leptons and neutrinos all couple to the $W^{\pm}$ and Z, while the right-handed leptons do not. While the electron, muon, and tau lepton are electrically charged, the neutrinos are electrically neutral. Since they lack both color and electric charge, they are experimentally difficult to detect and their presence generally inferred from conservation of momentum.

The Lagrangian in Equation (1.1) does not contain any explicit mass terms for fields other than ϕ. For gauge bosons, such terms would be proportional to $A^{\mu}_{a}A^{a}_{\mu}$, which is not invariant under gauge transformations. In the case of fermions, explicitly included masses would require terms such as $m\psi_{\mathrm{L}}\psi_{\mathrm{R}}$. Since the weak interaction is chiral and should not affect right-handed fermions, such terms are also disallowed by the $\mathrm{SU}_L(2)$ gauge symmetry.

Instead, the particles acquire mass via the Higgs mechanism. Equation (1.1) contains a potential term for the scalar Higgs field, $V(\phi) = -\mu^2\phi^{\dagger}\phi + \lambda(\phi^{\dagger}\phi)^2$, where the Higgs field ϕ is a complex scalar $\mathrm{SU}_L(2)$ doublet with two charged and two neutral real degrees of freedom. With $\mu^2 > 0$ and $\lambda > 0$, the minimum of the potential occurs is at nonzero ϕ, the vacuum expectation value of the Higgs field. One may choose a basis such that the vacuum expectation value is real and neutral and expand the field about this point so that

$$\phi = \frac{1}{\sqrt{2}} \begin{pmatrix} 0 \\ v + h \end{pmatrix}, \tag{1.3}$$

where $v = \sqrt{\frac{\mu^2}{\lambda}} \approx 246\,\text{GeV}$ and $\langle h \rangle = 0$. The expanded Higgs potential is

$$V(h) = \frac{m_{\text{H}}^2 v^2}{8} + \frac{m_{\text{H}}^2}{2} h^2 + \frac{m_{\text{H}}^2}{2v} h^3 + \frac{m_{\text{H}}^2}{8v^2} h^4, \tag{1.4}$$

with $m_{\text{H}} = \sqrt{2}\mu$ the mass of the Higgs boson. The expansion of the potential thus gives rise to an irrelevant constant term, a mass term, and two self-interaction terms.

The Higgs kinetic term in Equation (1.1),

$$(D_\mu \phi)^\dagger (D^\mu \phi) = \frac{v^2 g^2}{8} (\text{W}^+)^2 + \frac{v^2 g^2}{8} (\text{W}^-)^2 + \frac{v^2 [g^2 + (g')^2]}{8} \text{Z}^2, \tag{1.5}$$

can be expanded in the same manner, from which one may identify the masses for the weak gauge bosons: $m_{\text{W}^+} = m_{\text{W}^-} = \frac{vg}{2}$ and $m_{\text{Z}} = \frac{v}{2}\sqrt{g^2 + (g')^2}$. The coupling strengths g and g' of $\text{SU}_L(2)$ and $\text{U}_Y(1)$, respectively, are related by the Weinberg angle from Equation (1.2): $\cos\theta_{\text{W}} = \frac{g}{\sqrt{g^2 + (g')^2}}$. Note that the photon remains massless.

In a similar manner, expanding the Yukawa terms in Equation (1.1) gives rise to fermion masses.

Table 1.1 and Figure 1.1 show the particle content of the standard model, listing several important properties of the various particles.

Figure 1.2 shows the production cross section in 13 TeV proton-proton collisions for a variety of standard model particles. Impressively, the standard model predictions and experimental results agree over the nine orders of magnitude encompassed by the various processes.

Table 1.1: Particles of the standard model and their properties. Antiparticles are not listed in this table, but would have identical mass and opposite charges as their corresponding particle. In cases where the left- and right-handed particles differ, the values for the left-handed version are shown without parentheses, while the values for the right-handed particle are shown with parenthesis. Particle masses m are those reported by Reference [16]. Although the standard model assumes neutrinos are massless, they are known to have a small non-zero mass. This deficiency can be fixed by, for example, adding right-handed neutrinos to the standard model. Note that the choice of renormalization scheme can affect the quark masses; the scheme chosen for each quark is listed in Reference [16]. J is the spin of each particle. The $\mathrm{SU}_c(3)$ representations indicate the number of possible color charges for each particle and their transformation properties, with **8** denoting the adjoint representation, **3** the fundamental representation, $\bar{\mathbf{3}}$ the anti-fundamental representation (only relevant for anti-quarks and thus not present in this table), and **1** the trivial representation. T_3 is the third component of weak isospin and Y the weak hypercharge, the two of which are summed to find the conserved electric charge $Q = T_3 + \frac{Y}{2}$.

Particle	mc^2	J	$\mathrm{SU}_c(3)$ Rep.	T_3	Y	$Q = T_3 + \frac{Y}{2}$
g	0	1	**8**	0	0	0
γ	0	1	**1**	0	0	0
$\mathrm{W}^{\pm}$	80.385 GeV	1	**1**	± 1	0	± 1
Z	91.187 GeV	1	**1**	0	0	0
H	125.09 GeV	0	**1**	0	0	0
e	511.00 keV	$\frac{1}{2}$	**1**	$-\frac{1}{2}$ (0)	-1 (-2)	-1
μ	105.66 MeV	$\frac{1}{2}$	**1**	$-\frac{1}{2}$ (0)	-1 (-2)	-1
τ	1.7769 GeV	$\frac{1}{2}$	**1**	$-\frac{1}{2}$ (0)	-1 (-2)	-1
$\nu_{\mathrm{e},\mu,\tau}$	< 2 eV	$\frac{1}{2}$	**1**	$\frac{1}{2}$	-1	0
u	2.2 MeV	$\frac{1}{2}$	**3**	$\frac{1}{2}$ (0)	$\frac{1}{3}$ $\left(\frac{4}{3}\right)$	$\frac{2}{3}$
c	1.27 GeV	$\frac{1}{2}$	**3**	$\frac{1}{2}$ (0)	$\frac{1}{3}$ $\left(\frac{4}{3}\right)$	$\frac{2}{3}$
t	173.21 GeV	$\frac{1}{2}$	**3**	$\frac{1}{2}$ (0)	$\frac{1}{3}$ $\left(\frac{4}{3}\right)$	$\frac{2}{3}$
d	4.7 MeV	$\frac{1}{2}$	**3**	$-\frac{1}{2}$ (0)	$\frac{1}{3}$ $\left(-\frac{2}{3}\right)$	$-\frac{1}{3}$
s	96 MeV	$\frac{1}{2}$	**3**	$-\frac{1}{2}$ (0)	$\frac{1}{3}$ $\left(-\frac{2}{3}\right)$	$-\frac{1}{3}$
b	4.18 GeV	$\frac{1}{2}$	**3**	$-\frac{1}{2}$ (0)	$\frac{1}{3}$ $\left(-\frac{2}{3}\right)$	$-\frac{1}{3}$

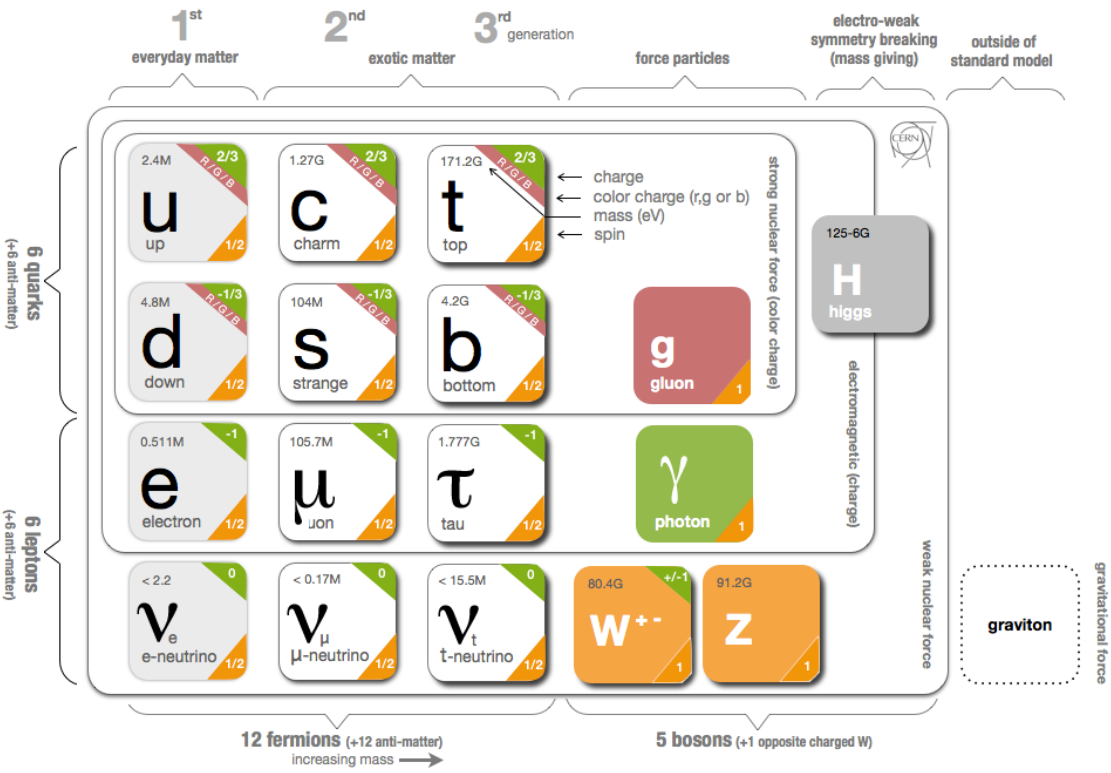

Figure 1.1: Particles of the standard model and several of their key properties, arranged in the commonly used "periodic table" of particles. Figure from Reference [1].

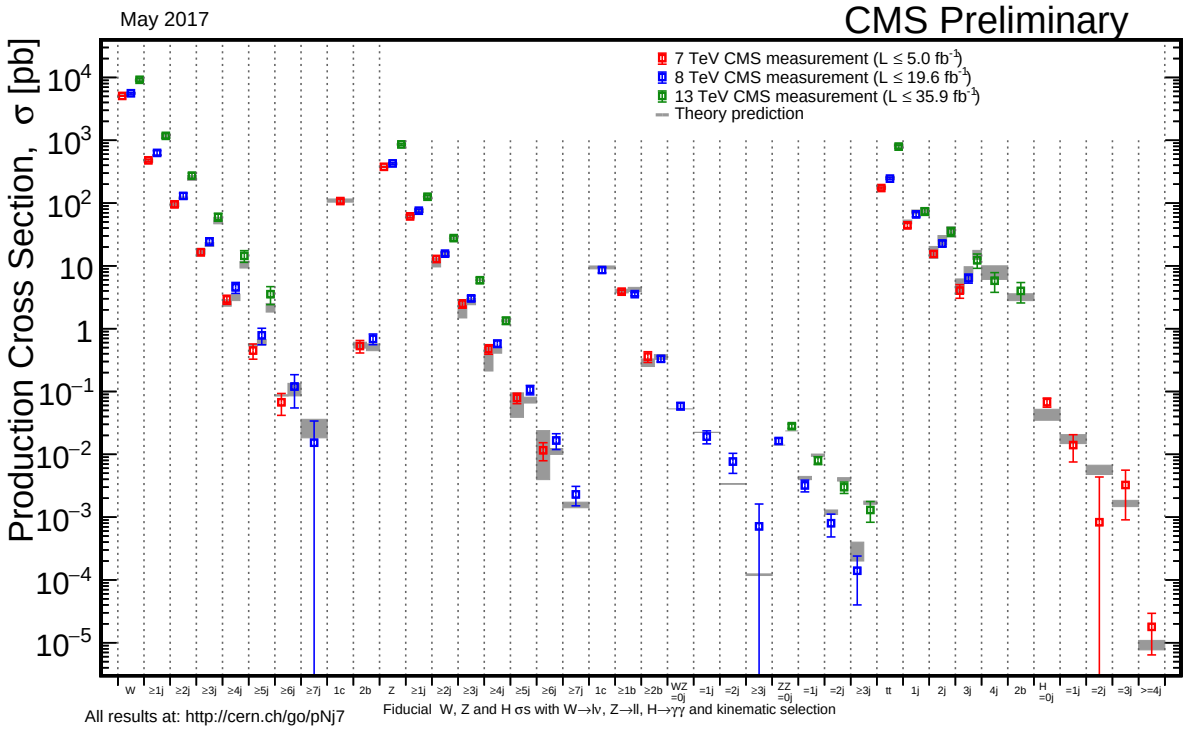

Figure 1.2: Cross section for production of selected standard model particles at the LHC. Figure from Reference [2].

1.2 Supersymmetry

While the standard model has been extraordinarily successful at predicting and explaining nearly all experimental results to date, there is strong evidence to suggest that it is not the full story. The failures to include explanations for the existence of gravity, dark matter [26, 27], and dark energy are all particularly suggestive. In light of such shortcomings, the standard model is frequently regarded as a low-energy effective field theory, with more fundamental physics becoming evident only at higher energies. This, however, raises several additional questions concerning the intriguingly low mass of the recently discovered Higgs boson, approximately 125 GeV. Two closely related concerns at the large seperation between the electroweak and Planck scales, known as the gauge hierarchy problem, and the potential fine-tuning of the mass of the Higgs boson in extensions of the standard model, known as the naturalness problem [28, 29, 30, 31, 32, 33].

In more detail, when calculating the physical mass of the Higgs boson in extensions of the standard model, renormalization requires a sum over all loop diagrams that can be inserted into the Higgs propagator. At one-loop order, the Higgs can couple to massive fermions via the diagram shown on the left in Figure 1.3. This diagram introduces a correction to the Higgs mass of

$$\Delta m_{\mathrm{H}}^2 = -\frac{\left|\lambda_{\mathrm{f}}\right|^2}{8\pi^2}\Lambda_{\mathrm{UV}}^2 + ..., \tag{1.6}$$

where Λ_{UV} is a momentum cutoff for the integral. In the case of quarks, an additional factor of three is needed to account for a sum over possible colors. Λ_{UV} should be approximately the mass scale at which the standard model is no longer valid. The presence of Λ_{UV}^2 means that the mass of the Higgs is likely to be highly sensitive to the mass of any new particles added to the standard model. For example, if $\Lambda_{\mathrm{UV}} \sim M_{\mathrm{Planck}}$,

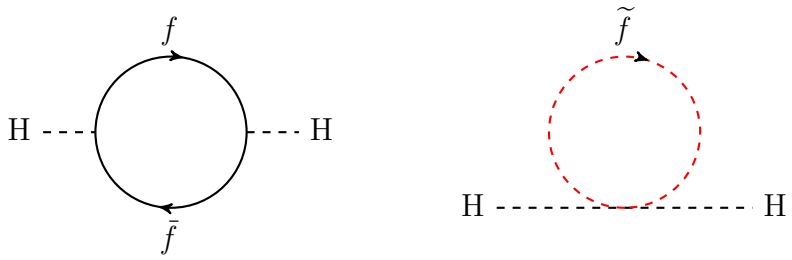

Figure 1.3: Left: correction to the Higgs propagator from a fermion loop. Right: hypothetical correction to the Higgs propagator from the fermion's scalar superpartner. Theoretical particles introduced by supersymmetry are drawn with red lines.

then Δm_{H}^2 can be thirty orders of magnitude larger than m_{H}^2. Introducing new physics to the standard model without significantly disturbing m_{H}^2 then requires either an unnatural fine-tuning of parameters or some mechanism for cancelling the Λ_{UV}^2 term.

One way to create such a cancellation is to introduce a new symmetry. More specifically, one can introduce an additional symmetry between fermions and bosons such that for every fermionic degree of freedom in the standard model, there is a bosonic superpartner, and vice versa. This symmetry is referred to as *supersymmetry*, or SUSY. For example, the correspondence between standard model and SUSY degrees of freedom is shown in Table 1.2.

The theoretical foundations of SUSY were developed during the early 1970s in, for example, References [34, 35, 36, 37, 38, 39, 40, 41]. We observe that for a scalar $\widetilde{f}$, the correction to the mass of the Higgs boson from the loop diagram on the right side of Figure 1.3 is

$$\Delta m_{\mathrm{H}}^2 = \frac{\lambda_{\widetilde{f}}}{16\pi^2}\Lambda_{\mathrm{UV}}^2 + ... \tag{1.7}$$

If $\lambda_{\widetilde{f}} = \left|\lambda_f\right|^2$, then this differs from the fermion loop correction in Equation (1.6) by a factor of exactly $-\frac{1}{2}$. The addition of two new scalar particles for each fermion (one per degree of freedom) in the standard model would therefore cancel the quadratic depen-

Table 1.2: Counting the degrees of freedom for the guage and Higgs bosons of the standard model and their superpartners. The left super-column shows the standard model particles; the center shows their superpartners; the right column shows the mass eigenstates of the superpartners, obtained by mixing the superpartners listed in the center super-column. The table assumes two complex Higgs doublets. Table reproduced from Reference [17].

SM Particle	J	D.o.F.	SUSY Particle	J	D.o.F.	SUSY Particle	J	D.o.F.
W^+	1	3	$\widetilde{W}^+$	$\frac{1}{2}$	2	$\widetilde{\chi}_1^+$	$\frac{1}{2}$	2
W^-	1	3	$\widetilde{W}^-$	$\frac{1}{2}$	2	$\widetilde{\chi}_1^-$	$\frac{1}{2}$	2
Z	1	3	$\widetilde{Z}$	$\frac{1}{2}$	2	$\widetilde{\chi}_2^+$	$\frac{1}{2}$	2
γ	1	2	$\widetilde{\gamma}$	$\frac{1}{2}$	2	$\widetilde{\chi}_2^+$	$\frac{1}{2}$	2
H	0	1	$\widetilde{H}$	$\frac{1}{2}$	2	$\widetilde{\chi}_1^0$	$\frac{1}{2}$	2
h	0	1	$\widetilde{h}$	$\frac{1}{2}$	2	$\widetilde{\chi}_2^0$	$\frac{1}{2}$	2
H^+	0	1	$\widetilde{H}^+$	$\frac{1}{2}$	2	$\widetilde{\chi}_3^0$	$\frac{1}{2}$	2
H^-	0	1	$\widetilde{H}^-$	$\frac{1}{2}$	2	$\widetilde{\chi}_4^0$	$\frac{1}{2}$	2
A	0	1						
Total		16	Total		16	Total		16

dence on $\Lambda_{\rm UV}$. In the case where $m_{\widetilde{f}} = m_f$, this cancellation of the quadratic term is exact even for higher-order contributions to $m_{\rm H}$ [42].

Of course, this abundance of new particles has not been observed. This can be explained by positing that supersymmetry is a broken symmetry. In order to maintain the cancellation of the $\Lambda_{\rm UV}^2$ divergences, one may consider only *soft SUSY breaking* scenarios in which the Lagrangian can be expressed as $\mathcal{L} = \mathcal{L}_{\rm SUSY} + \mathcal{L}_{\rm soft}$, where $\mathcal{L}_{\rm SUSY}$ is invariant under supersymmetric transformations and $\mathcal{L}_{\rm soft}$ contains only mass terms and couplings with positive mass dimension. Even within the Minimal Supersymmetric Standard Model (MSSM), the addition of $\mathcal{L}_{\rm soft}$ introduces over 100 new free parameters, including mass splittings between the standard model particles and their superpartners. This poses a serious experimental challenge as changing the parameters can dramatically alter the experimentally detectable signatures.

The principle of naturalness [3, 43, 44, 45, 46] provides some guidance as to likely values for some of the mass parameters. In the presence of a mass difference, the combined

correction to the Higgs mass from the fermion and two scalar loops amounts to

$$\Delta m_{\mathrm{H}}^2 = \frac{\left|\lambda_f\right|^2}{4\pi^2}\left(m_{\widetilde{f}}^2 - m_f^2\right)\ln\left(\frac{\Lambda_{\mathrm{UV}}}{m_{\widetilde{f}}}\right) + ... \tag{1.8}$$

While there is no longer a Λ_{UV}^2 dependence, the correction to the Higgs propagator may be unnaturally large if $m_{\widetilde{f}}$ is much larger than m_f. The constraints imposed on the masses depend on the the choice of cutoff scale Λ_{UV} and the degree of unnatural fine tuning one is willing to accept. At tree level, the Higgsino mass parameter μ is constrained to be $-\frac{m_{\mathrm{Z}}}{2} = |\mu|^2 + m_{\mathrm{H}}^2$, indicating that the Higgsino mass should be not too much greater than the electroweak scale. For the other superpartners, naturalness imposes constraints on their masses in rough accordance with their coupling to the Higgs boson. The top quark has a large Yukawa coupling, and its stop squark superpartners $\widetilde{\mathrm{t}}_{\mathrm{L}}$ and $\widetilde{\mathrm{t}}_{\mathrm{R}}$ couple to the Higgs boson at one loop order, implying that the stop squarks must be relatively light. The left-handed sbottom squark is in a doublet with $\widetilde{\mathrm{t}}_{\mathrm{L}}$ and should not be much heavier. Finally, the gluino couples to the Higgs boson at two loop order, but has a high production cross section and is therefore experimentally important in constraining natural SUSY models. A qualitative view of a potential natural SUSY spectrum is shown in Figure 1.4. After the first $1\,\mathrm{fb}^{-1}$ of LHC data, proposed natural masses for these particles were $m_{\widetilde{\mathrm{H}}} \leq 350\,\mathrm{GeV}$, $m_{\widetilde{\mathrm{t}}_{\mathrm{L}},\widetilde{\mathrm{t}}_{\mathrm{R}},\widetilde{\mathrm{b}}_{\mathrm{L}}} \leq 700\,\mathrm{GeV}$, and $m_{\widetilde{\mathrm{g}}} \leq 1.5\,\mathrm{TeV}$ [3].

To avoid conflict with experimentally observed conservation of baryon number B and lepton number L, many models of SUSY require conservation of R-parity, [47] defined per particle as $P_R \equiv (-1)^{(B-L)+2s}$, where s is the particle's spin. Particles from the standard model have $P_R = 1$, while their superpartners have $P_R = -1$. Conservation of R-parity thus requires that the standard model particles decay into an even number of SUSY particles. It also requires that the lightest supersymmetric particle (LSP) be stable. If the LSP is electrically neutral, this makes it a potential dark matter candidate.

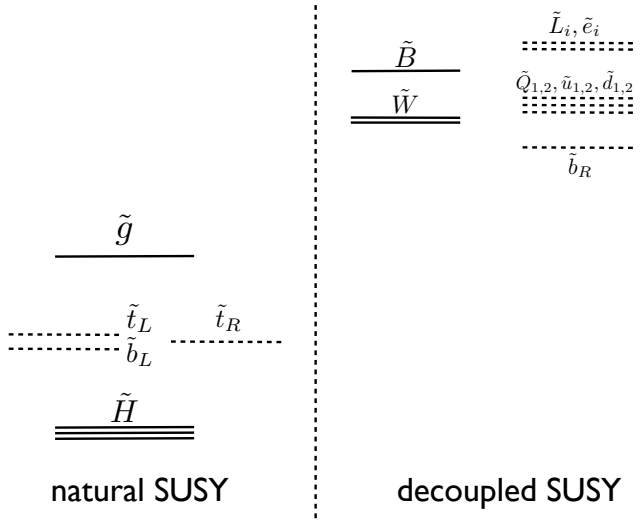

Figure 1.4: Qualitative example of a natural SUSY spectrum from Reference [3].

Even imposing naturalness and conservation of R-parity, a large variety of experimental signatures are possible. This complicates the design of experimental searches for supersymmetry as well as the reporting of results. Often, experimental results are reported in terms of their ability to exclude simplified model sprectra (SMS), where a particular decay chain is selected and all but two mass parameters fixed [48, 49, 50]. Even within this framework, there are a variety of potential models to look for.

In early searches, models with a high production cross section and a distinctive signature are the easiest targets. Generally, this means searching for models involving strongly interacting particles. Many of these models involve production of gluinos since they are both strongly interacting and potentially light (if naturalness can be trusted as a guiding principle). Others focus on direct production of squarks, which are also strongly interacting. The third generation squarks are of particular interest, both because they are closely tied to the naturalness of the Higgs boson mass and because decays of the stop squark often proceed through a top quark, resulting in events with high jet multiplicity and possibly containing leptons.

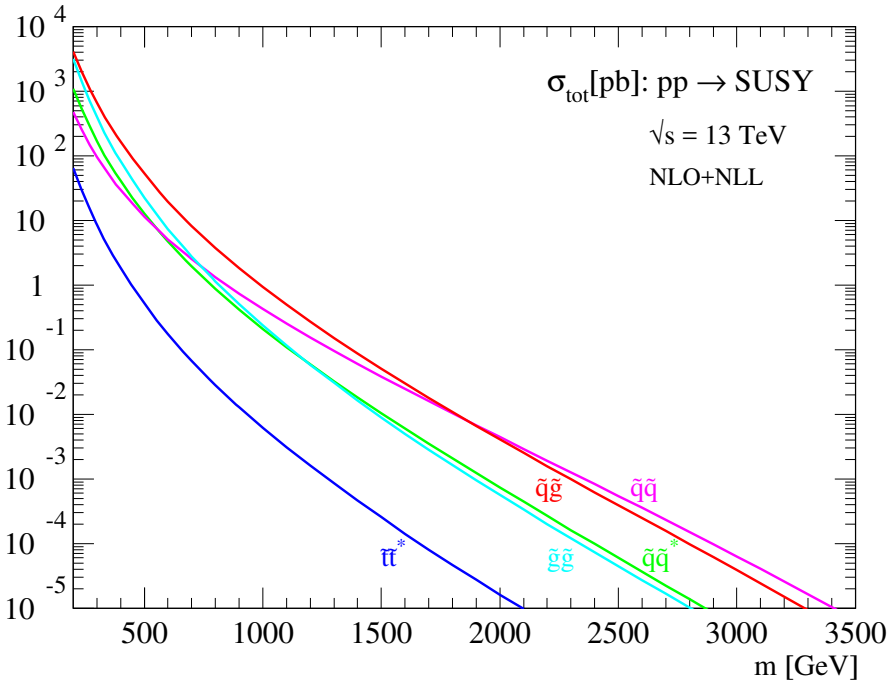

Figure 1.5: Comparison of gluino and squark production cross sections at a center-of–momentum collision energy of 13 TeV. The squark cross sections assume a ten-fold degeneracy among the squark flavors, not including the stop squark. Figure from Reference [4].

To give a sense of the relative cross-sections of these processes, Figure 1.5 provides a comparison of the gluino and squark production cross sections at a center-of-momentum energy of 13 TeV. At 1.9 TeV, the maximum gluino mass excluded by the search in this dissertation, the gluino pair production cross section is a factor of nearly 10^6 smaller than the inclusive $t\bar{t}$ production cross section shown in Figure 1.2.

For the search described in this dissertation, two models will be of particular importance. Referred to as T1tttt and T5tttt [51], both models involve pair production of gluinos with subsequent decay of the gluinos to two top quarks and an LSP each. In both cases, only the masses of the gluino and LSP are allowed to vary. For T1tttt, the intermediate stop squarks are heavy and produced off mass shell, resulting in a true three-body decay of the gluino. For T5tttt, the intermediate stop squarks are produced

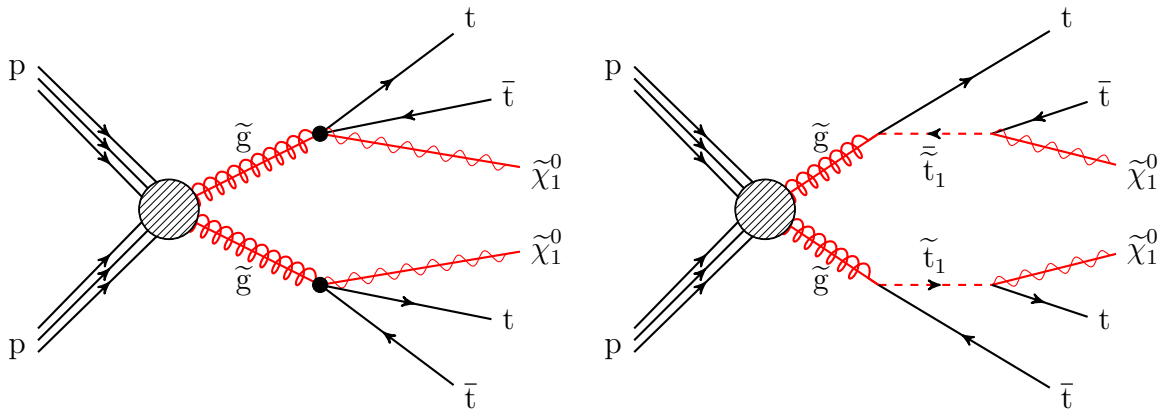

Figure 1.6: T1tttt (left) and T5tttt (right) Feynman diagrams. Note that the details of the underlying interaction are not shown, including the presence of additional final state particles produced from the proton remnants after the underlying parton-parton interaction, which are needed for charge conservation. Theoretical particles added by supersymmetry are drawn with red lines.

on mass shell, resulting in a sequential two-body decay. More specifically, the stop squark mass is fixed relative to the LSP mass, $m_{\tilde{t}_1} = m_{\tilde{\chi}_1^0} + 175\,\text{GeV}$, such that the decay of the stop squark is just barely able to produce an on-mass-shell top quark.

In the case of T1tttt, the gluino is assumed to decay to $t\bar{t}\tilde{\chi}_1^0$ with 100% branching fraction. Similarly, for T5tttt, the gluino is assumed to always decay to a top-stop pair, and the stop squark to always decay into $t\tilde{\chi}_1^0$. While this is by no means required by supersymmetry, the assumption of 100% branching fractions simplifies interpretation of cross-section limits, as discussed in later chapters. Feynman diagrams for both T1tttt and T5tttt are shown in Figure 1.6.

Even for a specific model, such as T1tttt, there may be multiple ways to conduct a search. The method described in this dissertation focuses on final states containing a single lepton. Approximately 40% of all T1tttt and T5tttt events contain a single lepton. Other searches involving a single lepton have been conducted at 7 TeV by the ATLAS [52, 53] and CMS [54] experiments, and at 8 TeV, again by both the ATLAS [55] and CMS [56] experiments. Even more recently both ATLAS [57] and CMS [58] have

carried out other searches in the single lepton channel at 13 TeV.

The search described in this thesis is only a part of a much broader search for supersymmetry at CMS. Other searches targeting strongly produced superpartners may search in events with no leptons (another approximately 40% of the T1tttt and T5tttt events) or have selections which allow sensitivity to a broader spectrum of models, such as gluino decays into other squark flavors or event direct production of squarks. On the other end of the spectrum are searches involving events with multiple leptons. Casting an even wider net, CMS also has searches for electroweakly produed particles, such as the higgsino. While these latter searches have lower signal cross sections than searches for strongly produced superpartners, they also typically have much lower background cross sections. Assuming no evidence of supersymmetry is found, these specialized searches are likely to become increasingly important as CMS continues to collect data and exclude the models with higher cross sections.

This search described in this dissertation will target the T1tttt and T5tttt models using events containing a single reconstructed lepton.

Chapter 2

Experimental Apparatus

Particle colliders are vital tools both for studying properties of the standard model and searching for evidence of physics beyond the standard model (BSM). Two properties of a collider are particularly important in determining its ability to produce evidence of BSM physics: the luminosity and center-of-momentum collision energy. During its 2016 run, the LHC produced collisions with an instantaneous luminosity of approximately $1.4 \times 10^{34}\,\mathrm{cm}^{-2}\,\mathrm{s}^{-1}$ and a center-of-momentum collision energy of 13 TeV, higher than any previous experiment.

This chapter discusses briefly some aspects of the hardware used in the production and collection of the data used in this thesis, including both the LHC and the CMS detector. More detailed descriptions of the LHC and CMS can be found in, for example, References [59] and [9].

2.1 Large Hadron Collider

Built in the former tunnel of the Large Electron Positron (LEP) collider, the LHC is part of a network of accelerators operated by CERN and located just outside of Geneva,

Switzerland. The other accelerators were built for earlier experiments and now serve to bring particles, either protons or lead ions, up to sufficient energy for injection into the main LHC rings. For protons, the initial source is a simple bottle of hydrogen gas. The ionized gas first passes through the Linear Accelerator 2 which increases their kinetic energy to 50 MeV. The gas is then divided into four parts, each of which is sent to one of the four rings of the Proton Synchrotron Booster, or PSB. The PSB raises their energy to 1.4 GeV. The four packets are then recombined and injected into the Proton Synchrotron, which accelerates the protons to 25 GeV and splits the beam into bunches of approximately 10^{11} protons. The bunches are sent to the Super Proton Synchrotron, where they are accelerated to 450 GeV. Finally, the bunches are injected into the two counter-circulating beam in the LHC, where they are accelerated to 6.5 TeV per beam. A schematic diagram of the network of accelerators connected to the LHC is shown in Figure 2.1.

The bunches are steered around the ring by a series of 1232 superconducting electromagnets, each capable of producing the 8.33 T field strength needed to keep the beams on course at the nominal design energy of 7 TeV. An additional 392 quadrupole magnets focuses the beam and thousands of sextupole and octupole magnets provide higher-order corrections to the beam shape. During each orbit, the beams are allowed to cross at four points along the ring which host the two general purpose, high luminosity experiments, CMS and ATLAS, and the two specialized detectors, ALICE, and LHCb.

At each crossing point, the instantaneous luminosity

$$L = \frac{N_{\mathrm{p}}^2 N_{\mathrm{bunches}} f \gamma F}{4\pi \epsilon_{\mathrm{n}} \beta^*} \tag{2.1}$$

gives the rate at which collisions occur for a given cross-section, where N_{p} is the number of protons per bunch, N_{bunches} is the number of bunches per beam, $f = 11\,245$ Hz is the orbit

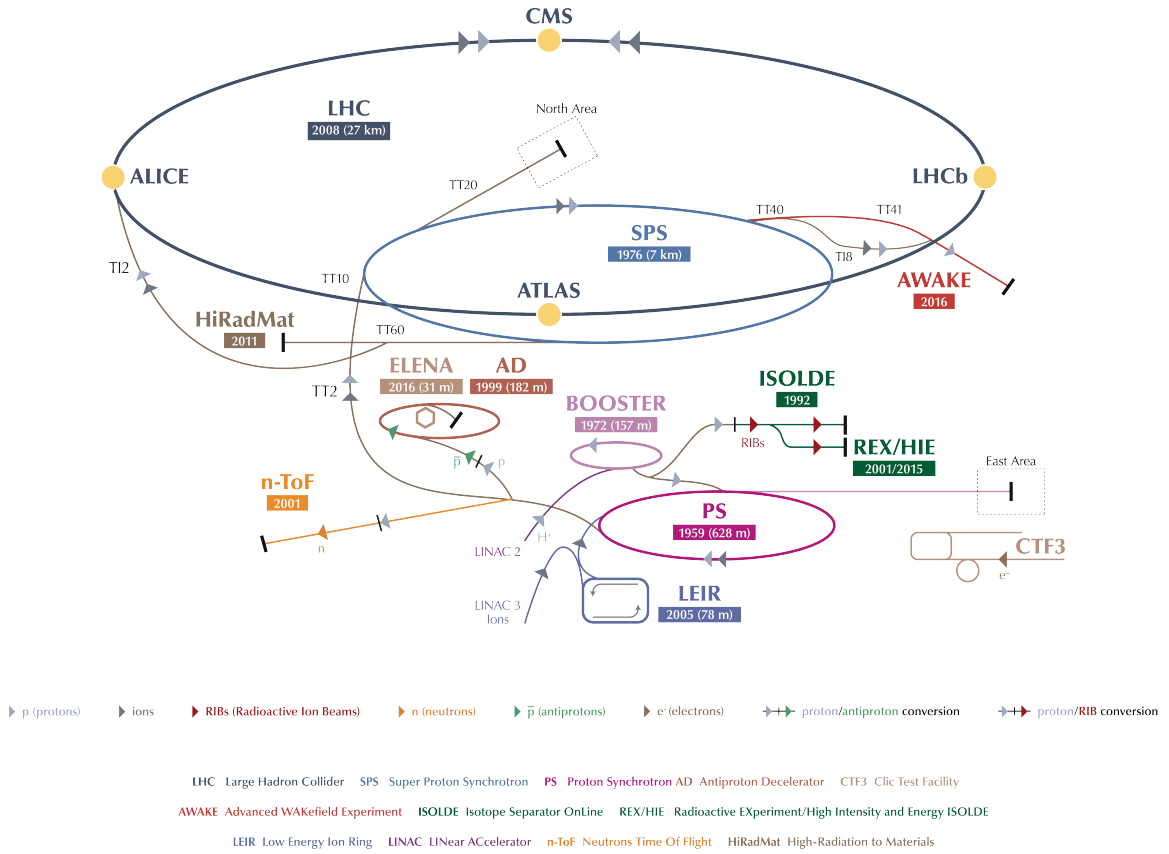

Figure 2.1: Diagram of the various accelerators connected to the LHC. Figure from Reference [5]

Table 2.1: Typical values of LHC beam parameters for several run years. Maximum number of bunches and peak luminosity are reported for Point 1 (ATLAS) and Point 5 (CMS), which have the highest luminosity [18].

Parameter	2012	2015	2016
Energy [TeV]	4	6.5	6.5
γ	4263	6928	6928
Bunch Spacing [ns]	50	25	25
β^* [cm]	60	80	40
Crossing Angle [µrad]	290	290	140
ϵ_{n} [µm]	2.5	3.5	2.0
Max. Protons per Bunch $[1 \times 10^{11}]$	1.6	1.15	1.15
Max. Bunches per Injected Train	144	144	96
Max. Bunches	1380	2244	2220
Colliding Bunch Pairs	1380	2232	2208
Max. Stored Energy [MJ]	140	270	265
Peak Luminosity $[10^{34}\,\mathrm{cm}^{-2}\,\mathrm{s}^{-1}]$	> 0.7	~ 0.5	1.4

frequency, γ is the relativistic Lorentz factor, ϵ_{n} is the normalized beam emittance, β^* is the betatron function evaluated at the collision point, and $F \approx 1$ is a geometric factor that arises due to nonzero crossing angle of the beams. While many of the parameters vary continuously during operation, representative values for the 2016 proton-proton collisions are shown in Table 2.1.

For a given process with cross-section σ, the expected number of events is $N = \sigma \int L\,dt$. The quantity $L_{\mathrm{int}} = \int L\,dt$ is referred to as the integrated luminosity and is a useful a measure of the total number of collisions produced over a time period. The integrated luminosity for 2016 proton-proton collisions is shown in Figure 2.2. Of the $41.07\,\mathrm{fb}^{-1}$ produced by the LHC, $37.82\,\mathrm{fb}^{-1}$ were recorded by CMS. The dataset used in for the search described in this thesis uses only $35.9\,\mathrm{fb}^{-1}$ of this sample after filtering out events measured with possible reconstruction errors [60]. The filtering process will be described in later chapters.

Unfortunately, the high luminosity of the LHC does not come for free. Figure 2.3 shows the distribution of the number of vertices per event for events passing the baseline

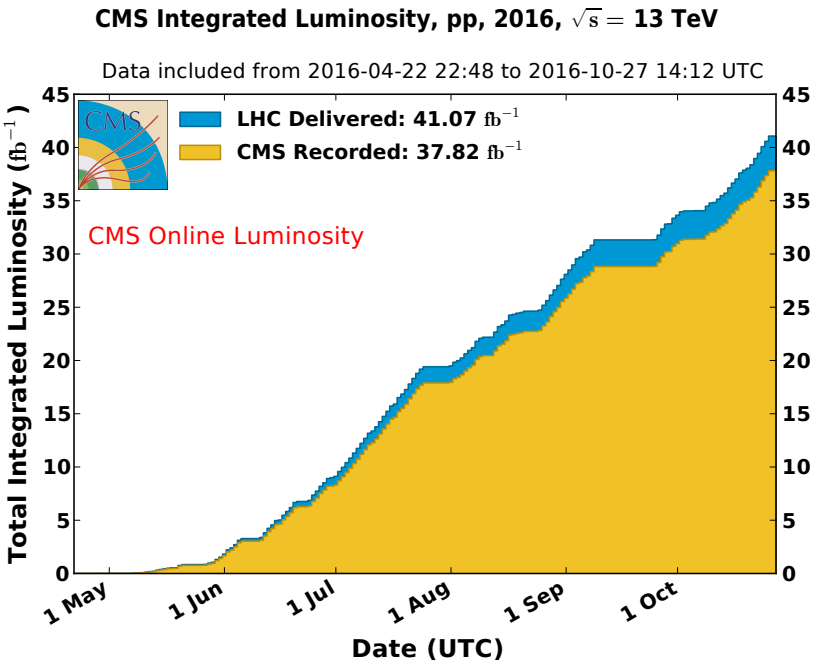

Figure 2.2: Integrated luminosity as a function of time for 2016 proton-proton collision. Figure from Reference [6]

selection of this analysis (described later in Chapter 5). Due to pileup, events have an average of nearly 23 primary vertices per event. This significantly complicates reconstruction of the events. Worse still, if care is not taken to account for pileup effects, the additional vertices can increase the apparent energy and jet multiplicity of an event, making it look more like a signal event.

2.2 Compact Muon Solenoid

Collisions occurring at the beam crossing at the LHC's Point 5 are recorded by the CMS detector. The overall shape of CMS is approximately cylindrical, with a length of 21.6 m, a diameter of 14.6 m, and a weight of 1.25×10^7 kg. The cylinder is centered on the nominal interaction point, which is defined as the origin of the coordinate system used by CMS. In this coordinate system, the x-axis points horizontally toward the center of

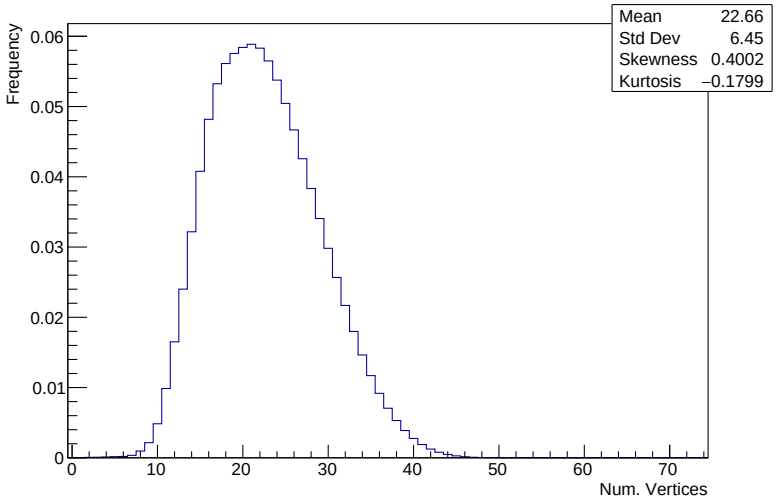

Figure 2.3: Number of vertices per event for events passing the baseline selection of this search. Due to pileup, events have an average of nearly 23 vertices each.

the LHC ring, while the y-axis points upward. The z-axis points along the circumference of the LHC, with the positive direction obeying a right-hand rule relative to the x- and y-axes. Rather than using Cartesian coordinates, it is often more useful to specify a radial position r and azimuthal angle ϕ in the xy-plane, or transverse plane. $\phi = 0$ is defined to lie along the x-axis. Outside the transverse plane, the pseudorapidity $\eta = -\ln\tan(\theta/2)$ is used as the third coordinate, where θ is the polar angle from the positive z-axis.

The detector itself consists of multiple layers, each designed to detect different classes of particles. These layers surround the collision point with nearly 4π of solid angle coverage, allowing measurement of momentum imbalances that may point to escaping weakly interacting particles. The layers, starting from those closest to the beam, are the pixel detector, silicon strip tracker, electromagnetic calorimeter, hadron calorimeter, and muon system. Sandwiched between the calorimeters and muon system is the namesake solenoid magnet. Figure 2.4 shows an exploded three-dimensional view of the CMS detectors, while Figure 2.5 shows a cross section through the barrel of the detector with the various layers labelled.

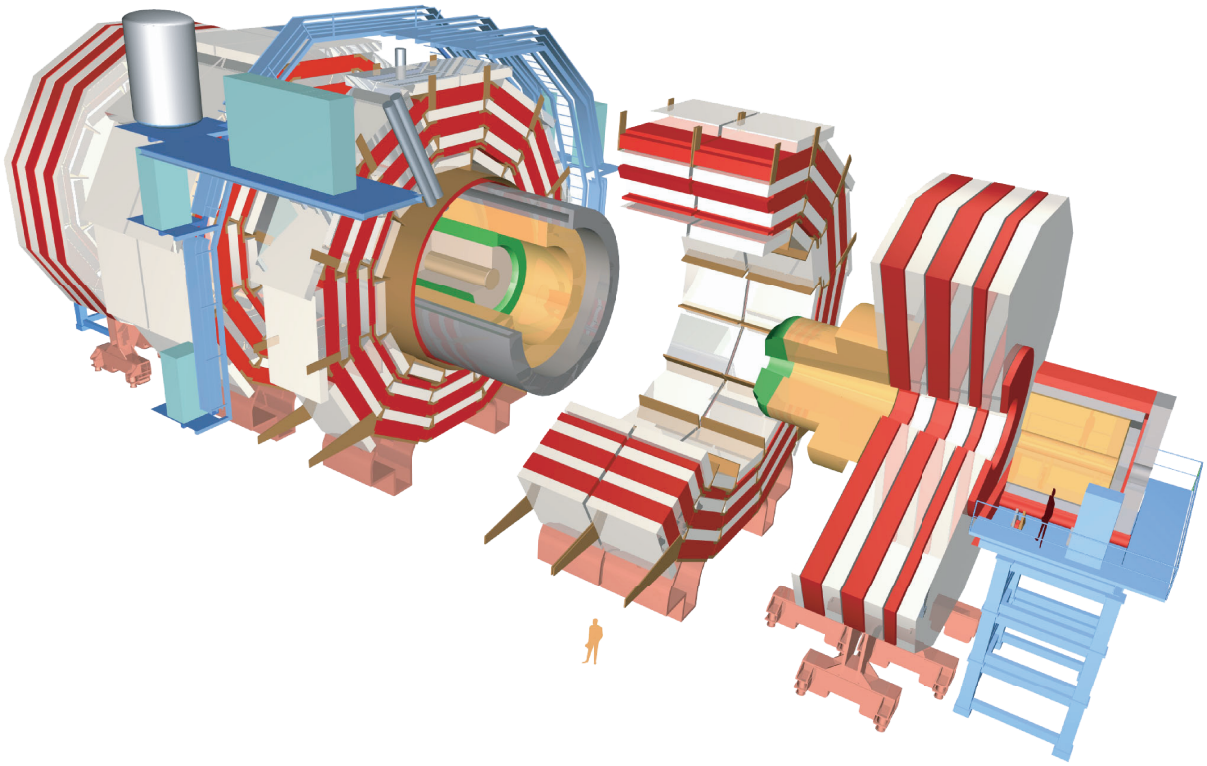

Figure 2.4: Exploded three-dimensional view of the CMS detector. Figure from Reference [7].

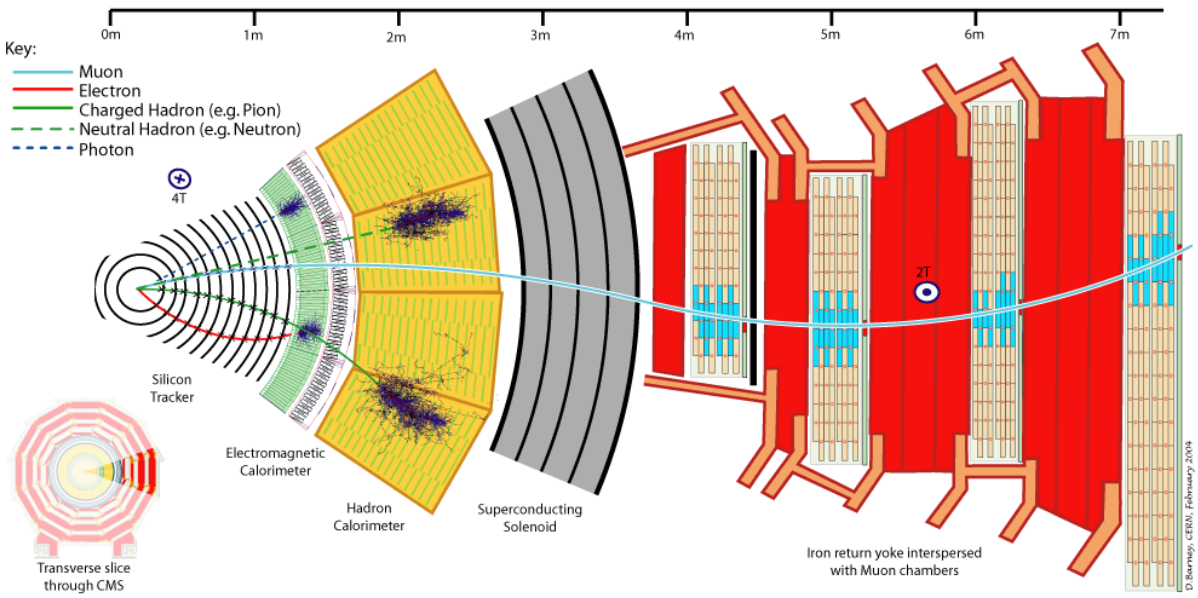

Figure 2.5: Cross sectional wedge of the CMS detector in the r-ϕ plane, showing the detector layers and the interaction of several types of particles with the various layers. Figure from Reference [8].

Many of the subdetectors are divided into "barrel" and "endcap" regions. The barrel regions are typically cylindrically shaped and provide coverage for low $|\eta|$. The endcaps are usually flat and lie in the transverse plane near the ends of the experiment to detect particles at high $|\eta|$. The exact meaning of "barrel" and "endcap" in terms of η coverage varies depending on the subdetector.

The remainder of this section describes briefly the main components of the CMS experiment.

2.2.1 Solenoid Magnet

CMS gets the last part of its name from its superconducting solenoid magnet. The magnet is 12.5 m long with an inner diameter of 6 m. It is the largest such magnet ever built, and was originally designed produce a 4 T magnetic field with a stored energy of 2.6 GJ. However, in order to mitigate aging effects, the magnet has thus far operated with a field strength of 3.8 T.

The solenoid shape of the magnet allows for a nearly uniform magnetic field parallel to the beam direction within the solenoid. This curves the tracks of charged particles in the transverse plane as they pass through the detector layers. The curvature begin at $r = 0$, allowing for precise momentum measurements and making it easier to trace which particles originated from which vertex. Momentum measurement requires detailed mapping of the magnetic field throughout the detector, such as that described in Reference [61].

The magnet is housed within an iron return yoke extending out to a diameter of 14 m and length of 21.6 m. Including the magnet itself, the yoke weighs approximately 10.8×10^6 kg. This large structure reduces the stray magnetic field outside the solenoid, increases uniformity of the field within the solenoid, provides structural support to other components of the detector, and acts as an absorber for the muon detector system.

2.2.2 Tracker

The component of the CMS detector nearest to the interaction point is the inner tracking system. The inner tracker is composed of two parts, a pixel detector and a silicon strip tracker. The innermost layer of the pixel tracker has a radius of just 4.4 cm. At such close proximity to the interaction point, the flux of particles through the detector can be as high as $1\,\mathrm{MHz\,mm^{-2}}$ [9]. The high flux requires using pixels rather than strips out to $r \approx 10\,\mathrm{cm}$ to keep occupancy of each detector element low. The pixel detector has three barrel layers and two endcap layers with a combined surface area of approximately $1\,\mathrm{m}^2$, covering the $|\eta| < 2.5$ region with 6.6×10^7 pixels. The pixels measure approximately $100\,\mu\mathrm{m} \times 150\,\mu\mathrm{m}$, but a resolution of $\sim 10\,\mu\mathrm{m}$ is obtained by interpolation of the analog signal strength in neighboring pixels.

Just outside the pixel layers are the silicon strip trackers. Beyond $r \approx 10\,\mathrm{cm}$, silicon strips are used in order to reduce the amount of data that must be read out with each event. The are four regions in which silicon strips are used: the Tracker Inner Barrel (TIB), Tracker Inner Disks (TID), Tracker Outer Barrel (TOB), and Tracker EndCaps (TEC). There are a total of approximately 9.3×10^6 silicon microstrips with a combined surface area of $198\,\mathrm{m}^2$, forming the largest silicon tracker yet built.

Within the TIB, there are four layers of strips parallel to the z-axis, with a pitches of $80\,\mu\mathrm{m}$ in the inner two layers and $120\,\mu\mathrm{m}$ in the inner two layers, giving resolutions of $23\,\mu\mathrm{m}$ and $35\,\mu\mathrm{m}$, respectively. The TOB has six layers with pitches of $183\,\mu\mathrm{m}$ in the inner four and $122\,\mu\mathrm{m}$ in the outer two, giving resolutions of $53\,\mu\mathrm{m}$ and $35\,\mu\mathrm{m}$, respectively. The TID consists of three disks of strips on each end, while the TEC has nine disks.

The silicon trackers extend to a radius of 1.1 m and cover $|\eta| < 2.5$ in pseudorapidity. The layout is such that outgoing particles with $|\eta| < 2.4$ typically pass through at least 9 layers.

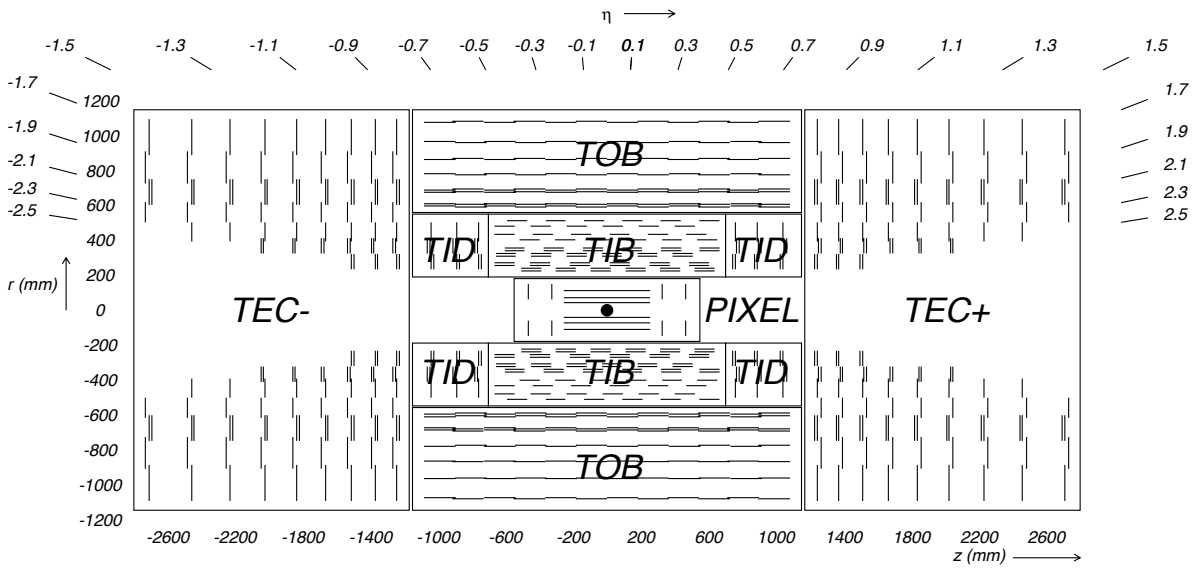

Figure 2.6: Layout of the pixel and silicon strip trackers. Figure from Reference [9].

The layout of the various tracker components in the configuration used to collect the data for this thesis is shown in Figure 2.6. The tracker has since been upgraded during the 2016-2017 LHC shutdown.

2.2.3 Electromagnetic Calorimeter

The electromagnetic calorimeter, or ECAL, is designed to measure the energy of electrically charged particles and photons after they pass through the tracker. The barrel of the ECAL contains 61 200 lead tungstate ($PbWO_4$) crystals and the endcaps contain another 7324 each. The lead tungstate crystals act as scintillators and are paired with avalanche photodiodes (APD) in the barrel and vacuum phototriodes (VPT) in the endcaps which act as photodetectors. The number of photoelectrons detected by the APDs and VPTs is roughly proportional to the energy of the incident particle, approximately 4.5 photoelectrons per MeV.

The barrel covers the region $|\eta| < 1.479$ with crystals measuring 0.0174×0.0174 in

η-ϕ coordinates. The endcap extends the ECAL coverage to $|\eta| < 3$ and contains crystals with inner faces measuring 28.62 mm $\times$ 28.62 mm.

The crystals are grouped in 5×5 sets for data readout, referred to as trigger towers in the barrel and as supercrystals in the endcap. As the name suggests, the trigger towers in the barrel are used to generate an "L1 trigger primitive" from the sum of energies in the component crystals. The role of the trigger primitives in the overall trigger decision is discussed later in this chapter. Trigger primitives are also generated from groups of endcap crystals. The trigger grouping in the endcap does not neatly correspond to supercrystals, but varies so that the groups are of roughly consistent size in η-ϕ coordinates across the endcap.

In addition to the barrel and endcap detectors, the ECAL contains an additional preshower detector mounted in front of the endcaps. The preshower detector improves electron and photon position resolution and helps identify neutral pions within the endcap. The preshower is approximately 20 cm thick and covers the region $1.653 < |\eta| < 2.6$. It consists of two layers, with each layer having a lead radiator the produces electromagnetic showers measured by silicon strip sensors. The silicon strips have a pitch of approximately 1.9 mm.

2.2.4 Hadronic Calorimeter

The hadronic calorimeter (HCAL) measures the energy of particles that interact primarily via the strong force and which are therefore able to pass through the ECAL. The HCAL has four main components: the HCAL barrel (HB), HCAL endcap (HE), outer calorimeter (HO), and forward calorimeter (HF). The HB and HE lie inside the solenoid, with the HB covering the $|\eta| < 1.3$ region and the HE covering $1.3 < |\eta| < 3$. The HO lies outside the solenoid and acts as a "tail catcher" for insufficiently contained showers over

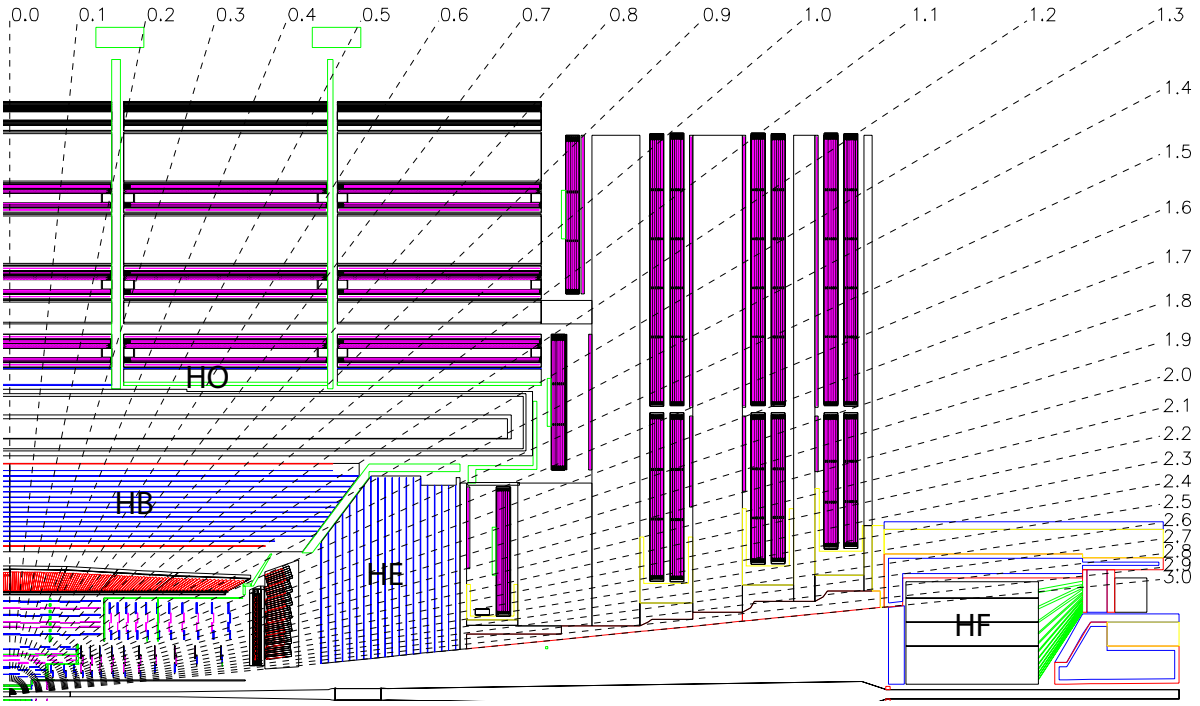

Figure 2.7: Diagram of one quarter of the CMS detector, veiwed in the r-η plane. The diagram highlights the location of the HCAL subdetector components, positioned outside the tracking detector and inside the muon chambers. Figure from Reference [9].

$|\eta| < 1.3$. The HF are 11.2 m away from the interaction point and cover the $3 < |\eta| < 5.2$ region. The layout of the HCAL components is shown in Figure 2.7.

The HB is a sampling calorimeter with alternating layers of metal absorber and plastic scintillator. There are 16 layers of absorber ranging from 40 mm to 75 mm thick. The innermost and outermost layers are made of steel, while the 14 intermediate layers are made of brass. Together, these layers provide a minimum of 5.39 interaction lengths of absorber throughout the barrel. Interleaved with the 16 layers of absorber are 17 layers of plastic scintillator segmented into regions measuring 0.087×0.087 in η-ϕ coordinates, each corresponding to one HCAL trigger tower. The first scintillator layer uses structural components between the ECAL and HCAL as its absorber. Light from the scintillators is picked up by 0.94 mm wavelength-shifting fibers and read out by hybrid photodiodes.

The HE is based on a design similar to the HB, with brass layers providing about 10

interaction lengths of absorber material. The scintillator is divided into regions measuring 0.087×0.087 in η-ϕ for $|\eta| < 1.6$ and approximately 0.17×0.17 for $|\eta| \geq 1.6$.

The HO uses the solenoid magnet itself as an absorber and has either one or two layers of scintillator with a tile size of 0.087×0.087. The photodetectors of the HO were upgraded to silicon photomultipliers during the LHC long shutdown one (LS1) period in 2013-2014.

Due to its position at high $|\eta|$, the HF is subjected to extraordinary amounts of radiation. To improve its radiation hardness, 600 µm diameter quartz fibers are used in place of the plastic scintillator. The steel absorber produces a shower which then generates Cherenkov radiation within these fibers. The fibers are bundled into towers measured 0.175×0.175 in η-ϕ coordinates, and the light collected by conventional photomultipliers.

2.2.5 Muon System

The muon system forms the outermost layers of the CMS detector and contains three different types of detector modules: drift tubes (DTs), which cover the barrel region out to $|\eta| < 1.2$; cathode strip chambers (CSCs), which instrument the endcap region in the pseudorapidity range $0.9 < |\eta| < 2.4$; and resistive plate chambers (RPCs), which cover both the barrel and a portion of the endcap in the pseudorapidity range $|\eta| < 1.6$ in order to provide redundancy and improved trigger performance.

Drift Tubes

The drift tube detector system is based on rectangular drift cells with a cross-section of 13 mm × 42 mm and a length of up to 2.4 m. An anode wire at 3600 V runs along the center of each cell while cathode strips at −1200 V line the narrow sides, as shown in Figure 2.8. Muons passing through the cell ionize the argon gas mixture. Within

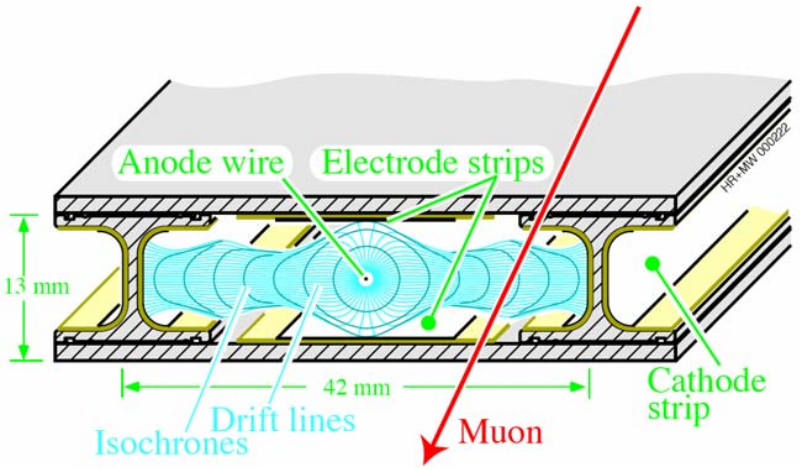

Figure 2.8: Cross-sectional view of a drift cell. Figure from Reference [9]

380 ns the resulting free electrons drift to the anode wire where they cause a measurable transient voltage change.

The drift tubes are arranged in superlayers, each containing four layers of parallel drift cells. Each of the four barrel rings, known as stations, contains 12 chambers. Chambers in the innermost three stations contain three superlayers each, two with the long dimension of the cells along the z-axis (to measure r and ϕ) and a middle superlayer with the long dimension in the ϕ direction (to measure r and η). The chambers in the outermost station do not contain the middle η-sensitive superlayer.

Cathode Strip Chambers

The large and non-uniform magnetic field present in the endcaps, as well as the significantly higher flux of particles, precludes the use of DTs. Instead, multi-wire proportional chambers called cathode strip chambers, or CSCs, are used. The four layers of CSC in each endcap are called stations. The stations are disk-shaped and contain two concentric rings of wedge-shaped CSCs, except for the innermost station, which has a third ring of CSCs.

Each CSC has six layers of anode wires alternating with seven layers of cathode panels divided into strips. The wires are approximately parallel to ϕ, while the cathode strips are oriented radially. The CSCs are filled with a 50% CO_2, 40% Ar, and 10% CF_4 gas mixture. As in the DTs, a muon passing through the CSCs will cause ionization of the gas. The freed electrons drift to the nearest wire, which provides an r-η position measurement. The ions induce charges on nearby cathodes, which can be interpolated to measure the r-ϕ position. The off-line spatial resolution is better than 75 µm for the inner two rings of the first station (ME1/1 and ME1/2), and 150 µm in other CSCs.

In order to accomodate an increasing muon flux, the CSC read-out electronics for the ME1/1 station were upgrade from copper to fiber optic lines. Figure 2.9 shows a portion of this system, highlighting the Optical Data Acquisition Motherboard (ODMB), which aggregates the data into ethernet packets that can be sent to a commercial ethernet card. I helped to developed some of the monitoring firmware for the ODMB and installed several of the ODMBs.

Resistive Plate Chambers

The resistive plate chambers (RPCs) used by CMS are yet another type of gas detector and are used to improve muon trigger performance. The RPCs consist of two Bakelite plates separated by 4 mm gap filled with a gas mixture containing over 95% $C_2H_2F_4$. Between the two plates is a layer of copper readout strips. The design has a time resolution of approximately 1 ns, much shorter than the 25 ns gap between bunch crossings, making it useful in disambiguating which crossing produced a muon at the trigger level before high resolution tracking is performed.

Within the barrel, stations one and two have RPCs mounted to both the near and far sides (relative to the beam line) of the DT chambers. Stations three and four have RPCs only on the near side, providing a total of six layers of RPCs throughout the barrel. The

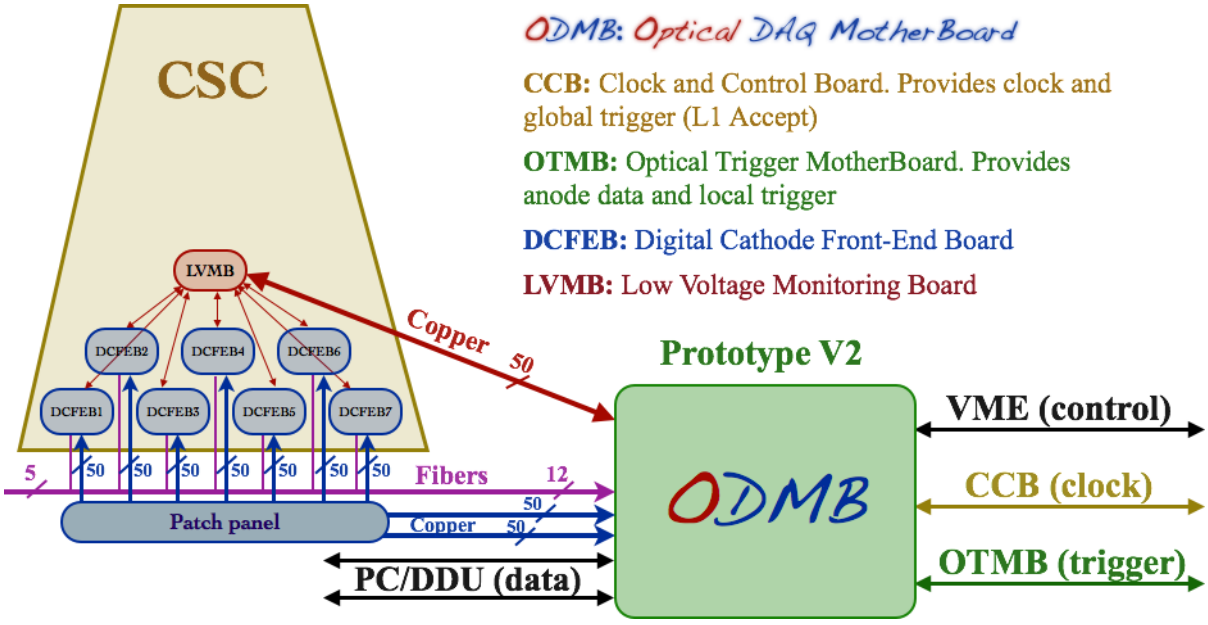

Figure 2.9: Schematic showing a portion of the data path for the ME1/1 stations, including the Optical Data Acquisition Motherboard (ODMB). Image from Reference [10].

readout strips vary in size, with each covering 0.3125° in ϕ.

In the endcap, RPCs are mounted on the inner face of the the outer rings of the four muon stations (outer two rings of the first station), providing coverage to $|\eta| < 1.6$. Strips are oriented radially and span 0.3125° in ϕ.

2.2.6 Trigger and Data Acquisition

The CMS trigger system [62] is divided into two levels, called the Level-1 Trigger (L1) and High-Level Trigger (HLT). At a bunch crossing frequency of 40 MHz, it is not possible to save every event, and it is the job of the L1 trigger to reduce this rate to a more manageable maximum of 100 kHz using specially designed hardware.

The L1 trigger has approximately 4 µs to determine whether an event should be saved. Due to the complexity of reconstructing tracks from the large number of hits typically present in the inner tracker, the decision is made using only information from

the calorimeters and muon system.

The calorimeter branch of the L1 trigger takes input from the both the HCAL and ECAL. The trigger decision starts from trigger primitives generated by the trigger towers. Trigger primitive generators compute the sum of transverse energies within one trigger tower. For $|\eta| < 1.74$, these correspond to an η-ϕ area of 0.087×0.087. The towers are larger at higher $|\eta|$. Trigger primitives are passed to the Regional Calorimeter Trigger (RCT). For $|\eta| < 2.5$, the RCT finds four isolated and four non-isolated electron/photon candidates per region, with each region consisting of a 4×4 grid of trigger towers. Note that electrons and photons cannot be distinguished at L1 due to the lack of tracker data. The RCT additionally computes several quantities needed for detection of minimum-ionizing particles, vetoing of tau leptons, and calculation of muon isolation. Finally, the global calorimeter trigger takes the information from the RCTs to construct L1 jets and to compute the event-level transverse energy, missing transverse energy, and final isolated and non-isolated electron/photon candidates.

The muon branch of the trigger is itself composed of two main parts, one which forms tracks from the DTs and CSCs, and one which uses the RPCs. The DTs and CSCs are both able to compute local trigger information. The DTs compute two-dimensional track segments in the transverse plane and hit patterns in the η direction, while the CSCs are able to compute fully three-dimensional track segments. These segments and patterns are sent to the DT and CSC Track Finders which connect the segments into full candidate tracks. Meanwhile, the RPCs produce a separate set of track candidates. The track candidates are all sent to the Global Muon Trigger which combines the information from the DTs, CSCs, and RPCs to construct up to four muon candidates.

The Global Calorimeter Trigger and Global Muon Trigger send their candidate particles and event-level information to the Global Trigger, which takes this input and checks whether any of 128 possible criteria are met. These criteria range from the presence of

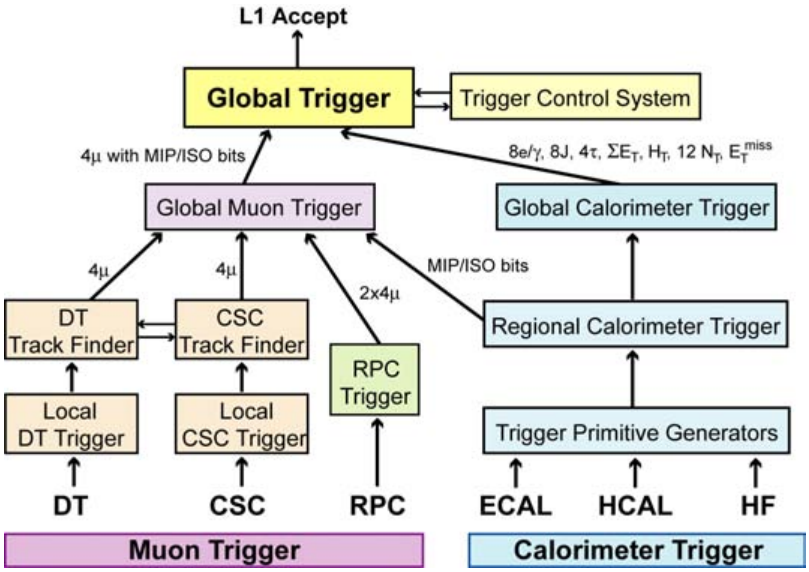

Figure 2.10: Schematic diagram showing how an L1A is generated from trigger primitives from the calorimeter and muon systems [9].

certain objects (e.g., muons) to global requirement on the summed transverse energy of the event. If the criteria are met, an L1-Accept (L1A) is generated, and the full read out of the event sent on to the Data Acquisition (DAQ) system. A schematic diagram showing the construction of an L1A is shown in Figure 2.10.

When an L1A is generated, it is sent to the various detector subsystems. Upon receipt of an L1A, the subsystems send any buffered data from the corresponding event to an event builder. The event builder aggregates the data from the various subsystems into a single event which is sent to a filter farm, where the software-based HLT decides whether to continue processing the event. The HLT has access to more information than the L1 trigger and has time to perform a more elaborate reconstruction before making a determination of whether to record and fully reconstruct the event. Within the HLT, a number of different triggers are implemented with varying requirements for the momentum and number of particles. To keep the total rate of events accepted by the HLT below 100 kHz, triggers with the loosest requirements are *prescaled*, so that only a

fraction of events nominally meeting the trigger requirements are accepted.

Chapter 3

Object and Event Reconstruction

This chapter describes the reconstruction of various physics objects, such as leptons and jets, and event-level variables relevant to this search for supersymmetry. The description starts from the output of the various subdetectors described in Section 2.2 and explains how they are used to form tracks, vertices, and calorimeter clusters. It then proceeds to describe the particle–flow algorithm used to connect these rudimentary objects into candidate particles. The jet-clustering and b-tagging algorithms are also included. Finally, important event-level variables such as $E_{\mathrm{T}}^{\mathrm{miss}}$, m_{T}, and M_J are defined.

3.1 Tracks

Reconstruction of tracks within the silicon trackers is a daunting task, requiring that the $\sim 10^3$ particles passing through the detector with each bunch crossing be reconstructed fast enough for use in the HLT, a rate of about 100 kHz. Further, tracks must be reconstructed over a wide range of energies, from as low as 100 MeV (needed to achieve decent jet momentum resolution in later reconstruction steps), up to the 1 TeV scale for high momentum leptons. The position of tracks must also be accurately measured in

order to reconstruct vertices, needed to identify b-hadron decays and to remove tracks produced by pileup interactions.

Reconstruction of tracks is performed by specialized software known as the Combinatorial Track Finder (CTF). The algorithm proceeds in four steps. First, track "seeds" are established. Each seed is built from either three three-dimensional hits in the pixel detector or two three-dimensional hits and an assumption that the track originates near the beam spot. These hits are sufficient to estimate the five parameters needed to describe the helical path of a charged particle through the nearly uniform magnetic field inside the solenoid. Pixel hits are preferred over strip hits for this step because they provide more information per hit (three coordinates instead of two), because their occupancy is lower due to their higher granularity, and to maintain efficiency for low momentum particles that inelastically scatter before reaching the outer layers of the tracker.

Second, once the seeds are established, the estimated parameters for the helical trajectory are used to search outwards through the tracker layers for additional hits. A Kalman filter updates the parameters as each new hit is added to the track.

The third step is to refit the track using all the identified hits. When refitting, any assumed constraints about the track passing through the beam spot are removed. Rather than assuming a uniform magnetic field, the equation of motion through the non-uniform field is solved via a fourth-order Runge-Kutta method. The fit is done both starting from the beam-line and tracing the track outwards, and starting from the outside and working inward. Averaging the two fits smooths the result and provides the best estimate of the track trajectory at each tracker layer. Spurious hits that do not match this fit are removed from the track at this stage.

The fourth step is to discard tracks not meeting various quality requirements, including constraints on the χ^2/N.D.o.F., impact parameter, and number of hit and missed layers of the tracker.

The entire process is repeated six times. Most tracks are found in the first iteration, but tracks with small transverse momentum p_{T} and large impact parameter are not found until later iterations when most tracker hits have already been assigned to tracks from earlier iterations.

The set of tracks is then used to reconstruct the primary vertices (vertices resulting from the initial collision rather than secondary decays of produced particles) for the event. This is done using a deterministic annealing algorithm to cluster tracks by their longitudinal impact parameter. First, a subset of the tracks are selected which have small transverse impact parameter, at least five hits (with at least two in the pixel layers), and good fit quality. The tracks are initially all assigned to a single vertex, but as the annealing "temperature" is lowered, the tracks are divided among multiple vertices. The algorithm terminates at a cutoff that compromises between the risk of accidentally splitting a true single vertex into multiple reconstructed vertices and the risk of merging unrelated vertices. Once the set of vertices is established, an adaptive vertex fitter estimates their three-dimensional positions from the constituent tracks.

The vertex reconstruction process generally results in multiple primary vertices, but even in high pileup scenarios, there is usually only one primary vertex of interest. It is understood that *the* primary vertex refers to the primary vertex with the highest sum of track p_{T}^2.

In addition to the above tracks obtained from the silicon tracker, standalone muon tracks are reconstructed using only the track segments in the muon system. Standalone muon tracks are not used for vertex finding.

A far more detailed description of the track and vertex reconstruction process can be found in Reference [63].

3.2 Calorimeter Clustering

Much as the numerous hits in the silicon tracker are joined to form tracks, the energy deposits in the various calorimeters are connected to form calorimeter clusters. These clusters, rather than the raw energy deposits, are the inputs for the particle–flow algorithm described in the next section. The clustering is done separately in each of calorimeters, including treating the first and second layers of the ECAL preshower independently. No clustering is applied for the forward hadron calorimeter.

The clustering algorithm has three steps. First, calorimeter towers/cells whose energy deposits are a local maximum and above a threshold are labeled as cluster seeds. In the second step, these seeds expand into groups called topological clusters by iteratively adding neighboring seeds with significant energy deposits. During this process, topological clusters may merge so that a single topological cluster contains multiple seeds. The final step in the clustering algorithm is to partition the energy in the topological cluster among the seeds to obtain the final particle–flow clusters.

3.3 Particle Flow

The tracks (both standard charged particle tracks in the tracker and standalone muon tracks) and calorimeter deposits described above make up the basic particle–flow (PF) elements. The PF algorithm [64, 65] is designed to take these elements and reconstruct them into candidate particles. The algorithm has two basic steps. First, related tracks and calorimeter clusters are grouped together to form *blocks* in a process known as *linking*. Once all blocks have been established, each block is reconstructed into one or more muons, electrons, photons, charged hadrons, and neutral hadrons.

3.3.1 Linking

In the linking step, a "distance" is defined between pairs of elements in an event. Elements with a smaller distance between them are more likely to originate from a single underlying particle and are grouped into a *block* of potentially related elements. Links only connect PF elements from different subdetectors, reflecting the fact that particles should not pass through the same subdetector twice in different ares. For example, two different HCAL clusters will never be linked.

In the case of links between charged particle tracks and calorimeter deposits, the trajectory of the track is extrapolated though the calorimeter, including an estimated depth at which maximum energy deposition should occur. If this point lies within a calorimeter cluster, the cluster and track are linked and the link distance defined as the η-ϕ distance between the extrapolated and measured cluster locations.

Potential Bremsstrahlung photons in the ECAL are linked to tracks by extrapolating tangent lines from the tracks to the ECAL. The distance measure is the η-ϕ distance between extrapolated and measured cluster location.

Links between an ECAL cluster and either an HCAL or preshower cluster are generated when the position of the cluster in the more granular detector is within the boundaries of the cluster in the less granular detector. The η-ϕ separation is again used as the distance measure.

Links between standalone muon tracks and charged particle tracks are produced when the two tracks can be accommodated by a single fit with small χ^2. The resulting block is called a global muon and the χ^2 of the fit used as the distance measure. The χ^2 is also used to disambiguate cases when a standalone muon is compatible with multiple charged particle tracks.

3.3.2 Classification and Reconstruction

The blocks generated in the linking step only describe which elements are related, but do not specify which particle type(s) generated the block. To reconstruct this information, the PF algorithm tries to assign portions of the momentum in the block to muon, electron, photon, charged hadron, or neutral hadron candidates. The algorithm proceeds hierarchically through theses categories and attempts to assign as much of the momentum as possible to the earlier ones which have more distinctive signatures and can be more easily identified.

First, any global muons compatible with their corresponding tracker muon are identified as particle flow muons and their tracks removed from the block.

After PF muons are removed, the next step is to identify electrons. Tracks are refit with a Gaussian-Sum Filter [66] and Bremsstrahlung photon deposits in the ECAL identified. If the track and ECAL deposits are consistent with an electron, they are labeled as PF electrons and removed from the block.

For each remaining track, if the track is linked to multiple HCAL clusters, only the single closest link is kept. In the case of a link to multiple ECAL clusters, the links are ranked by distance. The links with the largest distance parameter are dropped until the total HCAL and ECAL cluster energy is less than the track momentum. At this point, there are four possibilities:

- The track momentum is significantly larger than the calorimeter energy. This occurs in less than 0.03% of cases, and results in the extra track momentum being labeled as a muon or fake track.

- The track momentum and calorimeter energy are consistent within measurement uncertainty. A PF charged hadron is produced with momentum set to a weighted average of the track and calorimeter measurements and mass set to that of a charged

pion.

- The HCAL and ECAL total energy is greater than the track momentum, but the excess is less than the total ECAL energy. The track is considered a PF charged hadron as in the previous case, and the excess calorimeter energy assigned as a PF photon.

- The HCAL and ECAL total energy is greater than the track momentum, but the excess is greater than the total ECAL energy. The track is considered a PF charged hadron, the ECAL energy is assigned to a PF photon, and any remaining energy assigned to a PF neutral hadron. The photon is given the largest possible portion of the ECAL energy since photons typically comprise about 25% of the energy deposited by a jet in the ECAL, while neutral hadrons account for less than 3%.

3.4 Leptons

While the PF algorithm does identify electron and muon candidates, it applies only very weak identification requirements. Before electrons or muons can be counted in this analysis, several additional identification criteria must be applied. The additional identification criteria for muons [67] are listed in Table 3.1, while the identification criteria for electrons [68] are listed in Table 3.2.

Figure 3.1 shows the overall efficiency of the reconstruction, identification, isolation, and vertexing requirements for both muons and electrons as a function of p_{T} and η.

3.4.1 Mini Isolation

One is typically only interested in leptons produced by the decay of a $\mathrm{W}^{\pm}$ produced in the initial hard-scatter process. Such leptons are called *prompt*. Often, non-prompt

Table 3.1: Kinematic and quality requirements applied to muons. d_{xy} and d_z are the transverse and longitudinal impact parameters of the tracks associated to the muon. The "Is global or tracker muon" excludes standalone muons.

Muon Property	Requirement
p_{T} [GeV]	> 20
$\lvert\eta\rvert$	< 2.4
$\lvert d_{xy}\rvert$ [mm]	< 2
$\lvert d_z\rvert$ [mm]	< 5
$I^{\mathrm{rel}}_{\mathrm{mini}}$	< 0.2
PF muon ID	True
Is global or tracker muon	True
Fraction of valid tracker hits	> 0.8
Segment compatibility	> 0.303
Requirements below apply only if segment compatibility ≤ 0.451	
Normalized global track χ^2	< 3
χ^2 of tracker-standalone match	< 12
Track kink χ^2	< 20

Table 3.2: Kinematic and quality requirements applied to electrons. Different requirements are applied to electrons in the barrel ($\lvert\eta_{\mathrm{supercluster}}\rvert \leq 1.479$) and endcap ($\lvert\eta_{\mathrm{supercluster}}\rvert > 1.479$). d_{xy} and d_z are the transverse and longitudinal impact parameters of the tracks associated to the electron. $\sigma_{i\eta i\eta}$ is a shower shape variable which measures the width of the ECAL energy deposits in the η direction.

Electron Property	Barrel Requirement	Endcap Requirement
p_{T} [GeV]	> 20	> 20
$\lvert\eta_{\mathrm{supercluster}}\rvert$	N.A.	< 2.5
$\lvert d_{xy}\rvert$ [mm]	< 0.118	< 0.739
$\lvert d_z\rvert$ [mm]	< 3.73	< 6.02
$I^{\mathrm{rel}}_{\mathrm{mini}}$	< 0.1	< 0.1
$\sigma_{i\eta i\eta}$	< 0.0101	< 0.0283
$\Delta\eta$(supercluster, track)	< 0.0103	< 0.00733
$\Delta\phi$(supercluster, track)	< 0.0336	< 0.114
$E_{\mathrm{hadronic}}/E_{\mathrm{electromagnetic}}$	< 0.0876	< 0.0678
$\frac{1}{E} - \frac{1}{p}$ [GeV^{-1}]	< 0.0174	< 0.0898
Missing hits	≤ 2	≤ 1
Pass photon conversion	True	True

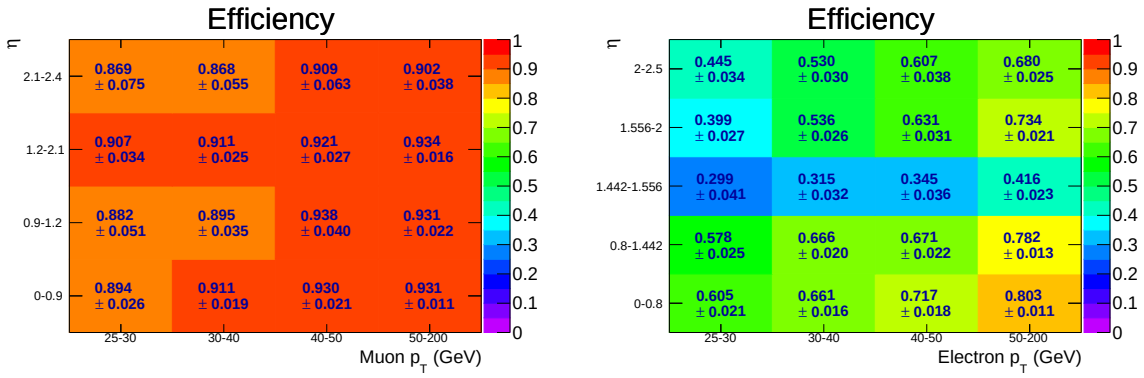

Figure 3.1: Overall efficiency of the reconstruction, identification, isolation, and vertexing requirements for both muons (left) and electrons (right) as a function of p_{T} and η. Plots from supplementary material for Reference [11] and published online in Reference [12].

leptons are produced in association with a number of other particles in secondary decays or hadronization processes. For example, the hadronization of b-quarks produces an electron or muon in approximately 20% of cases. Since the energy associated with such processes is generally much lower than the transverse momentum of the decaying or hadronizing particle, this results in a number of other particles produced within close proximity to the lepton. Prompt leptons, on the other hand, are more likely to be isolated.

The presence of nearby particles provides a useful means by which to distinguish prompt and non-prompt leptons. More specifically, one may use the *mini isolation* variable, $I^{\mathrm{abs}}_{\mathrm{mini}}$, originally described in Reference [69]. Mini isolation is defined as the sum of the transverse momenta of PF candidates within a p_{T}-dependent radius of the lepton in

η-ϕ space,

$$
\begin{aligned}
I_{\text{mini}}^{\text{abs}} = & \sum_{\text{cone}} p_{\text{T}}(\text{charged hadrons from PV}) \\
& + \max\Big[\sum_{\text{cone}} p_{\text{T}}(\text{photons}) + \sum_{\text{cone}} p_{\text{T}}(\text{neutral hadrons}) \\
& \quad - \frac{1}{2}\sum_{\text{cone}} p_{\text{T}}(\text{charged hadrons not from PV}),\, 0\Big],
\end{aligned} \tag{3.1}
$$

where the sum is over a cone of radius

$$
R_{\text{mini-iso}} = \begin{cases} 0.2, & p_{\text{T}}^{l} \leq 50\,\text{GeV}, \\ \frac{10\,\text{GeV}}{p_{\text{T}}^{l}}, & p_{\text{T}}^{l} \in (50\,\text{GeV},\, 200\,\text{GeV}), \\ 0.05, & p_{\text{T}}^{l} \geq 200\,\text{GeV}. \end{cases} \tag{3.2}
$$

The cone size is chosen to be small enough to minimize the possibility of accidental overlaps with jets in high-multiplicity or highly-boosted events, particularly overlap between a b-jet and lepton originating from a single boosted top quark. At the same time, the cone size remains large enough that, in the case of non-prompt leptons, it is able to contain the decay products of a b-hadron.

The specific form of the p_{T}-dependence is motivated by the angular separation of two daughter particles produced by the decay of a massive mother particle. In the high-momentum limit, the separation in η-ϕ space is $\Delta R_{\text{daughters}} \approx \frac{2M}{p_{\text{T}}^{\text{mother}}}$. This simple approximation does not include such complications as decays to more than two particles and the fact that the p_{T} in the denominator is that of the inaccessible mother particle rather than the visible daughter. It does, however, indicate that the cone radius should scale as p_{T}^{-1}. It also implies that the constant in the numerator should be of the same order of magnitude as the mass of a typical parent particle. The chosen 10 GeV is

approximately twice the mass of the b-quark whose hadrons produce many non-prompt leptons.

The upper limit of 0.2 on the cone size is chosen to prevent accidental overlaps with unrelated jets. At very small cone sizes, poorly understood detector resolution effects become relevant, and so a lower bound of 0.05 is imposed on the cone radius.

For non-prompt leptons, the momentum of nearby particles is correlated with the momentum of the lepton due to the shared mother particles. Discrimination between prompt and non-prompt leptons is improved by placing requirements on the relative isolation $I_{\text{mini}} \equiv I^{\text{abs}}_{\text{mini}}/p^{l}_{\text{T}}$, rather than the absolute isolation.

3.4.2 Veto Tracks

As discussed later in Chapter 5, the majority of background events contain two real leptons, with only one of the two passing the selection requirements listed in Tables 3.1 and 3.2. It is therefore useful to identify events which are likely to contain a lost lepton. We therefore define a collection of *veto tracks* containing candidates which are likely to be a lepton or a charged hadron track from the decay of a tau lepton, but which do not pass all of the identification requirements for leptons. This collection is built from both lepton PF candidates and charged hadron PF candidates. The selection requirements for these veto tracks vary depending on which type of PF candidate was used, with details of the selection provided in Table 3.3.

Like the charged leptons, the veto tracks are required to be isolated. For veto tracks produced from lepton PF candidates, the requirement is $I_{\text{mini}} < 0.2$, with I_{mini} defined as in Equation (3.1). For veto tracks originating from charged hadron PF candidates, only the first term in Equation (3.1), containing other charged hadrons from the primary vertex, is used to produce $I^{\text{chg. trk. only}}_{\text{mini}}$. Hadronically decaying tau leptons typically produce

Table 3.3: Selection requirements for veto tracks. In all cases, it is assumed the track has not already been identified as an electron or muon. m_{T2} requires an identified electron or muon to compute. If an event does not contain any leptons, the m_{T2} and charge requirements are omitted. For charged hadron tracks, the definition of mini-isolation is modified to exclude photons and neutral hadron candidates, retaining only the first term in Equation (3.1).

Track Property	Lepton PF Cand.	Charged Hadron PF Cand.
p_{T} [GeV]	> 10	> 15
d_{xy} [mm]	< 0.5	< 0.5
d_z [mm]	< 0.7	< 0.7
I_{mini}	< 0.2	N.A.
$I_{\mathrm{mini}}^{\text{chg. trk. only}}$	N.A.	< 0.1
Required only if event contains a lepton		
$m_{\mathrm{T2}}(\mathrm{track}, l, E_{\mathrm{T}}^{\mathrm{miss}})$ [GeV]	< 80	< 60
Opposite charge as lepton	True	True

several neutral particles in close proximity to the charged hadron PF candidate, but this modified version of I_{mini} allows the charged candidate into the veto track collection.

If the event in consideration has an identified electron or muon, an additional requirement is placed on potential veto tracks. This requirement uses the missing transverse momentum $E_{\mathrm{T}}^{\mathrm{miss}}$ (described in more detail in Section 3.6) and the lepton to construct the transverse mass variable

$$m_{\mathrm{T2}}(\mathrm{track},\, l,\, \vec{E}_{\mathrm{T}}^{\mathrm{miss}}) \equiv \min_{\vec{p}_{\mathrm{T},a}+\vec{p}_{\mathrm{T},b}=\vec{E}_{\mathrm{T}}^{\mathrm{miss}}} \{\max[m_{\mathrm{T}}(\mathrm{track},\, \vec{p}_{\mathrm{T},a}),\, m_{\mathrm{T}}(l,\, \vec{p}_{\mathrm{T},b})]\} \tag{3.3}$$

described in References [70, 71]. The variable m_{T2} uses and is in many ways similar to the simpler transverse mass

$$m_{\mathrm{T}}(a,\, b) \equiv m_a^2 + m_b^2 + 2(E_{\mathrm{T},a}E_{\mathrm{T},b} - \vec{p}_{\mathrm{T},a} \cdot \vec{p}_{\mathrm{T},b}), \tag{3.4}$$

where $E_{\mathrm{T}}^2 \equiv m^2 + {p_{\mathrm{T}}}^2$. Since m_{T} does not explicitly depend on the longitudinal momentum p_z, the missing transverse momentum $\vec{E}_{\mathrm{T}}^{\mathrm{miss}}$ may be used in place of one of the

momentum vectors. The mass of the $\vec{E}_{\mathrm{T}}^{\mathrm{miss}}$ "particle" is assumed to be 0. The variable m_{T} has the property that if particles a and b are produced by the decay of a common mother particle c, than $m_{\mathrm{T}}(a,b) \leq m(c)$. In particular, if an event has a single leptonically-decaying $\mathrm{W}^{\pm}$ and no other source of $E_{\mathrm{T}}^{\mathrm{miss}}$, then $m_{\mathrm{T}}(\mathrm{lepton}, \vec{E}_{\mathrm{T}}^{\mathrm{miss}}) \leq m_{\mathrm{W}^{\pm}}$. Similarly, for events with two leptonically decaying $\mathrm{W}^{\pm}$ and no other source of $E_{\mathrm{T}}^{\mathrm{miss}}$, $m_{\mathrm{T2}}(\mathrm{lepton}\ 1, \mathrm{lepton}\ 2, E_{\mathrm{T}}^{\mathrm{miss}}) \leq m_{\mathrm{W}^{\pm}}$. Rejecting those tracks which produce large values of m_{T2} reduces the number of fake leptons classified as veto tracks by ensuring the lepton, track, and $E_{\mathrm{T}}^{\mathrm{miss}}$ are consistent with having been produced by a dilepton-$\mathrm{t\bar{t}}$ event.

Distributions of the m_{T2} variable for leptonic and hadronic tracks are shown in Figure 3.2. For dilepton $\mathrm{t\bar{t}}$ events, the m_{T2} requirement for veto tracks has a high efficiency, while the majority of potential veto tracks in T1tttt events produce large values of $m_{\mathrm{T2}}(l, \mathrm{track}, E_{\mathrm{T}}^{\mathrm{miss}}) > m_{\mathrm{W}^{\pm}}$ and are rejected. Combined with the fact that only about 30% of T1tttt events produce an isolated track, this mean that only about 10% of T1tttt events will have an accepted veto track.

To avoid confusion, "leptons" will refer only to electrons and muons passing the full identification criteria and will not include the veto tracks. For counting purposes, the number of fully identified leptons will be written as N_{leps} and the number of veto tracks as N_{veto}.

3.5 Jets

Due to the large coupling constant associated with the strong force, hadron colliders like the LHC produce large numbers of color-charged objects, namely quarks and gluons. Such objects quickly hadronize before they can be directly observed in the detector, instead producing a collimated spray of particles known as a jet. Determining which of the resulting tracks belong to which quark/gluon, however, quickly becomes a non-trivial

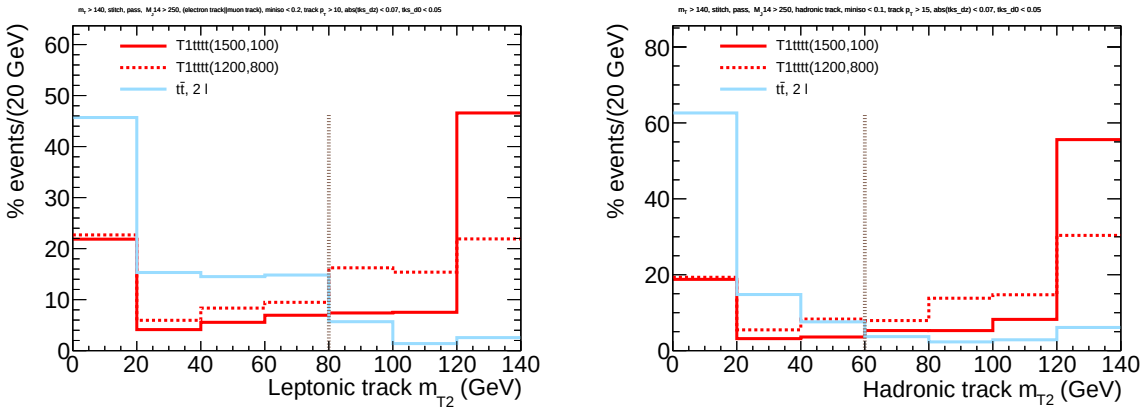

Figure 3.2: Distribution of $m_{\mathrm{T2}}(l, \mathrm{track}, \vec{E}_{\mathrm{T}}^{\mathrm{miss}})$ for leptonic tracks (left) and hadronic tracks(right) in simulated events. Only tracks from events passing the baseline selection of Chapter 5 and satisfying $m_{\mathrm{T}}(l, \vec{E}_{\mathrm{T}}^{\mathrm{miss}}) > 140\,\mathrm{GeV}$ and $M_J > 250\,\mathrm{GeV}$ are included, where M_J is as defined in Section 3.5.5. Dilepton $\mathrm{t\bar{t}}$ events are shown in blue, while T1tttt events are shown in red for mass parameters $m_{\tilde{\mathrm{g}}} = 1500\,\mathrm{GeV}$ and $m_{\tilde{\chi}^0_1} = 100\,\mathrm{GeV}$ (solid) and for $m_{\tilde{\mathrm{g}}} = 1200\,\mathrm{GeV}$ and $m_{\tilde{\chi}^0_1} = 800\,\mathrm{GeV}$ (dashed). Nearly all tracks in dilepton $\mathrm{t\bar{t}}$ events satisfy the expected $m_{\mathrm{T2}}(l, \mathrm{track}, \vec{E}_{\mathrm{T}}^{\mathrm{miss}}) < m_{\mathrm{W}^{\pm}}$, while the majority of tracks in T1tttt events have $m_{\mathrm{T2}}(l, \mathrm{track}, \vec{E}_{\mathrm{T}}^{\mathrm{miss}}) > m_{\mathrm{W}^{\pm}}$. Only about 30% of T1tttt events produce an isolated track, and so most events will not appear in these plots. This also means that only about 10% of T1tttt events will contain a veto track satisfying the m_{T2} and other requirements listed in Table 3.3. Figure from Reference [13].

task as the number of tracks grows.

3.5.1 Clustering

The recently developed FastJet [72] software package has allowed the use of sequential recombination jet algorithms in events with large numbers of tracks. Such algorithms define a distance measure between each pair of particles to be clustered and sequentially recombines the closest pair of particles into a single object, stopping when some algorithm-dependent condition is reached. One option is to take the distance measure to be

$$d_{ij} = \min\left(p_{\mathrm{T}i}^{2p}, p_{\mathrm{T}j}^{2p}\right) \frac{\Delta R_{ij}^2}{R^2}, \tag{3.5}$$

$$d_{i\mathrm{B}} = p_{\mathrm{T}i}^{2p}, \tag{3.6}$$

where $\Delta R_{ij}^2 = \Delta\eta_{ij}^2 + \Delta\phi_{ij}^2$, R is a jet radius parameter which controls approximate size of the resulting jets, and p is a parameter which alters the clustering order [73]. The d_{ij} parameter gives the distance between a pair of particles i and j, while $d_{i\mathrm{B}}$ is the distance between the particle i and the beam. During the clustering process, if the smallest distance is a $d_{i\mathrm{B}}$, then i is added to the list of output jets and removed from the list of particles to be clustered.

There are three common choices for p in this distance measure. Setting $p = 1$ gives the k_t algorithm, one of the earliest sequential recombination algorithms and one whose recombination sequence may contain useful information about the underlying showering sequence that produced the jet [74]. Choosing $p = 0$ gives the Cambridge–Aachen algorithm [75]. With $p = 0$, the distance measure is purely geometric, making the Cambridge–Aachen algorithm useful for jet substructure studies. Finally, taking $p = -1$

yields the anti-k_{T} algorithm which produces nearly circular jets, though such jets are less useful for substructure studies [76].

For any of the three choices of p, the sequential recombination algorithm described above has the desirable property of being infrared and collinear (IRC) safe. That is, the jets produced by the algorithm do not change if low-momentum radiation is added to the event (infrared safety) or if any high momentum track is split into two collinear tracks (collinear safety).

Unless otherwise mentioned, jets used in this thesis are anti-k_t jets with radius parameter $R = 0.4$ and are produced by clustering PF candidates. In case of any potential ambiguity, such jets may be referred to as AK4 jets. For PF charged hadrons, only those originating from the highest sum-of-track-p_{T}^2 primary vertex are included. The omission of other PF charged hadrons is referred to as charged hadron subtraction and helps mitigate the effects of pileup on the measured jet momentum.

3.5.2 Jet Energy Corrections

The primary goal of clustering particles into jets is to be able to measure as nearly as possible the momentum of the original decaying, radiating, and/or hadronizing particle. To make this jet momentum correspond as nearly as possible to the true particle momentum requires a multi-stage correction process [77].

The first corrections applied to jets are referred to as L1 corrections. The L1 correction applies an offset to the jet energy in order to compensate for the effect of pileup. The correction is calculated using a precomputed estimate of the expected energy density per unit area from pileup. Multiplying the energy density by the area of a jet gives an estimate for the pileup contribution to the p_{T} of the jet [78]. The ability to compute jet areas for arbitrarily shaped jets is a key feature of the IRC safe sequential recombination

algorithms described in Section 3.5.1. IRC safety allows a large number of "ghost" particles with infinitesimal momentum to be added to the event without changing the resulting jets. The area of each jet is determined by the area covered by the ghosts clustered into the jet. L1 corrections are applied to both simulated and real data, but in the latter case, the L1 correction has an additional component to account for differences in the pileup energy density with respect to simulation as a function of η.

Next, so-called L2L3 corrections are applied which make the jet response uniform as a function of η and ϕ. This correction accounts for potential differences in the jet momentum and original particle momentum due to, for example, missed neutrinos in the jet. L2L3 corrections are applied to both real and simulated events.

The last corrections applied are called L2L3Residuals. These compensate for small differences in jet response between real and simulated events and are applied only to real events.

3.5.3 Selection

Only a subset of the jets produced by the clustering of PF candidates are retained. First, any jets which contain a PF candidate identified as an electron or muon as defined in Section 3.4, or whose momenta are within $\Delta R = \sqrt{\Delta\eta^2 + \Delta\phi^2} = 0.4$ of such a lepton are removed from the jet collection in order to avoid double counting.

Additionally, jets are required to satisfy the kinematic selection and quality requirements listed in Table 3.4.

The variable N_{jets} is defined as the number of AK4 jets not associated with a lepton and passing all kinematic and quality requirements. Similarly, the variable H_{T} is defined as the scalar sum of the transverse momenta of such jets.

In the case of $\text{t}\bar{\text{t}}$ production, the main source of background events in this search, H_{T}

Table 3.4: Kinematic and quality requirements applied to the jets after removing those matched to leptons. The "fraction" requirements refer to the fraction of the energy of the jet coming from a particular source as identified by the PF algorithm.

Jet Property	Requirement
p_{T} (corrected)	$> 30\,\mathrm{GeV}$
$\lvert\eta\rvert$	< 2.4
Neutral hadron fraction	< 0.99
Charged hadron fraction	> 0
Neutral electromagnetic fraction	< 0.99
Charged electromagnetic fraction	< 0.99
Number of constituents	> 1
Charged multiplicity	> 0

is anti-correlated with the number of leptons present in an event since each leptonically-decaying $\mathrm{W}^{\pm}$ reduces the number of potential jet-producing quarks by two. To avoid this, the variable

$$S_{\mathrm{T}} = H_{\mathrm{T}} + \sum_{l \in \mathrm{leptons}} p_{\mathrm{T}}(l) \tag{3.7}$$

will be used in lieu of H_{T} wherever possible.

3.5.4 b-tagging

Third generation quarks often play an important role in supersymmetry searches at CMS. High jet-multiplicity requirements often result in top quarks decays comprising a large fraction of the background. Further, since naturalness may imply the third-generation squarks are relatively light, many SUSY models involve direct or indirect production of these squarks, which subsequently decay to produce the standard model third-generation quarks. This includes the T1tttt and T5tttt models discussed in Section 1.2.

For these reasons, it is important to be able to identify jets originating from b-quarks.

At CMS, this process is called b-tagging and is accomplished by an algorithm known as the Combined Secondary Vertex (CSV) tagger [79]. More specifically, an updated version using an Inclusive Vertex Finder (IVF) and multivariate analysis techniques is used, referred to as CSVv2 [80].

The b-quark can only decay via the weak interaction, with the branching fraction for u, c, and t determined by respective CKM matrix elements. Since $C_{\mathrm{tb}} \sim 1$, decays to u and c quarks are suppressed. Decays to the top quark are disallowed by its large mass. Combined, these effects result in a long lifetime for the bottom quark, allowing it to travel several millimeters before decaying in the detector. Like most b-tagging algorithms, CSVv2 relies extensively on the detection of these displaced vertices.

The weak decay of the b-quark also results in production of an e or μ in approximately 20% of b-decays. The presence of charged leptons gives an additional handle by which b-decays may be identified.

The full details of the CSVv2 algorithm are given in Reference [80], but a brief overview is provided here. For each jet, the algorithm attempts to produce a score in the range $[0, 1]$. To do this, a collection of tracks meeting the following requirements is generated for each jet:

- At least eight tracker hits,
- Transverse momentum at least 800 MeV,
- Longitudinal impact parameter less than 3 mm,
- $\Delta R < 0.3$ with respect to jet axis.

Of these tracks, any pair whose invariant mass is within 30 MeV of the $\mathrm{K}^0_{\mathrm{S}}$ mass are removed. If, after removal, no tracks remain, a negative output value is produced to signify that there is no valid input for the computation.

Using the remaining tracks, the algorithm attempts to reconstruct secondary vertices. This is done with the Inclusive Vertex Finder by identifying displaced tracks, using them as seeds to cluster the track collection, and then performing a fit to construct vertices from the clustered tracks. A number of intermediate variables are then computed, such as the number of vertices, the invariant masses of the vertices, and the flight distance significance for the vertices. If no vertices are found, the only available information comes from any displaced tracks.

The intermediate variables are combined using a multilayer perceptron with one hidden layer. This is in contrast to the older CSV algorithm where a likelihood fit was used and the number of input variables was smaller.

For this analysis, a standard "medium" working point with a target mis-tag rate of 1% is used. This corresponds to a CSVv2 output of 0.8484. Jets for which the CSVv2 output is above this value are classified as b-jets. The efficiency of this selection is shown in Figure 3.3. The variable N_{b} will be used for the number of AK4 jets meeting this criteria.

3.5.5 Large-Radius Jets

The $R = 0.4$ distance parameter used to cluster PF candidates into AK4 jets typically captures the decay products from a single gluon or light-flavor quark. In some cases, a larger jet radius is desirable, such as for capturing the decay of a top quark in a single jet or, as in this search, to create jets whose masses are sensitive to the momentum scale, multiplicity, and angular relationship of the AK4 jets.

Of course, jets with a larger radius can be constructed in precisely the same manner as the AK4 jets, by simply clustering PF candidates with a larger distance parameter. However, such an approach requires computing a new set of jet energy corrections for the

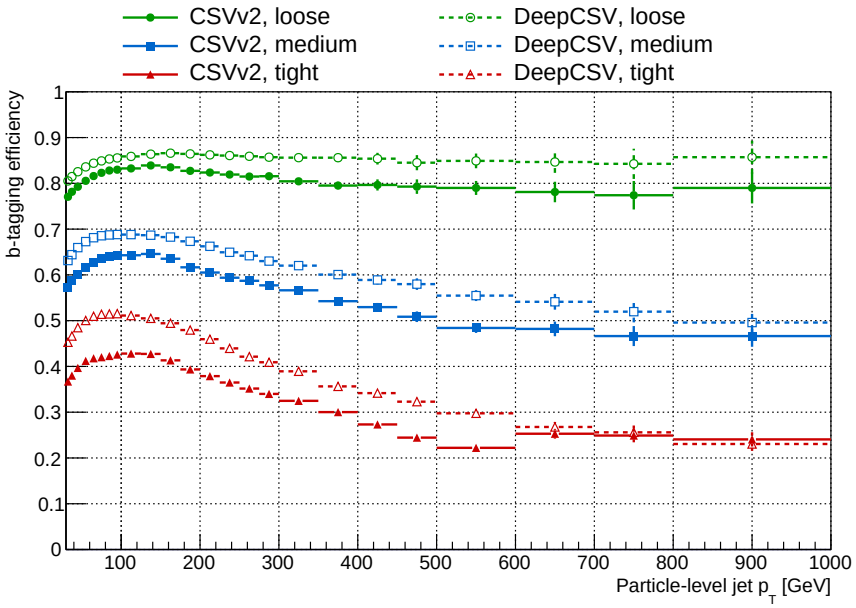

Figure 3.3: Efficiency of the CSVv2 and DeepCSV b-tagging efficiencies, computed in simulated $t\bar{t}$+jets events. The medium working point of CSVv2 is used in this analysis. Figure from Reference [12].

larger jet radius. Since no standardized set of such corrections was available for larger jet radii while this search was being developed, an alternate approach is used. Instead, the AK4 jets, including those jets associated with leptons, are clustered into larger-radius jets using the anti-k_{T} algorithm with distance parameter $R = 1.4$. The use of the already calibrated AK4 jets avoids the need to derive a new set of jet energy corrections. Such jets are referred to as large-R jets for the remainder of this document.

This technique of clustering jets with a small radius into jets with a large radius has been used previously by ATLAS in, for example, Reference [81].

The sum of the masses of the large-R jets is denoted by M_J. The phenomenology of this variable has been described extensively in References [82, 83, 84]. Basic properties and performance of the M_J variable have been studied using early $\sqrt{s} = 13\,\mathrm{TeV}$ data [85]. Similar variables have been used by ATLAS SUSY searches in all-hadronic final states in $\sqrt{s} = 8\,\mathrm{TeV}$ data [86, 87, 88, 89]. Properties of the M_J variable within the context of

this search are discussed in Chapter 5.

3.6 $\boldsymbol{E}_{\mathrm{T}}^{\mathrm{miss}}$

Particles that do not interact via the electromagnetic and strong forces, such as neutrinos and neutralinos, are generally undetectable as they pass through the CMS detector. However, the presence of such particles in an event can be inferred from the momentum of the detected particles. Since the beams initially have negligible momentum in the transverse plane, conservation of momentum implies that the sum of the momenta of all final state particles should also sum to zero in the transverse plane. On the other hand, since the interacting quarks and gluons carry variable and unknown fractions of the proton momentum, no such relation holds in the longitudinal direction.

If one or more particles escape CMS undetected, their combined transverse momentum should have the same magnitude and opposite direction as the summed transverse momentum of all the visible particles. Thus, a useful quantity is the PF missing transverse momentum, defined as $\vec{E}_{\mathrm{T}}^{\mathrm{miss}} \equiv -\sum \vec{p}_{\mathrm{T}}$, where the sum runs over all jets and PF candidates not clustered into a jet. For charged particles which leave a track in the silicon tracker, only those particles matched to the primary vertex are included. In principle, one could use the PF constituents of the jets directly in the sum, but using the L1- and L2L3-corrected jets provides a more accurate estimate of the total visible transverse momentum. The presence of large $E_{\mathrm{T}}^{\mathrm{miss}} \equiv |\vec{E}_{\mathrm{T}}^{\mathrm{miss}}|$ is generally an indication of the presence of invisible particles.

In events with precisely one identified lepton, m_{T} (written as a variable rather than a function) will refer to $m_{\mathrm{T}}(l, \vec{E}_{\mathrm{T}}^{\mathrm{miss}})$, as defined in Equation (3.4).

At the trigger level, the similar variable $H_{\mathrm{T}}^{\mathrm{miss}}$ is occsionally used. $H_{\mathrm{T}}^{\mathrm{miss}}$ only sums the transverse momenta of jets, excluding the other PF candidates.

Chapter 4

Real and Simulated Data Samples

Having given a brief overview of how the LHC and CMS produce and record events in Chapter 3, the logical next topic is to discuss which events we will be using. This chapter describes both the triggers used to collect data at CMS (Section 4.1) and the simulated events samples used to study the properties of the signal and background in more detail (Section 4.2).

4.1 Real Data

The dataset used for this analysis corresponds to approximately $35.9\,\mathrm{fb}^{-1}$ of proton-proton collisions with a center-of-momentum energy of 13 TeV. The dataset is divided into several eras during which operating conditions of CMS are kept as steady as possible. The eras used in this analysis are: Run2016B, Run2016C, Run2016D, Run2016E, Run2016F, Run2016G, and Run2016H. The corresponding luminosities of these eras are shown in Table 4.1. Only data meeting the requirements of CMS's Golden JSON, which requires all subdetectors to be functioning properly, are used.

The dataset comprises several overlapping primary datasets based on which HLT

Table 4.1: Integrated luminosity of the data eras used in this analysis, including only those passing the Golden JSON requirement in which all subdetectors are functioning properly. The uncertainty on the total integrated luminosity is 2.6%.

Era	L [fb^{-1}]
Run2016B	5.751
Run2016C	2.573
Run2016D	4.242
Run2016E	4.025
Run2016F	3.105
Run2016G	7.576
Run2016H	8.651
Total	35.922

requirements each event passes. This analysis uses the JetHT, MET, SingleElectron, and SingleMuon primary datasets.

Within each primary dataset, only events passing a subset of the HLT paths are retained. In short, the set of triggers used in this analysis require either a single lepton with $p_{\mathrm{T}} > 15\,\mathrm{GeV}$, possibly with an additional H_{T} requirement; or $E_{\mathrm{T}}^{\mathrm{miss}}$ or $H_{\mathrm{T}}^{\mathrm{miss}}$ greater than 100 GeV. The full set of triggers is provided in Table 4.2.

In order to ensure that the efficiency is as high as possible and independent of the offline threshold chosen, the HLT selection should be as loose as possible. The lepton p_{T}, $E_{\mathrm{T}}^{\mathrm{miss}}$, and $H_{\mathrm{T}}^{\mathrm{miss}}$ requirements used are the lowest available without prescaling. Since the loosest trigger without prescaling changes with the instantaneous luminosity, Table 4.2 includes a number of very similar triggers with varying thresholds.

In the case of lepton isolation, maintaining offline efficiency presents a unique challenge. Only fixed-cone size isolation is implemented within the HLT, and the isolation requirements cannot be completely removed from leptons without prescaling the trigger. In order to ensure efficiency of the offline mini-isolation requirements, the online fixed-cone isolation is made as loose as possible. Triggers with this loosened fixed-cone isolation contain "IsoVVVL" within their name.

Table 4.2: List of all triggers used in this analysis. The final trigger decision is the logical OR of the individual triggers.

HLT Path Name
HLT_Mu15_IsoVVVL_PFHT350
HLT_Mu15_IsoVVVL_PFHT400
HLT_Mu50_IsoVVVL_PFHT400
HLT_IsoMu22_eta2p1
HLT_IsoMu24
HLT_IsoTkMu24
HLT_Mu50
HLT_Ele15_IsoVVVL_PFHT350
HLT_Ele15_IsoVVVL_PFHT400
HLT_Ele50_IsoVVVL_PFHT400
HLT_Ele27_eta2p1_WPLoose_Gsf
HLT_Ele25_eta2p1_WPTight_Gsf
HLT_Ele27_WPTight_Gsf
HLT_Ele105_CaloIdVT_GsfTrkIdT
HLT_Ele115_CaloIdVT_GsfTrkIdT
HLT_PFMET100_PFMHT100_IDTight
HLT_PFMETNoMu100_PFMHTNoMu100_IDTight
HLT_PFMET110_PFMHT110_IDTight
HLT_PFMETNoMu110_PFMHTNoMu110_IDTight
HLT_PFMET120_PFMHT120_IDTight
HLT_PFMETNoMu120_PFMHTNoMu120_IDTight

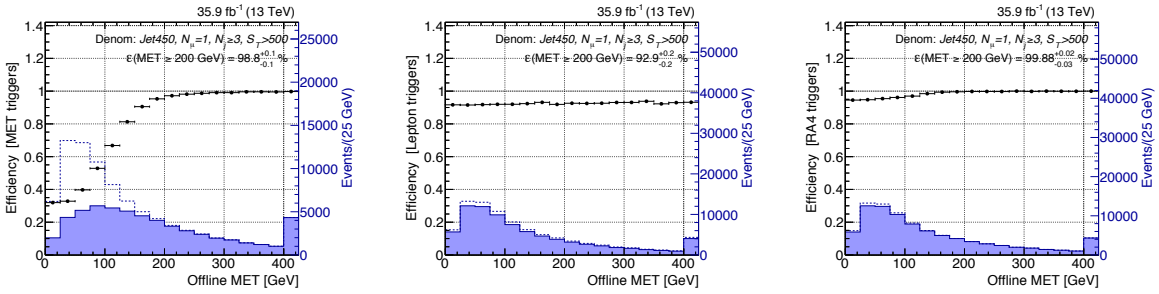

Figure 4.1: Efficiency of the $E_{\mathrm{T}}^{\mathrm{miss}}$- and $H_{\mathrm{T}}^{\mathrm{miss}}$-based triggers (left), leptonic triggers (center), and the logical OR of all triggers (right) as a function of offline $E_{\mathrm{T}}^{\mathrm{miss}}$ in events with an offline muon. The sample consists of events passing the HLT_PFJet450 trigger and an offline selection requiring three or more jets and $S_{\mathrm{T}} > 500\,\mathrm{GeV}$. Figure from Reference [13].

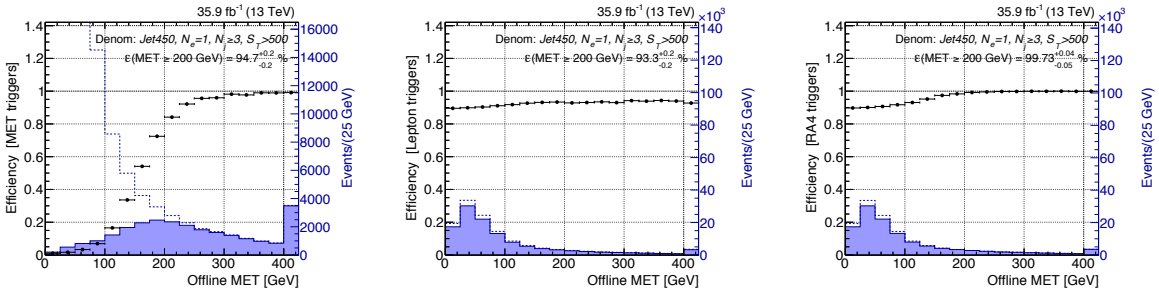

Figure 4.2: Efficiency of the $E_{\mathrm{T}}^{\mathrm{miss}}$- and $H_{\mathrm{T}}^{\mathrm{miss}}$-based triggers (left), leptonic triggers (center), and the logical OR of all triggers (right) as a function of offline $E_{\mathrm{T}}^{\mathrm{miss}}$ in events with an offline electron. The sample consists of events passing the HLT_PFJet450 trigger and an offline selection requiring three or more jets and $S_{\mathrm{T}} > 500\,\mathrm{GeV}$. Figure from Reference [13].

Figures 4.1 and 4.2 show the efficiency of the various triggers as a function of offline $E_{\mathrm{T}}^{\mathrm{miss}}$ for events containing an offline muon and events containing an offline electron, respectively. In both figures, events are obtained with the HLT_PFJet450 trigger and an offline selection requiring three or more jets and $S_{\mathrm{T}} > 500\,\mathrm{GeV}$.

The $E_{\mathrm{T}}^{\mathrm{miss}}$- and $H_{\mathrm{T}}^{\mathrm{miss}}$-based triggers are the main source of data for this analysis and reach a nearly constant efficiency over 99% for offline $E_{\mathrm{T}}^{\mathrm{miss}} > 300\,\mathrm{GeV}$, as seen in the left most plots in the two figures. The region for which the efficiency is nearly independent of the offline selection threshold is referred to as the *efficiency plateau*. For lower values

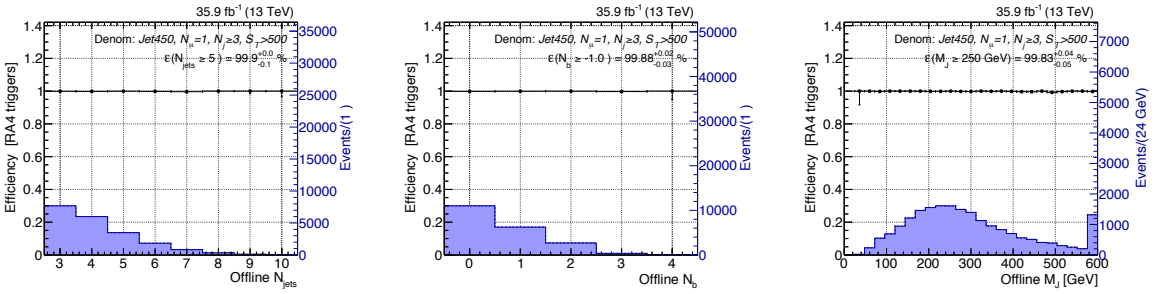

Figure 4.3: Combined efficiency of all triggers used in this analysis as a function of offline N_{jets}, N_{b}, and M_J for events containing an offline muon. The sample consists of events passing the HLT_PFJet450 trigger and an offline selection requiring three or more jets, $E_{\text{T}}^{\text{miss}} > 200\,\text{GeV}$, and $S_{\text{T}} > 500\,\text{GeV}$. Figure from Reference [13].

of offline $E_{\text{T}}^{\text{miss}}$, the online $E_{\text{T}}^{\text{miss}}$ requirements are not fully efficient and the efficiency changes rapidly with $E_{\text{T}}^{\text{miss}}$.

On the other hand, since the leptonic triggers do not have an online $E_{\text{T}}^{\text{miss}}$ requirement, their efficiencies are nearly constant with respect to offline $E_{\text{T}}^{\text{miss}}$. This property makes them useful for recovering triggering efficiency at low $E_{\text{T}}^{\text{miss}}$, as shown in the right-most plots. The logical OR of all of the triggers provides greater than 90% efficiency across the $E_{\text{T}}^{\text{miss}}$ spectrum.

The overall efficiency of the trigger as a function of N_{jets}, N_{b}, and M_J is shown in Figures 4.3 and 4.4 for muon and electron events, respectively, with $E_{\text{T}}^{\text{miss}} > 200\,\text{GeV}$. In all cases, the trigger is nearly 100% efficient and the efficiency independent of the offline variables.

4.2 Monte Carlo Simulation

In addition to true data recorded by CMS, we make use of a number of simulated event samples. These samples mimic various physics processes that can occur in proton-proton collisions and are used in situations where it is impossible or undesirable to use the true data, such as when:

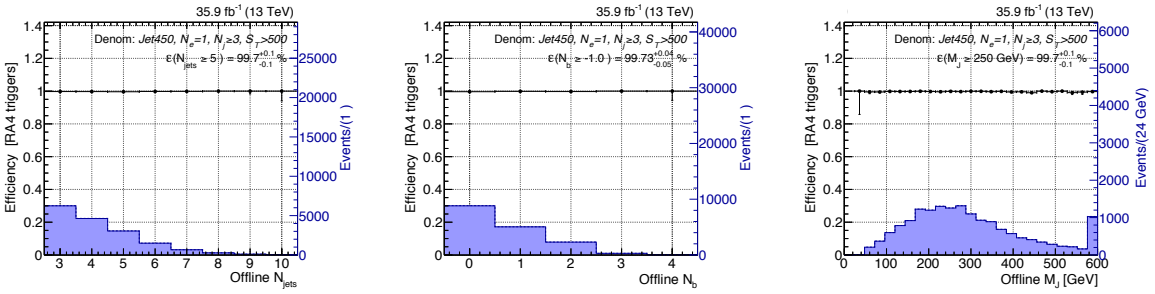

Figure 4.4: Combined efficiency of all triggers used in this analysis as a function of offline N_{jets}, N_{b}, and M_J for events containing an offline electron. The sample consists of events passing the HLT_PFJet450 trigger and an offline selection requiring three or more jets, $E_{\text{T}}^{\text{miss}} > 200\,\text{GeV}$, and $S_{\text{T}} > 500\,\text{GeV}$. Figure from Reference [13].

- real data are still blinded,
- one wants to know the "true" properties of an event,
- control regions for a sample are too small,
- one is studying a signal model which may or may not exist.

Generation of simulated events is done in a multi-step process. First, the hard scatter event is simulated using either the MadGraph5_aMC@NLO 2.2.2 [90] or POWHEG v2 [91, 92, 93] Monte Carlo (MC) generator. The MadGraph5_aMC@NLO generator is used at leading order (LO) accuracy for the simulation of signal processes and most backgrounds, including $\text{t}\bar{\text{t}}$ production. Other background processes, including single top quark and diboson production, are simulated at next-to-leading order (NLO) using either POWHEG or MadGraph5_aMC@NLO. The NLO simulation provides a more accurate estimate of the background properties by producing some events with a negative weight. This has the unfortunate consequence of requiring a larger number of events to be simulated for the same equivalent luminosity, typically resulting in reduced statistical precision. For example, in a sample where a fraction f of the simulated events have weight $-w$ and $1 - f$ have weight $+w$, the effective luminosity of the sample is

$L_{\text{eff}}/\sigma = Nw(1-2f)$, where σ is the cross-section of the simulated process. The effective luminosity of the sample decreases linearly with f and becomes zero when $f = \frac{1}{2}$. As such, the NLO samples typically have a lower effective luminosity.

The kinematic properties and cross-sections of the various processes depend on the parton distribution function (PDF) of the colliding protons, which are taken from NNPDF 3.0 [94].

For all processes, the highest order cross-section calculation available is used. For $t\bar{t}$ production, cross-sections are computed at next-to-next-to-leading order plus next-to-next-to-leading logarithmic order (NNLO+NNLL) [95], while for T1tttt and T5tttt models, cross-sections are computed at next-to-leading order plus next-to-leading logarithmic order (NLO+NLL).

Following simulation of the hard scatter process, showering and fragmentation of the partons are simulated with Pythia 8.205 [96] using the CUETP8M1 tune [94] for the underlying event model. Interactions of particles with the detector are simulated using the GEANT4 software package [97] for background processes and the CMS fast simulation package [98] for signal samples.

The presence of pileup and an underlying event are simulated by overlaying the event with multiple minimum bias events. The minimum bias events are themselves simulated using Pythia with the CUETP8M1 tune.

Table 4.3 lists the simulated background samples used in this analysis and their equivalent integrated luminosities.

The simulated signals are SMS-T1tttt_TuneCUETP8M1_13TeV-madgraphMLM-pythia8 and SMS-T5tttt_dM175_TuneCUETP8M1_13TeV-madgraphMLM-pythia8. For T1tttt, 628 different mass points are simulated, with gluino masses varying from 600 GeV to 2300 GeV and $\widetilde{\chi}_1^0$ masses varying from 1 GeV to 1600 GeV. For T5tttt, 580 mass points are simulated, with gluino masses varying from 800 GeV to 2300 GeV. When showing a

Table 4.3: Simulated background processes and their equivalent integrated luminosities.

Simulated Sample Name	Events	L [fb^{-1}]
TTJets_TuneCUETP8M1_13TeV-madgraphMLM-pythia8	10 259 872	12.57
TTJets_SingleLeptFromT_TuneCUETP8M1_13TeV-madgraphMLM-pythia8	61 973 977	346.80
TTJets_SingleLeptFromT_genMET-150_TuneCUETP8M1_13TeV-madgraphMLM-pythia8	16 959 409	1819.14
TTJets_SingleLeptFromTbar_TuneCUETP8M1_13TeV-madgraphMLM-pythia8	60 210 394	336.94
TTJets_SingleLeptFromTbar_genMET-150_TuneCUETP8M1_13TeV-madgraphMLM-pythia8	17 066 856	1830.66
TTJets_DiLept_TuneCUETP8M1_13TeV-madgraphMLM-pythia8	30 444 678	355.41
TTJets_DiLept_genMET-150_TuneCUETP8M1_13TeV-madgraphMLM-pythia8	9 890 329	1806.33
TTZToLLNuNu_M-10_TuneCUETP8M1_13TeV-amcatnlo-pythia8	1 992 438	1708.99
TTZToQQ_TuneCUETP8M1_13TeV-amcatnlo-pythia8	749 400	310.65
TTWJetsToLNu_TuneCUETP8M1_13TeV-amcatnloFXFX-madspin-pythia8	5 280 565	6838.97
TTWJetsToQQ_TuneCUETP8M1_13TeV-amcatnloFXFX-madspin-pythia8	833 298	547.04
TTTT_TuneCUETP8M1_13TeV-amcatnlo-pythia8	250 000	4811.39
ST_tW_antitop_5f_NoFullyHadronicDecays_13TeV-powheg_TuneCUETP8M1	11 408 144	586.04
ST_tW_top_5f_NoFullyHadronicDecays_13TeV-powheg_TuneCUETP8M1	11 345 619	582.83
ST_t-channel_antitop_4f_inclusiveDecays_TuneCUETP8M2T4_13TeV-powhegV2-madspin	3 928 063	48.52
ST_t-channel_top_4f_inclusiveDecays_TuneCUETP8M2T4_13TeV-powhegV2-madspin	5 993 676	44.06
ST_s-channel_4f_leptonDecays_13TeV-amcatnlo-pythia8_TuneCUETP8M1	1 000 000	116.20
WJetsToLNu_TuneCUETP8M1_13TeV-madgraphMLM-pythia8	57 026 058	0.93
WJetsToLNu_HT-70To100_TuneCUETP8M1_13TeV-madgraphMLM-pythia8	10 094 300	6.08
WJetsToLNu_HT-100To200_TuneCUETP8M1_13TeV-madgraphMLM-pythia8	78 236 266	48.00
WJetsToLNu_HT-200To400_TuneCUETP8M1_13TeV-madgraphMLM-pythia8	38 328 549	87.99
WJetsToLNu_HT-400To600_TuneCUETP8M1_13TeV-madgraphMLM-pythia8	7 759 701	130.93
WJetsToLNu_HT-600To800_TuneCUETP8M1_13TeV-madgraphMLM-pythia8	18 687 480	1281.68
WJetsToLNu_HT-800To1200_TuneCUETP8M1_13TeV-madgraphMLM-pythia8	7 745 467	1163.65
WJetsToLNu_HT-1200To2500_TuneCUETP8M1_13TeV-madgraphMLM-pythia8	6 290 216	3911.61
WJetsToLNu_HT-2500ToInf_TuneCUETP8M1_13TeV-madgraphMLM-pythia8	2 388 086	61 368.93
QCD_HT100to200_TuneCUETP8M1_13TeV-madgraphMLM-pythia8	80 160 711	0.00
QCD_HT200to300_TuneCUETP8M1_13TeV-madgraphMLM-pythia8	57 580 393	0.03
QCD_HT300to500_TuneCUETP8M1_13TeV-madgraphMLM-pythia8	54 537 903	0.15
QCD_HT500to700_TuneCUETP8M1_13TeV-madgraphMLM-pythia8	62 271 343	2.12
QCD_HT700to1000_TuneCUETP8M1_13TeV-madgraphMLM-pythia8	45 412 780	6.96
QCD_HT1000to1500_TuneCUETP8M1_13TeV-madgraphMLM-pythia8	15 127 293	14.22
QCD_HT1500to2000_TuneCUETP8M1_13TeV-madgraphMLM-pythia8	11 826 702	97.34
QCD_HT2000toInf_TuneCUETP8M1_13TeV-madgraphMLM-pythia8	6 039 005	237.57
DYJetsToLL_M-50_TuneCUETP8M1_13TeV-madgraphMLM-pythia8	49 144 274	8.16
DYJetsToLL_M-50_HT-70to100_TuneCUETP8M1_13TeV-madgraphMLM-pythia8	9 616 188	44.60
DYJetsToLL_M-50_HT-100to200_TuneCUETP8M1_13TeV-madgraphMLM-pythia8	10 391 819	60.61
DYJetsToLL_M-50_HT-200to400_TuneCUETP8M1_13TeV-madgraphMLM-pythia8	9 404 362	178.85
DYJetsToLL_M-50_HT-400to600_TuneCUETP8M1_13TeV-madgraphMLM-pythia8	9 950 320	1471.66
DYJetsToLL_M-50_HT-600to800_TuneCUETP8M1_13TeV-madgraphMLM-pythia8	8 292 957	4946.62
DYJetsToLL_M-50_HT-800to1200_TuneCUETP8M1_13TeV-madgraphMLM-pythia8	2 668 730	3210.09
DYJetsToLL_M-50_HT-1200to2500_TuneCUETP8M1_13TeV-madgraphMLM-pythia8	596 079	4177.73
DYJetsToLL_M-50_HT-2500toInf_TuneCUETP8M1_13TeV-madgraphMLM-pythia8	399 492	125 304.88
WJetsToQQ_HT-600ToInf_TuneCUETP8M1_13TeV-madgraphMLM-pythia8	1 026 587	8.92
WH_HToBB_WToLNu_M125_13TeV_amcatnloFXFX_madspin_pythia8	2 179 687	2872.12
WWTo2L2Nu_13TeV-powheg	1 999 000	164.15
WWToLNuQQ_13TeV-powheg	1 999 200	39.99
WZTo1L1Nu2Q_13TeV_amcatnloFXFX_madspin_pythia8	23 939 924	735.80
WZTo1L3Nu_13TeV_amcatnloFXFX_madspin_pythia8	1 703 772	170.78
WZTo2L2Q_13TeV_amcatnloFXFX_madspin_pythia8	26 517 272	1699.59
WZTo3LNu_TuneCUETP8M1_13TeV-powheg-pythia8	1 993 200	449.97
ZH_HToBB_ZToNuNu_M125_13TeV_amcatnloFXFX_madspin_pythia8	2 159 477	6950.97
ZZ_TuneCUETP8M1_13TeV-pythia8	990 064	59.92
ttHTobb_M125_13TeV_powheg_pythia8	3 936 004	3936.00

Table 4.4: Weights to correct the ISR multiplicity distribution in simulated event samples. For $t\bar{t}$ events, $C = 1.071$. For signal events, $C = 1.143$. The correction is not applied to other samples.

$N_{\text{ISR-jets}}$	weight/C
0	1
1	0.920
2	0.821
3	0.715
4	0.662
5	0.561
≥ 6	0.511

particular signal mass point in a figure or table, the non-compressed (NC) benchmark mass point will refer to $m_{\tilde{g}} = 1800\,\text{GeV}$, $m_{\tilde{\chi}1}^{0} = 100\,\text{GeV}$, while the compressed (C) mass point will refer to $m_{\tilde{g}} = 1400\,\text{GeV}$, $m_{\tilde{\chi}1}^{0} = 1000\,\text{GeV}$.

To improve the agreement of simulation with data, simulated $t\bar{t}$ events are weighted based on the number of ISR jets present in the event [99, 100]. The weights are computed using a dilepton $t\bar{t}$ sample with two b-tagged jets, and are shown in Table 4.4.

Chapter 5

Event Selection

Even if supersymmetry proves true, the vast majority of events selected by the trigger are produced by purely standard model background processes. This chapter will give a brief overview of how we select potential events of interest and how some of the remaining background events manage to look like signal events.

5.1 The Baseline Selection, M_J, and m_{T}

Before applying any physics-motivated selection criteria, we first apply a number of filters designed to remove any events that are likely to contain reconstruction errors, particularly errors which can produce fake $E_{\mathrm{T}}^{\mathrm{miss}}$. These filters, standard to CMS SUSY searches, remove events with noise in the hadronic calorimeters, noise in the ECAL superclusters, dead cells in the ECAL, beam halo, or jets failing to pass quality criteria. Additionally, we require that events have at least one good primary vertex. Finally, we apply a "muon jet filter" developed for the SUSY search described in Reference [101], which removes any events containing a jet with $p_{\mathrm{T}} > 200\,\mathrm{GeV}$, $\Delta\phi(\mathrm{jet}, \vec{E}_{\mathrm{T}}^{\mathrm{miss}}) > \pi - 0.4$, and at least half its energy coming from a muon.

To improve the signal-to-background ratio, it is necessary to select a subset of those events which are more likely to be of interest. This is the role of the *baseline selection*, which requires that $N_{\text{leps}} = 1$, $S_{\text{T}} > 500\,\text{GeV}$, $E_{\text{T}}^{\text{miss}} > 200\,\text{GeV}$, $N_{\text{veto}} = 0$, $N_{\text{jets}} \geq 6$, and $N_{\text{b}} \geq 1$. The first three requirements, in addition to increasing the signal-to-background ratio, ensure that the analysis reaches the trigger efficiency plateau.

After applying the baseline selection, more than 80% of the remaining standard model background events are the result of a $\text{t}\bar{\text{t}}$+jets process. Contributions from the production of a either single top quark or a $\text{W}^{\pm}$ boson amount to 6% to 8% of the background each. In these events, the top quark or $\text{W}^{\pm}$ generally must be produced in association with additional jets in order to pass the $N_{\text{jets}} \geq 6$ requirement. The expected number of background events from QCD processes is negligible. Table 5.1 gives a more detailed breakdown of the background composition after each stage of the baseline selection. Yields in the table are taken from simulation and normalized to an integrated luminosity of $35.9\,\text{fb}^{-1}$. The requirements above the horizontal line are part of the baseline selection, while those below the line represent requirements used to separate the events into various bins, as described below.

Figure 5.1 shows "$N-1$" distributions for the variables S_{T}, $E_{\text{T}}^{\text{miss}}$, N_{jets}, and N_{b} following application of all requirements in the baseline selection, except for any pertaining to the variable whose distribution is being plotted.

After applying the baseline selection, we partition the accepted events into several bins of M_J, m_{T}, $E_{\text{T}}^{\text{miss}}$, N_{jets}, and N_{b}. The bins form non-overlapping categories of events with varying kinematic properties. These bins improve the signal-to-background ratio and will be used in the background estimation procedure described in Chapter 6. Rows below the horizontal line in Table 5.1 show the effect of some bin requirements on the background composition.

The first step in the binning process is to split the events into three M_J ranges

Table 5.1: Expected yields from simulated standard model background and SUSY signal process after sequential application of event selection criteria. Yields are normalized to an integrated luminosity of $35.9\,\mathrm{fb}^{-1}$. The "Other" category includes Drell-Yan processes and production of $\mathrm{t\bar{t}t\bar{t}}$, Z + jets, ZZ, $\mathrm{W^{\pm}Z}$, $\mathrm{W^{\pm}W^{\pm}}$, $\mathrm{t\bar{t}H}$, $\mathrm{W^{\pm}H}$, ZH, and ggZH. In cases where a Higgs boson is produced, it is assumed to decay to $\mathrm{b\bar{b}}$. The "$\mathrm{t\bar{t}}\,V$" category includes $\mathrm{t\bar{t}W^{\pm}}$, $\mathrm{t\bar{t}Z}$, and $\mathrm{t\bar{t}}\gamma$. The "NC" and "C" T1tttt signal models correspond to the ($m_{\tilde{\mathrm{g}}} = 1800\,\mathrm{GeV}$, $m_{\tilde{\chi}1}^{0} = 100\,\mathrm{GeV}$) and ($m_{\tilde{\mathrm{g}}} = 1400\,\mathrm{GeV}$, $m_{\tilde{\chi}1}^{0} = 1000\,\mathrm{GeV}$) mass points, respectively, as described in Section 4.2. Rows above the horizontal line correspond to requirements included in the baseline selection. For entries with an expected yield of 0, statistical uncertainties are at most 0.15 events. The precision is limited by the number of simulated events available. Table from Reference [13].

$L = 35.9\,\mathrm{fb}^{-1}$	Other	QCD	$\mathrm{t\bar{t}}\,V$	Single t	$\mathrm{W}^{\pm}$ + jets	$\mathrm{t\bar{t}}$ (1l)	$\mathrm{t\bar{t}}$ (2l)	SM bkg.	T1tttt NC	T1tttt C
$N_{\mathrm{leps}} = 1$, $S_{\mathrm{T}} > 500\,\mathrm{GeV}$, $E_{\mathrm{T}}^{\mathrm{miss}} > 200\,\mathrm{GeV}$	8468.1	3623.0	1624.4	9096.5	96 033.4	49 212.8	11 813.9	179 872.1	31.0	92.6
$N_{\mathrm{veto}} = 0$	6783.3	3414.2	1367.6	8103.3	92 184.9	45 789.0	7605.8	165 248.1	28.5	80.2
$N_{\mathrm{jets}} \geq 6$	420.2	200.8	512.1	1149.3	4185.5	11 588.4	1435.9	19 492.2	25.0	74.5
$N_{\mathrm{b}} \geq 1$	125.9	105.4	411.6	913.4	1007.1	9408.2	1183.0	13 154.6	23.7	70.8
$M_J > 250\,\mathrm{GeV}$	107.8	79.4	357.9	749.5	819.4	7943.3	919.1	10 976.5	23.6	66.1
$m_{\mathrm{T}} > 140\,\mathrm{GeV}$	9.5	6.7	42.3	43.2	28.2	87.2	369.1	586.2	19.3	39.4
$M_J > 400\,\mathrm{GeV}$	5.5	6.1	20.4	25.7	16.9	51.2	143.8	269.5	18.9	25.1
$N_{\mathrm{b}} \geq 2$	1.8	0.6	8.3	11.1	3.8	25.1	69.4	120.1	14.2	18.8
$E_{\mathrm{T}}^{\mathrm{miss}} > 350\,\mathrm{GeV}$	0.29	0.16	2.30	2.82	0.81	2.36	15.19	23.93	12.50	9.08
$E_{\mathrm{T}}^{\mathrm{miss}} > 500\,\mathrm{GeV}$	0.00	0.00	0.63	0.70	0.27	0.35	3.50	5.40	9.96	3.82
$N_{\mathrm{jets}} \geq 9$	0.03	0.00	0.12	0.06	0.05	0.04	0.39	0.69	3.82	2.61
	Other	QCD	$\mathrm{t\bar{t}}\,V$	Single t	$\mathrm{W}^{\pm}$ + jets	$\mathrm{t\bar{t}}$ (1l)	$\mathrm{t\bar{t}}$ (2l)	SM bkg.	T1tttt NC	T1tttt C

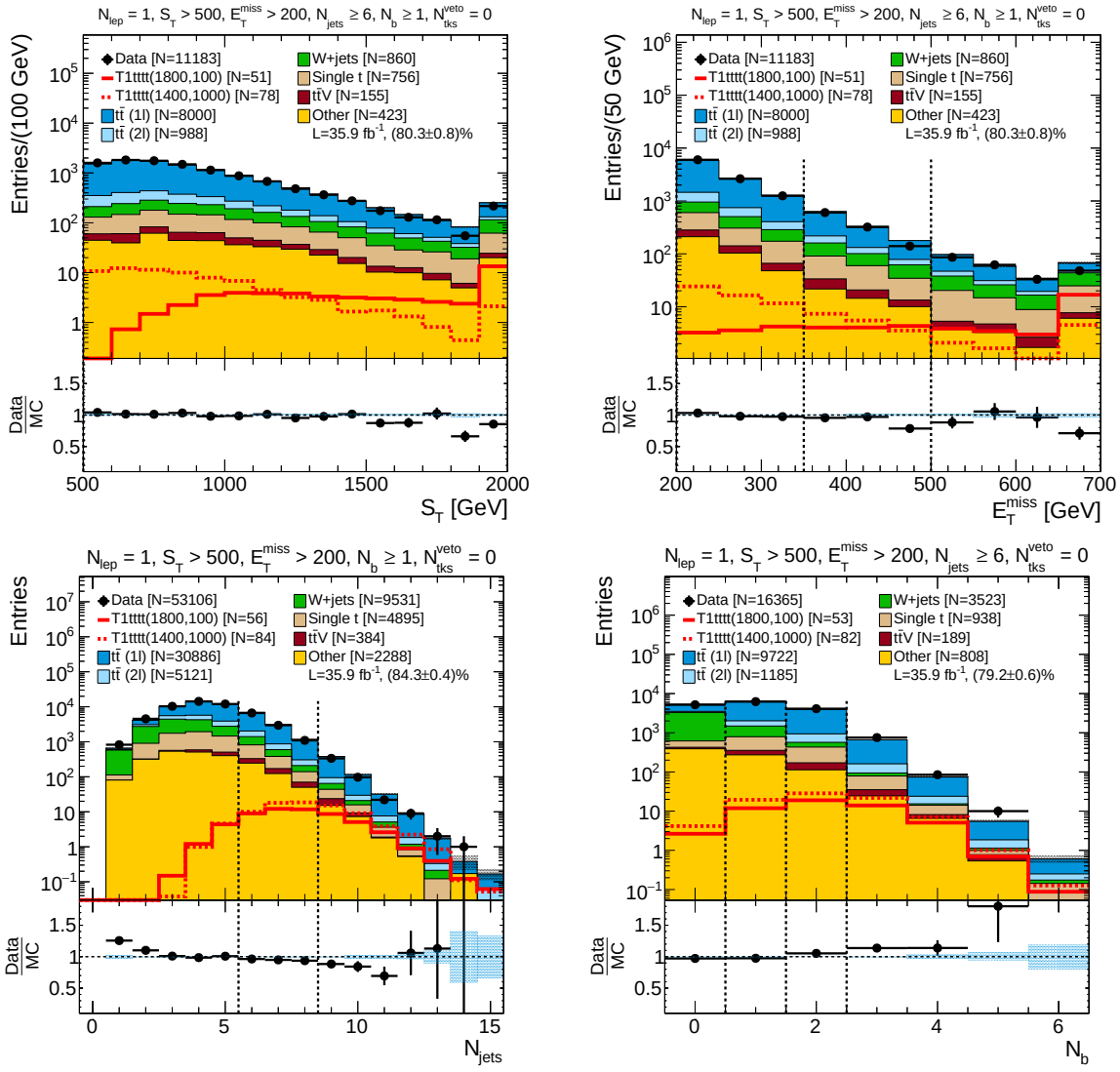

Figure 5.1: Distribution of baseline selection variables S_{T} (top left), $E_{\mathrm{T}}^{\mathrm{miss}}$ (top right), N_{jets} (bottom left), and N_{b} (bottom right). Distributions are shown in an "$N-1$" fashion with all requirements of the baseline selection applied, except for any pertaining to the variable whose distribution is shown. The blue shaded region in the ratio plots (bottom panels) indicates statistical uncertainty from the limited sample size of the Monte Carlo simulation. Plots from Reference [13].

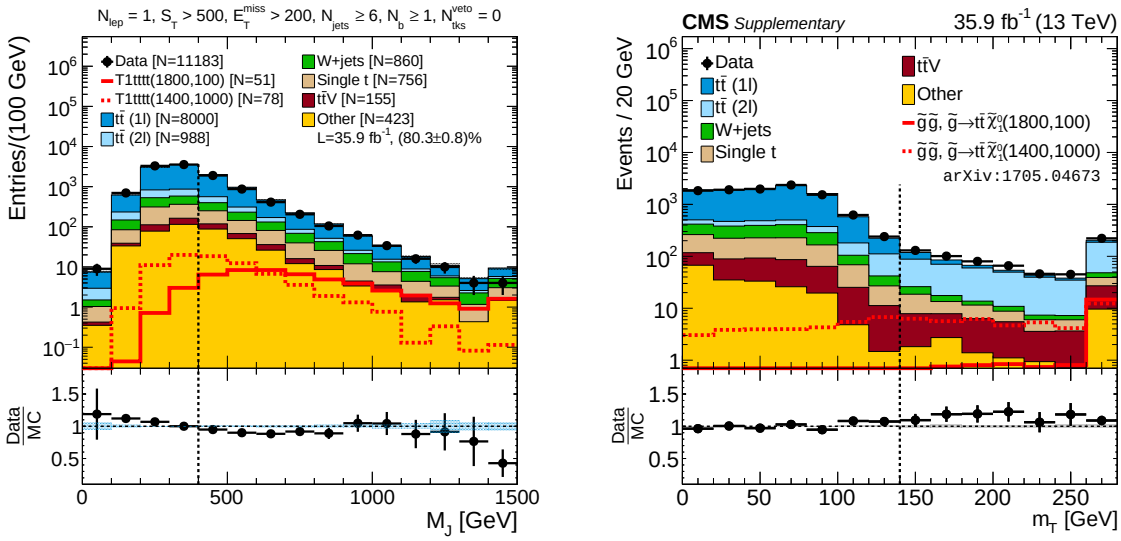

Figure 5.2: Distribution of M_J and m_T after the baseline selection. The blue shaded region in the ratio plots (bottom panels) indicates statistical uncertainty from the limited sample size of the Monte Carlo simulation. Left plot from Reference [13]. Right plot from supplementary technical material of Reference [11].

($M_J \leq 250\,\mathrm{GeV}$, $250\,\mathrm{GeV} < M_J \leq 400\,\mathrm{GeV}$, and $400\,\mathrm{GeV} < M_J$) and two m_T ranges ($m_\mathrm{T} \leq 140\,\mathrm{GeV}$ and $m_\mathrm{T} > 140\,\mathrm{GeV}$). Figure 5.2 shows the M_J and m_T distributions for events passing the baseline selection.

5.2 ISR and M_J

For $\mathrm{t\bar{t}}$ + jets production, the dominant source of background events passing the baseline selection, the M_J distribution depends strongly on the amount of initial state radiation (ISR). For example, Figure 5.3 compares the distributions of M_J in events with $p_{\mathrm{T,ISR}} < 10\,\mathrm{GeV}$ and in events with $p_{\mathrm{T,ISR}} > 100\,\mathrm{GeV}$. For $\mathrm{t\bar{t}}$ + jets events with negligible ISR, the M_J distribution has the interesting property that $M_J < 2m_\mathrm{t}$. This is because, in the absence of ISR, the two top quarks are produced approximately back-to-back. The largest possible M_J for low-ISR events occurs when the decay products of each top quark are clustered into a single large-R jet. This results in two large-R jets, each with a mass

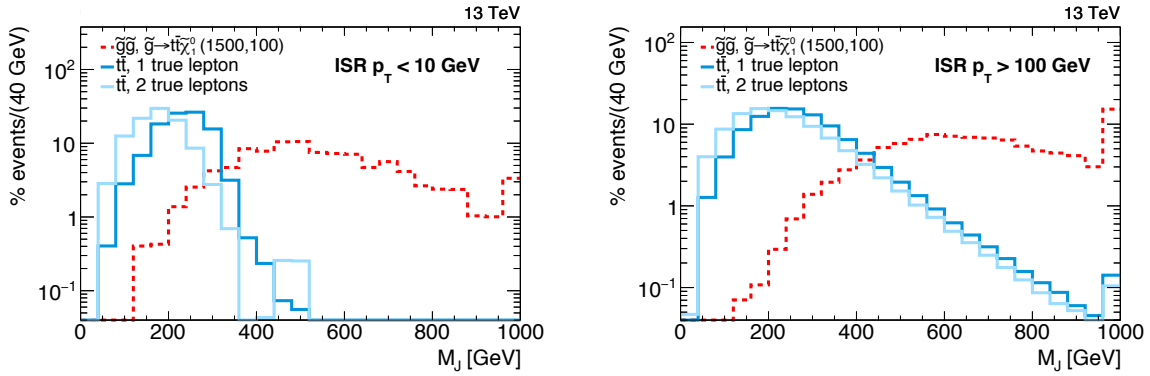

Figure 5.3: Distribution of M_J for events with $p_{\mathrm{T,ISR}} < 10\,\mathrm{GeV}$ and events with $p_{\mathrm{T,ISR}} > 100\,\mathrm{GeV}$. The distribution is shown for $\mathrm{t\bar{t}}$ events with either one or two true leptons (dark and light blue, respectively) and for an example T1tttt model (red). When large amounts of ISR are present, the high-M_J tails become similar for two $\mathrm{t\bar{t}}$ components. The events shown have at least one reconstructed lepton and satisfy $E_{\mathrm{T}}^{\mathrm{miss}} > 200\,\mathrm{GeV}$ and $H_{\mathrm{T}} > 500\,\mathrm{GeV}$. Figure from Reference [13].

no larger than that of the original top quark. If the decay products of a top quark do not fit within a large-R jet, the masses of the two resulting jets are even smaller.

On the other hand, in events with large amounts of ISR, there are two common ways to produce events with $M_J > 2m_{\mathrm{t}}$. First, the ISR jets may be clustered into one of the large-R jets along with a top quark. Alternatively, the two top quarks may recoil off of the ISR, causing their decay products to overlap in η-ϕ space and form a single large-R jet. In both cases, the masses of the resulting large-R jets may exceed m_{t}. In principle, it is also possible for multiple AK4-jets from ISR to be clustered into a single large-R jet with large mass, but contributions from such configurations are negligible compared to the previous two cases.

Figure 5.4 shows a simple diagram of the expecte configuration of objects clustered into large-R jets for an event without ISR (left) and with ISR (right). The diagram with ISR shows the ISR jets overlapping with the decay products from the top quarks. It is also possible that the two top quarks recoil against the ISR jet and overlap with each other. Figure 5.5 shows the large-R jets reconstructed for high-M_J event from 2015 in

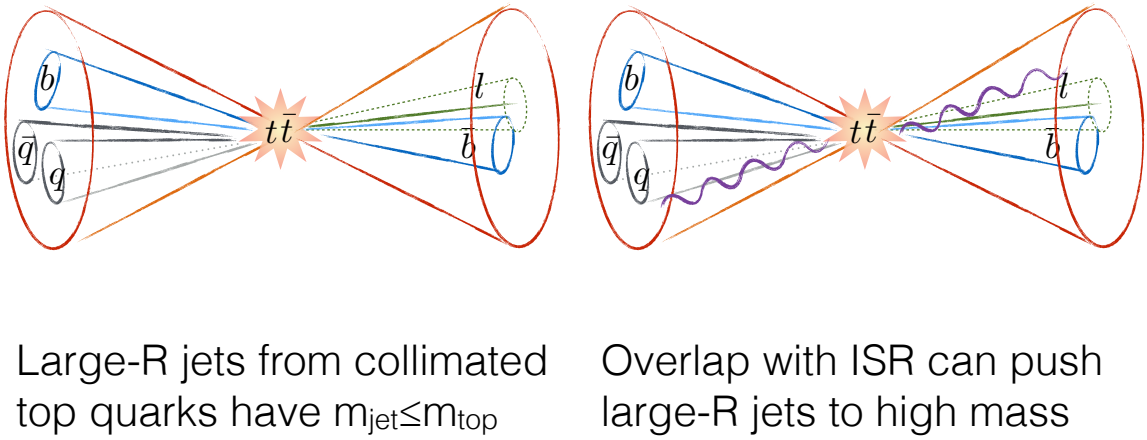

Figure 5.4: Simple diagram showing how objects are clustered into large-R jets in a $t\bar{t}$ + jets event without ISR (left) or with ISR (right). Here, the ISR is shown overlapping with the ISR jets. High ISR may also result from the two top quarks recoiling against the ISR and overlapping with each other.

which this latter configuration occurs. Note that in 2015, large-R jets where clustered with $R = 1.2$ instead of $R = 1.4$ [14, 11].

Another interesting property of events with significant ISR is that the tail of the M_J distribution for $t\bar{t}$ + jets events is approximately independent of the number of leptons in the event. This is because the contributions to M_J come primarily from ISR rather than the top quark decay products themselves, so the missed neutrino has minimal effect on M_J. The approximate independence of M_J and the number of leptons will be an important part of the background estimation method described later in Chapter 6.

The distribution of M_J in signal events is dependent on the difference in the masses of the gluino and LSP. Large mass differences tend to result in larger values of M_J because the extra available energy increases the p_T of the top quarks, collimating them and preferentially clustering the decay products into a single higher-mass large-R jet. Figure 5.6 provides examples of M_J spectra for two selected T1tttt mass points. The plots show the M_J distributions when large-R jets are clustered with radius parameters of $R = 1.2$ (left plot) and $R = 1.4$ (right plot, the standard used in this analysis). The

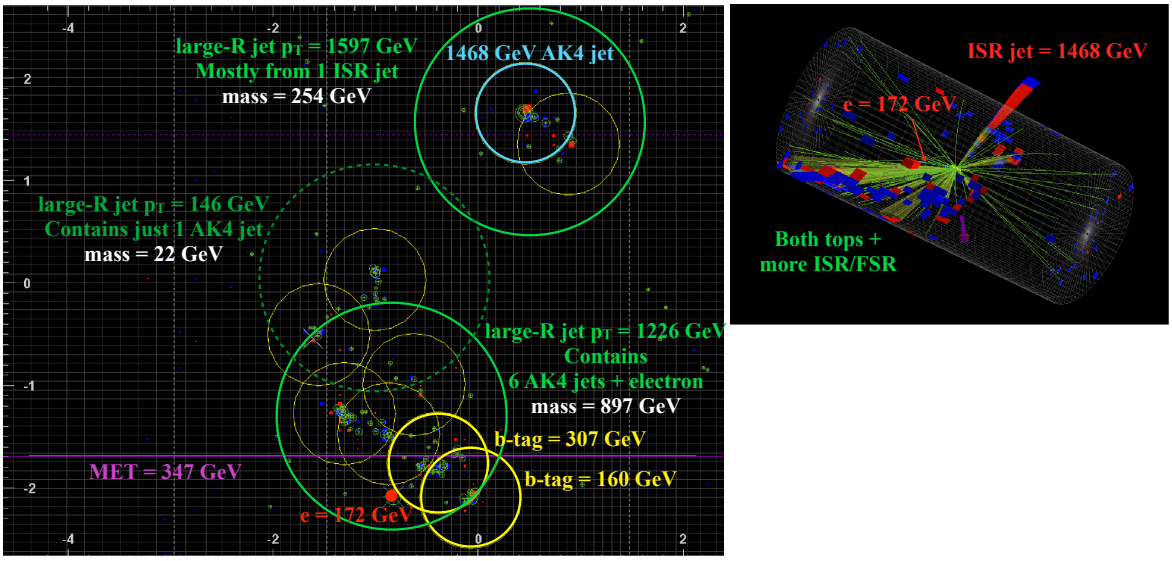

Figure 5.5: Reconstruction of a 2015 event (run number 256843, lumi block 282, event 408328426) with $M_J = 1173\,\text{GeV}$. The event has an electron and nine jets (yellow circles), two of which are b-tagged (bold yellow circle). It appears to be a $\mathrm{t\bar{t}}$+jets event in which the two top quarks recoiled off of an ISR jet with $p_\mathrm{T} = 1468\,\text{GeV}$, causing their decay producets to overlap. Many of the decay products are clustered into a single large-R jet with mass 897 GeV, causing the large M_J. Note that the large-R jets shown in green circles were clustered with $R = 1.2$ rather than the $R = 1.4$ used for the 2016 version of the search described in this dissertation [14, 11]. The left image shows a two-dimensional projection in η-ϕ space. The event is displayed using the Fireworks software from CMS.[15]

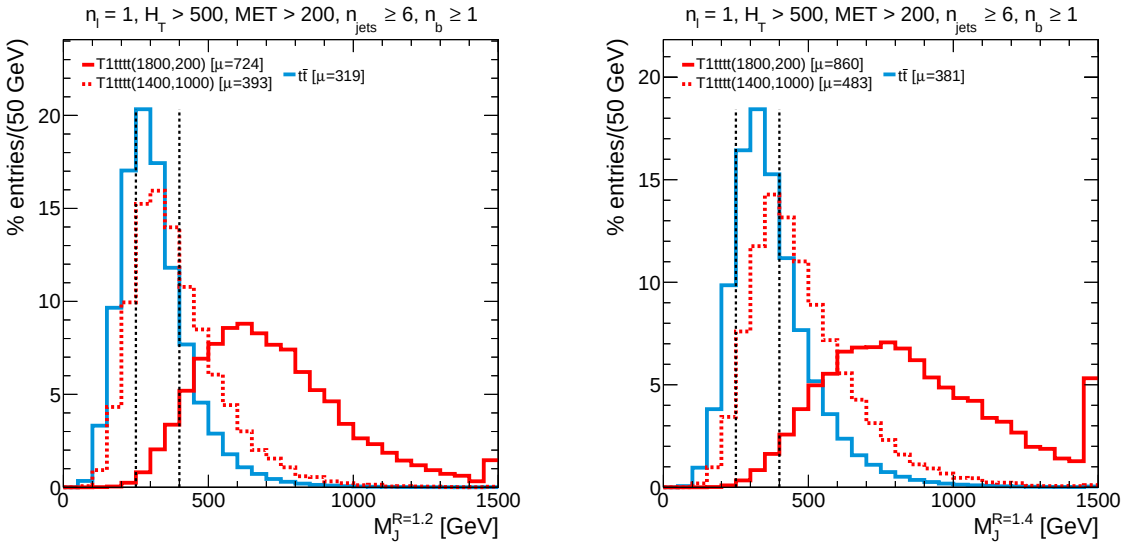

Figure 5.6: Distribution of M_J when large-R jets are clustered with radius parameters $R = 1.2$ (left) and $R = 1.4$ (right). The distributions are shown for $t\bar{t}$ (blue) events and two selected T1tttt mass points (red). The solid red line corresponds to the non-compressed benchmark with mass parameters $m_{\tilde{g}} = 1800\,\text{GeV}$ and $m_{\tilde{\chi}1^0} = 100\,\text{GeV}$, while the dashed red line corresponds to the compressed benchmark with $m_{\tilde{g}} = 1400\,\text{GeV}$ and $m_{\tilde{\chi}1^0} = 1000\,\text{GeV}$. In all cases, a selection of $N_{\text{leps}} = 1$, $H_{\text{T}} > 500\,\text{GeV}$, $E_{\text{T}}^{\text{miss}} > 200\,\text{GeV}$, $N_{\text{jets}} \geq 6$, and $N_{\text{b}} \geq 1$ is applied. Figure from Reference [13].

M_J spectrum shifts towards higher values as the clustering radius for the large-R jets increases.

Interestingly, changing the radius parameter R affects the signal and background distributions differently. This is especially true for compressed signal models. For example, in Figure 5.6, as the clustering radius increases from $R = 1.2$ to $R = 1.4$, the efficiency for a selection requirement of $M_J > 400\,\text{GeV}$ increases from about 40% to approximately 65%, while the $t\bar{t}$ efficiency only increases by roughly 10%. Figure 5.7 provides a clearer way of examining the effect of altering the clustering radius. It shows the efficiencies of the M_J requirement in signal and $t\bar{t}$ + jets samples for various choices of clustering radius and M_J threshold. The clustering radius has little effect for non-compressed models. For compressed models, performance improves as the clustering radius is increased

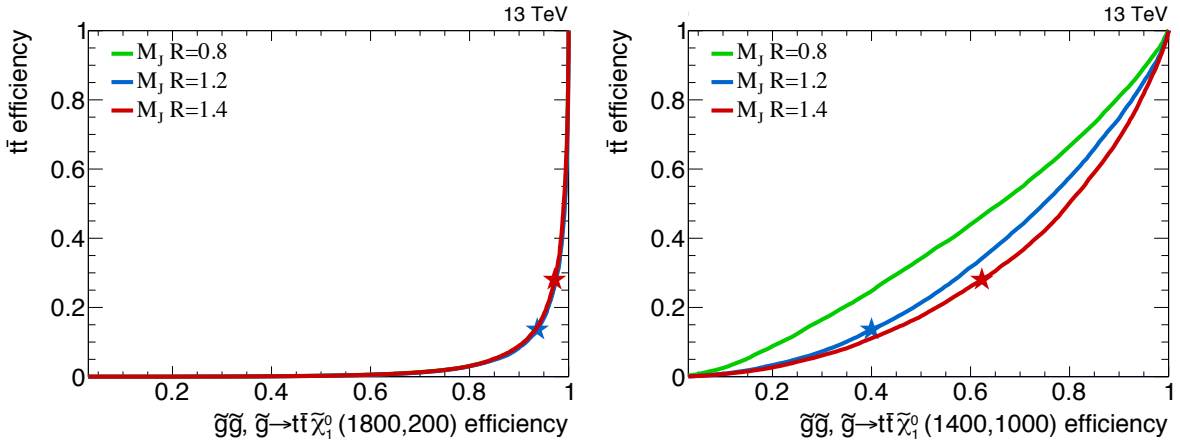

Figure 5.7: "Receiver Operating Characteristic," or ROC, curves showing the efficiency with which background $t\bar{t}$ + jets events pass an M_J-requirement (y-axis) as a function of the efficiency for signal events (x-axis). Each curve corresponds to a particular choice of clustering radius R for the large-R jets, while points along a single curve correspond to varying M_J selection thresholds. The largest M_J requirements are in the bottom-left corner. Points near the bottom-right corner are the most desirable since they simultaneously have high signal efficiency and strong background rejection. The left plot uses the non-compressed T1tttt benchmark point, while the right right uses the compressed benchmark. The clustering radius makes little difference in the performance of the M_J requirement for non-compressed models. For compressed models, increasing the radius improves performance up until approximately $R = 1.4$, after which further increases do not produce significant improvement, motivating the choice of $R = 1.4$ in this search. Figure from Reference [13].

up to approximately $R = 1.4$. Improvements for larger radius parameters are negligible, motivating the choice of $R = 1.4$ for this search.

5.3 Removing Single Lepton Events with m_{T}

The m_{T} variable allows one to filter out events containing a single leptonically-decaying $\mathrm{W}^{\pm}$. For well-reconstructed $t\bar{t}$ + jets events with a single charged lepton and all $E_{\mathrm{T}}^{\mathrm{miss}}$ resulting from a single neutrino, $m_{\mathrm{T}} < m_{\mathrm{W}^{\pm}}$. Due to finite $E_{\mathrm{T}}^{\mathrm{miss}}$-resolution, among other effects, these events do occasionally have larger values of m_{T}. Therefore, the m_{T} categories are separated at the higher value of 140 GeV rather than exactly at

the $W^{\pm}$-mass. Following application of the $m_T > 140\,\text{GeV}$ requirement in Table 5.1, less than 1% of the $t\bar{t}$ + jets events with a single lepton remain, leaving a high-M_J, high-m_T background that consists predominantly of dilepton $t\bar{t}$ + jets events with one of the leptons escaping undetected.

Since T1tttt and T5tttt models both have E_T^{miss} contributions from the pair of neutralinos, m_T is not bounded by the $W^{\pm}$-mass in single-lepton signal events.

Chapter 6

Background Estimation

Chapter 6 described how we select potentially interesting events that may be the result of SUSY processes, but it did not provide a way of determining whether the selected events were, in fact, produced by SUSY processes. In this chapter, we will explore an "ABCD" background estimation procedure that allows one to estimate how many of the selected events are due to known standard model processes. The chapter proceeds pedagogically, starting with the basic principle (extrapolation of the M_J distribution from low m_{T} to high m_{T}) in Section 6.1. It then adds the necessary mathematical details one by one before concluding with the likelihood function used to determine the background yield in Section 6.6.

6.1 Extrapolating from Low m_{T} to High m_{T}

The baseline selection is intended to reduce the number of accepted events produced by standard model background processes while preserving as many signal events as possible. Determining whether signal events are present among those that remain requires an estimate of the number of background events passing the baseline selection.

The $m_{\mathrm{T}} > 140\,\mathrm{GeV}$ requirement discussed in Chapter 5 leaves a sample which consists mainly of dilepton $\mathrm{t\bar{t}}$ + jets events in which one of the leptons is lost. We observed that the M_J distributions for $\mathrm{t\bar{t}}$ + jets events with a single charged lepton and with two charged leptons become similar when a large amount of ISR is present. This suggests one potential way of predicting the M_J distribution in the dilepton-dominated high-m_{T} sample: use a control sample in which most events have a single true lepton. Of course, the true number of leptons in an event is not experimentally accessible, but the majority of the low m_{T} events meet this description. Although the low- and high-m_{T} sample may have slight kinematic differences, one might expect the two samples to have similar M_J distributions.

Figure 6.1 shows the joint distribution of M_J and m_{T} in simulated $\mathrm{t\bar{t}}$ + jets and T1tttt events after application of the baseline selection. The $\mathrm{t\bar{t}}$ + jets component is split into two components: events with a single true lepton (dark blue, downward pointing triangle) and events with two true leptons (light blue, upward pointing triangle). All events have exactly one identified lepton, as required by the baseline selection. Below the dashed horizontal line at $m_{\mathrm{T}} = 140\,\mathrm{GeV}$, most of the $\mathrm{t\bar{t}}$ + jets events have a single lepton, while above the line, most $\mathrm{t\bar{t}}$ + jets events have two. For both populations, the correlations between M_J and m_{T} are small (less than 5%). Even more interestingly, the overall correlation coefficient for all $\mathrm{t\bar{t}}$ events passing the baseline selection is just 0.01.

This lack of correlation between M_J and m_{T} allows extrapolation of the M_J distribution from low-m_{T} to high-m_{T}. This extrapolation will be the basis of the background estimation procedure used in this analysis. Given that the composition, particularly with regard to the number of leptons, is different for the low- and high-m_{T} samples, it is worth checking that the events with one and two true leptons do in fact behave similarly. Figure 6.2 shows the normalized M_J and N_{jets} distributions for two categories of $\mathrm{t\bar{t}}$ + jets events: those with low-m_{T} and a single true lepton and those with high-m_{T} and two true

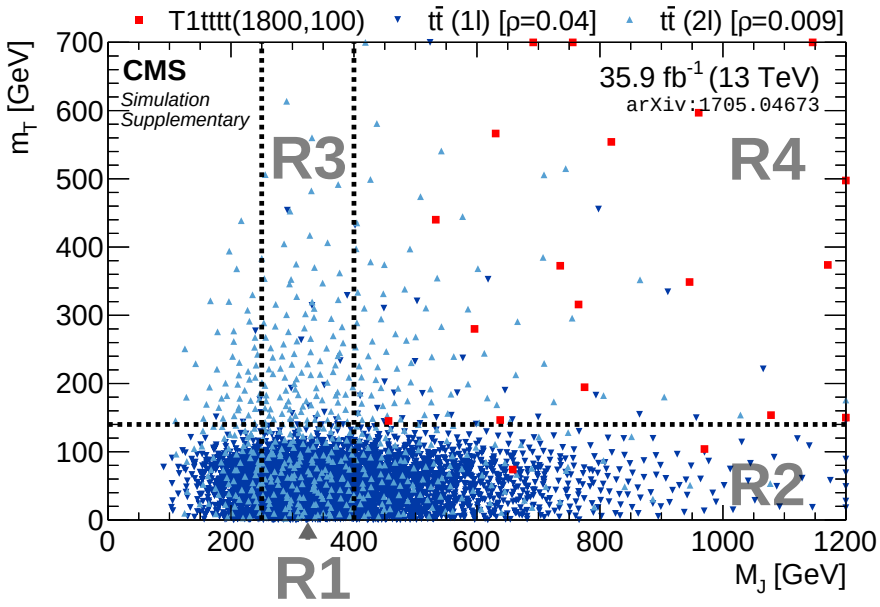

Figure 6.1: Scatter plot of m_{T} versus M_J. Dark blue, downward pointing triangles represent $\mathrm{t\bar{t}}$ events with a single true charged lepton. Light blue, upward pointing triangles represent $\mathrm{t\bar{t}}$ events with two true charged leptons. The red squares represent T1tttt events for the NC mass point. The scatter plot is normalized such that one point represent one expected event at an integrated luminosity of $35.9\,\mathrm{fb}^{-1}$. The correlation coefficients for the two $\mathrm{t\bar{t}}$ components, indicated in the legend, are both small. If all $\mathrm{t\bar{t}}$ events are considered together, the overall correlation coefficient is $\rho \approx 0.01$. Figure from supplementary technical material for Reference [11].

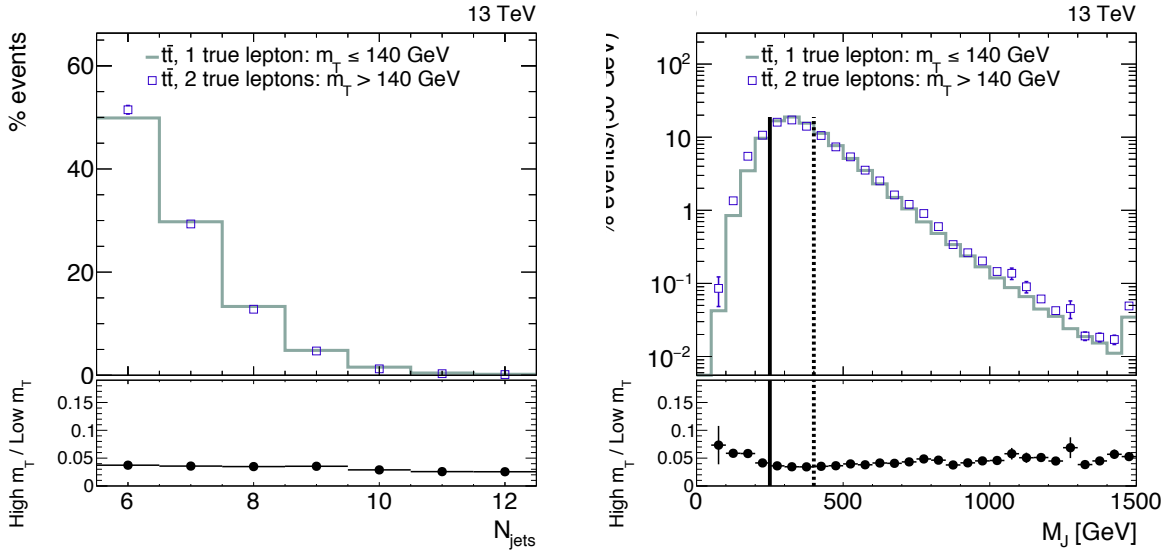

Figure 6.2: Comparison of normalized M_J and N_{jets} distributions for two categories of simulated $t\bar{t}$ events: those with a single true lepton and reconstructed $m_T \leq 140\,\text{GeV}$ and those with two true leptons and reconstructed $m_T > 140\,\text{GeV}$. These samples constitute the dominant source of background events in their respective m_T ranges. For both M_J and N_{jets}, the distributions are similar for the low- and high-m_T samples. Figure from Reference [13].

leptons. As expected, the M_J distributions for the two sets of events are similar. Even more impressively, the N_{jets} distributions are similar for $N_{\text{jets}} \geq 6$ despite the change in the $W^{\pm}$-decay needed in order to get a second true lepton.

6.2 The "ABCD" Method

The first step in estimating the number of background events is to partition the M_J-m_T plane into four regions, as labeled in Figure 6.1:

- Control Region R1: $250\,\text{GeV} < M_J \leq 400\,\text{GeV}$, $m_T \leq 140\,\text{GeV}$,
- Control Region R2: $M_J > 400\,\text{GeV}$, $m_T > 140\,\text{GeV}$,
- Control Region R3: $250\,\text{GeV} < M_J \leq 400\,\text{GeV}$, $m_T \leq 140\,\text{GeV}$,

- Signal Region R4: $M_J > 400\,\text{GeV}$, $m_\text{T} > 140\,\text{GeV}$.

For the T1tttt and T5tttt models studied in this search, most signal events are expected to reside in R4, and so we label R4 as the "signal region" and regions R1, R2, and R3 as "control regions." We will refer to the four regions collectively as "analysis regions." Events with $M_J \leq 250\,\text{GeV}$ will not be used in the search.

Assuming that M_J and m_T are completely uncorrelated, the expected background yield for the signal region R4 can be expressed in terms of the expected background yields of the control regions as

$$\mu_{\text{R4}}^{\text{bkg}} = \frac{\mu_{\text{R2}}^{\text{bkg}} \cdot \mu_{\text{R3}}^{\text{bkg}}}{\mu_{\text{R1}}^{\text{bkg}}}. \tag{6.1}$$

For a single Poisson counting experiment, the maximum likelihood estimator for the Poisson mean parameter is simply $\hat{\mu} = N$. By using this estimator in the control regions, we obtain a simple estimator for the background yield in the signal region,

$$\hat{\mu}_{\text{R4}}^{\text{bkg}} = \frac{N_{\text{R2}} \cdot N_{\text{R3}}}{N_{\text{R1}}}. \tag{6.2}$$

If N_{R4} is significantly greater than $\hat{\mu}_{\text{R4}}^{\text{bkg}}$, the excess events may be attributed to signal processes and interpreted as a discovery. Conversely, if N_{R4} is significantly less than $\hat{\mu}_{\text{R4}} = \hat{\mu}_{\text{R4}}^{\text{bkg}} + \hat{\mu}_{\text{R4}}^{\text{sig}}$, then the observed yield is incompatible with the signal model, and we consider the signal model excluded. In such a setup, $\hat{\mu}_{\text{R4}}^{\text{sig}}$ would typically be obtained from a simulate signal sample.

This approach is often referred to as the "ABCD method." Perhaps its greatest strength is the fact that the background estimation is *data-driven*. That is, no Monte Carlo simulation is used in the calculation of $\hat{\mu}_{\text{R4}}^{\text{bkg}}$, though it may be used for studies validating the method, for corrections to the background estimate, and to obtain the

expected signal yield.

Unfortunately, this simple formulation also has a few shortcomings. Most notably, it assumed that all signal events will fall into the signal region R4. The presence of any signal contamination in the control regions will cause an overestimation of their background yields and thereby bias the background estimate in R4.

To address these difficulties, a more general approach is needed. As a first step, it is useful to reparameterize the expected yields in the four regions as

$$\mu_{\mathrm{R1}} = r \cdot \mu_{\mathrm{R1}}^{\mathrm{MC,sig}} + \mu_{\mathrm{R1}}^{\mathrm{bkg}} = r \cdot \mu_{\mathrm{R1}}^{\mathrm{MC,sig}} + \lambda, \tag{6.3}$$

$$\mu_{\mathrm{R2}} = r \cdot \mu_{\mathrm{R2}}^{\mathrm{MC,sig}} + \mu_{\mathrm{R2}}^{\mathrm{bkg}} = r \cdot \mu_{\mathrm{R2}}^{\mathrm{MC,sig}} + \lambda \cdot R(M_J), \tag{6.4}$$

$$\mu_{\mathrm{R3}} = r \cdot \mu_{\mathrm{R3}}^{\mathrm{MC,sig}} + \mu_{\mathrm{R3}}^{\mathrm{bkg}} = r \cdot \mu_{\mathrm{R3}}^{\mathrm{MC,sig}} + \lambda \cdot R(m_{\mathrm{T}}), \tag{6.5}$$

$$\mu_{\mathrm{R4}} = r \cdot \mu_{\mathrm{R4}}^{\mathrm{MC,sig}} + \mu_{\mathrm{R4}}^{\mathrm{bkg}} = r \cdot \mu_{\mathrm{R4}}^{\mathrm{MC,sig}} + \lambda \cdot R(M_J) \cdot R(m_{\mathrm{T}}) \cdot \kappa, \tag{6.6}$$

where the double-ratio

$$\kappa = \frac{\mu_{\mathrm{R4}}^{\mathrm{MC,bkg}} / \mu_{\mathrm{R2}}^{\mathrm{MC,bkg}}}{\mu_{\mathrm{R3}}^{\mathrm{MC,bkg}} / \mu_{\mathrm{R1}}^{\mathrm{MC,bkg}}} \tag{6.7}$$

is a correction factor from simulation which accounts for correlations between M_J and m_{T}.

In this formulation, there are four parameters specifying the shape of the background: λ, $R(M_J)$, $R(m_{\mathrm{T}})$, and κ. The parameter λ is simply an overall normalization of the expected background yields across the four regions.

$$R(m_{\mathrm{T}}) = \frac{\mu(\mathrm{bkg},\, m_{\mathrm{T}} > 140\,\mathrm{GeV})}{\mu(\mathrm{bkg},\, m_{\mathrm{T}} \leq 140\,\mathrm{GeV})}. \tag{6.8}$$

is a shape parameter describing the ratio of the expected background yield at high m_{T}

to the expected background yield at low m_{T}. $R(M_J)$ is an analogous shape parameter for the M_J distribution. The κ parameter controls the amount of correlation between M_J and m_{T}. One may readily check that when $\kappa = 1$, the expected background yields $\mu_{\mathrm{R}i}^{\mathrm{bkg}}$ satisfy the constraint of Equation (6.1).

In addition to the four background parameters, there are five parameters controlling the expected signal yields in the four regions. The four $\mu_{\mathrm{R}i}^{\mathrm{MC,sig}}$ parameters are the expected yields in the four regions at the nominal cross section of the signal model. We multiply these expected signal yields by an additional signal strength multiplier r, with $r = 0$ corresponding to the absence of signal and $r = 1$ corresponding to the presence of a signal at its nominal cross section.

Since there are a total of nine parameters (four for the background and five for the signal), one must either fix a subset of the parameters or have at least nine observables. Roughly speaking, the four expected signal yields $\mu_{\mathrm{R}i}^{\mathrm{MC,sig}}$ are obtained from the four simulated signal yields $N_{\mathrm{R}i}^{\mathrm{MC,sig}}$; the three background parameters λ, $R(M_J)$, and $R(m_{\mathrm{T}})$ are constrained by the observed yields $N_{\mathrm{R1}}^{\mathrm{data}}$, $N_{\mathrm{R2}}^{\mathrm{data}}$, and $N_{\mathrm{R3}}^{\mathrm{data}}$; the signal strength r is determined by $N_{\mathrm{R4}}^{\mathrm{data}}$; and κ is either fixed to unity for a fully data-driven estimate of the other parameters or obtained from the simulated background yields $N_{\mathrm{R1}}^{\mathrm{bkg,MC}}$.

Section 6.4 will provide a more formal and rigorous explanation of how we measure the parameters.

6.3 Sensitivity of the ABCD Method

One of the most important questions about any background estimation procedure is whether it is precise enough to allow for discovery or exclusion of signal models of interest. Figure 6.3 gives a sense of how many signal events are needed for a simple ABCD method to discover or exclude a model. In order to simplify the study enough

to fit in a two dimensional plot, we must make a few simplifying assumptions. First, we will assume that signal events only occur in the signal region R4. Second we assume that the background ratio parameters are equal so that we may use a common ratio $R = R(M_J) = R(m_{\mathrm{T}})$ on the y-axis. The x-axis will show the expected background yield $B = \lambda \cdot R(M_J) \cdot R(m_{\mathrm{T}})$ in R4. Each point in the plane then specifies a different background normalization and distribution of background events across the four regions. The solid curves indicate the expected signal yield in R4 needed for a discovery with a standard score of $Z \geq 5$, often referred to as "5σ" significance. The dashed lines indicated the expected number of signal events needed to exclude a model at a 95% confidence level.

It is simpler to think of the x-position as determining the expected number of background events in the signal region, and the y-position as determining the accuracy with which that background rate can be measured. The ideal search is as close as possible to the upper left corner of the plane where the background is both small and precisely measured. One immediately notes that the limit curves (dashed lines) are nearly vertical, indicating that the ability to exclude a model is only weakly dependent on the precision with which the background yield is measured. This is because it is always possible to observe a deficit relative to the signal model, regardless of how poorly the background yield is measured. That is, since the expected total yield $\mu_{\mathrm{sig}} < \mu_{\mathrm{bkg}} + \mu_{\mathrm{sig}}$ for any μ_{bkg}, a model can be excluded whenever the number of observed events is significantly less than μ_{sig}, regardless of how poorly the background is measured.

On the other hand, the number of expected signal events needed for a discovery is highly dependent on the precision of the background measurement. Below a certain ratio R, the expected number of signal events needed for a discovery rapidly increases. This is because the expected yield (and the precision of any measurements thereof) in the control regions decreases to the point that excesses in R4 can be attributed to mere statistical fluctuations in the control region yields rather than the presence of signal events.

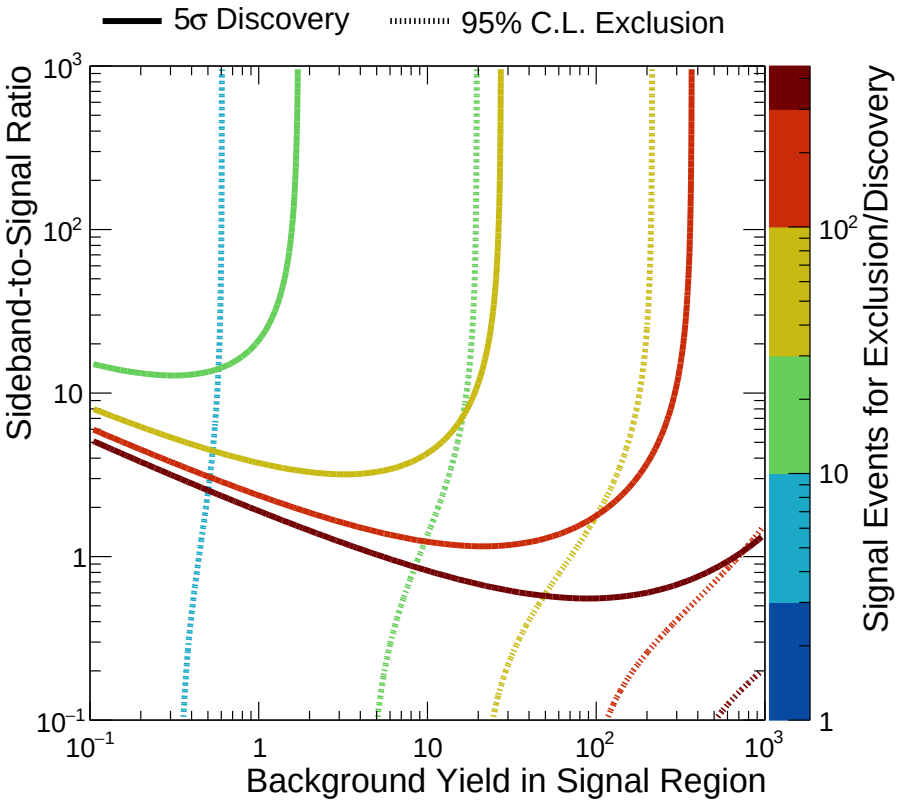

Figure 6.3: Expected number of signal events in R4 needed for a "5σ" discovery (solid lines) or exclusion at a 95% confidence level, as a function of the expected number of background events in R4 (along x-axis) and the signal-to-background ratio $R = R(M_J) = R(m_{\mathrm{T}})$ (along the y-axis). Note that sensitivity is computed using an asymptotic approximation which may not be fully accurate in the limit of very small yields.

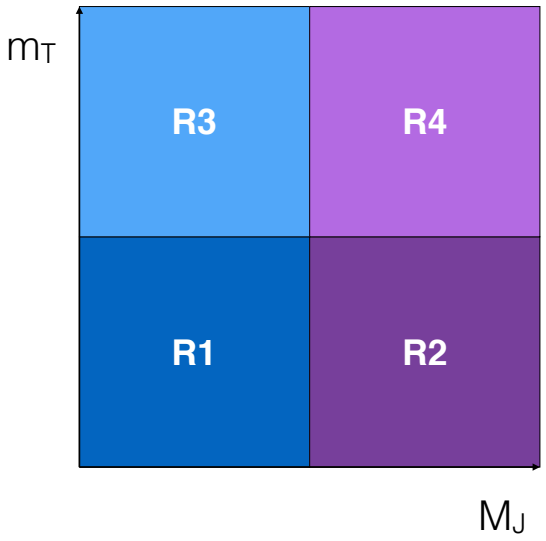

Figure 6.4: Schematic representation of an unbinned ABCD plane in M_J and m_{T}.

6.4 Adding Bins

While the parameterization described in the previous section is mathematically sufficient to measure the signal strength parameter r (and all the other signal- and background-related nuisance parameters), it is not optimal in terms of sensitivity to the presence or absence of signal events. On one hand, Section 6.3 showed that one may increase sensitivity by reducing the expected background yield in R4. On the other hand, it also showed that one does not want to lose too many events from the control regions. One potential way around this problem is to keep all the events passing the baseline selection, but separate them into various bins. Bins with higher $E_{\mathrm{T}}^{\mathrm{miss}}$, N_{jets}, and N_{b} requirements typically have a higher fraction of events originating from signal processes (assuming the signal exists), as seen in Table 5.1, but the bins with lower requirements may still be useful in estimating the background yields.

For the remainder of this section, we will represent binning options by diagrams such as that shown in Figure 6.4, which shows an unbinned ABCD plane in M_J and m_{T}.

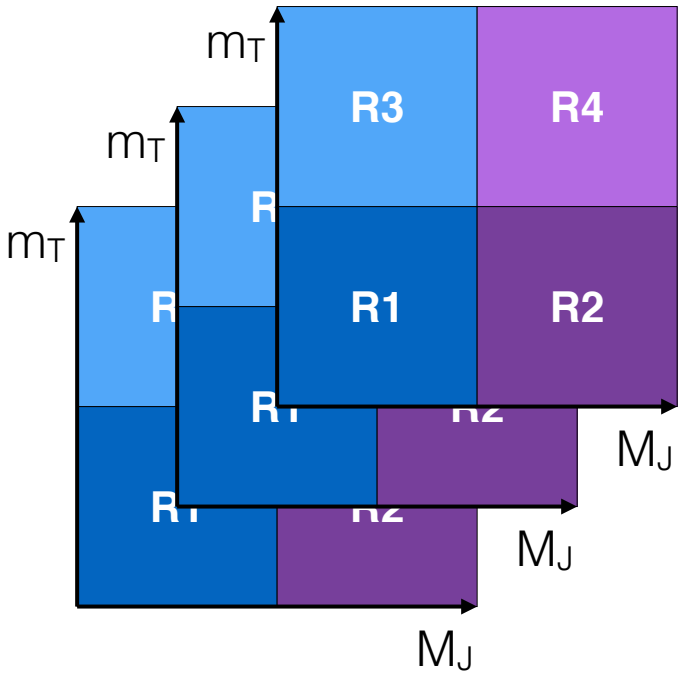

Figure 6.5: Schematic representation of an ABCD background estimation method split into three bins by using separate planes.

The question then is how to adapt the ABCD method to multiple bins. There are two main ways to do this. The first, and perhaps more obvious way of introducing binning is to subdivide each of the four analysis regions into identical bins and simply perform a separate ABCD background estimation for each bin. Note that, because all bins should test the same signal hypothesis, a common signal strength parameter r is shared across all bins in this approach. This binning option can is shown schematically in Figure 6.5.

This method of binning allows the background to be estimated for every bin in each of the four analysis regions, but comes at the expense of adding a large number of parameters to the model. For example, with a background-only model without any κ corrections ($\kappa_i = 1$ for each bin and $r = 0$), each bin adds four observables (one per analysis region) and three background parameters (one copy each of λ, $R(M_J)$, and $R(m_T)$).

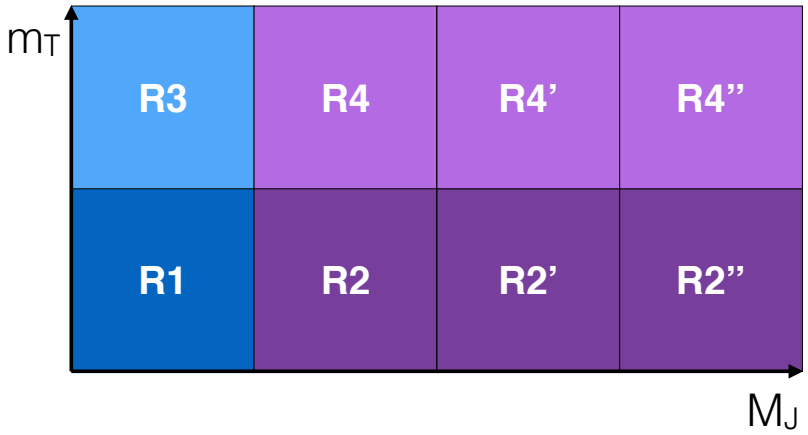

Figure 6.6: Diagram showing an $m \times n$ (in this case, 2×4) "ABCD" plane using M_J and m_{T}. The ABCD method can be generalized to an $m \times n$ plane as long as the x-axis and y-axis variables are either independent or simulation can be trusted to correctly model any correlations between them.

There is, however, another way to implement bins. In Section 6.2, we divided the M_J and m_{T} axes into two ranges, but there is nothing to prevent one from using finer subdivisions. In the general case, rather than a 2×2 ABCD model, one can use an arbitrary $m \times n$ grid as long as the x and y variables are independent or simulation can be trusted to correct for any correlations. An schematic representation of such an $m \times n$ ABCD plane is shown in Figure 6.6.

In the general case, one can use both binning options and use multiple $m \times n$ ABCD planes. The expected yields are then parameterized as

$$\mu_{\mathrm{R1},i} = r \cdot \mu^{\mathrm{MC,sig}}_{\mathrm{R1},i} + \mu^{\mathrm{bkg}}_{\mathrm{R1},i} = r \cdot \mu^{\mathrm{MC,sig}}_{\mathrm{R1},i} + \lambda_i, \tag{6.9}$$

$$\mu_{\mathrm{R2},i,j} = r \cdot \mu^{\mathrm{MC,sig}}_{\mathrm{R2},i,j} + \mu^{\mathrm{bkg}}_{\mathrm{R2},i,j} = r \cdot \mu^{\mathrm{MC,sig}}_{\mathrm{R2},i,j} + \lambda_i \cdot [R(M_J)]_{i,j}, \tag{6.10}$$

$$\mu_{\mathrm{R3},i} = r \cdot \mu^{\mathrm{MC,sig}}_{\mathrm{R3},i} + \mu^{\mathrm{bkg}}_{\mathrm{R3},i} = r \cdot \mu^{\mathrm{MC,sig}}_{\mathrm{R3},i} + \lambda_i \cdot [R(m_{\mathrm{T}})]_i, \tag{6.11}$$

$$\mu_{\mathrm{R4},i,j} = r \cdot \mu^{\mathrm{MC,sig}}_{\mathrm{R4},i,j} + \mu^{\mathrm{bkg}}_{\mathrm{R4},i,j} = r \cdot \mu^{\mathrm{MC,sig}}_{\mathrm{R4},i,j} + \lambda_i \cdot [R(M_J)]_{i,j} \cdot [R(m_{\mathrm{T}})]_i \cdot \kappa_{i,j}, \tag{6.12}$$

where $i \in [1, N_{\mathrm{planes}}]$ specifies a particular $E_{\mathrm{T}}^{\mathrm{miss}}$ bin's ABCD plane, $j \in [1, N_{\mathrm{R2},i}]$ specifies

an M_J column within plane i. For this analysis, we will not need to use any additional subdivisions along the m_{T} axis, but we could add them by simply adding an additional index to the $R(m_{\mathrm{T}})$ and κ parameters which would specify an m_{T} row within plane i. To prevent the already cumbersome notation from becoming even more complicated, we omit this additional index in the above equations. Note that there is now one κ per bin in R4, with

$$\kappa_{i,j} = \frac{\mu_{\mathrm{R4},i,j}^{\mathrm{MC,bkg}} / \mu_{\mathrm{R2},i,j}^{\mathrm{MC,bkg}}}{\mu_{\mathrm{R3},i}^{\mathrm{MC,bkg}} / \mu_{\mathrm{R1},i}^{\mathrm{MC,bkg}}}. \tag{6.13}$$

There is one last generalization needed for this search. In the above description of $m \times n$ ABCD planes, each column represented a different M_J range. However, the only requirement of the ABCD method is that each column share the same $R(m_{\mathrm{T}})$ parameter (possibly with small differences correctable via κ factors). In principle, each column can represent binning in variables completely unrelated to M_J, as long as the variables are independent of m_{T}.

For this analysis, there are three bins of $E_{\mathrm{T}}^{\mathrm{miss}}$ ($200\,\mathrm{GeV} < MET \leq 350\,\mathrm{GeV}$, $350\,\mathrm{GeV} < E_{\mathrm{T}}^{\mathrm{miss}} \leq 500\,\mathrm{GeV}$, and $E_{\mathrm{T}}^{\mathrm{miss}} > 500\,\mathrm{GeV}$), two bins of N_{jets} ($6 \leq N_{\mathrm{jets}} \leq 8$ and $N_{\mathrm{jets}} \geq 9$), and three bins of N_{b} ($N_{\mathrm{b}} = 1$, $N_{\mathrm{b}} = 2$, and $N_{\mathrm{b}} \geq 3$). This gives a total of $3 \times 2 \times 3 = 18$ bins in the signal region. N_{jets} and N_{b} are minimally correlated with m_{T}, so we may treat bins in these variables as columns in the ABCD plane. $E_{\mathrm{T}}^{\mathrm{miss}}$, while useful for signal-versus-background discrimination, is highly correlated with m_{T}, so we must instead treat $E_{\mathrm{T}}^{\mathrm{miss}}$ bins as separate ABCD planes. Effectively, we bin the high-M_J regions R2 and R4 in $E_{\mathrm{T}}^{\mathrm{miss}}$, N_{jets}, and N_{b}, but only bin the low-M_J regions R1 and R3 in $E_{\mathrm{T}}^{\mathrm{miss}}$, integrating over N_{jets} and N_{b}. The binning configuration is illustrated in Figure 6.7.

In terms of the above parameterization, the index $i \in [1, 3]$ specifies an ABCD plane

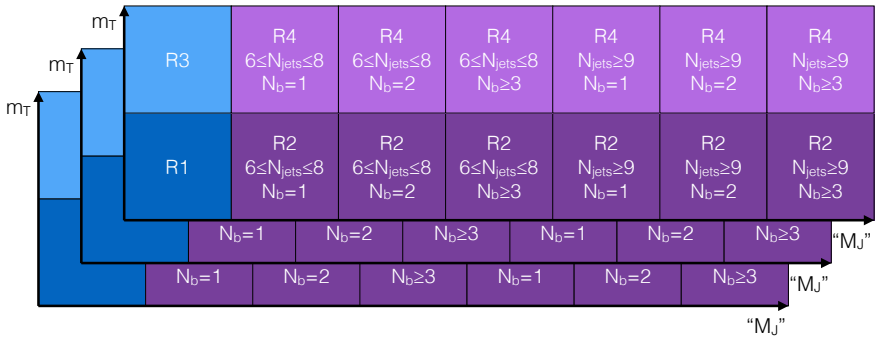

Figure 6.7: Schematic representation of the ABCD binning used in this search. The separate planes represent the three $E_{\mathrm{T}}^{\mathrm{miss}}$ bins $200\,\mathrm{GeV} < MET \leq 350\,\mathrm{GeV}$, $350\,\mathrm{GeV} < E_{\mathrm{T}}^{\mathrm{miss}} \leq 500\,\mathrm{GeV}$, and $E_{\mathrm{T}}^{\mathrm{miss}} > 500\,\mathrm{GeV}$.

corresponding to one of the three $E_{\mathrm{T}}^{\mathrm{miss}}$ bins. The index $j \in [1, 6]$ specifies one of the $2 \times 3 = 6$ N_{jets} and N_{b} bins. In total, there are three copies of a 2×7 ABCD plane, so that $N_{\mathrm{bins}}(\mathrm{R1}) = N_{\mathrm{bins}}(\mathrm{R3}) = 3$ and $N_{\mathrm{bins}}(\mathrm{R2}) = N_{\mathrm{bins}}(\mathrm{R4}) = 18$.

Since each of the three $E_{\mathrm{T}}^{\mathrm{miss}}$ planes has just one $R(m_{\mathrm{T}})$ parameter, binning in this way requires that N_{jets} and N_{b} are approximately independent of m_{T} within each $E_{\mathrm{T}}^{\mathrm{miss}}$ bin. Figure 6.8 confirms this assumption by showing the value of $R(m_{\mathrm{T}})$ in simulation as a function of N_{jets} and N_{b}, integrated over the whole $E_{\mathrm{T}}^{\mathrm{miss}} > 200\,\mathrm{GeV}$ range. As long as $N_{\mathrm{jets}} \geq 6$ (required by the baseline selection), $R(m_{\mathrm{T}})$ has negligible dependence on N_{jets} in both the low- and high-M_J regions. For smaller values of N_{jets}, the value of $R(m_{\mathrm{T}})$ increases, particularly for $M_J > 400\,\mathrm{GeV}$. This is because the assumption that ISR jets are the dominant contribution to M_J breaks down when fewer jets are present.

Figure 6.8 indicates that $R(m_{\mathrm{T}})$ does have a slight dependence on N_{b}, especially for $M_J > 400\,\mathrm{GeV}$. If the N_{b} dependence were precisely the same for the low- and high-M_J, then no κ-correction would be needed. The difference between the N_{b} dependence at low- and high-M_J can be seen more easily in Figure 6.9, which shows the κ correction factors needed for each of the 18 bins. There is a residual N_{b} dependence, but it is small enough that the simulation can model it with sufficient accuracy.

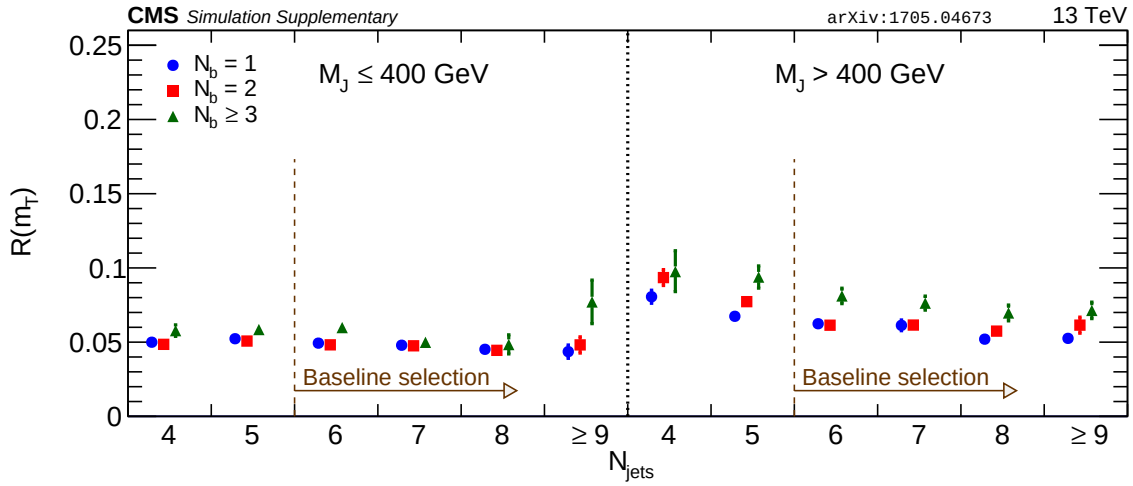

Figure 6.8: Measured value of $R(m_{\mathrm{T}})$ in simulation as a function of N_{jets} and N_{b} for the low-M_J (left half) and high-M_J (right half) regions. If the $R(m_{\mathrm{T}})$ value at low-M_J matches the corresponding value at high-M_J, then no κ correction is needed. If the differences are small, simulation can be generally be trusted to provide an appropriate correction. $R(m_{\mathrm{T}})$ is only mildly dependent on N_{jets} and N_{b}, particularly for $M_J \leq 400\,\mathrm{GeV}$. The lack of complex kinematic dependencies makes it more likely that the simulation will accurately model the behavior. Figure from supplementary technical material of Reference [11].

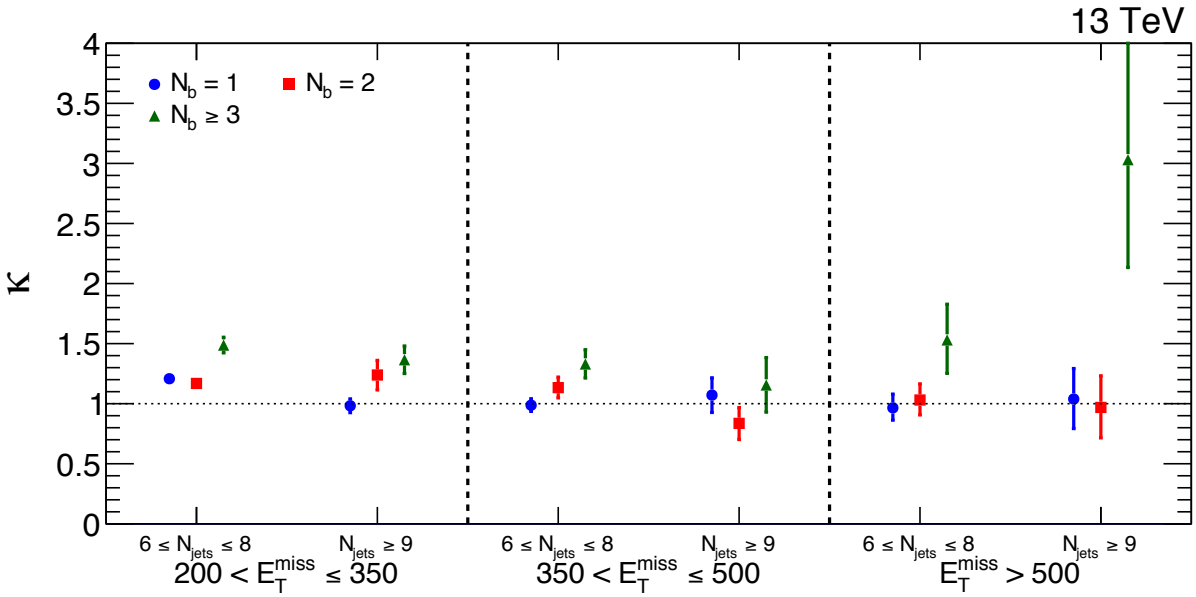

Figure 6.9: Measured values of κ in simulation with their associated uncertainties. The κ values are typically close to unity and do not show any strong dependence on N_{jets} and N_{b}. This adds confidence in the ability of the simulation to accurately model κ. Figure from Reference [13].

6.5 Adding Systematic Uncertainties

The final detail that needs to be added to the background parameterization is the implementation of systematic uncertainties in the κ corrections. We will postpone discussion of the various sources of systematic uncertainty considered in this analysis and their relative sizes until Chapters 7 and 8. This section will focus only on the mathematical implementation of the uncertainties.

In the previous section, $\kappa_{i,j}$ carried two indices, the first specifying a $E_{\mathrm{T}}^{\mathrm{miss}}$ plane and the second specifying an N_{jets}-N_{b} bin. We incorporate systematic uncertainties in $\kappa_{i,j}$ by multiplying it by a factor of the form $\exp(\sum_k \varsigma_{i,j,k} Z_k)$, where the sum indexed by k runs over all systematic uncertainties. The Z_k are unknown nuisance parameters and the $\varsigma_{i,j,k}$ are constants which specify the size of the effect of uncertainty k on $\kappa_{i,j}$. Note that the Z_k must be shared across bins in order to allow for (anti-)correlated effects. Anti-correlations between bins are implemented by choosing the $\varsigma_{i,j,k}$ for those two bins to have opposite signs, while positive correlations are implemented by choosing the $\varsigma_{i,j,k}$ to have the same sign. Uncertainties which have uncorrelated effects on the $\kappa_{i,j}$ can be implemented by using multiple Z_k and setting all but one of the $\varsigma_{i,j,k}$ to zero for each k.

With all systematic uncertainties included, the expected yields are parameterized as

$$\mu_{\mathrm{R1},i} = r \cdot \mu_{\mathrm{R1},i}^{\mathrm{MC,sig}} \cdot \exp\left(\sum_{k=1}^{N_{\mathrm{systs}}} \varsigma_{\mathrm{R1},i,j,k}^{\mathrm{sig}} Z_k\right) + \lambda_i, \tag{6.14}$$

$$\mu_{\mathrm{R2},i,j} = r \cdot \mu_{\mathrm{R2},i,j}^{\mathrm{MC,sig}} \cdot \exp\left(\sum_{k=1}^{N_{\mathrm{systs}}} \varsigma_{\mathrm{R2},i,j,k}^{\mathrm{sig}} Z_k\right) + \lambda_i \cdot [R(M_J)]_{i,j} \cdot \exp\left(\sum_{k=1}^{N_{\mathrm{systs}}} \varsigma_{i,j,k}^{\mathrm{bkg}} Z_k\right), \tag{6.15}$$

$$\mu_{\mathrm{R3},i} = r \cdot \mu_{\mathrm{R3},i}^{\mathrm{MC,sig}} \cdot \exp\left(\sum_{k=1}^{N_{\mathrm{systs}}} \varsigma_{\mathrm{R3},i,j,k}^{\mathrm{sig}} Z_k\right) + \lambda_i \cdot [R(m_{\mathrm{T}})]_i, \tag{6.16}$$

$$\mu_{\mathrm{R4},i,j} = r \cdot \mu_{\mathrm{R4},i,j}^{\mathrm{MC,sig}} \cdot \exp\left(\sum_{k=1}^{N_{\mathrm{systs}}} \varsigma_{\mathrm{R4},i,j,k}^{\mathrm{sig}} Z_k\right) + \lambda_i \cdot [R(M_J)]_{i,j} \cdot [R(m_{\mathrm{T}})]_i \cdot \kappa_{i,j}. \tag{6.17}$$

As before, the index $i \in [1,3]$ specifies a $E_{\mathrm{T}}^{\mathrm{miss}}$ plane and the index $j \in [1,6]$ specifies an N_{jets}-N_{b} bin. The index k, which only appears within sums on the right-hand side, specifies a particular source of systematic uncertainty.

Note that, while systematic uncertainties in the signal contribution are present for all four analysis regions, background uncertainties are applied only in the control region R2. This is because the only way for the background estimation to be biased is through mismodeling of κ in simulation, as discussed further in Chapter 7. Therefore, one only needs to multiply κ by an $\exp(\varsigma Z)$ term rather than the expected background yield for all four regions. In principle, this could be implemented by putting the systematic uncertainty in R4. However, in Chapter 9, we will occasionally need to omit the R4 contributions to the likelihood function. Placing the uncertainty terms in R2 ensures that the systematic uncertainty is still present when the R4 contributions are removed. With Gaussian contraints on the Z_k, as discussed in Section 6.6, the two treatments are mathematically equivalent.

To prevent the number of nuisance parameters from growing beyond the number of

observables as more systematic uncertainties are added, each Z_k must be constrained. For this analysis, we append a normal distribution term to the likelihood for each Z_k, so that $\exp(\varsigma_{i,j,k} Z_k)$ is log-normally constrained. Section 6.6 will discuss such constraints in more detail.

6.6 Maximum Likelihood Parameter Estimation

We measure the parameters via a maximum likelihood fit. The likelihood function

$$L = L^{\text{data}} \cdot L^{\text{MC,bkg}} \cdot L^{\text{MC,sig}} \cdot L^{\text{syst}} \tag{6.18}$$

can be factored into four parts. To describe these four components, two distributions are needed: the Poisson distribution with probability mass function $\text{Pois}(N|\mu) = \frac{\mu^N \exp(-\mu)}{N!}$ and the standard normal (or Gaussian) distribution with probability density function $\text{Gaus}(x) = \frac{1}{\sqrt{2\pi}} \exp\left(\frac{x^2}{2}\right)$.

The "data" factor in the likelihood,

$$\begin{aligned} L^{\text{data}} = &\left[\prod_{i=1}^{3} \text{Pois}(N_{\text{R1},i}|\mu_{\text{R1},i})\right] \times \left[\prod_{i=1}^{3}\prod_{j=1}^{6} \text{Pois}(N_{\text{R2},i,j}|\mu_{\text{R2},i,j})\right] \\ &\times \left[\prod_{i=1}^{3} \text{Pois}(N_{\text{R3},i}|\mu_{\text{R3},i})\right] \times \left[\prod_{i=1}^{3}\prod_{j=1}^{6} \text{Pois}(N_{\text{R4},i,j}|\mu_{\text{R4},i,j})\right], \end{aligned} \tag{6.19}$$

incorporates information from the integer number of observed events N in each of the bins of the four analysis regions. The expected yields μ are those defined in Equations (6.14), (6.14), (6.14), and (6.14).

The next two components are similar products of Poisson probabilities, but come with additional complications due to the weighting of simulated event samples. These weights arise from the difference between the integrated luminosities of the real and simulated

datasets, as shown in Table 4.3, and from corrections applied to the simulated samples to better reproduce the properties of the real dataset. First, consider a simplified case in which a bin contains N events all with weight w. The likelihood for the Poisson mean parameter μ is

$$L_w(\mu|N) = \text{Pois}\left(N\middle|\frac{\mu}{w}\right) = \frac{\left(\frac{\mu}{w}\right)^N \exp\left(-\frac{\mu}{w}\right)}{N!}. \tag{6.20}$$

One may recognize the right-hand side of the equation as the gamma distribution.

Unfortunately, the composition of each bin typically comprises multiple types of events with different weights. Suppose for example that there are N_{raw} simulated events with weights w_i. The approach used in this analysis is to approximate the Poisson distribution using effective values of the parameters

$$N_{\text{eff}} \equiv \frac{\left(\sum_{i=1}^{N_{\text{raw}}} w_i\right)^2}{\sum_{i=1}^{N_{\text{raw}}} w_i^2}, \tag{6.21}$$

$$w_{\text{eff}} \equiv \frac{\sum_{i=1}^{N_{\text{raw}}} w_i^2}{\sum_{i=1}^{N_{\text{raw}}} w_i}. \tag{6.22}$$

Importantly, this choice of parameters will not bias the estimated Poisson mean parameter $\hat{\mu} = N_{\text{eff}} w_{\text{eff}} = \sum_{i=1}^{N_{\text{raw}}} w_i$.

It is useful to check that this is a reasonable approximation with a few simple test cases. For example, if all event weights w_i are identical, then w_{eff} will be equal to this common weight and $N_{\text{eff}} = N_{\text{raw}}$. That is, if all weights are identical, the approximation is exact. Alternatively, if $N_{\text{raw}} = 2$ and $w_1 \gg w_2$, then $N_{\text{eff}} = 1 + O\left(\frac{w_2}{w_1}\right)$ and $w_{\text{eff}} = w_1 \cdot \left[1 - O\left(\frac{w_2}{w_1}\right)\right]$, reflecting the fact that adding an event with very small weight should not change the likelihood function at leading order.

One can also show that $0 \leq N_{\text{eff}} \leq N_{\text{raw}}$. The lower bound ensures the Poisson

distribution will never be evaluated with negative N_{eff}, while the upper bound ensures that the uncertainty in μ is never underestimated. N_{eff} may take on non-integer values, in which case Equation (6.20) is simply evaluated as though it were a continuous distribution in N. The astute reader will notice that the normalization is incorrect when interpreted in this way, but this does not affect the maximum likelihood parameter estimators. Further, the statistics used to test for discovery or exclusion of a model always compute a ratio of likelihood in which the normalization cancels out. Section 9.3 presents additional details about the test statistics.

There are two troublesome edge cases in this procedure. First, the denominator in Equation (6.22) may be negative if any of the w_i are negative. In practice, this may happen in bins which are not well-populated by the simulated data and where Poisson fluctuations may produce more events with negative weights than with positive weights. If this happens, then the effective parameters are set to $N_{\text{eff}} = 0$ and $w_{\text{eff}} = \sqrt{\left(\sum_{i=1}^{N_{\text{raw}}} w_i\right)^2 + \sum_{i=1}^{N_{\text{raw}}} w_i^2}$. This approximates adding the negative yield in quadrature with its uncertainty to obtain w_{eff}.

The second potential problem occurs when there are no simulated events in a bin, in which case both N_{eff} and w_{eff} are undefined. When this occurs, the requirements for the bin are relaxed until passing event(s) are found. These events are then used to compute w_{eff} in the usual manner and N_{eff} is set to zero.

With this prescription for computing effective yields and weights, the next two pieces

of the likelihood function in Equation (6.18) can be computed. The term

$$L^{\mathrm{MC,bkg}} = \left[\prod_{i=1}^{3} \mathrm{Pois}\left(N_{\mathrm{R1},i}^{\mathrm{MC,bkg}} \middle| \frac{\mu_{\mathrm{R1},i}^{\mathrm{MC,bkg}}}{w_{\mathrm{R1},i}^{\mathrm{MC,bkg}}}\right)\right] \times \left[\prod_{i=1}^{3}\prod_{j=1}^{6} \mathrm{Pois}\left(N_{\mathrm{R2},i,j}^{\mathrm{MC,bkg}} \middle| \frac{\mu_{\mathrm{R2},i,j}^{\mathrm{MC,bkg}}}{w_{\mathrm{R2},i,j}^{\mathrm{MC,bkg}}}\right)\right] \times \left[\prod_{i=1}^{3} \mathrm{Pois}\left(N_{\mathrm{R3},i}^{\mathrm{MC,bkg}} \middle| \frac{\mu_{\mathrm{R3},i}^{\mathrm{MC,bkg}}}{w_{\mathrm{R3},i}^{\mathrm{MC,bkg}}}\right)\right] \times \left[\prod_{i=1}^{3}\prod_{j=1}^{6} \mathrm{Pois}\left(N_{\mathrm{R4},i,j}^{\mathrm{MC,bkg}} \middle| \frac{\mu_{\mathrm{R4},i,j}^{\mathrm{MC,bkg}}}{w_{\mathrm{R4},i,j}^{\mathrm{MC,bkg}}}\right)\right] \tag{6.23}$$

determines the expected backgrounds in simulation, which in turn determine the κ-corrections via Equation (6.13). All the observed yields "N" and weights "w" are effective yields and weights as defined above.

Similarly, the signal likelihood component

$$L^{\mathrm{MC,sig}} = \left[\prod_{i=1}^{3} \mathrm{Pois}\left(N_{\mathrm{R1},i}^{\mathrm{MC,sig}} \middle| \frac{\mu_{\mathrm{R1},i}^{\mathrm{MC,sig}}}{w_{\mathrm{R1},i}^{\mathrm{MC,sig}}}\right)\right] \times \left[\prod_{i=1}^{3}\prod_{j=1}^{6} \mathrm{Pois}\left(N_{\mathrm{R2},i,j}^{\mathrm{MC,sig}} \middle| \frac{\mu_{\mathrm{R2},i,j}^{\mathrm{MC,sig}}}{w_{\mathrm{R2},i,j}^{\mathrm{MC,sig}}}\right)\right] \times \left[\prod_{i=1}^{3} \mathrm{Pois}\left(N_{\mathrm{R3},i}^{\mathrm{MC,sig}} \middle| \frac{\mu_{\mathrm{R3},i}^{\mathrm{MC,sig}}}{w_{\mathrm{R3},i}^{\mathrm{MC,sig}}}\right)\right] \times \left[\prod_{i=1}^{3}\prod_{j=1}^{6} \mathrm{Pois}\left(N_{\mathrm{R4},i,j}^{\mathrm{MC,sig}} \middle| \frac{\mu_{\mathrm{R4},i,j}^{\mathrm{MC,sig}}}{w_{\mathrm{R4},i,j}^{\mathrm{MC,sig}}}\right)\right]. \tag{6.24}$$

uses effective yields and weights from simulation to constrain the expected signal yields. Note that the signal strength parameter r does not appear in $L^{\mathrm{MC,sig}}$, which determines the expected signal yields at the nominal cross section for the signal model.

Finally, the nuisance parameters Z_k from the systematic uncertainties are constrained by the term

$$L^{\mathrm{syst}} = \prod_{i=k}^{N_{\mathrm{systs}}} \mathrm{Gaus}(Z_k). \tag{6.25}$$

The sizes of the effects of the uncertainties is controlled by the $\varsigma_{i,j,k}$ in Equations (6.14), (6.15), (6.16), and (6.17), so a standard normal distribution is used for all Z_k.

Chapter 7

Systematic Uncertainty in Background Estimates

The ABCD background estimation method described in Chapter 6 relies on the approximate independence of M_J and m_{T} and the ability of the simulated data to correctly model any correlation between the two variables. The independence of m_{T} and M_J was itself built on two properties of the background events: first, that most background events come from $\mathrm{t\bar{t}}+\mathrm{jets}$ processes and have significant ISR and two leptons, one of which is lost during reconstruction of the event; and second, that for such events, the ISR is the main contributor to M_J, producing similar M_J distributions for the $m_{\mathrm{T}} \leq 140\,\mathrm{GeV}$ and $m_{\mathrm{T}} > 140\,\mathrm{GeV}$ samples despite differences in the number of leptons and jets in the two ranges.

Chapter 6 also established a procedure to using κ factors from simulation to correct for residual M_J-m_{T} correlations. It is important to note that if the simulation were able to perfectly reproduce the behavior of the real data, then by construction, the background estimation procedure would be perfectly unbiased for every bin.

While the simulated samples can be used to correct for small correlations, they may

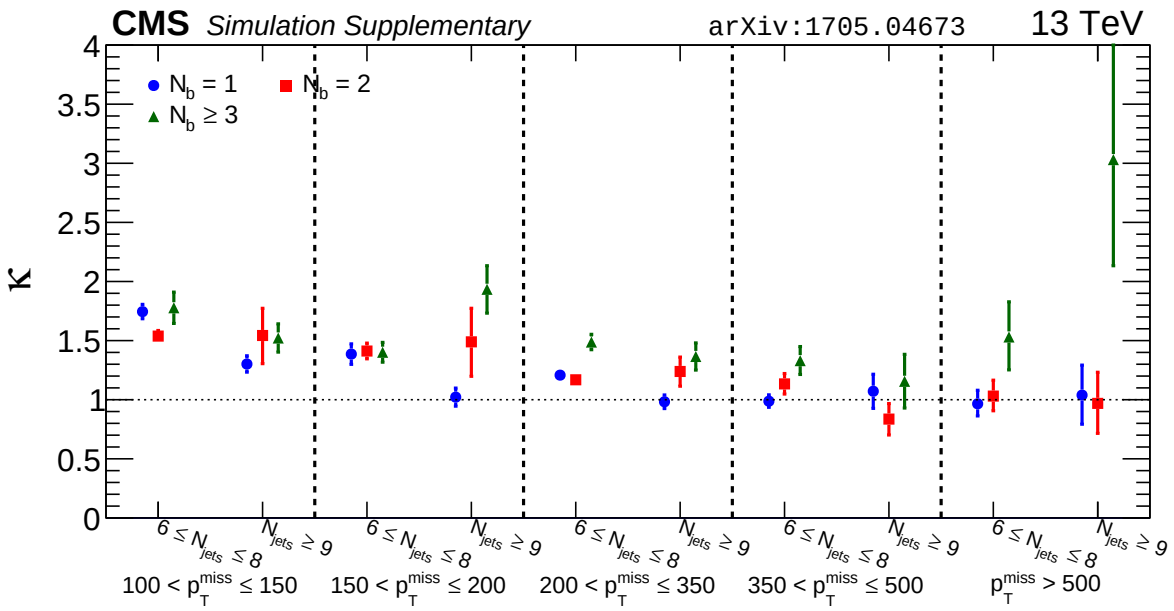

Figure 7.1: Values of κ for an extended $E_{\mathrm{T}}^{\mathrm{miss}}$ range, including the $E_{\mathrm{T}}^{\mathrm{miss}} > 200\,\mathrm{GeV}$ analysis regions and $100\,\mathrm{GeV} < E_{\mathrm{T}}^{\mathrm{miss}} \leq 200\,\mathrm{GeV}$ validation region. Figure from supplementary technical material for Reference [11].

not always perfectly reproduce the behavior of the real dataset. It particular, the exact kinematic dependence of κ on $E_{\mathrm{T}}^{\mathrm{miss}}$, N_{jets}, and N_{b} may be difficult to model accurately. For example, Figure 7.1 shows that for low values of $E_{\mathrm{T}}^{\mathrm{miss}}$, κ increases significantly. While the $E_{\mathrm{T}}^{\mathrm{miss}} \leq 200\,\mathrm{GeV}$ region is excluded by the baseline selection, the trend indicates that κ can have strong kinematic dependencies.

The systematic uncertainties $\varsigma_{i,j}$ introduced in Section 6.5 allow the ABCD method to absorb minor imperfections in the simulation. Properly accounting for potential mismodeling requires one to choose appropriate values for the $\varsigma_{i,j}$. This chapter discusses how the $\varsigma_{i,j}$ are determined, beginning with studies of potential sources of mismodeling to get a sense of how they affect the measurement of κ in simulation. It then explores how various categories of events contribute to the kinematic dependence of κ and introduces two control samples used to study how the contributions from these categories change across the bins. Finally, it establishes, validates, and uses a procedure to obtain

appropriate values for the $\varsigma_{i,j}$.

7.1 Effects of Mismodeling in Simulation

Before attempting to evaluate potential systematic uncertainties, it is useful to get a sense of how mismodeling can affect κ. Since one cannot know *a priori* whether there is a difference between the real and simulated datasets, we perform these studies using only the simulated data. First, we intentionally modify the simulated data in various ways. We treat the modified simulated data as "pseudodata" and measure κ for each pseudodata sample. The modifications mean that the unmodified simulation will not reproduce the pseudodata with complete accuracy. In particular, there may be some difference Δ_κ between the κ values observed in the pseudodata and in the unmodified simulation.

Using the above scheme, we obtain one Δ_κ per bin per mismodeling scenario. Then, we study the size and any kinematic dependencies of Δ_κ for each scenario. Due to the double-ratio nature of κ, the effects of the added mismodeling largely cancel out in many cases, keeping Δ_κ small even for severe mismodeling scenarios. This provides confidence that the method is robust against mismodeling in simulation. Table 7.1 contains a summary of the scenarios studied in this section, showing that Δ_κ is typically only a few percent even for extreme scenarios. Despite many of the mismodeling scenarios introducing unrealistically large errors into the simulation, the observed changes in κ are smaller than the typical statistical fluctuations expected in the data for an integrated luminosity of $\sim 35\,\mathrm{fb}^{-1}$.

Note that we use the scenarios described below only to provide insight into how mismodeling can affect κ; we do not use them directly in the determination of the systematic uncertainties.

Table 7.1: Summary of the effect of various intentionally applied mismodeling scenarios on κ. Note that these values are intended to represent the potential size of changes in κ caused by various mismodeling scenarios. They are not assigned as systematic uncertainties.

Mismodeling Studied	How Modeled	Δ_κ [%]	Comments
ISR p_{T}	ISR tail weight $\times 0.25$ or $\times 0.5$	0-6	Stronger at high $E_{\mathrm{T}}^{\mathrm{miss}}$
ISR Multiplicity	2 s.d. change in ISR weight	2-4	Flat across bins
$E_{\mathrm{T}}^{\mathrm{miss}}$ Resolution	Double weight if $[E_{\mathrm{T}}^{\mathrm{miss}}(\mathrm{reco}) - E_{\mathrm{T}}^{\mathrm{miss}}(\mathrm{true})]/E_{\mathrm{T}}^{\mathrm{miss}}(\mathrm{true}) > 0.5$	0-6	Strong at low $E_{\mathrm{T}}^{\mathrm{miss}}$
b-Tagging Efficiency	3 s.d. variation of scale factors	0-7	
QCD Cross Section	QCD$\times 4$	1-7	Stronger at low $E_{\mathrm{T}}^{\mathrm{miss}}$
$\mathrm{W}^{\pm}$ + jets Cross Section	$\mathrm{W}^{\pm}$ + jets $\times 3$	2-8	Increased κ at low $E_{\mathrm{T}}^{\mathrm{miss}}$, decreased κ at high $E_{\mathrm{T}}^{\mathrm{miss}}$
$\mathrm{t\bar{t}W}^{\pm}$ Cross Section	$\mathrm{t\bar{t}W}^{\pm} \times 3$	0-3	Flat across bins
$\mathrm{t\bar{t}Z}$ Cross Section	$\mathrm{t\bar{t}Z} \times 3$	1-11	11% likely a statistical fluctuation

7.1.1 Two S.D. Change in ISR Correction for $t\bar{t}$ + jets Events

Section 4.2 described the reweighting of simulated events based on the number of ISR jets present in each event. The weights listed in Table 4.4 may not be perfectly accurate. This and similar scenarios are of particular interest since the ISR multiplicity directly affects M_J.

One realistic mismodeling scenario is a two standard deviation (s.d.) change in the ISR weights applied to the $t\bar{t}$ + jets events. Such a variation causes a 2% to 3% change in κ. We find no significant kinematic dependence for Δ_κ.

7.1.2 Over-Prediction of High ISR Yield

The previous scenario studies the effect of having an incorrect ISR multiplicity distribution in simulation. It is also possible that the simulation could incorrectly model the transverse momentum of the ISR jets. We study the effects of such mismodeling by modifying the weights of events with a large $p_{\mathrm{T}}^{\mathrm{ISR}}$, defined as the scalar sum of the transverse momenta of ISR jets. Specifically, we multiply the weights for events satisfying $600\,\mathrm{GeV} < p_{\mathrm{T}}^{\mathrm{ISR}} \leq 800\,\mathrm{GeV}$ by 0.5 and the weights for events satisfying $p_{\mathrm{T}}^{\mathrm{ISR}} > 800\,\mathrm{GeV}$ by 0.25. This is approximately twice the size of the largest mismodeling not ruled out by comparisons of real and simulated data.

For all but one bin, $\Delta_\kappa \leq 4\%$ in this scenario. The one exception is consistent with $\Delta_\kappa = 0$ within statistical uncertainty.

7.1.3 Under-Prediction of $\boldsymbol{E}_{\mathrm{T}}^{\mathrm{miss}}$ Mismeasurement

As discussed in earlier chapters, the most background events for the $m_{\mathrm{T}} > 140\,\mathrm{GeV}$ analysis regions are produced by $t\bar{t}$ + jets process and have two leptons, since events with a single lepton should satisfy $m_{\mathrm{T}} \leq m_{\mathrm{W}^{\pm}}$. Of course, mismeasurement of $E_{\mathrm{T}}^{\mathrm{miss}}$ can

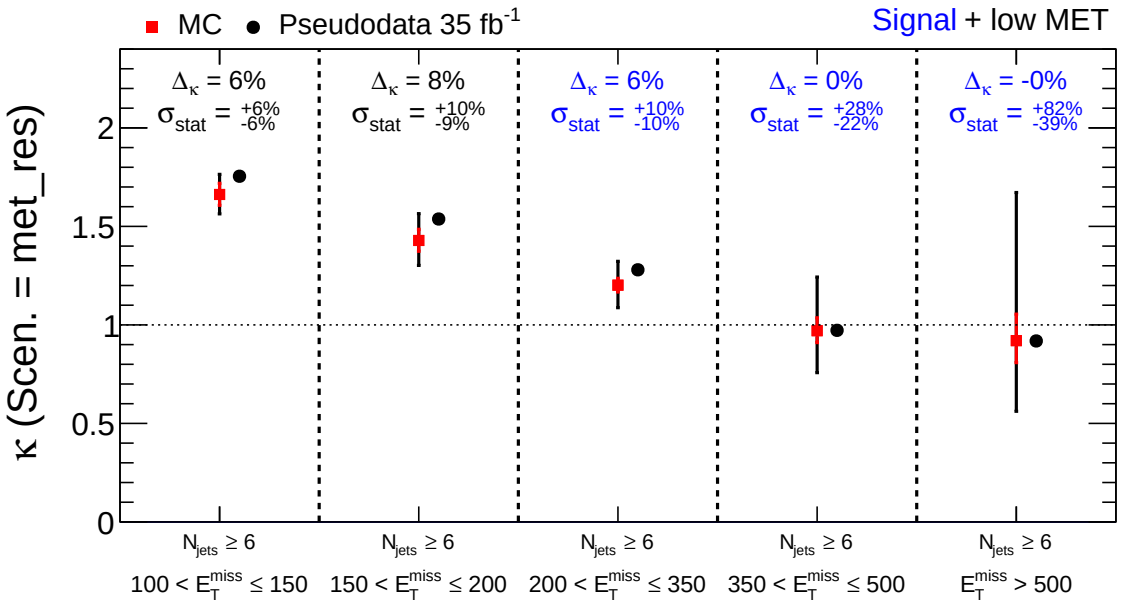

Figure 7.2: Changes in κ caused by doubling the weight of events satisfying $[E_{\mathrm{T}}^{\mathrm{miss}}(\mathrm{reco}) - E_{\mathrm{T}}^{\mathrm{miss}}(\mathrm{true})]/E_{\mathrm{T}}^{\mathrm{miss}}(\mathrm{true}) > 0.5$. The effect is largest in low $E_{\mathrm{T}}^{\mathrm{miss}}$ bins where events with fake $E_{\mathrm{T}}^{\mathrm{miss}}$ are relatively more common. Figure from Reference [13].

also increase m_{T} and cause events to land in the high-m_{T} regions. The frequency with which this occurs depends strongly on the resolution with which $E_{\mathrm{T}}^{\mathrm{miss}}$ is measured. If the simulation has incorrect $E_{\mathrm{T}}^{\mathrm{miss}}$ resolution, it is also likely to have an incorrect composition of the background events at high m_{T}, potentially affecting the distribution of background events across the $E_{\mathrm{T}}^{\mathrm{miss}}$ bins.

To study the effects of mismodeling of the $E_{\mathrm{T}}^{\mathrm{miss}}$ resolution, we double the weights of events satisfying $\frac{E_{\mathrm{T}}^{\mathrm{miss}}(\mathrm{reco}) - E_{\mathrm{T}}^{\mathrm{miss}}(\mathrm{true})}{E_{\mathrm{T}}^{\mathrm{miss}}(\mathrm{true})} > \frac{1}{2}$. For most bins in this scenario, $\Delta_\kappa \leq 6\%$. The largest changes occur in the low $E_{\mathrm{T}}^{\mathrm{miss}}$ bins where events with fake $E_{\mathrm{T}}^{\mathrm{miss}}$ make up a larger fraction of the background yield. Figure 7.2 demonstrates this trend.

In this figure, there are five columns corresponding to different $E_{\mathrm{T}}^{\mathrm{miss}}$ ranges (integrating over N_{jets} and N_{b} bins). Within each column are two markers. The black circle on the right shows the value of κ obtained from the modified simulation treated as pseudodata. The red square on the left shows the value of κ in the unmodified simulation. The red

square has a two part error bar. The inner red portion of the error bar indicates the uncertainty in κ due to the finite size of the simulated data sample. The outer black portion of the error bar show the typical size of variations in the observed $\hat{\kappa}$ for a data sample with an integrated luminosity of $\sim 35\,\mathrm{fb}^{-1}$. Note that the outer black error bars are stacked on top of the inner red error bar, such that the full size of the error bar represents the combined uncertainty in the true value of κ and the fluctuations about that value.

At the top of each column, two numbers are provided. Δ_κ is the fractional difference in the values of κ obtained from the unmodified simulation (red square) and the pseudodata (black circle). σ_{stat} is the statistical uncertainty in Δ_κ. Since the mismeasured and pseudodata values of κ are obtained using the same event sample, they are highly correlated, but there is some statistically uncertainty in the difference due to potential fluctuations in the number of events with modified and unmodified weights.

7.1.4 Incorrect QCD, $\mathrm{W}^{\pm}$+jets, $\mathrm{t\bar{t}}\,V$ Cross Sections

Since the various background processes have different distributions across the four analysis regions, changing the relative amounts of the various processes could affect κ. We study this effect with three scenarios: one each modifying the QCD, $\mathrm{W}^{\pm}$+jets, and $\mathrm{t\bar{t}}\,V$ cross sections.

For QCD, we opt to multiply the cross section by a factor of four. For events passing the baseline selection, $\Delta_\kappa \leq 7\%$, though this scenario can have a larger effect in lower $E_{\mathrm{T}}^{\mathrm{miss}}$ ranges excluded by the baseline requirement of $E_{\mathrm{T}}^{\mathrm{miss}} > 200\,\mathrm{GeV}$.

For $\mathrm{W}^{\pm}$+jets and $\mathrm{t\bar{t}}\,V$, we multiply the cross sections by a factor of three. The finite size and statistical precision of the simulation limits our ability to study the Δ_κ caused by these two mismodeling scenarios. We observe changes as large as $\Delta_\kappa = 11\%$, but with

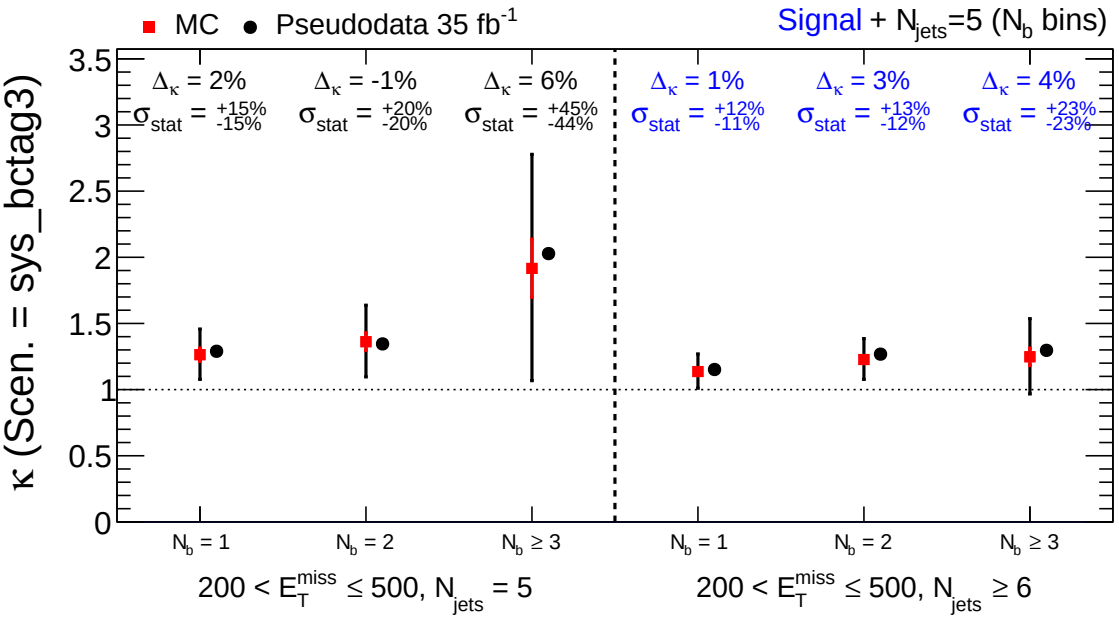

Figure 7.3: Shift in κ caused by modifying the b-tagging scale factors by three times their measured uncertainties. Figure from Reference [13].

large uncertainties that make the shift consistent with $\Delta_\kappa = 0$.

In all three of these scenarios, Δ_κ has negligible dependence on N_{jets} and a small dependence on $E_{\text{T}}^{\text{miss}}$ that is reproducible in the $N_{\text{jets}} = 5$ control sample discussed later in Section 7.3.

7.1.5 Three S.D. Variation of b-Tag Scale Factors

The above scenarios probe effects that have minimal effect on the N_{b} distribution. As a final scenario, we modify the b-tagging scale factors by three times their measured uncertainty. This scenario causes Δ_κ to have an N_{b} dependence visible in Figure 7.3. The largest shifts occur in the $N_{\text{b}} \geq 3$ bins, reaching a maximum of $\Delta_\kappa = 6\%$.

7.2 Categorizing High-m_{T} Events

Section 7.1 showed that most mismodeling scenarios have a relatively small effect on κ. On the other hand, changes in κ are possible, and Figure 7.1 showed that κ can change significantly at low $E_{\mathrm{T}}^{\mathrm{miss}}$. Understanding what causes these changes in κ is important to establishing a procedure for evaluating systematic uncertainties.

Figure 7.4 shows the composition of the simulated high-m_{T} background in various $E_{\mathrm{T}}^{\mathrm{miss}}$ bins, with events categorized by the physics process which produced the event. In the high $E_{\mathrm{T}}^{\mathrm{miss}}$ bins, most events come from $\mathrm{t\bar{t}}+\mathrm{jets}$ process and have either two prompt light leptons (electrons or muons, possible from decay of τ leptons) or one prompt light lepton and one hadronically decaying τ lepton. Both types of events contain multiple neutrinos from the decay of the $\mathrm{W}^{\pm}$ that produces that produced the charged leptons. The additional neutrinos contribute to the $E_{\mathrm{T}}^{\mathrm{miss}}$ of the event and allow such events to reach values of m_{T} above $m_{\mathrm{W}^{\pm}}$. Such background contributions are well-predicted by the ABCD background estimation method.

At lower values of $E_{\mathrm{T}}^{\mathrm{miss}}$, $\mathrm{t\bar{t}}+\mathrm{jets}$ processes producing events with a single light lepton become increasingly important, comprising approximately half the background of the $100\,\mathrm{GeV} < E_{\mathrm{T}}^{\mathrm{miss}} \leq 150\,\mathrm{GeV}$ bin despite making up 16% or less of the higher $E_{\mathrm{T}}^{\mathrm{miss}}$ analysis regions. These events have a single prompt neutrino and would typically be expected satisfy $m_{\mathrm{T}} \leq m_{\mathrm{W}^{\pm}}$.

The means by which events reach high values of m_{T} provides anther possible option for categorizing events. This categorization scheme offers two advantages over that used in Figure 7.4. First, the number of categories can be reduced, greatly simplifying the analysis. Second, and more importantly, the categorization can provide insight into how correlations between M_J and m_{T} arise.

Figure 7.5 shows the M_J distribution for several categories of events passing the

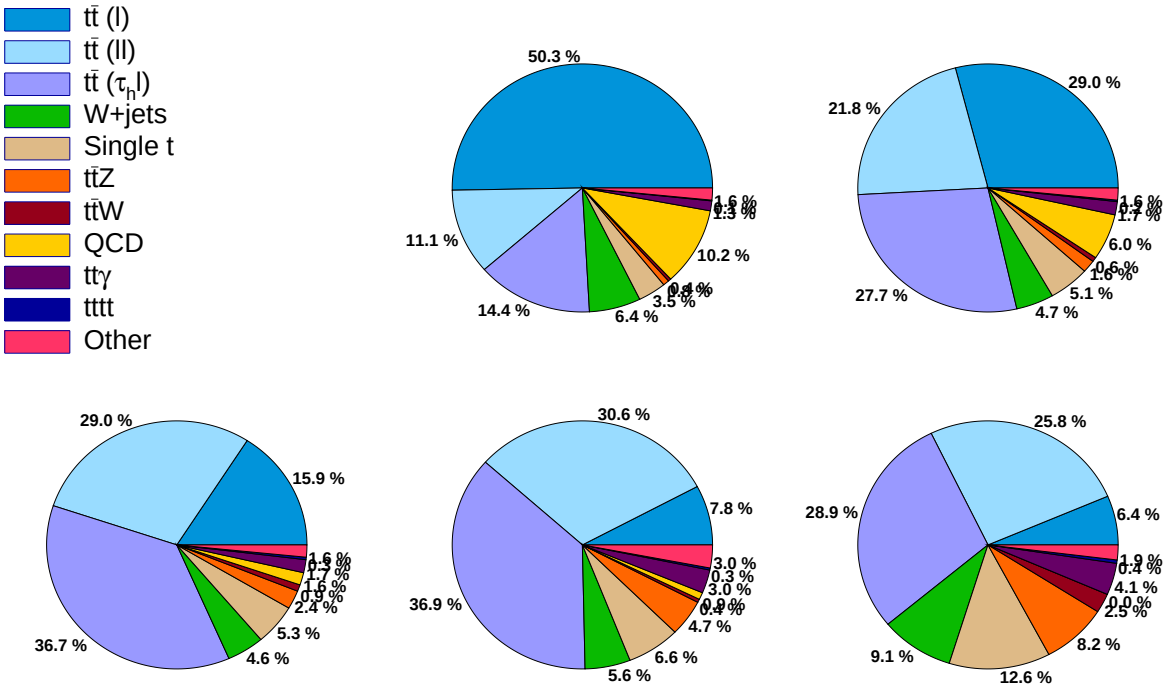

Figure 7.4: Physics processes contributing to the high-m_{T} background in five $E_{\mathrm{T}}^{\mathrm{miss}}$ bins. From left to right, the top row shows the composition of the $100\,\mathrm{GeV} < E_{\mathrm{T}}^{\mathrm{miss}} \leq 150\,\mathrm{GeV}$ and $150\,\mathrm{GeV} < E_{\mathrm{T}}^{\mathrm{miss}} \leq 200\,\mathrm{GeV}$ bins, while the bottom row shows the composition of the $200\,\mathrm{GeV} < E_{\mathrm{T}}^{\mathrm{miss}} \leq 350\,\mathrm{GeV}$, $350\,\mathrm{GeV} < E_{\mathrm{T}}^{\mathrm{miss}} \leq 500\,\mathrm{GeV}$, and $E_{\mathrm{T}}^{\mathrm{miss}} > 500\,\mathrm{GeV}$ bins. Figure from Reference [13].

baseline selection with a relaxed $E_{\mathrm{T}}^{\mathrm{miss}} > 100\,\mathrm{GeV}$ requirement, including only $\mathrm{t\bar{t}}$ + jets processes. The black line shows the distribution for events with $m_{\mathrm{T}} \leq 140\,\mathrm{GeV}$, while the four colored lines show distributions for events with $m_{\mathrm{T}} > 140\,\mathrm{GeV}$. The light blue line corresponds to events with two prompt light leptons and the purple line to events with one prompt light lepton and one hadronically decaying τ lepton. For $M_J > 250\,\mathrm{GeV}$, the M_J distributions for these two categories are similar to that of the low m_{T} background, as seen in the ratios in the lower panel. The green and red lines show the M_J distributions for the remaining events with a single prompt light lepton. The green distribution contains events for which the true transverse mass $m_{\mathrm{T}}^{\mathrm{tru}}$ is above 140 GeV, while the red distribution contains events with $m_{\mathrm{T}}^{\mathrm{tru}} \leq 140\,\mathrm{GeV}$. We compute the true value of m_{T} using the true momentum of the highest p_{T} lepton and the generated $E_{\mathrm{T}}^{\mathrm{miss}}$. Put another way, the red distribution contains events in which mismeasurement is responsible for the large measured m_{T}. Both of the single lepton components at high m_{T} have significantly higher average M_J than the low-m_{T} events.

The two plots in Figure 7.6 provide some insight into why these single lepton components have a different M_J distribution than the low-m_{T} background. The left-hand plot shows that events with mismeasured m_{T} (red distribution in Figure 7.5) have, on average, a larger difference between the true and measured values of $E_{\mathrm{T}}^{\mathrm{miss}}$. Since $E_{\mathrm{T}}^{\mathrm{miss}}$ mismeasurement is correlated with large jet multiplicity and momentum, these mismeasured events also tend to have larger M_J.

Unsurprisingly, the left-hand plot shows that events with large but well-measured m_{T} (green distribution in Figure 7.5) also tend to have well-measured $E_{\mathrm{T}}^{\mathrm{miss}}$. The larger average M_J of such events seen in Figure 7.5 must be explained in another way. The right-hand plot of Figure 7.6 shows that the events with large and well-measured m_{T} tend to have a b-quark with large transverse momentum. The b-jets are more likely to contain non-prompt neutrinos than other flavors of jets. The non-prompt neutrinos with

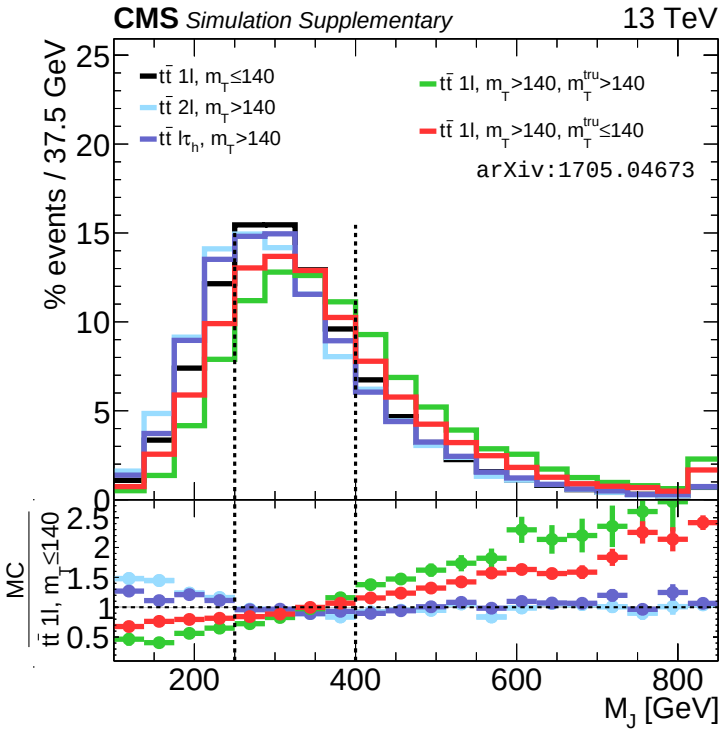

Figure 7.5: M_J distributions for several categories of events passing the baseline selection with relaxed $E_{\mathrm{T}}^{\mathrm{miss}} > 100\,\mathrm{GeV}$ requirement. Only events from $\mathrm{t\bar{t}}$ + jets processes are included. High-m_{T} events with either two prompt light leptons (light blue) or a single prompt light lepton and a hadronically decaying τ lepton (purple) are able to reproduce the M_J distribution of the low-m_{T} background in the $M_J > 250\,\mathrm{GeV}$ region. The single lepton backgrounds with well-measured (green) or mismeasured (red) m_{T} have a different M_J distribution, potentially causing κ to deviate from unity. Figure from supplementary technical material for Reference [11].

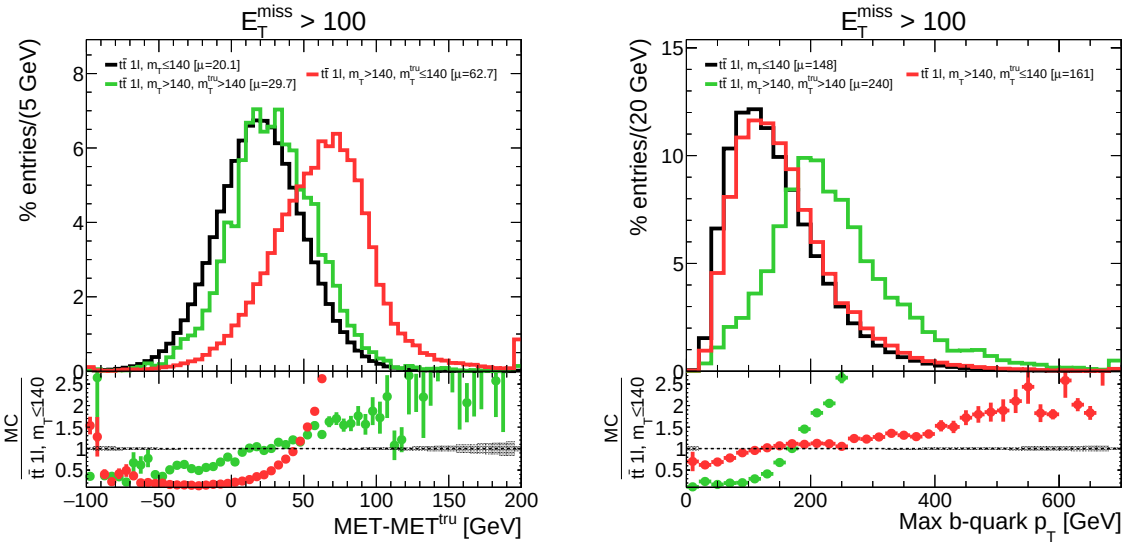

Figure 7.6: $E_{\mathrm{T}}^{\mathrm{miss}}$ mismeasurement and maximum b-quark p_{T} distributions for $\mathrm{t\bar{t}}$+jets events at low and high m_{T}. The baseline selection is applied with a relaxed $E_{\mathrm{T}}^{\mathrm{miss}} > 100\,\mathrm{GeV}$ requirement. Figure from Reference [13].

sufficient momentum to produce $m_{\mathrm{T}} > 140\,\mathrm{GeV}$ are more likely to come from highly boosted b-jets, which in turn contribute to larger M_J.

These patterns motivate the use of several categories:

Multi-neutrino: Contains all events with at least two prompt neutrinos. This category combines the events with multiple prompt electrons or muons, and those with a single prompt light lepton and a hadronically decaying τ lepton, the two types of events with minimal M_J-m_{T} correlation. It is the largest contribution to the background for the high $E_{\mathrm{T}}^{\mathrm{miss}}$ bins.

Mismeasured $\boldsymbol{E_{\mathrm{T}}^{\mathrm{miss}}}$: Contains events with no more than one prompt neutrino and $m_{\mathrm{T}}^{\mathrm{tru}} \leq 140\,\mathrm{GeV}$. This category contains events with mismeasured m_{T}, which is usually due to mismeasurement in $E_{\mathrm{T}}^{\mathrm{miss}}$. This category comprises a larger fraction of the background at low $E_{\mathrm{T}}^{\mathrm{miss}}$.

Non-prompt neutrino: Contains events with no more than one prompt neutrino, $m_{\mathrm{T}}^{\mathrm{tru}} >$

140 GeV, and no off-shell $W^{\pm}$. This category contains most of the remaining well-measured single lepton events.

Off-shell $W^{\pm}$: Contains events with no more than one prompt neutrino, $m_T^{tru} > 140\,GeV$, and an off-shell $W^{\pm}$. Events not belonging to the above categories end up here and generally reach high m_T by virtue of an off-shell $W^{\pm}$-boson. Events in this category are the least common in most bins.

Figure 7.7 show the values of κ for each of these categories in events from $t\bar{t}$ + jets processes. As expected, the κ values for the multi-neutrino background are approximately independent of E_T^{miss} and typically have $\kappa \approx 1$. This is not true for the other categories. For the mismeasured E_T^{miss} category, $\kappa > 1$ across the E_T^{miss} bins, reaching a maximum value near $E_T^{miss} \approx 300\,GeV$. For the non-prompt neutrino category, κ is even greater and increases with E_T^{miss}. Note that all $W^{\pm}$ are produced on mass shell in the simulation of $t\bar{t}$ + jets processes, so the off-shell $W^{\pm}$ category is omitted.

Better still, the behavior of these categories generalizes beyond $t\bar{t}$+jets processes. For example, Figure 7.8 shows κ for three of the four categories in $W^{\pm}$ + jets processes. The multi-neutrino category is omitted since $W^{\pm}$ + jets processes produce only one prompt neutrino. For the mismeasured E_T^{miss} and non-prompt neutrino categories, the behavior of κ is similar to that observed for the $t\bar{t}$ + jets processes in Figure 7.7. The off-shell $W^{\pm}$ category shows only small deviations from $\kappa = 1$, with κ decreasing slightly with increased E_T^{miss}.

Of course, the more interesting test is whether these categories can be extended to the background as a whole. Figure 7.9 shows κ in various bins for the full background with all simulated processes included. As in the separate $t\bar{t}$ + jets and $W^{\pm}$ + jets processes, $\kappa \approx 1$ and is nearly constant across the bins for the multi-neutrino component of the background. This holds true whether binned in E_T^{miss} or in N_{jets}, and in a sample with

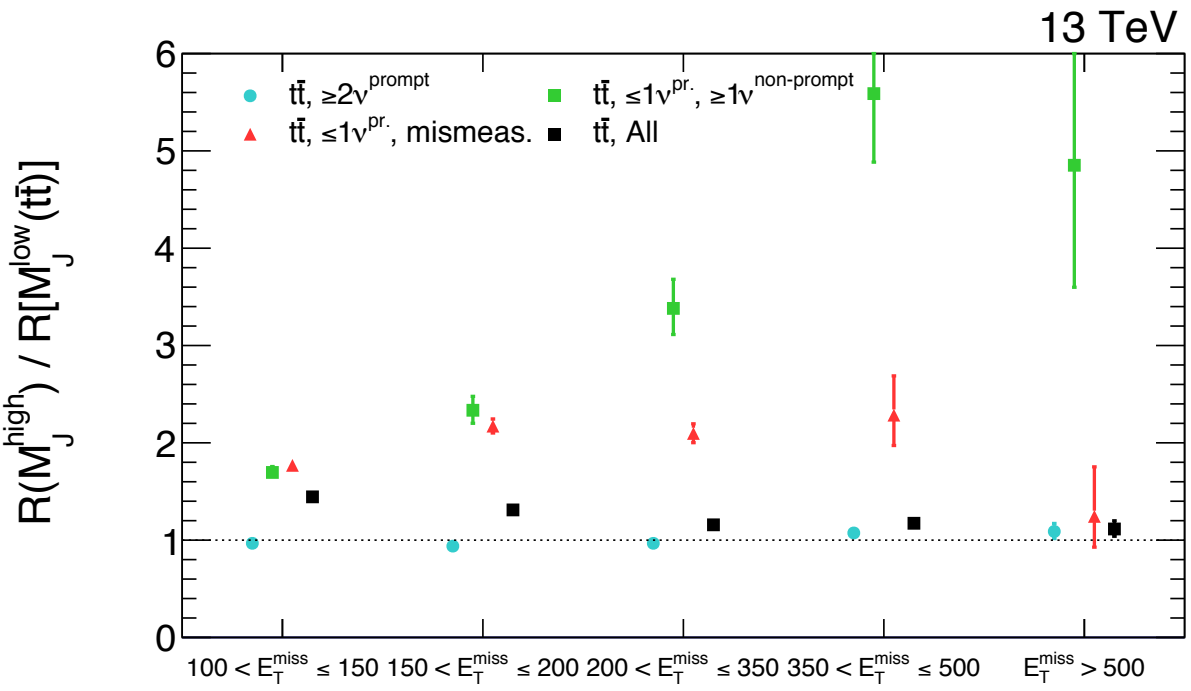

Figure 7.7: κ values as measured in simulated events from $t\bar{t}$ + jets processes. For the multi-neutrino component (cyan circles), $\kappa \approx 1$ independent of E_T^{miss}. For the mis-measured E_T^{miss} (red triangle) and non-prompt neutrino (green squares) components, κ has a strong E_T^{miss} dependence and can be far from unity. The presence of these components is responsible for causing κ to deviate from unity. Fortunately, events in the latter two categories are less common than the multi-neutrino events, so the overall κ in simulated $t\bar{t}$ + jets events (black square) remains near unity. The simulated $t\bar{t}$ + jets events never contain an off-shell $W^{\pm}$. Figure from Reference [13].

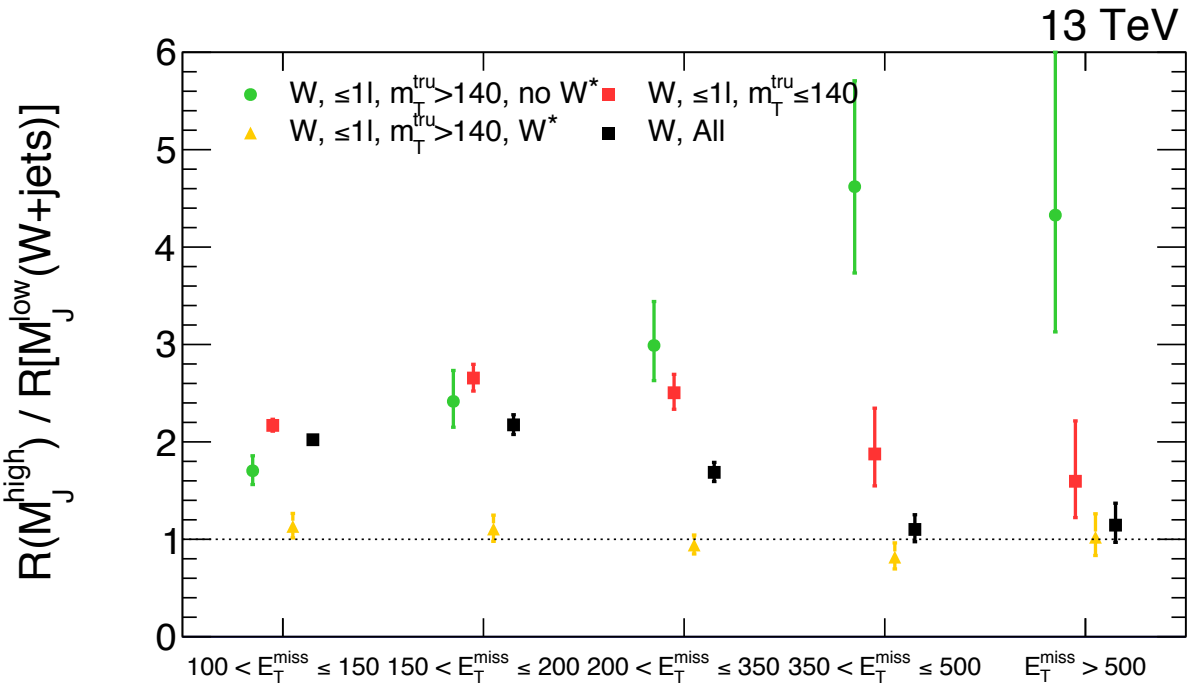

Figure 7.8: κ values as measured in simulated events from $W^{\pm}$+jets processes. For the mismeasured E_T^{miss} (red square) and non-prompt neutrino (green circle) components, κ has a strong E_T^{miss} dependence and can be far from unity, but shows similar E_T^{miss} dependency as the κ values for the simulated $t\bar{t}$ + jets events shown in Figure 7.7. The events containing an off-shell $W^{\pm}$ (yellow triangle) typically have κ closer to unity and have a milder E_T^{miss} dependence. No multi-neutrino events are include in the simulation of $W^{\pm}$+jets events, and so the overall κ (black square) is not necessarily close to unity. Figure from Reference [13].

the jet multiplicity requirement changed to $N_{\text{jets}} = 5$. The other categories have more complex behavior.

Figure 7.10 shows the composition of the high-m_{T} background in terms of these categories. In the high-$E_{\text{T}}^{\text{miss}}$ analysis region, the multi-neutrino background is dominant. At low-$E_{\text{T}}^{\text{miss}}$, the contribution from events with mismeasured $E_{\text{T}}^{\text{miss}}$ becomes more important. Intriguingly, the composition is approximately constant with respect to N_{jets}.

7.3 Dilepton and $N_{\text{jets}} = 5$ Control Samples

The previous section showed that the high-m_{T} background events can be separated into four categories. The behavior of κ across kinematic bins was different for each of these categories, with $\kappa \approx 1$ in all bins for the multi-neutrino background. In this section, we will use control sample to study how well this behavior is modeled in simulation. There are two main effects to study: whether the simulation correctly models any M_J-m_{T} correlation within each category and whether the simulation produces the categories in the correct relative amounts.

First, we establish a control sample which explicitly selects dilepton events to test the independence of M_J and m_{T} in the multi-neutrino background dominant at high $E_{\text{T}}^{\text{miss}}$. The second control sample is motivated by Figure 7.10. Since the relative amounts of each of the four background categories is nearly independent of N_{jets}, we use a control sample with a relaxed $N_{\text{jets}} = 5$ requirement to study modeling of the background composition as a function of $E_{\text{T}}^{\text{miss}}$.

For each control sample, we perform a modified ABCD background estimation. The precision of the modified ABCD test represents the precision with which the ABCD method is known to work in the control sample. Therefore, we use the uncertainty in the predicted mean background yield and the expected size of Poisson fluctuations about

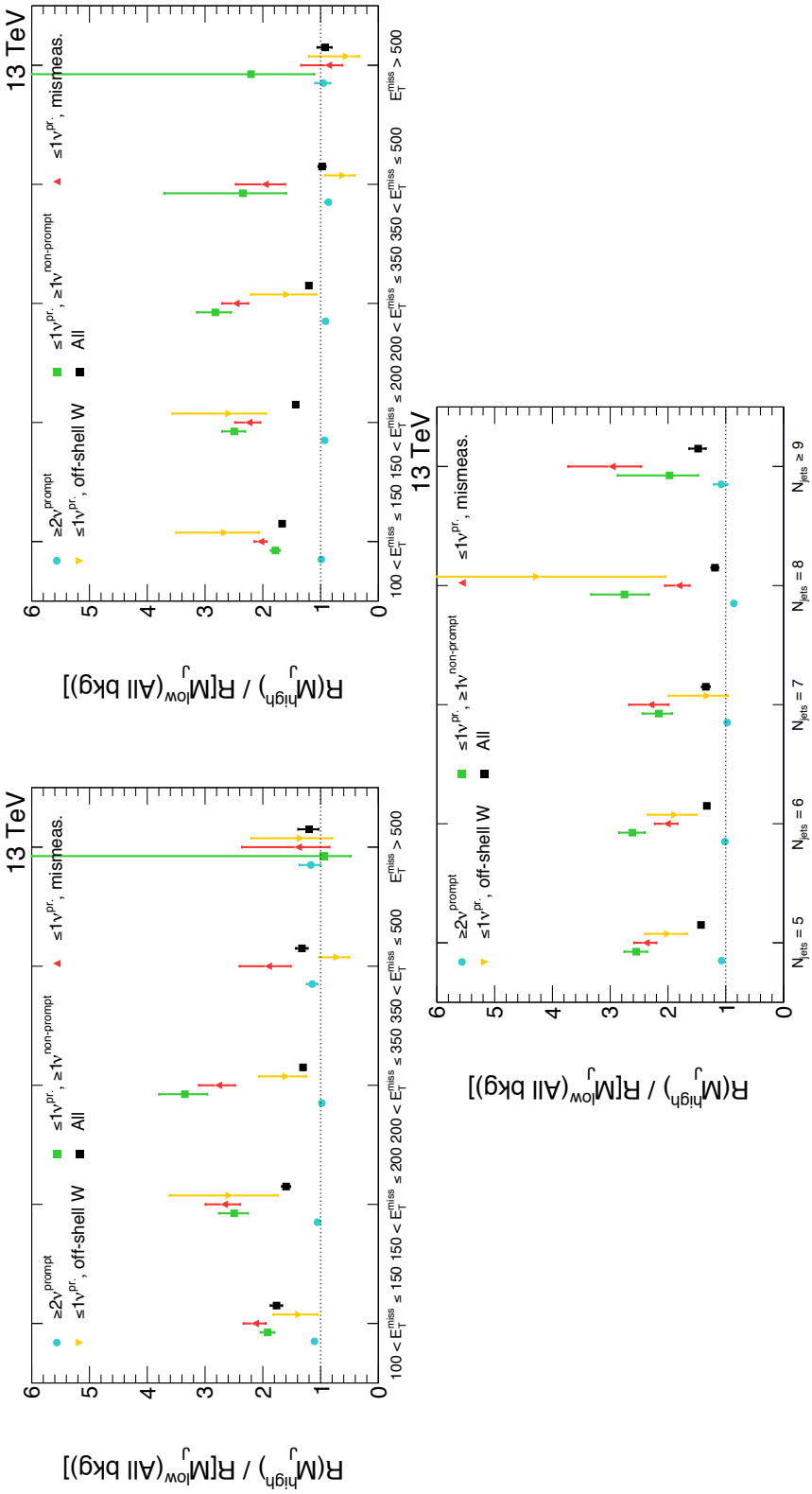

Figure 7.9: κ values measured in simulation (all processes) for the $N_{\text{jets}} = 5$ control sample (top left), analysis region (top right), and $150\,\text{GeV} \leq E_{\text{T}}^{\text{miss}} < 200\,\text{GeV}$ validation sample (bottom). $\kappa \approx 1$ in all bins for the multi-neutrino component (blue circles). At high-$E_{\text{T}}^{\text{miss}}$, these events make up a higher fraction of the background, making the overall $\kappa \approx 1$ (black squares). The values for the non-prompt neutrino (green square), mismeasured $E_{\text{T}}^{\text{miss}}$ (red upward-pointing triangle), and off-shell $\text{W}^{\pm}$ (yellow downward-pointing triangle) components have more complicated $E_{\text{T}}^{\text{miss}}$-dependencies. Within each category, κ does not have clear N_{jets} dependence. Figure from Reference [13].

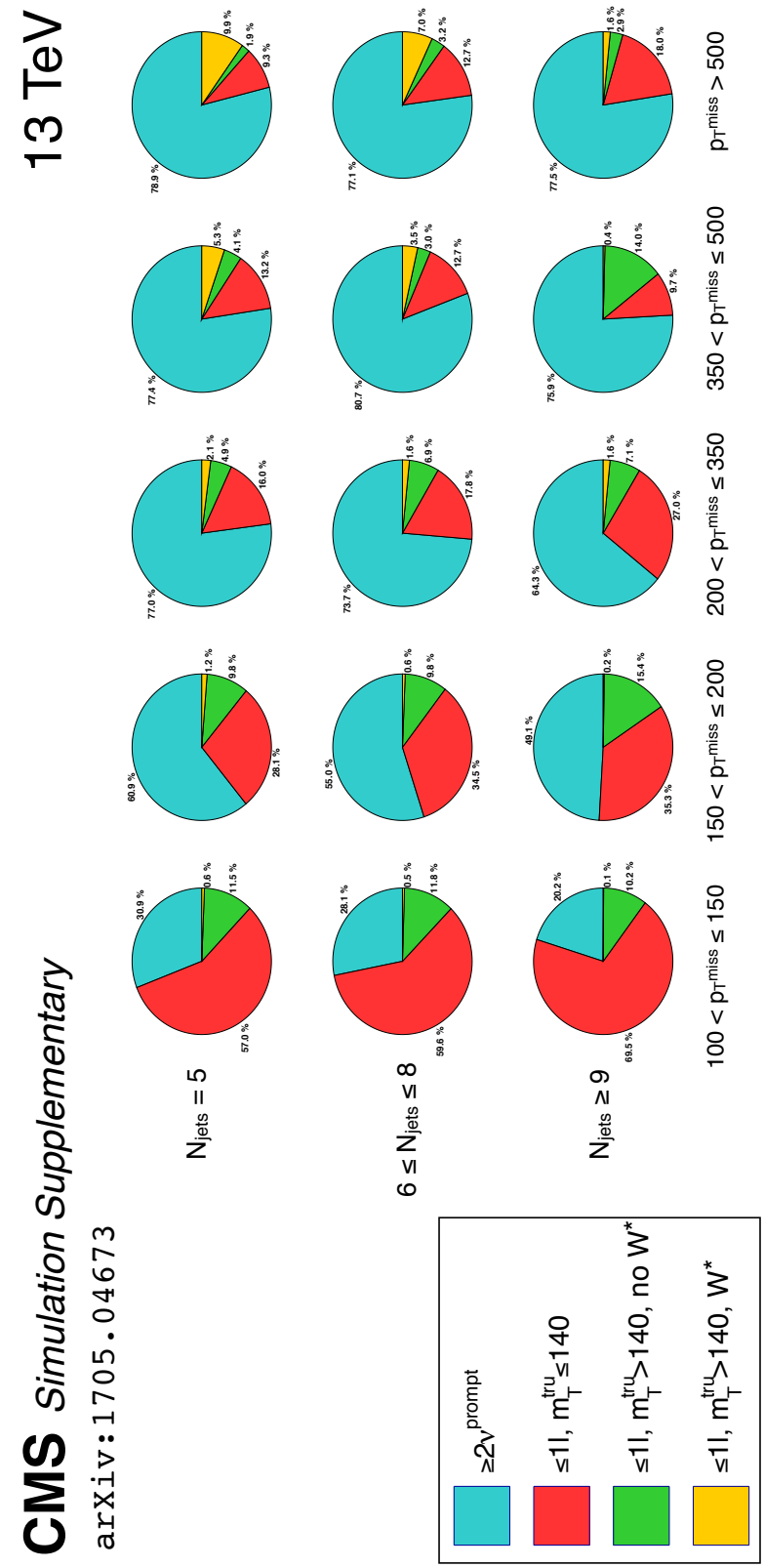

Figure 7.10: Composition of high-m_{T} background in bins of $E_{\mathrm{T}}^{\mathrm{miss}}$ (left to right: $100\,\mathrm{GeV} < E_{\mathrm{T}}^{\mathrm{miss}} \leq 150\,\mathrm{GeV}$, $150\,\mathrm{GeV} < E_{\mathrm{T}}^{\mathrm{miss}} \leq 200\,\mathrm{GeV}$, $200\,\mathrm{GeV} < E_{\mathrm{T}}^{\mathrm{miss}} \leq 350\,\mathrm{GeV}$, and $E_{\mathrm{T}}^{\mathrm{miss}} > 500\,\mathrm{GeV}$) and N_{jets} (top to bottom: $N_{\mathrm{jets}} = 5$, $6 \leq N_{\mathrm{jets}} \leq 8$, and $N_{\mathrm{jets}} \geq 9$). Multi-neutrino events dominate at high $E_{\mathrm{T}}^{\mathrm{miss}}$, but events with mismeasured $E_{\mathrm{T}}^{\mathrm{miss}}$ are more common at low $E_{\mathrm{T}}^{\mathrm{miss}}$. The composition is nearly constant with respect to N_{jets}. Figure from supplementary technical material for Reference [11].

that mean yield as a systematic uncertainty, assuming that the cross-checks described in Section 7.5 do not show any significant problems.

7.3.1 Dilepton Control Sample

As discussed in Chapter 6, the ABCD background estimation relies on the ability to extrapolate the M_J distribution from the low-m_{T} regions to the high-m_{T} regions. Most events in the low-m_{T} sample had a single lepton, while the high-m_{T} events usually had two leptons. In the presence of ISR, however, the two M_J distributions at became similar. The lack of correlation between M_J and m_{T} meant that only small κ corrections were needed from the simulation, making the background prediction more trustworthy. Section 7.2 refined this explanation and showed that, in simulation, $\kappa \approx 1$ for the multi-neutrino component of the background.

In this section, we will use a dilepton control sample to check that the multi-neutrino background behaves similarly in the real and simulated data. To construct this control sample, we modify the selection requirements for the high-m_{T} regions R3 and R4 by removing the $m_{\mathrm{T}} > 140\,\mathrm{GeV}$ requirements and instead requiring either $N_{\mathrm{leps}} = 2$ or $N_{\mathrm{leps}} = N_{\mathrm{veto}} = 1$.

Additionally, the N_{jets} requirements must by modified so that the number of objects clustered into the large-radius jets is unchanged. Specifically, we replace the bin requirements $6 \leq N_{\mathrm{jets}} \leq 8$ and $N_{\mathrm{jets}} \geq 9$ with $5 \leq N_{\mathrm{obj}} \leq 7$ and $N_{\mathrm{obj}} \geq 8$, respectively, where $N_{\mathrm{obj}} = N_{\mathrm{jets}} + N_{\mathrm{leps}}$.

In order to prevent signal contamination, we exclude events in the highest $E_{\mathrm{T}}^{\mathrm{miss}}$ or N_{b} bins ($E_{\mathrm{T}}^{\mathrm{miss}} > 500\,\mathrm{GeV}$ or $N_{\mathrm{b}} \geq 3$). We include events with $N_{\mathrm{b}} = 0$ and merge all N_{b} bins in order to increase the size of the sample. Finally, we merge the $E_{\mathrm{T}}^{\mathrm{miss}}$ bins into the ranges $100\,\mathrm{GeV} < E_{\mathrm{T}}^{\mathrm{miss}} \leq 200\,\mathrm{GeV}$ and $200\,\mathrm{GeV} < E_{\mathrm{T}}^{\mathrm{miss}} \leq 500\,\mathrm{GeV}$. The lower of these

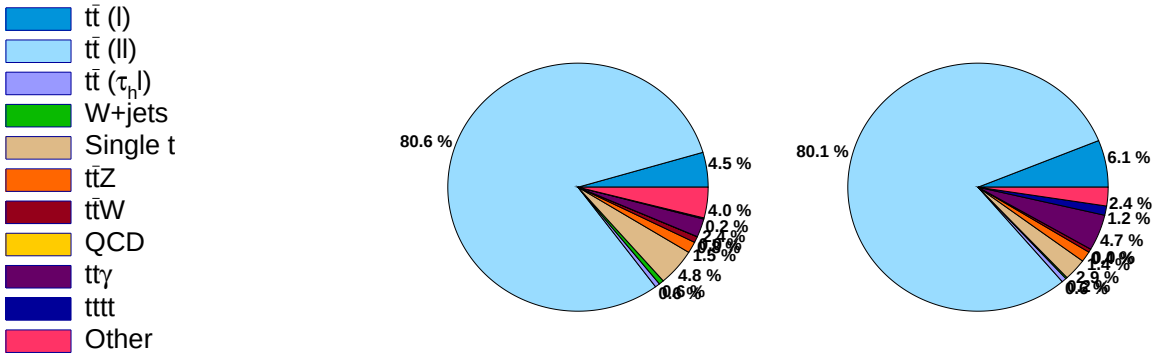

Figure 7.11: Composition of the events satisfying $N_{\text{leps}} = 2$ in the dilepton control sample, split into $M_J \leq 400\,\text{GeV}$ (left) and $M_J > 400\,\text{GeV}$ (right) events. The compositions of the two M_J ranges are similar, with most events containing two prompt light leptons and originating from $\text{t}\bar{\text{t}} + \text{jets}$ processes. Events with $N_{\text{leps}} = 2$ are roughly six times as common as events with $N_{\text{leps}} = N_{\text{veto}} = 1$, so these pie charts approximate the overall composition of the dilepton control sample well. Figure from Reference [13].

two ranges will not be used in assigning a systematic uncertainty directly, but provides additional confidence in the use of the dilepton control sample.

We refer to the modified dilepton versions of R3 and R4 as D3 and D4, respectively. Figure 7.11 shows the composition of the events with $N_{\text{leps}} = 2$ events, while Figure 7.12 shows the composition for events with $N_{\text{leps}} = N_{\text{veto}} = 1$. Note that there are approximately six times as many $N_{\text{leps}} = 2$ events as $N_{\text{leps}} = N_{\text{veto}} = 1$ events, so the overall composition is similar to that of Figure 7.11.

We use the dilepton regions D3 and D4 along with the single lepton regions R1 and R2 to perform an ABCD background estimation, the results of which are shown in Table 7.2. Since the dilepton regions have minimal signal contamination, a difference between the predicted and observed D4 yields would indicate that the ABCD method is not able to predict the dilepton background accurately. Since we do not observe any such deviation, we may take the statistical uncertainty in the predicted background for D4, convolved with the expected size of Poisson fluctuations about that yield, as a systematic uncertainty in κ. The uncertainties are 6% for the low-N_{jets} bins and 16% for

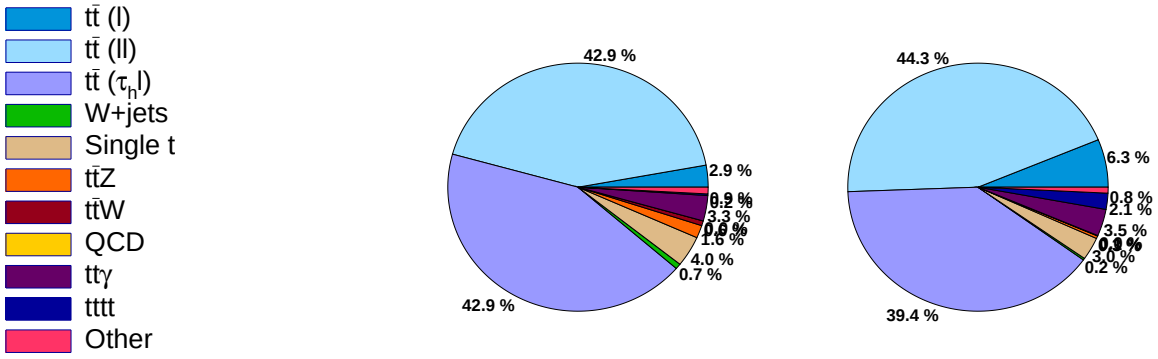

Figure 7.12: Composition of the events satisfying $N_{\text{leps}} = N_{\text{veto}} = 1$ in the dilepton control sample, split into $M_J \leq 400\,\text{GeV}$ (left) and $M_J > 400\,\text{GeV}$ (right) events. The compositions of the two M_J ranges are similar. In both cases, events from $\text{t}\bar{\text{t}} + \text{jets}$ process and containing either two prompt light leptons, or one prompt light lepton and a hadronically decaying τlepton are the most common. Figure from Reference [13].

the high-N_{jets} bins.

In the notation of Section 6.5, this introduces two new Z_i nuisance parameters, one each for the low- and high-N_{jets} bins. Recall that the $\varsigma_{i,j,k}$ uncertainties carry three indices, with the first index i specifying a $E_{\text{T}}^{\text{miss}}$ bin, the second index j specifying an N_{jets}-N_{b} bin, and the third index k referring to a specific source of systematic uncertainty. The 6% and 16% uncertainties for the low- and high-N_{jets} bins are encoded as $\varsigma = \ln(1+\sigma)$ so that, to two significant figures,

$$\varsigma_{i,j,k} = \begin{cases} 0.058, & j \in \{\text{low-}N_{\text{jets}}\text{ bins}\},\ k = \text{low-}N_{\text{jets}}\text{ nuisance}, \\ 0.15, & j \in \{\text{high-}N_{\text{jets}}\text{ bins}\},\ k = \text{high-}N_{\text{jets}}\text{ nuisance}, \\ 0, & j \in \{\text{low-}N_{\text{jets}}\text{ bins}\},\ k = \text{high-}N_{\text{jets}}\text{ nuisance}, \\ 0, & j \in \{\text{high-}N_{\text{jets}}\text{ bins}\},\ k = \text{low-}N_{\text{jets}}\text{ nuisance}. \end{cases} \tag{7.1}$$

For example, the 16% high-N_{jets} systematic uncertainty translates to $\ln(1+0.16) \approx 0.15$.

Table 7.2: Yields and maximum likelihood ABCD predictions for the dilepton control region, including a $100\,\text{GeV} < E_\text{T}^\text{miss} \leq 200\,\text{GeV}$ validation sample. The observed yields are consistent with the predictions for both E_T^miss ranges and for both the low- and high-N_jets bins. Were the simulation to have significant inaccuracies in its modeling of κ for this sample, it would bias the predictions, causing an inconsistency that would appear in this table. The T1tttt yields shown are not used in the background-only fit, but are provided to show that the dilepton control sample does not suffer from significant signal contamination. The significances reported in the rightmost column are Z-scores, sometimes quoted in "σ" or standard deviations. Note that the "Pred." column contains true predictions. The R4 bins are excluded from the likelihood to create a "predictive fit." The procedure for doing this is described in Section 9.1. While the systematic uncertainties derived from the dilepton control sample are typically obtained from Figure 7.19, they can in principle be computed from the predictions in the bottom two rows. Table from Reference [13].

$L = 36\,\text{fb}^{-1}$	T1tttt(NC)	T1tttt(C)	κ	Sim. Bkg.	Pred.	Obs.	Obs./Sim.	Signif.
$100\,\text{GeV} < E_\text{T}^\text{miss} \leq 200\,\text{GeV}$ (Obs./Sim. $= 0.87 \pm 0.01$)								
R1: All N_jets	0.03	21.02		22 449.55		22 506	1.00 ± 0.01	
R2: $6 \leq N_\text{jets} \leq 8$	0.38	6.91		7744.93		7684	0.99 ± 0.01	
R2: $N_\text{jets} \geq 9$	0.35	5.41		1099.01		1060	0.96 ± 0.03	
D3: All N_jets	0.04	8.36		3013.45		3064	1.02 ± 0.02	
D4: Low N_jets	0.33	2.52	$1.09^{+0.01}_{-0.01}$	1132.93	$1140.00^{+28.79}_{-28.48}$	1142	1.01 ± 0.03	0.1 s.d.
D4: High N_jets	0.11	1.62	$1.00^{+0.11}_{-0.11}$	147.14	$143.94^{+16.64}_{-16.41}$	131	0.89 ± 0.12	-0.6 s.d.
$200\,\text{GeV} < E_\text{T}^\text{miss} \leq 500\,\text{GeV}$ (Obs./Sim. $= 0.81 \pm 0.01$)								
R1: All N_jets	0.07	10.37		5054.89		5173	1.02 ± 0.01	
R2: $6 \leq N_\text{jets} \leq 8$	1.23	6.80		3086.58		2895	0.94 ± 0.02	
R2: $N_\text{jets} \geq 9$	0.81	9.02		372.39		325	0.87 ± 0.05	
D3: All N_jets	0.15	7.83		809.67		911	1.13 ± 0.04	
D4: Low N_jets	2.04	3.69	$1.09^{+0.01}_{-0.01}$	537.31	$554.08^{+23.03}_{-22.91}$	564	1.05 ± 0.04	0.3 s.d.
D4: High N_jets	0.79	3.92	$0.99^{+0.02}_{-0.02}$	59.16	$56.77^{+3.97}_{-3.94}$	52	0.88 ± 0.12	-0.5 s.d.

7.3.2 $N_{\text{jets}} = 5$ Control Sample

While the dilepton region probes the ability of the simulation to model the multi-neutrino background accurately, it is equally important to check that it is able to model the relative amounts of the other background components in each of the bins, particularly as a function of $E_{\text{T}}^{\text{miss}}$. Figure 7.10 showed that the composition in terms of the four categories identified in Section 7.2 is approximately constant with respect to N_{jets}, and Figure 7.9 showed that the κ values for each category are not strongly dependent on N_{jets}. This motivates the use of an $N_{\text{jets}} = 5$ control sample to study the modeling of the background composition.

To study any $E_{\text{T}}^{\text{miss}}$ dependence, we use the same $E_{\text{T}}^{\text{miss}}$ bins in the $N_{\text{jets}} = 5$ control sample as in the analysis regions. We then compute an ABCD background estimate, the results of which are shown in Table 7.3. As in the dilepton sample, we use the uncertainty in the predicted yield convolved with the size of expected fluctuations about the yield as the systematic uncertainty. To avoid potential signal contamination, we take the uncertainty for the $E_{\text{T}}^{\text{miss}} > 500\,\text{GeV}$ from the $350\,\text{GeV} < E_{\text{T}}^{\text{miss}} \leq 500\,\text{GeV}$ bin of the $N_{\text{jets}} = 5$ control sample. This introduces two new Z_i nuisance parameters, with one for each of the $E_{\text{T}}^{\text{miss}}$ ranges $200\,\text{GeV} < E_{\text{T}}^{\text{miss}} \leq 350\,\text{GeV}$ and $E_{\text{T}}^{\text{miss}} > 350\,\text{GeV}$. The uncertainty for the low-$E_{\text{T}}^{\text{miss}}$ region is 16% and the uncertainty for the high-$E_{\text{T}}^{\text{miss}}$ region is 41%, so that

$$\varsigma_{i,j,k} = \begin{cases} 0.15, & i \in \{\text{low-}E_{\text{T}}^{\text{miss}}\text{ bins}\},\ k = \text{low-}E_{\text{T}}^{\text{miss}}\text{ nuisance}, \\ 0.34, & i \in \{\text{high-}E_{\text{T}}^{\text{miss}}\text{ bins}\},\ k = \text{high-}E_{\text{T}}^{\text{miss}}\text{ nuisance}, \\ 0, & i \in \{\text{low-}E_{\text{T}}^{\text{miss}}\text{ bins}\},\ k = \text{high-}E_{\text{T}}^{\text{miss}}\text{ nuisance}, \\ 0, & i \in \{\text{high-}E_{\text{T}}^{\text{miss}}\text{ bins}\},\ k = \text{low-}E_{\text{T}}^{\text{miss}}\text{ nuisance}. \end{cases} \tag{7.2}$$

Table 7.3: Yields and maximum likelihood ABCD predictions for the $N_{\text{jets}} = 5$ control sample, binned in $E_{\text{T}}^{\text{miss}}$ and including low-$E_{\text{T}}^{\text{miss}}$ validation regions. As in Table 7.2, inaccuracies in the modeling of κ in simulation would appear here. We would typically read off the systematic uncertainties derived from the $N_{\text{jets}} = 5$ control samples from Figure 7.19, but we can in principle compute them from the uncertainties in the background predictions for the R4 rows in the $E_{\text{T}}^{\text{miss}}$ ranges $200\,\text{GeV} < E_{\text{T}}^{\text{miss}} \leq 350\,\text{GeV}$ and $350\,\text{GeV} < E_{\text{T}}^{\text{miss}} \leq 500\,\text{GeV}$. Table from Reference [13].

$L = 36\,\text{fb}^{-1}$	T1tttt(NC)	T1tttt(C)	κ	Sim. Bkg.	Pred.	Obs.	Obs./Sim.	Signif.
$100\,\text{GeV} < E_{\text{T}}^{\text{miss}} \leq 150\,\text{GeV}$ (Obs./Sim. $= 0.90 \pm 0.01$)								
R1: All N_{jets}	0.01	0.59		12 867.62		12 792	0.99 ± 0.01	
R2: $N_{\text{jets}} = 5$	0.03	0.10		1683.07		1697	1.01 ± 0.03	
R3: All N_{jets}	0.00	0.30		1046.26		1095	1.05 ± 0.04	
R4: $N_{\text{jets}} = 5$	0.03	0.08	$1.67^{0.08}_{-0.08}$	229.05	$243.13^{+15.44}_{-14.99}$	242	1.06 ± 0.08	0.0 s.d.
$150\,\text{GeV} < E_{\text{T}}^{\text{miss}} \leq 200\,\text{GeV}$ (Obs./Sim. $= 0.87 \pm 0.01$)								
R1: All N_{jets}	0.00	0.57		6019.39		6040	1.00 ± 0.01	
R2: $N_{\text{jets}} = 5$	0.01	0.24		922.55		892	0.97 ± 0.03	
R3: All N_{jets}	0.02	0.44		331.80		351	1.06 ± 0.06	
R4: $N_{\text{jets}} = 5$	0.03	0.04	$1.66^{0.09}_{-0.09}$	84.26	$85.89^{+7.20}_{-7.22}$	75	0.89 ± 0.11	-0.9 s.d.
$200\,\text{GeV} < E_{\text{T}}^{\text{miss}} \leq 350\,\text{GeV}$ (Obs./Sim. $= 0.83 \pm 0.01$)								
R1: All N_{jets}	0.01	1.08		4744.06		4733	1.00 ± 0.02	
R2: $N_{\text{jets}} = 5$	0.07	0.26		1024.74		994	0.97 ± 0.03	
R3: All N_{jets}	0.05	0.79		255.97		292	1.14 ± 0.07	
R4: $N_{\text{jets}} = 5$	0.23	0.26	$1.34^{0.06}_{-0.05}$	74.23	$82.33^{+6.64}_{-6.44}$	80	1.08 ± 0.13	-0.2 s.d.
$350\,\text{GeV} < E_{\text{T}}^{\text{miss}} \leq 500\,\text{GeV}$ (Obs./Sim. $= 0.81 \pm 0.03$)								
R1: All N_{jets}	0.03	0.17		525.10		531	1.01 ± 0.04	
R2: $N_{\text{jets}} = 5$	0.05	0.03		233.26		217	0.93 ± 0.06	
R3: All N_{jets}	0.06	0.14		33.55		43	1.28 ± 0.21	
R4: $N_{\text{jets}} = 5$	0.29	0.11	$1.08^{0.09}_{-0.08}$	16.09	$18.97^{+3.71}_{-3.46}$	17	1.06 ± 0.26	-0.3 s.d.

Table 7.4: Fractional systematic uncertainties, expressed in percentages, for the signal bins. Uncertainties combine those from the dilepton and $N_{\text{jets}} = 5$ control samples by treating them as independent, as in Equation (7.3).

Bkg. Syst. Uncert. [%]	$6 \leq N_{\text{jets}} \leq 8$	$N_{\text{jets}} \geq 9$
$200\,\text{GeV} < E_{\text{T}}^{\text{miss}} \leq 350\,\text{GeV}$	17	23
$350\,\text{GeV} < E_{\text{T}}^{\text{miss}} \leq 500\,\text{GeV}$	41	44
$E_{\text{T}}^{\text{miss}} > 500\,\text{GeV}$	41	44

The full treatment of the systematic uncertainties in the likelihood function was described in Section 6.5, but by treating the uncertainties from the two control regions as uncorrelated, we may approximate the combined effect on the signal regions as

$$(\sigma_{\text{SR}})^2_{i,j} \approx (\sigma_{N_{\text{jets}}=5})^2_i + (\sigma_{\text{dilepton}})^2_j. \tag{7.3}$$

As usual, the index i specifies a $E_{\text{T}}^{\text{miss}}$ bin and j specifies an N_{jets}-N_{b} bin. Table 7.4 shows the approximate uncertainties obtained in this way.

Before accepting these as the final systematic uncertainties, we must check that

- any significant mismodeling of κ would appear in at least one of the two control samples, and
- that the control samples do not show any evidence of such mismodeling.

If the first condition were to fail, we would need additional control samples to further validate the method. If the second condition were to fail, it would indicate the background estimation may be biased and we would need to re-evaluated. The remaining sections in this chapter confirm that these two conditions are met.

7.4 Validation of Control Samples

For the control samples to work, any change in κ in the main analysis regions must be accompanied by a comparable change in one of the two control samples. This is necessary to ensure that potential mismodeling can be detected using the two control samples. In this section, we intentionally introduce mismodeling into the simulation, similar to the treatment in Section 7.1. We then compute Δ_κ using the unmodified simulation and the modified simulation (treated as pseudodata). For each scenario, the Δ_κ values obtained in the analysis region should be paired with similar Δ_κ values in the control samples.

The two scenarios described in this section introduce unrealistically large mismodeling in order to produce changes in κ that would in principle be detectable with the $35.9\,\text{fb}^{-1}$ dataset. For more realistic mismodeling scenarios, the changes in κ are typically too small to be detectable in either the control samples or analysis regions with only $35.9\,\text{fb}^{-1}$ of data. However, studies in simulation confirm that the small changes in the analysis regions would in principle be present in the control samples.

7.4.1 Doubling κ for Mismeasured Single Lepton Events

The first extreme scenario we consider doubles the weight of high-m_T, high-M_J events with a single lepton and mismeasured E_T^miss. This effectively doubles κ for the mismeasured E_T^miss category of events described in Section 7.2. It also doubles the number of events belonging to this category at high m_T and M_J.

Figure 7.13 shows that this scenario has a negligible effect on κ in the dilepton sample and that this holds across all the N_jets and E_T^miss bins. There is, however, a significant shift in κ in both the analysis region and the $N_\text{jets} = 5$ control sample, as shown in Figure 7.14. For both samples, we show Δ_κ in bins of E_T^miss, with Δ_κ as large as 66–68% at low E_T^miss and decreasing to 10–13% at high E_T^miss. The important feature is that for each E_T^miss bin

in the $N_{\text{jets}} \geq 6$ sample, Δ_κ is consistent with that seen in the corresponding bin of the $N_{\text{jets}} = 5$ control sample. This implies that if such mismodeling were present, it could be measured in the $N_{\text{jets}} = 5$ control sample and a suitable correction developed before unblinding the data in the signal region.

As a further check, Figure 7.15 shows that the shift in κ cause by this particular mismodeling scenario is approximately independent of N_{jets} and N_{b}.

7.4.2 Two Standard Deviation Change of ISR Correction for Single Lepton $\mathrm{t\bar{t}}$ + jets

The second extreme scenario considered decreases the ISR correction for the $\mathrm{t\bar{t}}$ + jets process by twice its uncertainty in events with a single lepton. Unlike the previous scenario, this does not produce a $E_{\text{T}}^{\text{miss}}$-dependent change in κ, as seen in Figure 7.16 for the analysis regions and the two control samples. There is minimal change in κ even in the lowest $100\,\text{GeV} < E_{\text{T}}^{\text{miss}} \leq 150\,\text{GeV}$ bin, in contrast to the 68% shifts caused by the κ mismodeling scenario.

On the other hand, this scenario does introduce an N_{jets} dependent shift in κ, as seen in Figure 7.17. Δ_κ is negligible for the low N_{jets} bins, but reaches $\Delta_\kappa = -11\%$ and $\Delta_\kappa = -18\%$ for the $N_{\text{jets}} \geq 9$ bins of the signal region and dilepton control sample, respectively.

Figure 7.18 shows that Δ_κ has negligible N_{b} dependence in this scenario.

7.5 Checking for Mismodeling in Control Samples

The previous section established that the control regions are able to detect potential mismodeling. The final step before finalizing the systematic uncertainties from Table 7.4

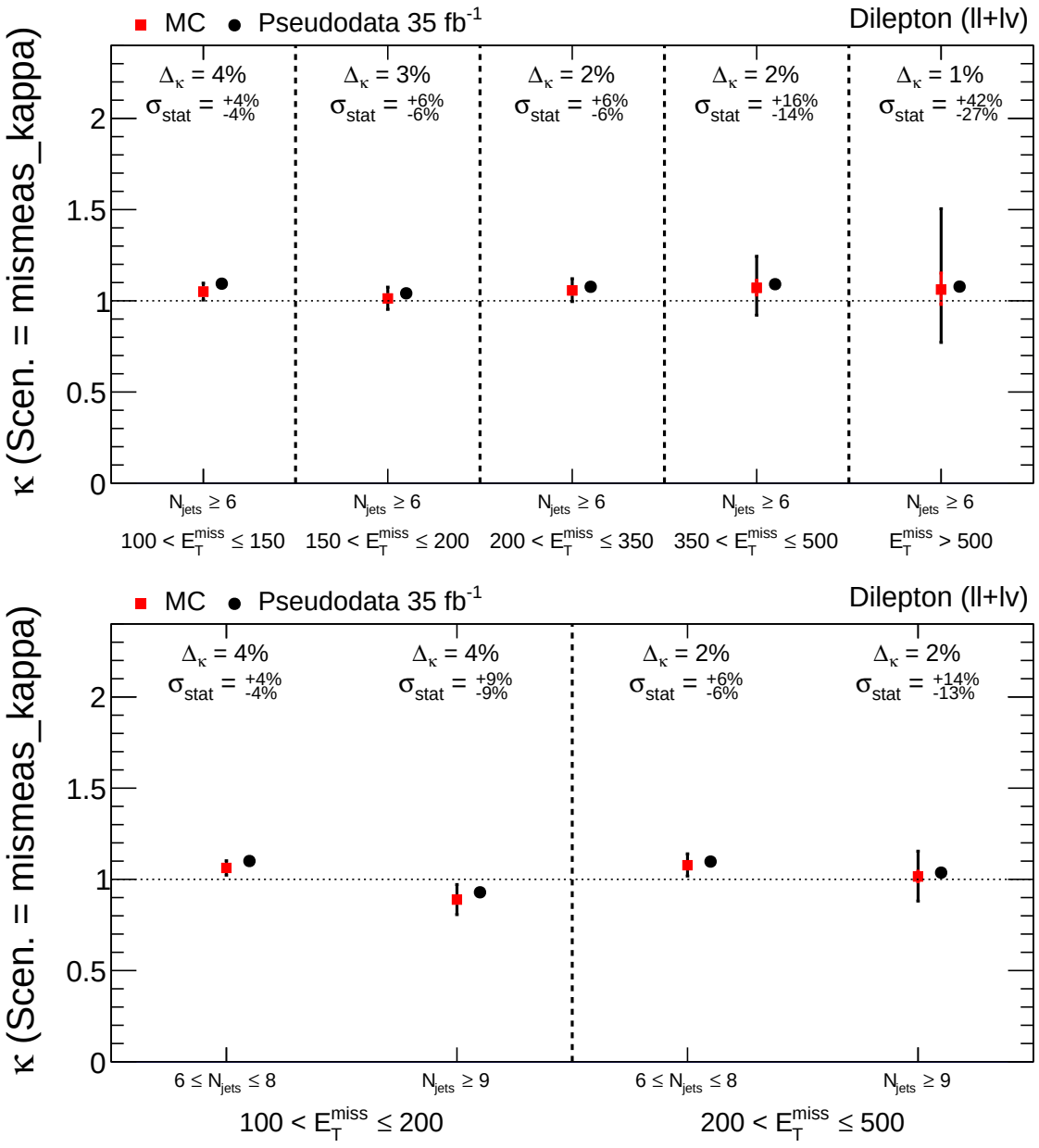

Figure 7.13: Shift in κ in the dilepton sample caused by doubling the weight of events in R4 with a single lepton and mismeasured $E_{\mathrm{T}}^{\mathrm{miss}}$. Changes are measured in bins of $E_{\mathrm{T}}^{\mathrm{miss}}$ (top) and N_{jets} (bottom). Red points show unmodified κ from simulation with a two-part error bar. The inner red part shows statistical uncertainty due to the number of simulated events available. The outer black part represents the expected size of fluctuations about the underlying κ in $35\,\mathrm{fb}^{-1}$ of real data. Black points shows the modified simulation with added mismodeling, treated as real data. Negligible change is observed for all $E_{\mathrm{T}}^{\mathrm{miss}}$ and N_{jets} bins. Figure from Reference [13].

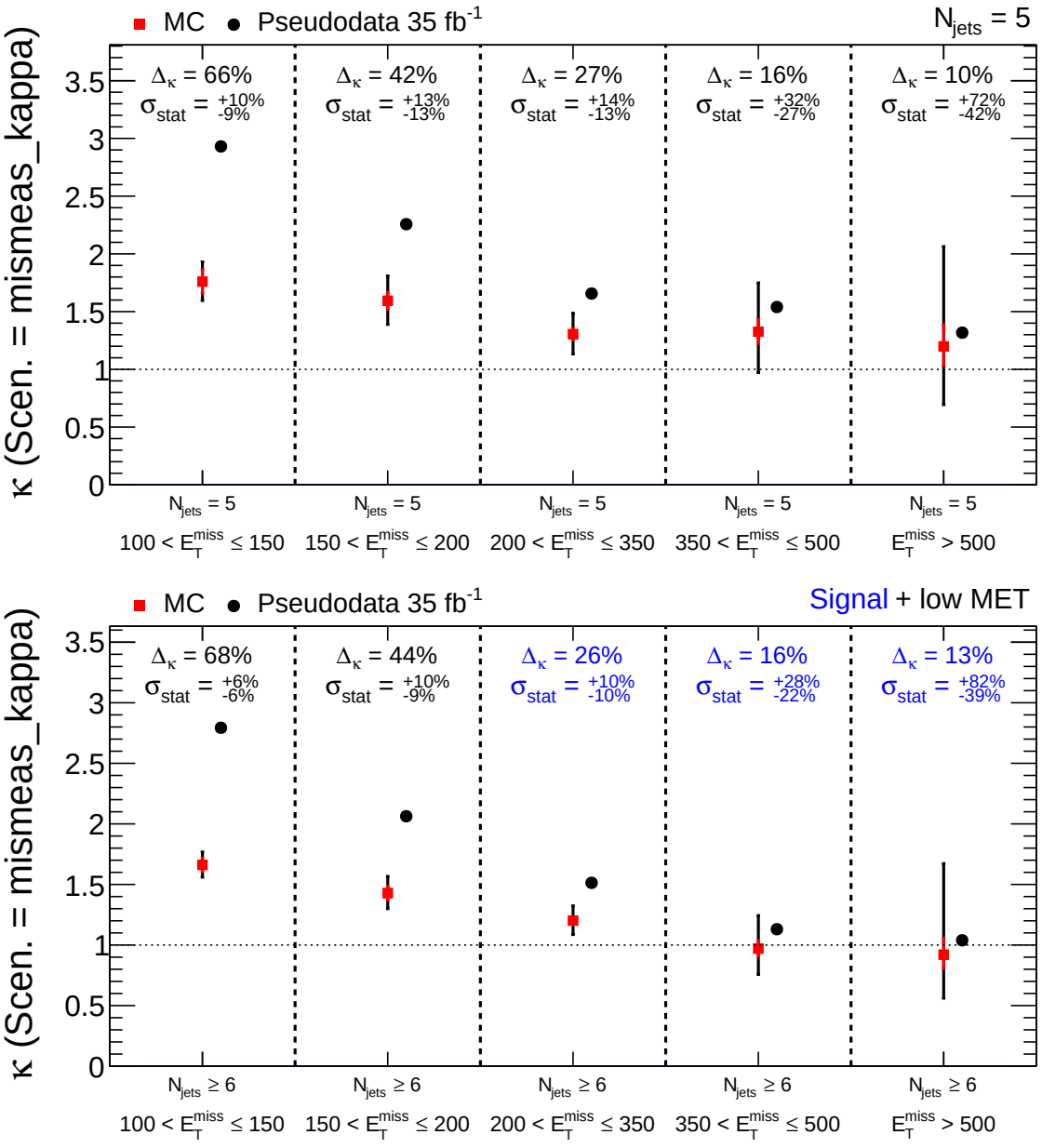

Figure 7.14: Shift in κ caused by doubling the weight of events in R4 with a single lepton and mismeasured $E_{\mathrm{T}}^{\mathrm{miss}}$, as measured in the $N_{\mathrm{jets}} = 5$ control sample (top) and analysis regions (bottom). Both samples are binned in $E_{\mathrm{T}}^{\mathrm{miss}}$, and changes in κ in the analysis region are mirrored by similar changes in the $N_{\mathrm{jets}} = 5$ control sample. The largest shifts in κ for this scenario occur at low $E_{\mathrm{T}}^{\mathrm{miss}}$, where events with mismeasured $E_{\mathrm{T}}^{\mathrm{miss}}$ make up a larger fraction of the background composition. Figure from Reference [13]

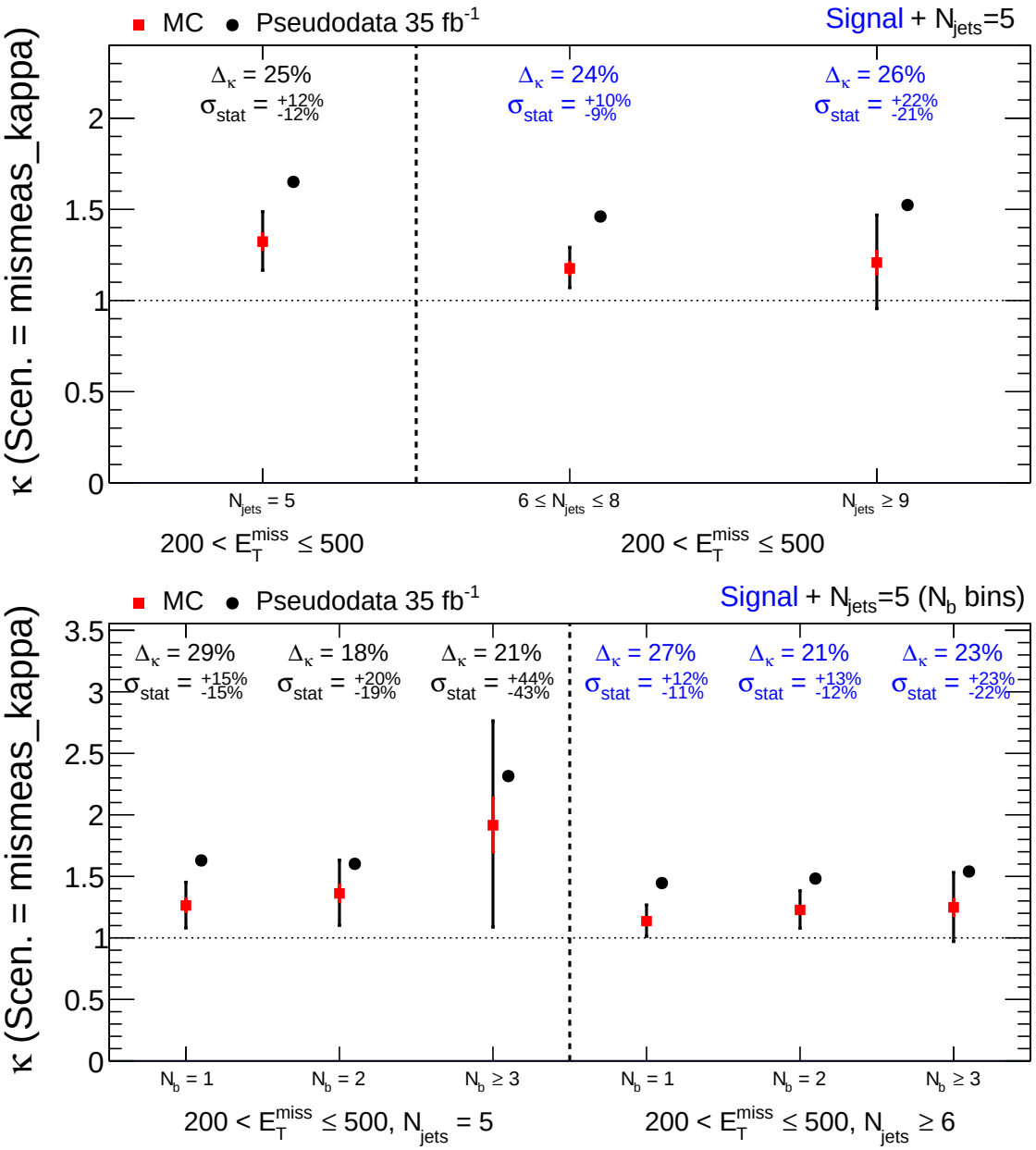

Figure 7.15: Shifts in κ caused by doubling the weight of events in R4 with a single lepton and mismeasured $E_{\mathrm{T}}^{\mathrm{miss}}$ are approximately independent of N_{jets} (top) and N_{b} (bottom), shown here in the analysis region and $N_{\mathrm{jets}} = 5$ control samples. Figure from Reference [13].

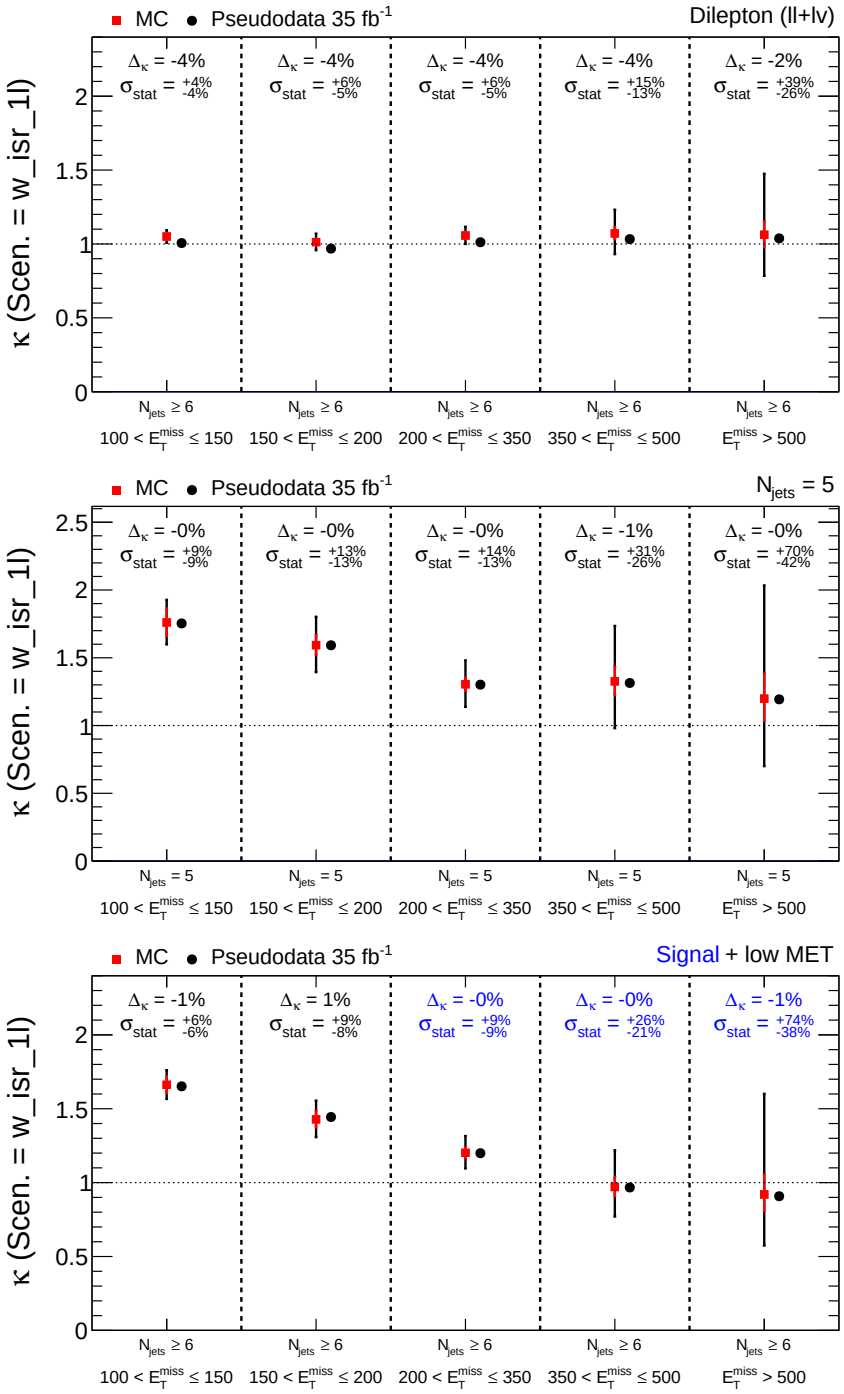

Figure 7.16: Shift in κ caused by changing the ISR corrections by twice their uncertainty in $t\bar{t}$ + jets events with a single lepton, as seen in the dilepton (top) and $N_{\text{jets}} = 5$ (middle) control samples and analysis region (bottom). In all cases, changes in κ are approximately independent of $E_{\text{T}}^{\text{miss}}$. Figure from Reference [13].

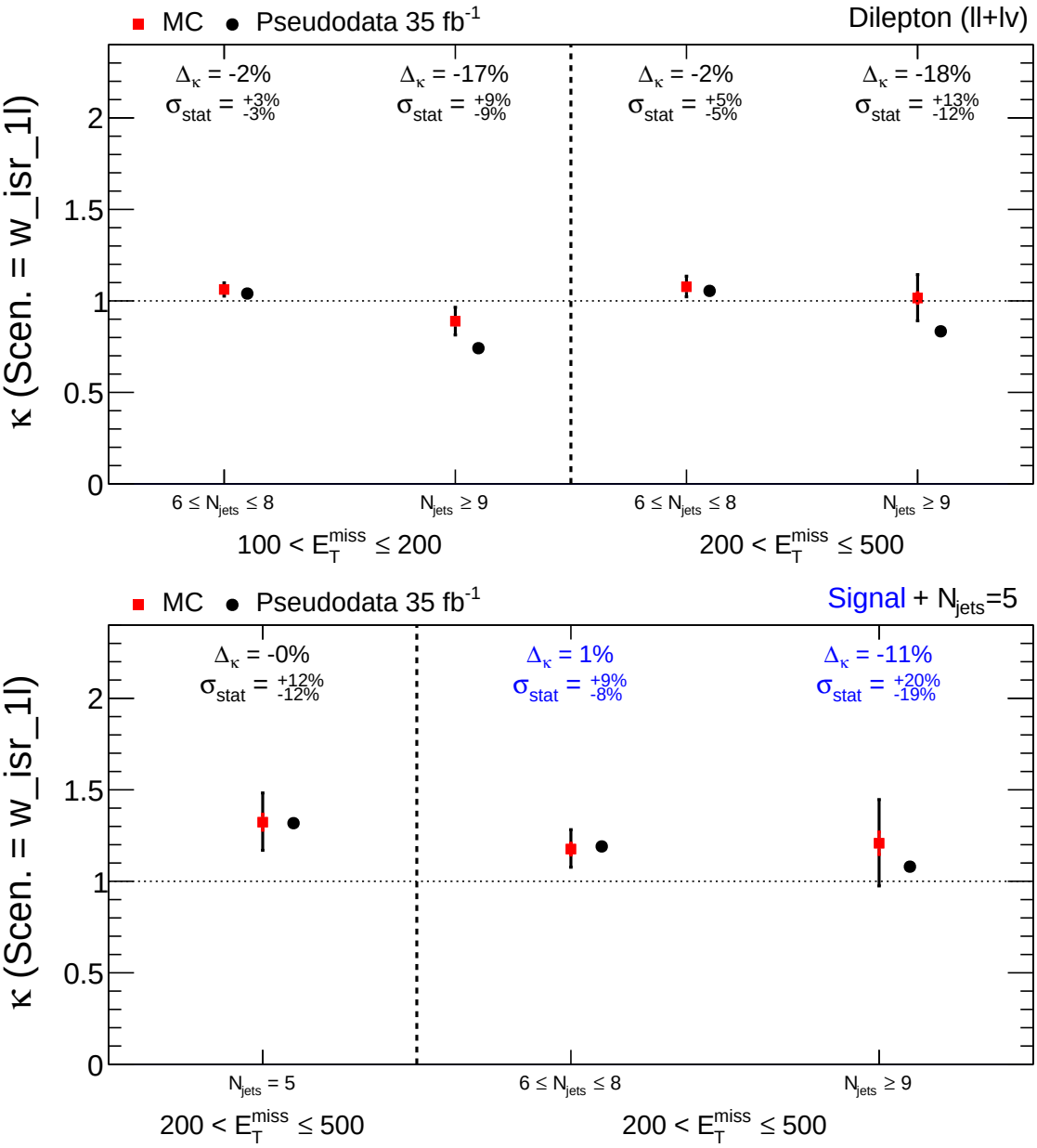

Figure 7.17: Shifts in κ caused by changing the $t\bar{t}$ + jets ISR corrections by twice their uncertainty in events with a single lepton are largest in the high-N_{jets} bins. The -11% shift observed in the $N_{\text{jets}} \geq 9$ bin of the analysis region (bottom) is matched by similar changes in the $N_{\text{jets}} \geq 9$ bins of the dilepton control sample (top). Figure from Reference [13].

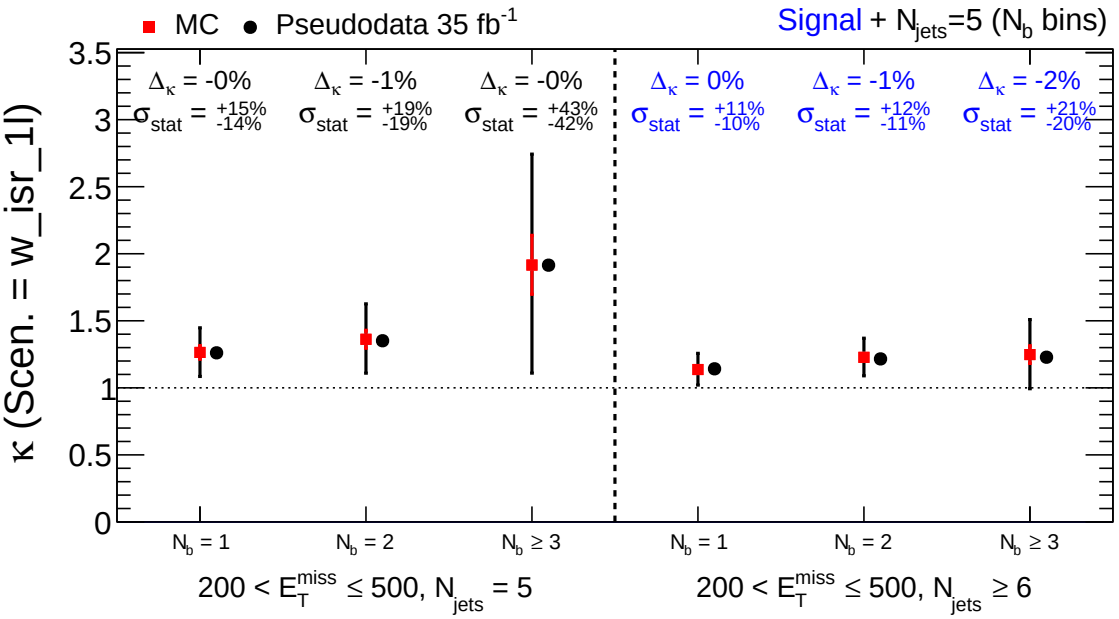

Figure 7.18: Shifts in κ caused by changing the ISR corrections by twice their uncertainty in $t\bar{t}$ + jets events with a single lepton are approximately independent of N_b, as shown here for the $N_{jets} = 5$ control sample and $N_{jets} \geq 6$ analysis region. Figure from Reference [13].

and unblinding the signal region, is to check that the control regions do not in fact show any evidence of systematic mismodeling in simulation. In this section, rather comparing the unmodified simulation with modified simulation (pseudodata), we compared the unmodified simulation with the real data.

Figure 7.19 shows the κ values obtained from the dilepton and $N_{jets} = 5$ control samples, binned in N_{jets} and E_T^{miss}, respectively. The κ values observed in the real data are consistent with those computed from simulation to within one standard deviation across all eight bins. This provides confidence that the simulation is modeling the true data well. While we do not use the $E_T^{miss} \leq 200$ GeV bins of Figure 7.19 explicitly in setting systematic uncertainties, they provide additional confidence in the simulation.

The uncertainties mentioned in Sections 7.3.1 and 7.3.2 are derived from these plots. For example, the 6% systematic uncertainty assigned to the low-N_{jets} bins from the

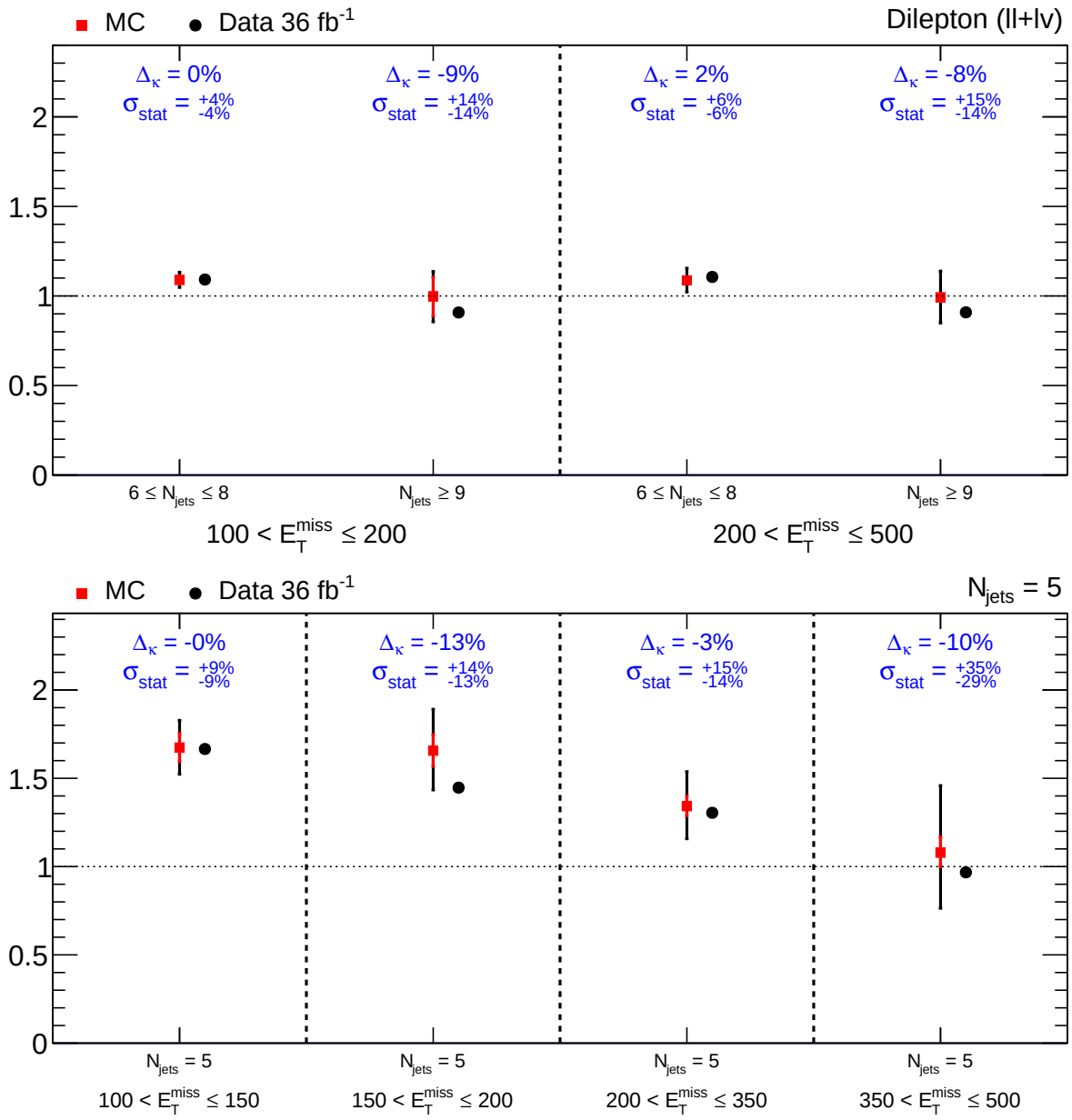

Figure 7.19: Differences in the observed and simulated κ for the dilepton (top) and $N_{\text{jets}} = 5$ (bottom) control samples. Observed values are consistent with those predicted by simulation. Systematic uncertainties assigned from the control regions are taken from the σ_{stat} reported in these plots. The dilepton control sample yields 6% and 16% $= \frac{14\%}{100\%-14\%}$ uncertainties for the $6 \leq N_{\text{jets}} \leq 8$ and $N_{\text{jets}} \geq 9$ bins, respectively. The $N_{\text{jets}} = 5$ control samples yields 16% $= \frac{14\%}{100\%-14\%}$ and 41% $= \frac{29\%}{100\%-29\%}$ uncertainties for the $200\,\text{GeV} < E_{\text{T}}^{\text{miss}} \leq 350\,\text{GeV}$ and $E_{\text{T}}^{\text{miss}} > 350\,\text{GeV}$ bins, respectively. The remaining low $E_{\text{T}}^{\text{miss}}$ bins shown here are not used to assign uncertainties, but provide confidence in the accuracy of the simulation. Figure from Reference [13].

dilepton control region corresponds to the σ_{stat} in the third column of the upper plot in Figure 7.19. The σ_{stat} shown in Figure 7.19 are asymmetric, but the $\varsigma_{i,j,k}$ parameters of Section 6.5 only allow for symmetric uncertainties. To address this difficulty, we use the symmetrized uncertainty

$$\sigma = \max\left(\sigma_+,\ \frac{\sigma_-}{1-\sigma_-}\right), \tag{7.4}$$

effectively taking the larger of the upper (σ_+) and lower (σ_-) uncertainties. Corrections to κ are multiplicative, so a downward correction which, for example, halves κ should be comparable to an upward correction which doubles κ; using the lower uncertainty term $\frac{\sigma_-}{1-\sigma_-}$ rather than just σ_- in Equation (7.4) accounts for this effect. Taking the maximum of the two ensures that the assigned systematic uncertainty is not underestimated. We then compute the likelihood parameters $\varsigma_{i,j,k} = \ln(1+\sigma_{i,j,k})$ from the symmetrized uncertainties.

The standard binning of the control regions in Figure 7.19 does not show evidence of mismodeling, but we perform several additional checks before unblinding the main analysis regions. For example, Figure 7.20 shows four additional checks using the control samples. The upper left plot checks for mismodeling in the $N_{\text{leps}} = N_{\text{veto}} = 1$ subset of the dilepton control sample. In the analysis regions, approximately half of the high-m_{T} $\text{t}\bar{\text{t}}+\text{jets}$ events with two true leptons had a decaying τ lepton, as seen in Figure 7.4. On the other hand, most events in the dilepton control sample have two prompt light leptons. The subset of events with $N_{\text{leps}} = N_{\text{veto}} = 1$, however, has a very similar composition to the high-m_{T} analysis regions, as seen in Figure 7.12. The upper left plot is therefore useful in checking the modeling of hadronic τ decays.

The upper right plot of Figure 7.20 bins the dilepton control sample in $E_{\text{T}}^{\text{miss}}$ rather than the usual N_{jets}. There is no indication of significant $E_{\text{T}}^{\text{miss}}$-dependent mismodeling

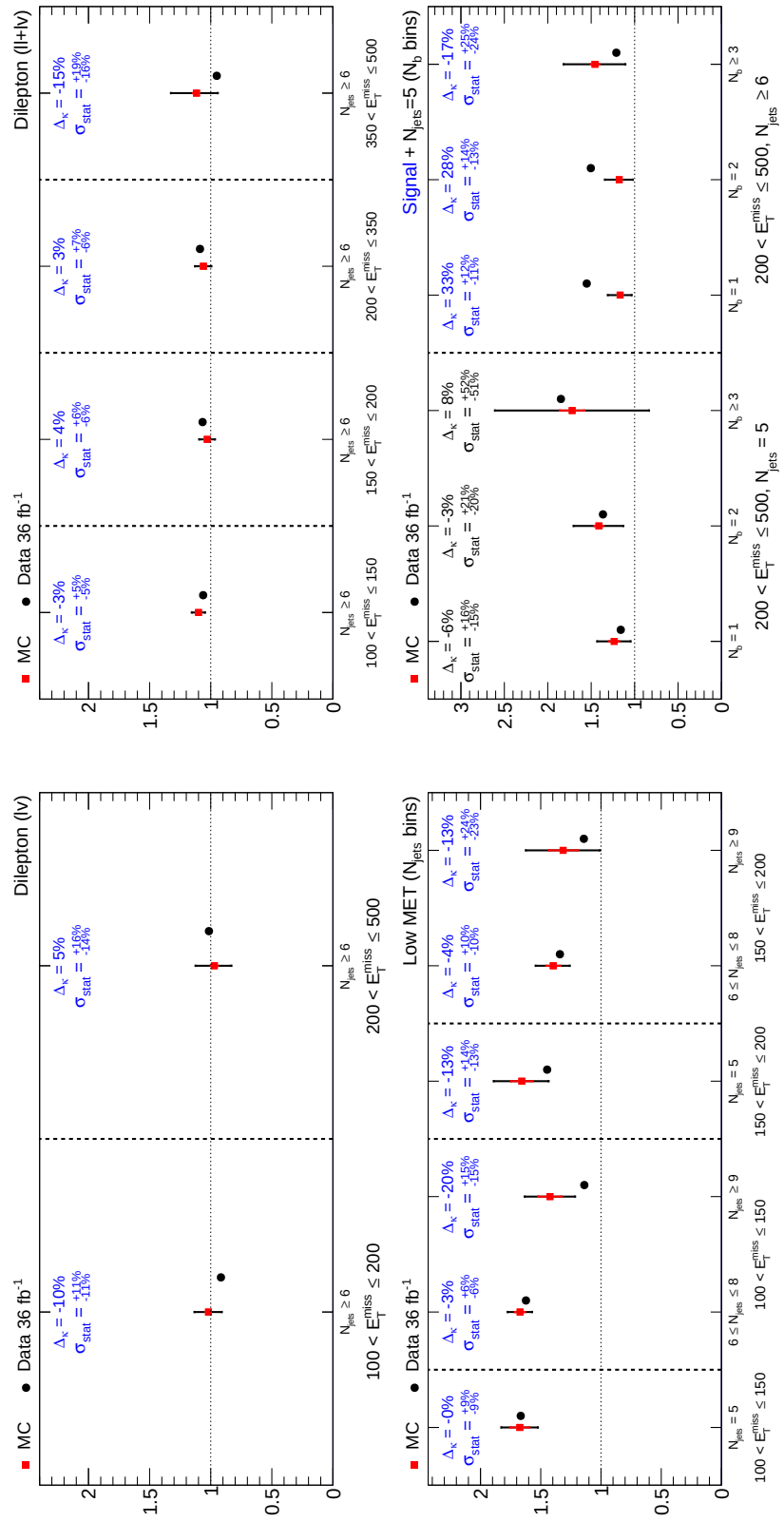

Figure 7.20: Additional checks for mismodeling in simulation performed before unblinding the signal region. No significant differences between simulated and observed κ values are seen in the $N_{leps} = N_{veto} = 1$ subset of the dilepton control sample (top left), the full dilepton control sample binned in N_{jets} (top right), the low E_T^{miss} validation region (bottom left), or the $N_{jets} = 5$ control sample and analysis region binned in N_b (bottom right). Note that the bottom right plot shown here does show κ values obtained by unblinding the signal region. In practice, these are initially hidden until the other values have been checked. Figure from Reference [13].

in the dilepton sample, adding confidence in the modeling of the high-$E_{\mathrm{T}}^{\mathrm{miss}}$ bins.

The lower left plot in Figure 7.20 takes the $E_{\mathrm{T}}^{\mathrm{miss}} \leq 200\,\mathrm{GeV}$ validation region and divides it into bins of N_{jets} and $E_{\mathrm{T}}^{\mathrm{miss}}$. Again, we observe no significant mismodeling.

Finally, the bottom right plot in Figure 7.20 takes the $N_{\mathrm{jets}} = 5$ control sample and the main analysis region and partitions them into N_{b} bins. In practice, we keep the analysis regions blinded until we have finished examining the $N_{\mathrm{jets}} = 5$ control sample, but both are included here for convenience. This check confirms that no dedicated N_{b}-dependent systematic uncertainty is needed.

Having confirmed that κ is well-modeled in the control samples, the analysis regions can be unblinded, the results of which are shown in Figure 7.21, binned in both $E_{\mathrm{T}}^{\mathrm{miss}}$ (left plot) and N_{jets} (right plot). The observed κ values are generally consistent with those found in simulation. There is a modest (between two and three standard deviations) upward fluctuation in κ relative to the simulated value in the $E_{\mathrm{T}}^{\mathrm{miss}} > 500\,\mathrm{GeV}$ bin. Having at least one such fluctuation of this size is expected considering the number of bins tested in this section.

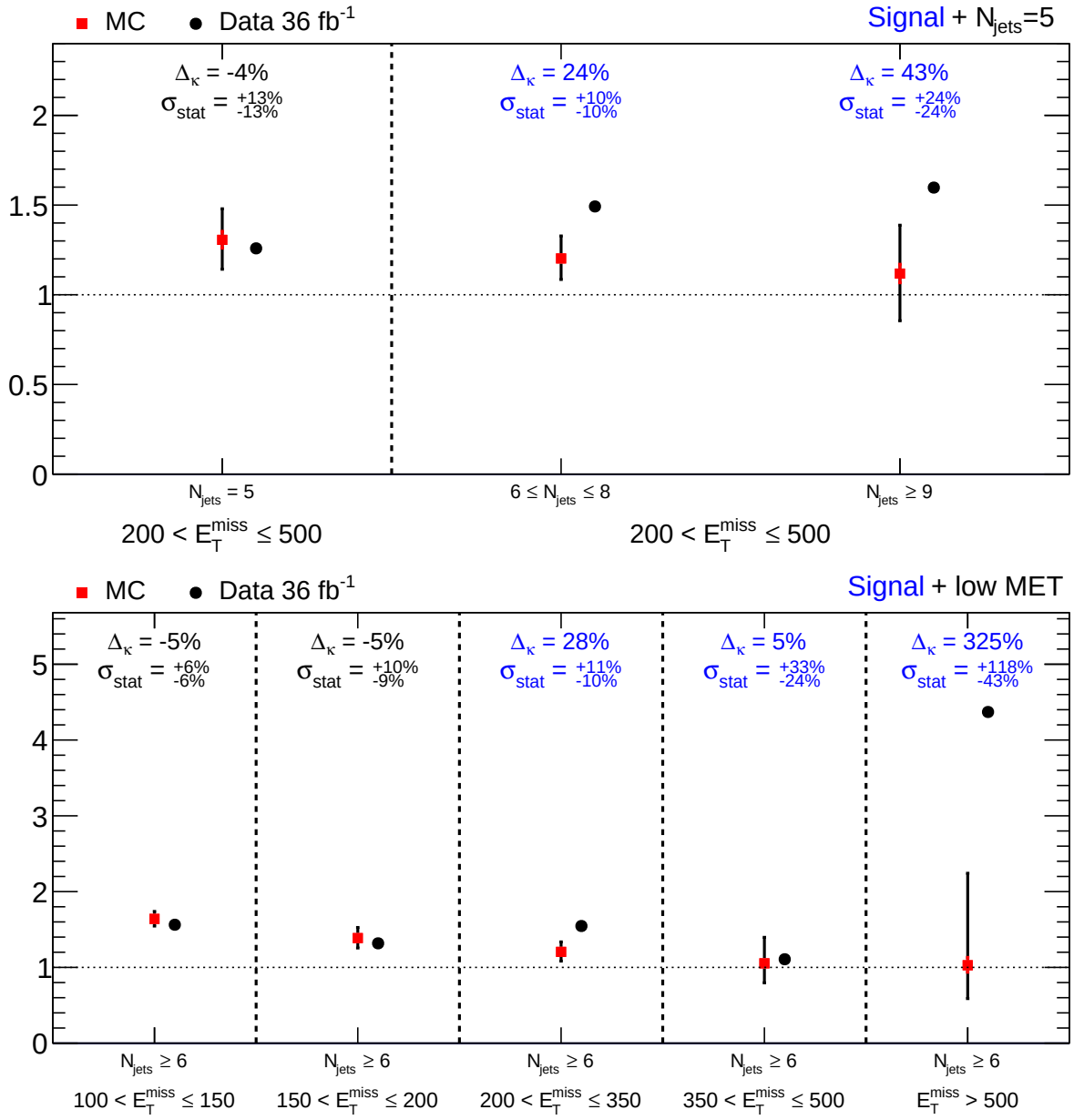

Figure 7.21: Comparison of κ values measured in simulation and real data for the analysis regions. There is a modest (between two and three standard deviations) upward fluctuation in κ relative to the simulated value in the $E_{\mathrm{T}}^{\mathrm{miss}} > 500\,\mathrm{GeV}$ bin. Having at least one such fluctuation of this size is expected considering the number of bins tested in this section. Figure from Reference [13].

Chapter 8

Systematic Uncertainty in Signal Model

In Chapter 7, we assigned background systematic uncertainties by using two control samples to study the ability of the simulation to properly model the behavior of κ. Rather than emphasizing specific causes of mismodeling, the procedure relied on the control samples having similar properties compared to the analysis regions. This allowed us to test the ABCD background estimation in the control samples, knowing that if it works there, it should also work in the analysis regions. Unfortunately, the kinematic properties of the signal can vary dramatically depending on the particle masses, and the T1tttt and T5tttt models may behave differently even for the same gluino and LSP masses. These complications necessitate a different approach to evaluate systematic uncertainties in the signal model. Instead, we will separately quantify each specific sources of uncertainty using a dedicated study. While systematic uncertainties in the background were only coarsely binned, we will evaluate the size of each systematic uncertainty in each bin separately for the signal models.

Table 8.1 gives a summary of the fractional uncertainties in the R4 bins for several

signal models. While the procedures for evaluating the sizes of the systematic uncertainties is different, the mathematical implementation is largely the same as that used for the background uncertainties. Like the background uncertainties, the signal uncertainties are implemented using Gaussian-constrained nuisance parameters Z_k and constants $\varsigma_{i,j,k}$, which control the sizes of the uncertainties, as described in Section 6.5. For the signal uncertainties, however, some uncertainties have an effect on the signal yield that is anti-correlated across bins. Such anti-correlation is represented by negative values in Table 8.1. Within any row, two columns of opposite sign are anti-correlated, while those with the same sign are correlated. To accommodate the anti-correlations, the fractional uncertainties $\sigma_{i,j,k}$ shown in the table are translated into the fit constants

$$\varsigma_{i,j,k} = \begin{cases} \ln(1+\sigma_{i,j,k}), & \sigma_{i,j,k} \geq 0, \\ -\ln(1-\sigma_{i,j,k}), & \sigma_{i,j,k} < 0. \end{cases} \tag{8.1}$$

Note that uncertainties from different rows will carry a different index k and are uncorrelated with each other.

The lepton efficiency uncertainties are derived from a "tag-and-probe" study of the lepton reconstruction and isolation efficiencies in Z-enriched samples. This study uses real data and both FullSim and FastSim simulated data. For each event, a "tag" lepton passing strict identification requirements is identified. Then, a set of "probes" are identified for which the invariant mass of the tag-plus-probe pair is within a narrow window around the mass of the Z boson. Widening the window around the Z mass produces a sideband sample containing mostly fake leptons. The invariant mass distribution in the sideband is then fit using a parametric or template shape. Extending the shape into the narrow Z-window allows one to subtract out the fake leptons from the set of probes. The fraction of the remaining probes which pass a particular identification requirement then

Table 8.1: Sizes of systematic uncertainties assigned to the R4 bins for two selected signal models. Systematic uncertainties in different rows are treated as uncorrelated. Uncertainties within a row are treated as fully correlated if they have the same sign, and fully anti-correlated if they have opposite signs. Table from Reference [13].

Uncertainty [%]	$200\,\text{GeV} < E_\text{T}^\text{miss} \leq 350\,\text{GeV}$						$350\,\text{GeV} < E_\text{T}^\text{miss} \leq 500\,\text{GeV}$						$E_\text{T}^\text{miss} > 500\,\text{GeV}$					
	$6 \leq N_\text{jets} \leq 8$			$N_\text{jets} \geq 9$			$6 \leq N_\text{jets} \leq 8$			$N_\text{jets} \geq 9$			$6 \leq N_\text{jets} \leq 8$			$N_\text{jets} \geq 9$		
	$N_\text{b}=1$	$N_\text{b}=2$	$N_\text{b} \geq 3$	$N_\text{b}=1$	$N_\text{b}=2$	$N_\text{b} \geq 3$	$N_\text{b}=1$	$N_\text{b}=2$	$N_\text{b} \geq 3$	$N_\text{b}=1$	$N_\text{b}=2$	$N_\text{b} \geq 3$	$N_\text{b}=1$	$N_\text{b}=2$	$N_\text{b} \geq 3$	$N_\text{b}=1$	$N_\text{b}=2$	$N_\text{b} \geq 3$
Signal Model: T1tttt(1800,100)																		
Lepton Efficiency	3	3	4	3	3	4	4	4	3	4	4	4	4	4	4	3	4	4
FastSim Lepton Efficiency	4	4	4	3	4	4	4	3	4	4	4	4	4	4	4	4	4	4
Trigger Efficiency	1	1	1	1	1	1	1	1	1	1	1	1	1	1	1	1	1	1
b-Tag Efficiency	−4	<1	4	−5	−1	3	−3	<1	5	−5	−1	4	−4	<1	5	−5	−1	4
FastSim b-Tag Efficiency	−16	12	5	5	5	4	−8	2	10	−9	14	4	−1	2	7	−1	12	6
Mistag Efficiency	−1	<1	1	1	−1	<1	−1	<1	<1	−1	−1	<1	−1	<1	1	−1	−1	1
FastSim Mistag Efficiency	3	3	3	4	3	3	3	3	3	3	3	4	3	3	4	3	3	3
FastSim E_T^miss	−5	−7	1	7	2	−1	1	6	−5	−1	−1	−2	<1	<1	1	<1	<1	1
Jet Energy Corrections	−5	2	−7	4	5	8	−4	−2	−4	−7	5	4	−1	−1	−2	10	8	7
QCD Scales	<1	<1	<1	<1	<1	<1	<1	<1	<1	<1	<1	<1	<1	<1	<1	<1	<1	<1
ISR	−2	−4	−3	5	8	4	−2	−3	−3	9	8	8	−2	−3	−3	8	8	7
Jet ID	1	1	1	1	1	1	1	1	1	1	1	1	1	1	1	1	1	1
Pile Up	10	10	10	15	15	15	10	10	10	15	15	15	15	15	15	15	15	15
Integrated Luminosity	3	3	3	3	3	3	3	3	3	3	3	3	3	3	3	3	3	3
Signal Model: T1tttt(1400,1000)																		
Lepton Efficiency	3	4	4	3	4	3	3	4	4	3	4	4	4	3	3	3	3	3
FastSim Lepton Efficiency	3	3	3	3	3	3	3	3	3	3	3	3	3	3	3	3	3	3
Trigger Efficiency	1	1	1	1	1	1	1	1	1	1	1	1	1	1	1	1	1	1
b-Tag Efficiency	−3	<1	3	−5	−1	4	−3	<1	4	−4	−1	2	−3	<1	3	−4	−2	3
FastSim b-Tag Efficiency	−1	−1	1	−1	−1	2	−1	−1	1	−1	<1	−1	<1	−1	−1	−2	−3	28
Mistag Efficiency	−1	<1	1	−1	<1	<1	−1	−1	<1	−1	−1	1	−1	<1	1	−1	−1	2
FastSim Mistag Efficiency	<1	<1	<1	<1	<1	<1	<1	<1	<1	<1	<1	1	<1	<1	<1	<1	<1	8
FastSim E_T^miss	<1	−8	11	−4	4	<1	7	13	−3	7	10	4	−8	−3	−8	4	−3	2
Jet Energy Corrections	−7	−6	−4	18	13	8	−7	3	11	24	21	4	−6	8	−15	6	6	7
QCD Scales	<1	<1	<1	<1	<1	<1	<1	<1	<1	<1	<1	<1	<1	<1	<1	<1	<1	<1
ISR	1	−1	<1	11	10	8	5	2	3	12	13	12	3	6	2	16	13	16
Jet ID	1	1	1	1	1	1	1	1	1	1	1	1	1	1	1	1	1	1
Pile Up	10	10	10	15	15	15	10	10	10	15	15	15	15	15	15	15	15	15
Integrated Luminosity	3	3	3	3	3	3	3	3	3	3	3	3	3	3	3	3	3	3

gives the efficiency for that requirement. Comparing the data and FullSim efficiencies gives a multiplicative correction to the efficiency, or "scale factor", to make the FullSim efficiency match the real data. Similar scale factors make the FastSim efficiency match the FullSim efficiency (both sets of scale factors are applied to make the FastSim match the real data). Scale factors are computed as a function of p_{T} and η on a per-lepton basis. The scale factors modify the event weights in simulation. Varying the scale factors within their uncertainties causes a small change in the event weights and, therefore, the simulated yields in each bin. The size of this change is taken as the uncertainty for the signal yield in that bin. This results in an approximately 3% uncertainty for each set of scale factors.

The full details of the b-tag (and mistag) scale factors are beyond the scope of this document, but are conceptually similar to those used for the leptons. Each jet carries its own scale factor which may depend on the jet flavor, p_{T}, η, and CSVv2 discriminator. These scale factors alter the weights of the events and thereby the yield in each bin. The change in the signal yield in each bin induced by varying the scale factors within their uncertainties gives the systematic uncertainty for that bin. The FastSim b-tagging uncertainties are the largest, reaching approximately 15% for the low $E_{\mathrm{T}}^{\mathrm{miss}}$ bins in signal models with large mass splitting.

The uncertainty due to the trigger efficiency is a flat 0.5% across all bins. This result is derived from studies of the trigger efficiency as a function of several kinematic variables, as in Figures 4.1, 4.2, 4.3, and 4.4.

The systematic uncertainty due to the jet energy corrections is computed by altering the jet momenta within their uncertainties. The event is then reconstructed using the modified jet momenta in order to propagate the changes into the other events variables (N_{jets}, N_{b}, M_J, $E_{\mathrm{T}}^{\mathrm{miss}}$, and m_{T}). The resulting changes in signal yields are assigned as systematic uncertainties.

The QCD scale systematic addresses potential differences between the kinematic properties of the signal at leading and next-to-leading order. While holding the overall cross-section fixed, the QCD renormalization and factorization scales [102] are each varied by a factor of two, in such a way that if one is multiplied by a factor of two, the other is never divided by two. The resulting changes in the signal yields give rise to a less than one percent uncertainty in each bin.

Like the QCD scale uncertainty, the ISR uncertainty addresses a theoretical uncertainty in the modeling of the signal rather than an experimental limitation. The ISR weights listed in Table 4.4 are varied within their uncertainties and the resulting change in signal yield taken as a systematic uncertainty. This uncertainty is largest in the $N_{\text{jets}} \geq 9$ bins, reaching approximately 15% for models with small mass splitting.

The FastSim signal samples do not properly model the variables needed for jet identification. Jets in simulated signal samples are therefore assumed to pass the jet identification requirements. The difference in efficiency is accounted for with a one percent uncertainty fully correlated across all bins.

The FastSim simulated samples are produced with fewer pileup vertices per event than are typically observed in the real data. The finite size of the simulated signal samples limits the precision with which one can probe the effects of this difference, so a conservative 10% to 15% uncertainty is assigned. The larger 15% uncertainty is assigned for the highest $E_{\text{T}}^{\text{miss}}$ and N_{jets} bins where the number of pileup vertices per event is typically higher.

A final 2.6% systematic uncertainty is assigned to account for the resolution with which CMS measures the integrated luminosity of the $35.9\,\text{fb}^{-1}$ data set.

Chapter 9

Results and Interpretations

Chapter 6 described an "ABCD" method for determining the standard model contributions to the observed events. Chapters 7 and 8 determined the systematic uncertainties associated with this procedure. In this chapter, we will use these ingredients to evaluate whether or not the dataset contains evidence of supersymmetry and how confident we are in this assesment. We first estimate the standard model background contribution and evaluate whether the observed yields are consistent with this background estimate in Sections 9.1 and 9.2. Next, we develop the statistical tools needed to test various SUSY models in Section 9.3, and apply those tools in Section 9.4. Finally, we provide a simplified version of the results in Section 9.5, which allows for easy reinterpretation in terms of other signal models not included in this dissertation.

9.1 Estimated Backgrounds

Figure 7.21 already showed that κ is near unity in the analysis regions (to within a few tens of percent, which is correctable using simulation), but it is useful to examine the M_J and m_{T} distributions in the real data in a bit more detail before applying the

background estimation procedure. Figure 9.1 shows the M_J distribution in six bins of $E_{\mathrm{T}}^{\mathrm{miss}}$ and N_{b}. Two distributions are shown for each bin, one for low-m_{T} events satisfying $m_{\mathrm{T}} \leq 140\,\mathrm{GeV}$ and one for high-m_{T} events satisfying $m_{\mathrm{T}} > 140\,\mathrm{GeV}$. For all six bins, the two distributions are similar. This is a stronger statement about the independence of M_J and m_{T} than the claim that $\kappa \approx 1$, which only requires the high-to-low M_J *ratios* be similar for the two samples, rather than the full distributions. The $200\,\mathrm{GeV} < E_{\mathrm{T}}^{\mathrm{miss}} \leq 350\,\mathrm{GeV}$ bins in the left column have the largest number of events, making it easiest to test the similarity of the M_J distributions in these bins. Conversely, the right column ($E_{\mathrm{T}}^{\mathrm{miss}} > 500\,\mathrm{GeV}$) and bottom row ($N_{\mathrm{b}} \geq 2$) have higher sensitivity to the presence of signal.

An even stronger demonstration of M_J-m_{T} independence can be found in Figure 9.2, which shows two-dimensional scatter plots of M_J and m_{T} in three bins of $E_{\mathrm{T}}^{\mathrm{miss}}$. The black dots show the observed events while the underlying color map shows the density of standard model background events in simulation for comparison. The red squares show a representative distribution of T1tttt signal events with $m_{\tilde{\mathrm{g}}} = 1800\,\mathrm{GeV}$ and $m_{\tilde{\chi}1}^{0} = 100\,\mathrm{GeV}$. Each square represents one expected event at an integrated luminosity of $35.9\,\mathrm{fb}^{-1}$. In all cases, events lying outside the visible M_J-m_{T} window are shown on the border of the plot. For the chosen signal model, most signal events lie in the highest $E_{\mathrm{T}}^{\mathrm{miss}}$ bin and in the signal region R4.

With the M_J and m_{T} distributions available, the next step is to carry out the background estimation procedure described in Chapter 6. The results of the maximum likelihood background estimation are shown in Table 9.1. The T1tttt columns show the expected signal yield in each bin for two selected models at their nominal cross-sections. They are meant only to indicate which bins would be sensitive to particular models; they do not imply the presence of signal in the observed data.

The rest of the table contains two different sets of fit results, one from the *predictive fit*

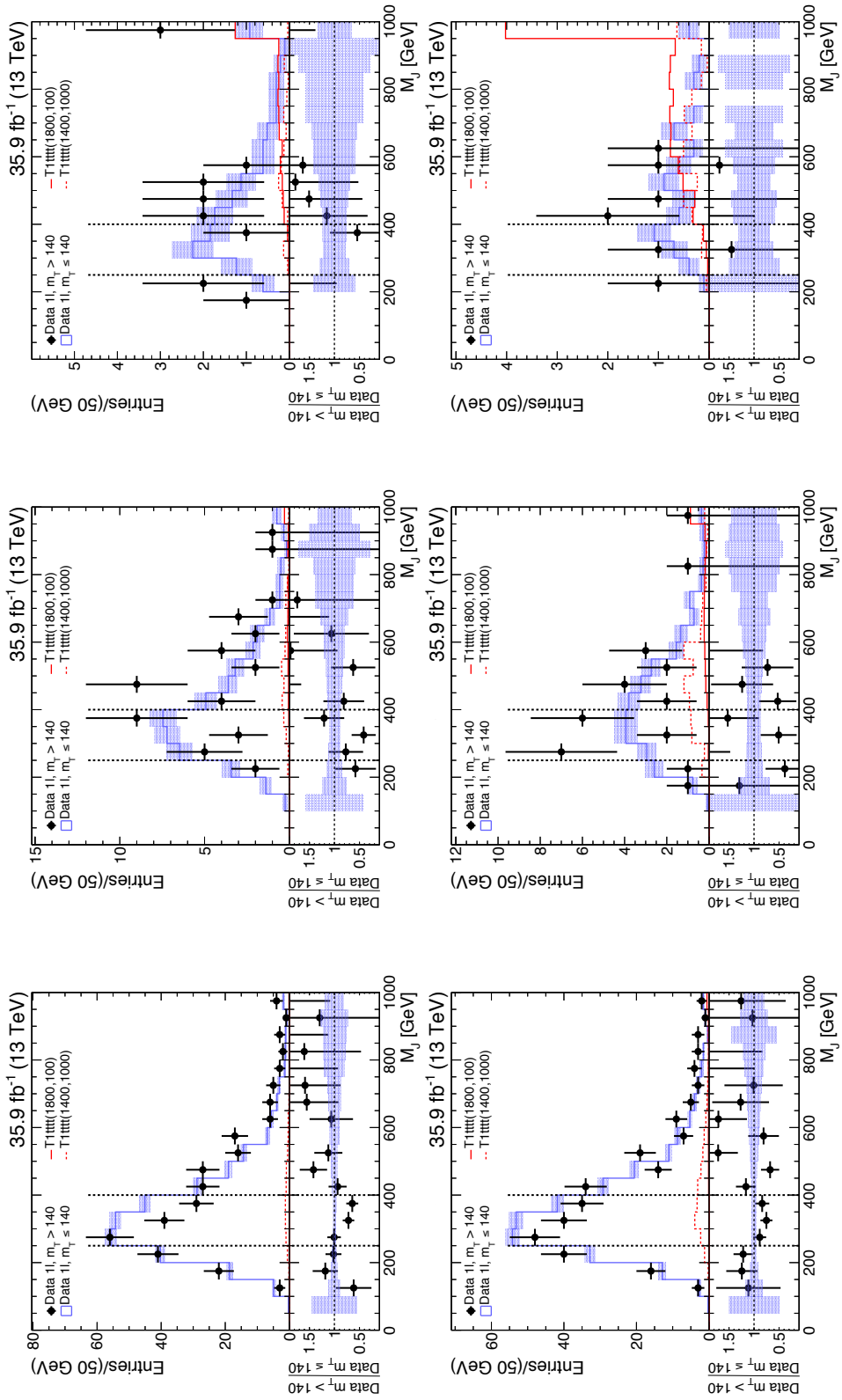

Figure 9.1: M_J distribution in bins of $E_{\mathrm{T}}^{\mathrm{miss}}$ (left-to-right: 200 GeV $< E_{\mathrm{T}}^{\mathrm{miss}} \leq$ 350 GeV, 350 GeV $< E_{\mathrm{T}}^{\mathrm{miss}} \leq$ 500 GeV, $E_{\mathrm{T}}^{\mathrm{miss}} >$ 500 GeV) and N_{b} ($N_{\mathrm{b}} = 1$ in top row, $N_{\mathrm{b}} \geq 2$ in bottom row). The black points show the M_J distribution for events with $m_{\mathrm{T}} >$ 140 GeV. The blue line shows the corresponding distribution for events with $m_{\mathrm{T}} \leq$ 140 GeV, normalized to have the same integral as the low-m_{T} distribution. In all $E_{\mathrm{T}}^{\mathrm{miss}}$ and N_{b} bins, the distributions are similar. Figure from Reference [13].

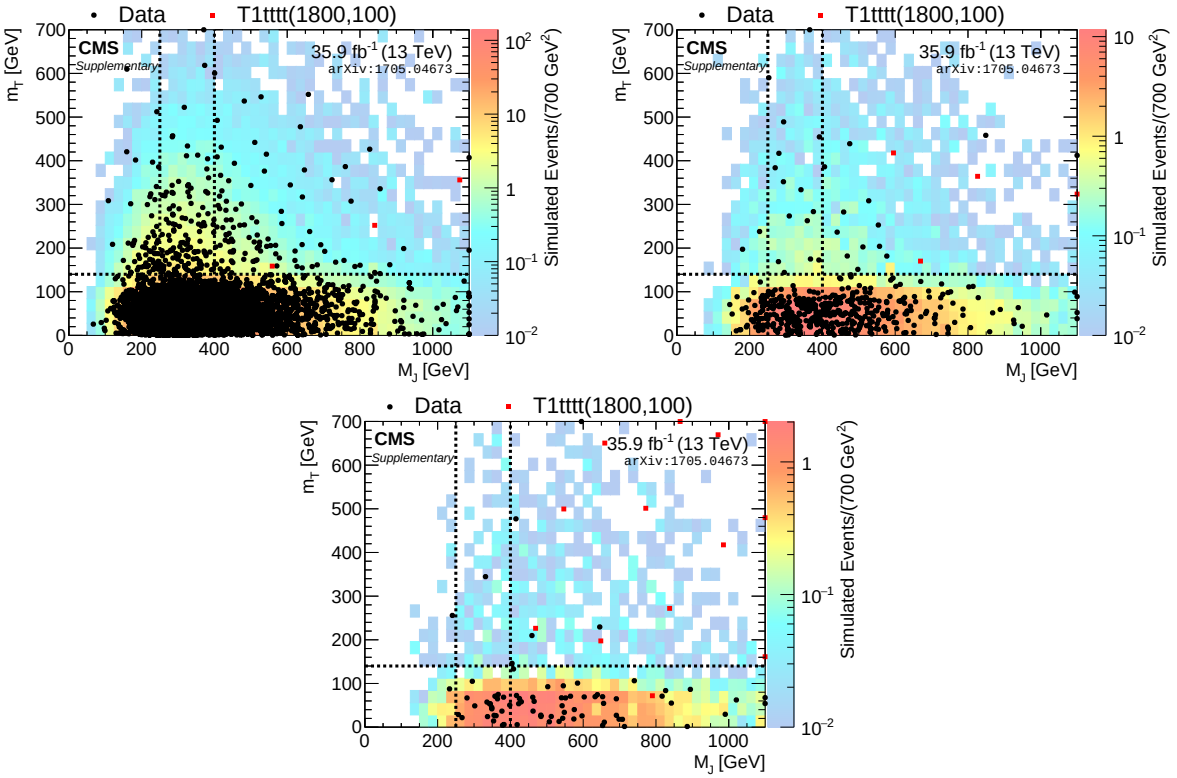

Figure 9.2: Two-dimensional scatter plot showing M_J and m_{T} for the observed events satisfying $200\,\mathrm{GeV} < E_{\mathrm{T}}^{\mathrm{miss}} \leq 350\,\mathrm{GeV}$ (top left), $350\,\mathrm{GeV} < E_{\mathrm{T}}^{\mathrm{miss}} \leq 500\,\mathrm{GeV}$ (top right), and $E_{\mathrm{T}}^{\mathrm{miss}} > 500\,\mathrm{GeV}$ (bottom). The underlying color map indicates the weighted density of events in simulation. The red squares show a representative sample of points from a selected signal model, T1tttt(1800,100), normalized such that each square corresponds to one event at an integrated luminosity of $35.9\,\mathrm{fb}^{-1}$. Figure from supplementary technical material for Reference [11].

Table 9.1: Estimated backgrounds with fixed $r = 0$. Results are independent of signal model, but two T1tttt columns give a sense of which bins would be sensitive to the presence of signal. The $\hat{\kappa}$ columns include systematic uncertainty. The two values are from the predictive fit (R4 bins not included in the likelihood) and global fit (all bins included). Predictive and global background estimates are shown along with expected yields from simulation. Observed yields are consistent with background estimates. Table in part from supplementary material for Reference [11].

	T1tttt		$\hat{\kappa}$		Background			
Bin	(1800,100)	(1400,1000)	Pred. Fit	Glob. Fit	Sim.	Pred. Fit	Glob. Fit	Obs.
$200\,\text{GeV} < E_\text{T}^\text{miss} \leq 350\,\text{GeV}$								
R1: All N_jets, N_b	0.0	9.1			5662.6		4753.4 ± 68.3	4761
R2: $6 \leq N_\text{jets} \leq 8$, $N_\text{b} = 1$	0.1	1.2			1814.9		1354.9 ± 35.9	1353
R2: $6 \leq N_\text{jets} \leq 8$, $N_\text{b} = 2$	0.3	2.1			1140.9		916.7 ± 29.4	910
R2: $6 \leq N_\text{jets} \leq 8$, $N_\text{b} \geq 3$	0.3	1.7			229.1		210.4 ± 13.9	214
R2: $N_\text{jets} \geq 9$, $N_\text{b} = 1$	0.1	1.0			192.0		129.5 ± 11.0	127
R2: $N_\text{jets} \geq 9$, $N_\text{b} = 2$	0.1	2.0			153.1		119.1 ± 10.5	118
R2: $N_\text{jets} \geq 9$, $N_\text{b} \geq 3$	0.2	3.1			45.7		32.1 ± 5.4	33
R3: All N_jets, N_b	0.1	12.5			282.0		254.6 ± 14.9	247
R4: $6 \leq N_\text{jets} \leq 8$, $N_\text{b} = 1$	0.4	1.9	1.2 ± 0.2	1.4 ± 0.1	109.5	84.6 ± 14.3	104.1 ± 7.2	106
R4: $6 \leq N_\text{jets} \leq 8$, $N_\text{b} = 2$	0.6	3.0	1.2 ± 0.2	1.4 ± 0.1	66.7	55.1 ± 9.3	68.3 ± 4.9	75
R4: $6 \leq N_\text{jets} \leq 8$, $N_\text{b} \geq 3$	0.6	2.2	1.5 ± 0.2	1.7 ± 0.2	16.8	16.4 ± 3.0	19.6 ± 1.9	16
R4: $N_\text{jets} \geq 9$, $N_\text{b} = 1$	0.2	1.6	1.0 ± 0.2	1.2 ± 0.2	9.5	6.5 ± 1.5	8.5 ± 1.3	11
R4: $N_\text{jets} \geq 9$, $N_\text{b} = 2$	0.3	2.1	1.2 ± 0.3	1.6 ± 0.3	9.5	7.6 ± 1.9	9.9 ± 1.7	11
R4: $N_\text{jets} \geq 9$, $N_\text{b} \geq 3$	0.4	3.1	1.4 ± 0.3	1.7 ± 0.3	3.1	2.3 ± 0.7	2.9 ± 0.6	2
$350\,\text{GeV} < E_\text{T}^\text{miss} \leq 500\,\text{GeV}$								
R1: All N_jets, N_b	0.0	1.0			529.3		413.7 ± 20.2	412
R2: $6 \leq N_\text{jets} \leq 8$, $N_\text{b} = 1$	0.2	0.4			352.0		231.3 ± 14.8	226
R2: $6 \leq N_\text{jets} \leq 8$, $N_\text{b} = 2$	0.2	0.7			198.7		150.7 ± 11.9	155
R2: $6 \leq N_\text{jets} \leq 8$, $N_\text{b} \geq 3$	0.2	0.5			40.2		34.2 ± 5.6	37
R2: $N_\text{jets} \geq 9$, $N_\text{b} = 1$	0.1	0.7			31.8		15.5 ± 3.8	15
R2: $N_\text{jets} \geq 9$, $N_\text{b} = 2$	0.1	1.0			24.0		25.1 ± 4.9	25
R2: $N_\text{jets} \geq 9$, $N_\text{b} \geq 3$	0.2	1.0			7.2		6.4 ± 2.4	7
R3: All N_jets, N_b	0.1	2.3			31.6		30.3 ± 4.8	32
R4: $6 \leq N_\text{jets} \leq 8$, $N_\text{b} = 1$	0.7	1.1	1.0 ± 0.3	1.2 ± 0.2	20.9	17.4 ± 6.6	19.6 ± 3.0	25
R4: $6 \leq N_\text{jets} \leq 8$, $N_\text{b} = 2$	0.9	1.3	1.1 ± 0.4	1.3 ± 0.3	13.2	13.7 ± 5.3	14.2 ± 2.3	10
R4: $6 \leq N_\text{jets} \leq 8$, $N_\text{b} \geq 3$	0.8	0.9	1.3 ± 0.4	1.5 ± 0.3	3.1	3.8 ± 1.6	3.8 ± 0.8	1
R4: $N_\text{jets} \geq 9$, $N_\text{b} = 1$	0.3	1.0	1.1 ± 0.4	1.3 ± 0.3	2.1	1.3 ± 0.6	1.5 ± 0.5	2
R4: $N_\text{jets} \geq 9$, $N_\text{b} = 2$	0.5	1.1	0.8 ± 0.3	1.0 ± 0.3	1.2	1.6 ± 0.8	1.9 ± 0.6	2
R4: $N_\text{jets} \geq 9$, $N_\text{b} \geq 3$	0.7	2.1	1.2 ± 0.5	1.4 ± 0.4	0.5	0.6 ± 0.4	0.6 ± 0.3	0
$E_\text{T}^\text{miss} > 500\,\text{GeV}$								
R1: All N_jets, N_b	0.1	0.4			72.8		70.9 ± 8.2	74
R2: $6 \leq N_\text{jets} \leq 8$, $N_\text{b} = 1$	0.5	0.4			123.7		72.9 ± 8.3	71
R2: $6 \leq N_\text{jets} \leq 8$, $N_\text{b} = 2$	0.6	0.4			56.2		33.0 ± 5.5	32
R2: $6 \leq N_\text{jets} \leq 8$, $N_\text{b} \geq 3$	0.5	0.3			10.4		9.7 ± 2.9	10
R2: $N_\text{jets} \geq 9$, $N_\text{b} = 1$	0.2	0.4			8.7		9.1 ± 2.9	8
R2: $N_\text{jets} \geq 9$, $N_\text{b} = 2$	0.3	0.7			6.8		4.6 ± 2.1	5
R2: $N_\text{jets} \geq 9$, $N_\text{b} \geq 3$	0.6	0.8			1.3		0.8 ± 0.8	1
R3: All N_jets, N_b	0.3	0.5			4.5		5.1 ± 1.5	2
R4: $6 \leq N_\text{jets} \leq 8$, $N_\text{b} = 1$	2.5	0.6	1.0 ± 0.3	1.2 ± 0.2	7.5	1.9 ± 1.5	6.1 ± 1.6	8
R4: $6 \leq N_\text{jets} \leq 8$, $N_\text{b} = 2$	3.6	1.0	1.0 ± 0.4	1.2 ± 0.3	3.6	0.9 ± 0.7	3.0 ± 0.9	4
R4: $6 \leq N_\text{jets} \leq 8$, $N_\text{b} \geq 3$	3.2	0.4	1.5 ± 0.6	1.8 ± 0.5	1.0	0.4 ± 0.4	1.3 ± 0.5	1
R4: $N_\text{jets} \geq 9$, $N_\text{b} = 1$	1.0	0.7	1.0 ± 0.4	1.4 ± 0.4	0.6	0.2 ± 0.2	0.9 ± 0.4	2
R4: $N_\text{jets} \geq 9$, $N_\text{b} = 2$	1.8	1.2	1.0 ± 0.4	1.2 ± 0.4	0.4	0.1 ± 0.1	0.4 ± 0.2	0
R4: $N_\text{jets} \geq 9$, $N_\text{b} \geq 3$	2.3	1.7	3.1 ± 1.5	3.7 ± 1.5	0.2	0.1 ± 0.1	0.2 ± 0.2	0

and one from the *global fit*. In both cases, the signal strength parameter r is fixed to zero to perform a background-only fit that does not depend on particular signal model. For the global fit, the likelihood function in Equation (6.18) is maximized over all parameters (except the fixed $r = 0$). The predictive fit is similar, except that the Poisson factors corresponding to R4 bins are omitted from the L^{data} part of the likelihood function. Since the modified likelihood is independent of the observed R4 yields, it can be used in a truly predictive manner before examining the signal region yields. While the global fit is over-constrained (there are 18 more observations than parameters, corresponding to the 18 R4 bins), the predictive fit has the same number of parameters as observables. This means that for any observed yields in the control regions R1, R2, and R3, there exists some way to set the fit parameters λ_i, $[R(M_J)]_{i,j}$, and $[R(m_{\text{T}})]_i$ such that the expected background yields from the predictive fit perfectly match those observed yields. The estimated background in these bins is therefore omitted from the table for the predictive fit. This simplifies the interpretation of the results somewhat, as one only needs to check the 18 R4 bins for compatibility with the predicted background instead of all 42 bins.

On the other hand, the omission of R4 bins from the likelihood means that the signal strength parameter r cannot be allowed to float without making the predictive fit under-constrained. Testing of particular signal models, as done later in Section 9.4, will therefore require the use of the global fit.

The $\hat{\kappa}$ values in the next columns are computed from the fitted background yields, including the effects of all of the nuisance parameters. Since the predictive fit is not over-constrained, the $\hat{\kappa}$ values obtained from the predictive fit match those computed directly from the simulation shown in Figure 7.1.

Three different estimates of the expected background yield are included in the table: the values obtained directly from simulation without any fit, and the results from both the predictive and global fits. The fitted background yields are consistent with the observed

yields in the rightmost column.

A graphical depiction of the comparison with the global fit can be found in Figure 9.3. The observed yields are shown as black dots, while the fitted background is shown as a filled histogram. The partitioning of the fitted background into two components ($t\bar{t}$+jets in blue and other background processes in green) is done by taking the fraction of events coming from $t\bar{t}$ + jets processes from simulation, and is meant only to give a rough sense of the background composition rather than to convey any particular knowledge obtained from the fit. Although the fit used to produce the plot has fixed $r = 0$, the expected signal yield for the T1tttt(1800,100) model is shown stacked on top of the background as a dashed red line. Note that if the signal strength r were allowed to float, the fitted background shape would change slightly, so a fit with $\hat{r} = 1$ would appear slightly different in such a plot. Nonetheless, the dashed red line provides a rough guide to where signal events could lie.

Of course, one cannot fully interpret the results without knowing the correlations among the uncertainties in the estimated backgrounds for different bins. The correlation matrices for the predictive and global fit results are shown in Figures 9.4 and 9.5, respectively. For the predictive fit, the R4 background estimates within each $E_{\mathrm{T}}^{\mathrm{miss}}$ plane are highly correlated, particular for the $E_{\mathrm{T}}^{\mathrm{miss}} > 500\,\mathrm{GeV}$ bins. This correlation due to the low yields in the R3 bins, which causes a large uncertainty in the $R(m_{\mathrm{T}})$ parameters. Since the expected R4 yields are all proportional to $R(m_{\mathrm{T}})$, this induces a large correlation. There is also a correlation across the $E_{\mathrm{T}}^{\mathrm{miss}}$ planes for bins with similar N_{jets} requirements. This is caused by the relatively large 16% and 41% systematic uncertainties assigned from the dilepton control sample, which are correlated across bins with the same N_{jets} range.

The correlation matrix for the global fit, shown in Figure 9.5, contains similar patterns, but the correlation coefficients are typically closer to zero. The incorporation of

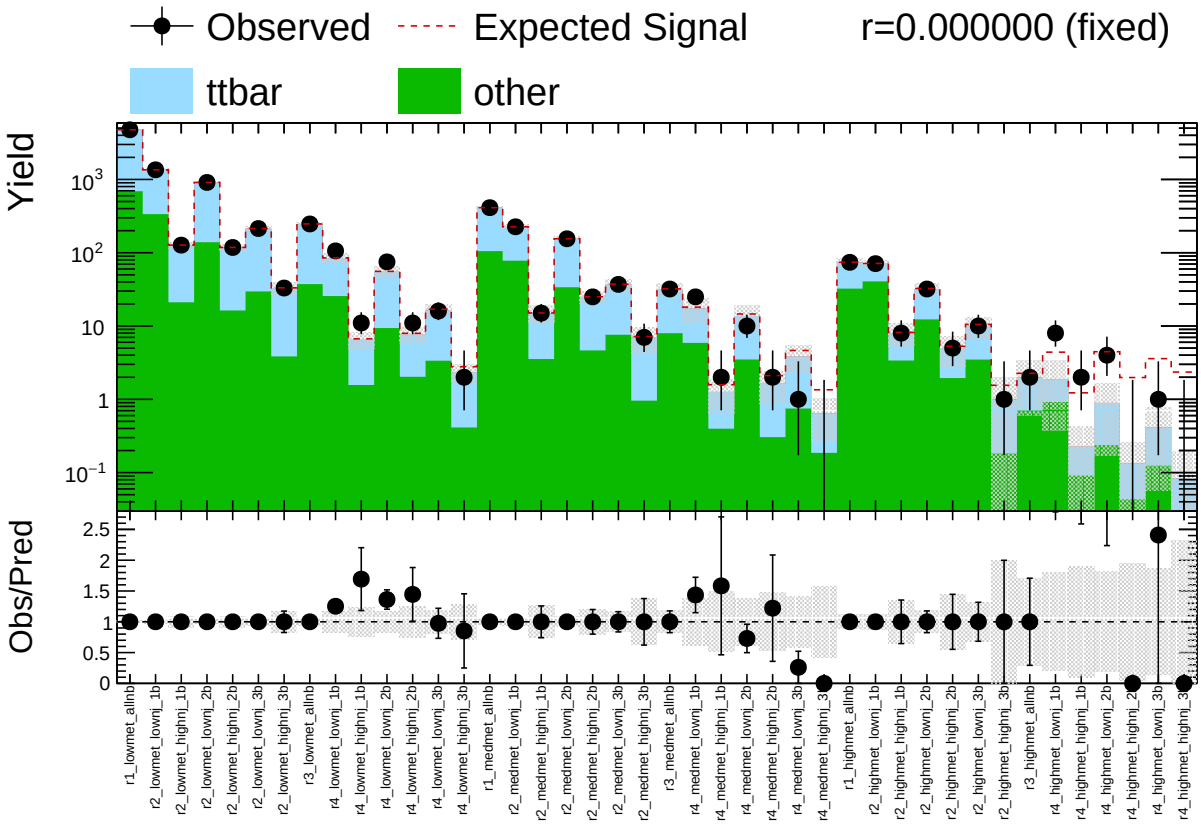

Figure 9.3: Graphical representation of the global fit results shown in Table 9.1. The observed yields are shown as black dots, while the fitted background is shown as a filled histogram. The partitioning of the fitted background into two components ($t\bar{t}$ + jets in blue and other background in green) is done by taking the fraction of events coming from $t\bar{t}$ + jets processes from simulation, and is meant only to give a rough sense of the background composition rather than to convey any particular knowledge obtained from the fit. Although the fit used to produce the plot has fixed $r = 0$, the expected signal yield for the T1tttt(1800,100) process is shown stacked on top of the background as a dashed red line. Figure from Reference [13].

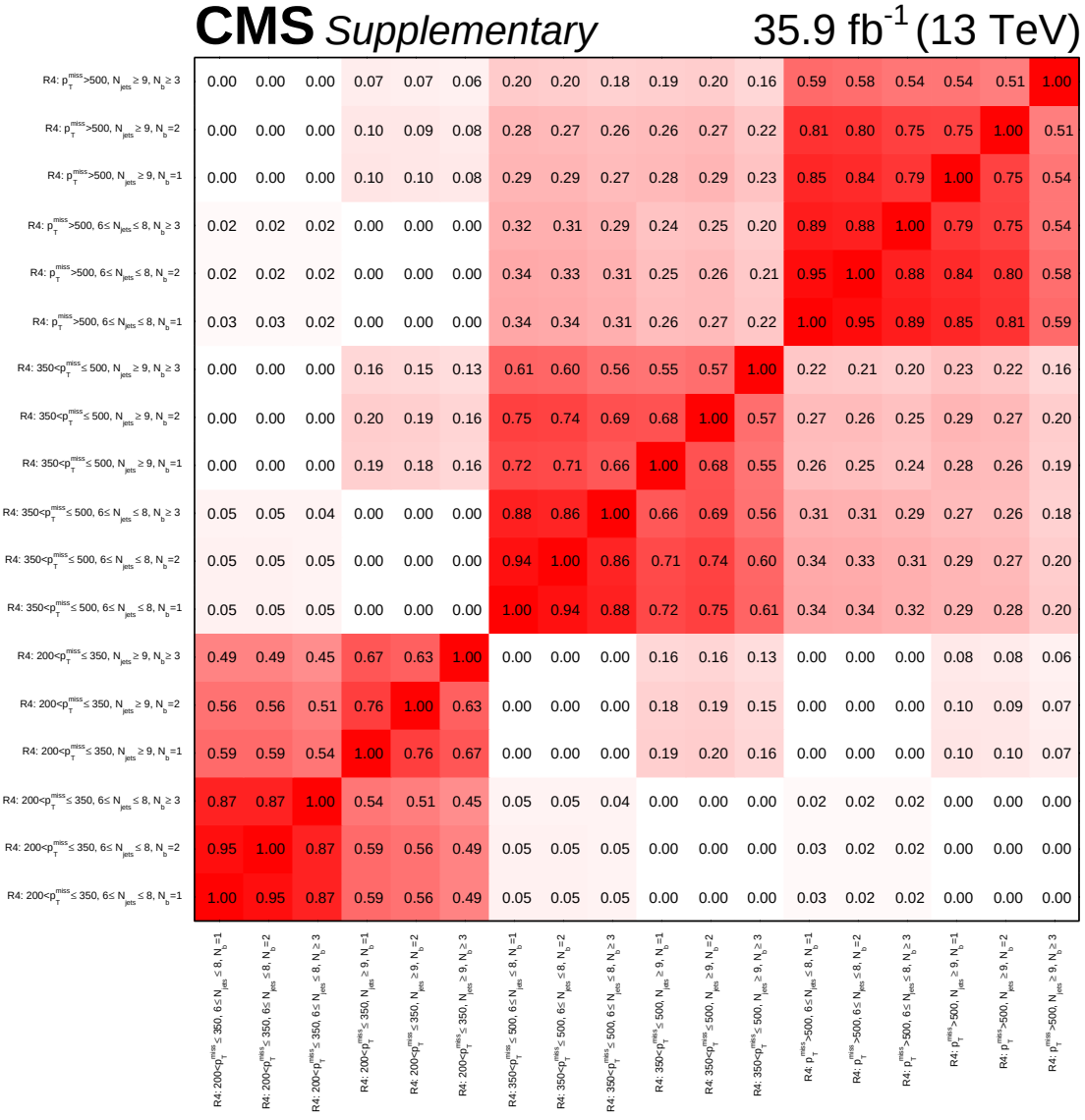

Figure 9.4: Correlation matrix for the background estimates produced by the predictive fit. The covariance matrix can be obtained using the uncertainties listed in the "Pred. Fit" background column of Table 9.1. Figure from supplementary material for Reference [11].

the R4 bins in the likelihood function provides additional information about the $R(m_{\mathrm{T}})$ parameter, reducing its uncertainty and therefore the correlation for different R4 bins within a $E_{\mathrm{T}}^{\mathrm{miss}}$ range. The correlation matrix for the global fit also includes the R1, R2, and R3 bins. There is a negative correlation between the expected background yields in the R2 bins and the R4 bins of the same $E_{\mathrm{T}}^{\mathrm{miss}}$ range. This anti-correlation is again due mainly to the uncertainty in $R(m_{\mathrm{T}})$. Increasing $R(m_{\mathrm{T}})$ (and therefore the expected R4 background yields) causes a decrease in the expected R2 background yields. Uncertainty in the $R(M_J)$ parameter means that the estimated background yield for a particular R2 bin is positively correlated with that of the corresponding R4 bin, producing the off-diagonal red stripes in Figure 9.5.

The covariance matrices can be obtained by scaling the correlation matrix rows and columns by the square root of the corresponding uncertainties in the fitted background columns in Table 9.1.

9.2 Simple Interpretation of Results

While the background estimations in Table 9.1 and the correlation matrices in Figures 9.4 and 9.5 are sufficient to get an approximate measure of whether the observed yields are consistent with the estimated background yields, there is a better approach. In order to estimate the ABCD parameters, we maximize the likelihood function over all possible parameter values. While the value of the likelihood function at its maximum is not particularly useful by itself, the relative values of the likelihood function for different parameter values are very informative.

Wilks' Theorem [103] states that, for a null hypothesis which is a special case of an

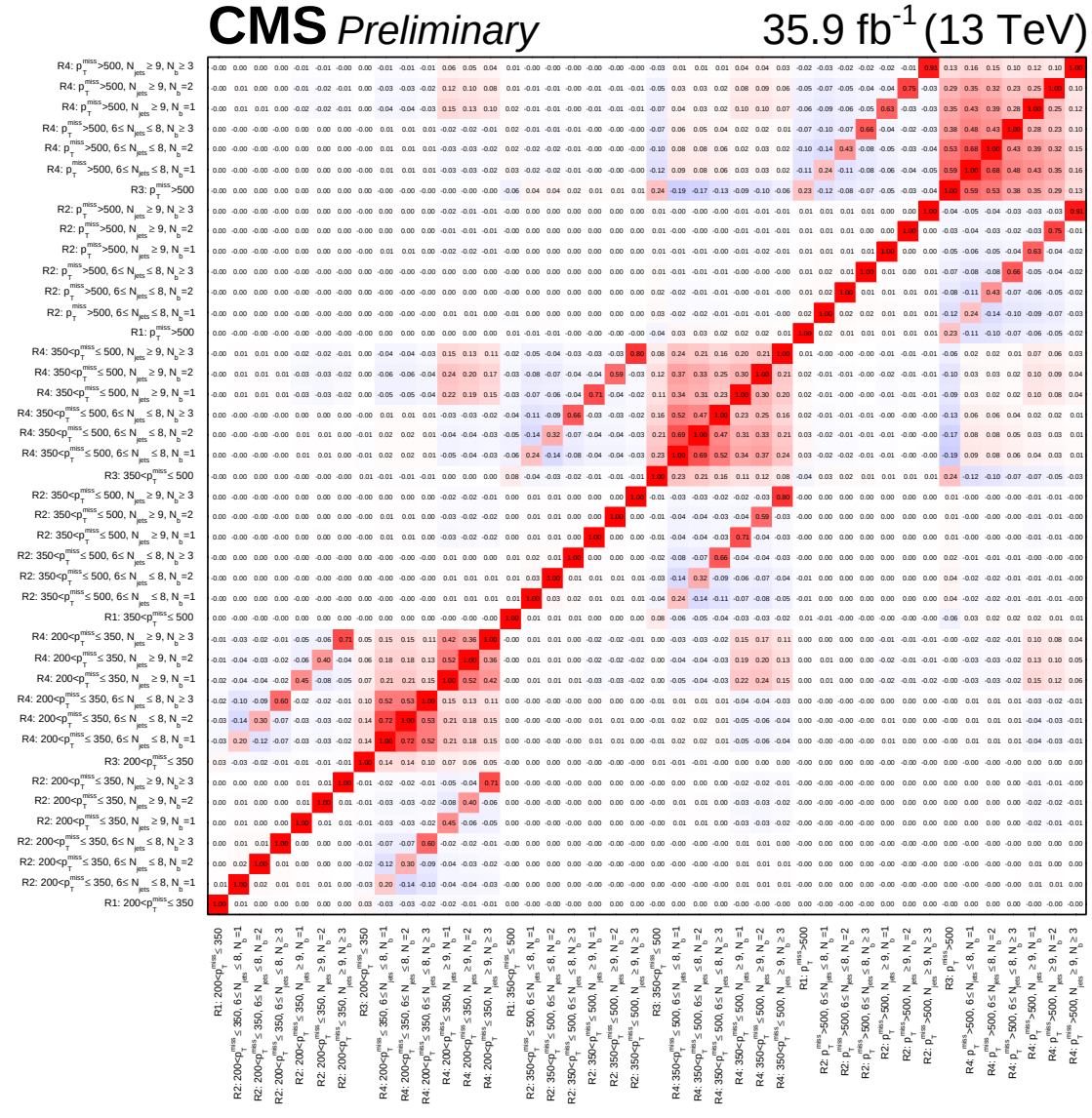

Figure 9.5: Correlation matrix for the background estimates produced by the global fit. The covariance matrix can be obtained using the uncertainties listed in the "Glob. Fit" background column of Table 9.1. Figure from supplementary material for Reference [11].

alternative hypothesis, the likelihood ratio

$$q = -2 \ln \left[\frac{L(\text{null})}{L(\text{alternative})} \right] \tag{9.1}$$

is approximately χ^2-distributed with a number of degrees of freedom equal to the difference in the number of free parameters in the alternative and null models. A detailed explanation of the conditions required for this approximation to hold are beyond the scope of this thesis, but it is important that the fitted parameter values for the two models are far from any bounds.

Wilks' Theorem provides a means of testing the consistency of the fit results with observation. The global fit with fixed $r = 0$ will serve as the null hypothesis. As a model-independent alternative hypothesis, we may assume that the yields in each of the 42 bins are Poisson distributed with independent mean yield parameters. To ensure that the normalization of the alternative likelihood is correct, the 42 Poisson functions must be multiplied by the same L^{syst} as appears in Equation Eq. (6.18). Allowing each bin to have its own Poisson parameter produces a saturated model with 18 free parameters more than the ABCD model. Assuming that Wilks' Theorem holds, the test statistic $q \approx 18.9$ and corresponds to a p-value of $p = 0.40$.

The likelihood ratio can be factored into contributions from each bins (and a ratio of L^{syst} contributions). This allows an estimation of the contribution of each bin to the significance, as shown in Figure 9.6. The values in each of the bins (including the systematic uncertainty contribution) sum to the total $q \approx 18.9$ for the 42 bins. Bins with a higher value in this plot give larger contributions to the significance, or put another way, lower the p-value by a larger amount. Note that using the saturated model as an alternative hypothesis mean that any deviation from the estimated background is interpreted as "signal," even if the observed yield is lower than the estimated background.

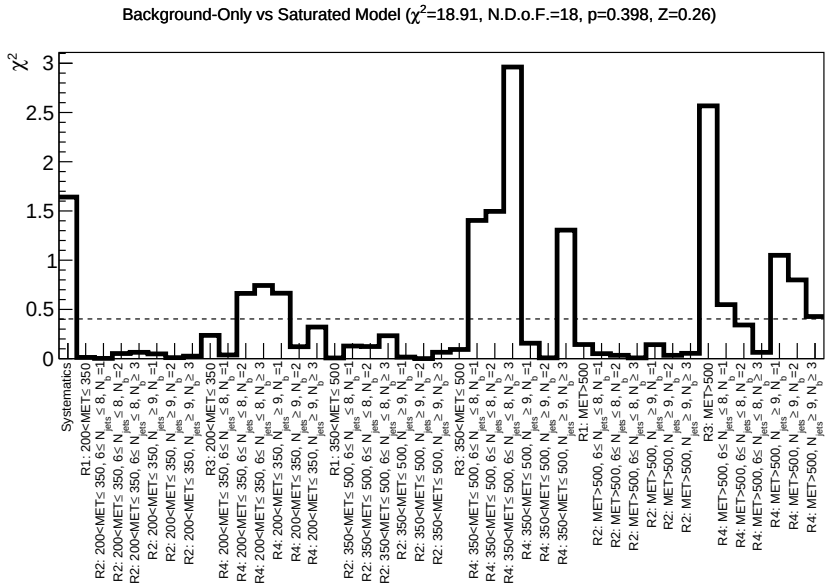

Figure 9.6: Contributions of the 42 bins (and one systematic uncertainty factor) to the approximately χ^2-distributed test-statistic q from Equation (9.1). The null hypothesis is the usual background-only fit with fixed $r = 0$. The alternative hypothesis used for comparison is a saturated model in which each bin is allowed to have an independent Poisson mean parameter. The horizontal line shows the median expected significance per bin in the absence of signal. If the significance contribution from each bin were set to this value, one would obtain $p = 0.5$.

The horizontal dashed line shows the median expected significance per bin in the absence of signal. If the significance contribution from each bin were set to this value, one would obtain $p = 0.5$.

The same technique used to find a model-agnostic p-value can also be used to interpret the results in terms of specific signal models. Instead of using a saturated model as the alternative, the signal strength parameter r is allowed to float. This trivially makes the alternative an extension of the background-only null hypothesis, such that the resulting test statistic q should be chi-squared distributed with one degree of freedom. The resulting test statistic of course depends on the choice of signal model. Using a specific signal model does introduce one additional complication: the significance contribution from a bin may be negative. This occurs when fitting the signal strength r causes the expected yield for that bin to move farther from the observed yield (despite improving the fit overall when all bins are included).

Figures 9.7, 9.8, and 9.9 provide some insight into the relative importance of the various bins for the T1tttt(1800,100), T1tttt(1400,1000), and T1tttt(1300,1075) models, respectively. For the T1tttt(1800,100) model, which has a large mass splitting, the high-$E_{\mathrm{T}}^{\mathrm{miss}}$ bins have the largest contributions to q. Checking Table 9.1 confirms that these bins have the largest T1tttt(1800,100) signal yields. For the T1tttt(1400,1000) model, the lower $E_{\mathrm{T}}^{\mathrm{miss}}$ bins become more important, but the largest contributions remain concentrated at high N_{jets}. Again, the largest significance contributions come from the bins with the largest expected number of signal events. For the T1tttt(1300,1075) model, which has very small mass splitting, it is hard to decipher a pattern. Low multiplicity bins in the medium $E_{\mathrm{T}}^{\mathrm{miss}}$ bins have the largest significance contributions.

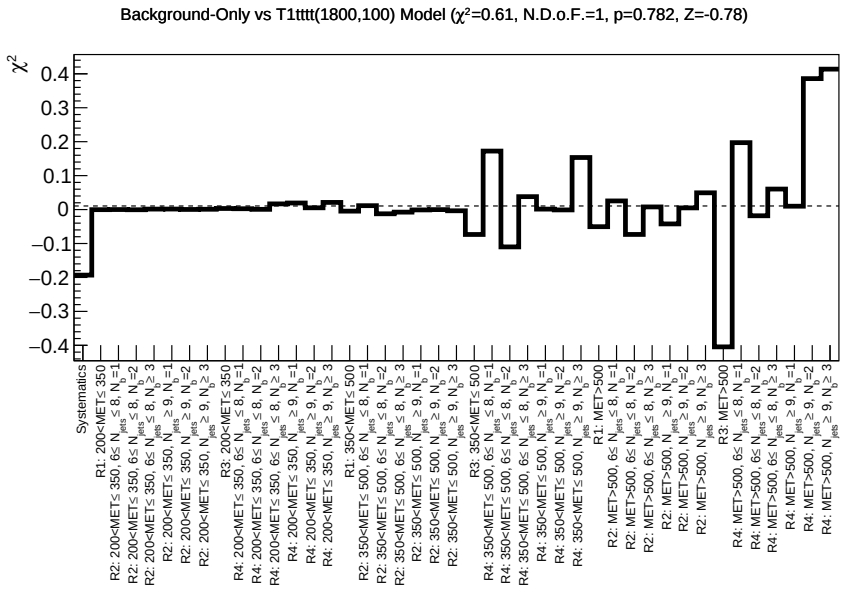

Figure 9.7: Contributions of the 42 bins (and one systematic uncertainty factor) to the approximately chi-square distributed test-statistic q from Equation (9.1). The null hypothesis is the usual background-only fit with fixed $r = 0$. The alternative hypothesis used for comparison has a floating r and uses T1tttt(1800,100) for the signal shape.

9.3 Statistical Methods

The test statistic q as defined in Equation (9.1) has a few shortcomings that make it unsuitable for direct use in setting cross-section limits or estimating the significance of a possible excess. For these tasks, we need to make some slight changes to q. To illustrate the modified test statistic, consider a simple one bin counting experiment with no systematic uncertainties. Further, suppose that the expected background $B = 10^6$ and the expected signal at the nominal cross-section $S = 3 \times 10^3$. The large yields ensure that the necessary conditions for Wilks' Theorem will hold and that the discreteness of the Poisson distribution will not be relevant. It will be useful to have a separate test

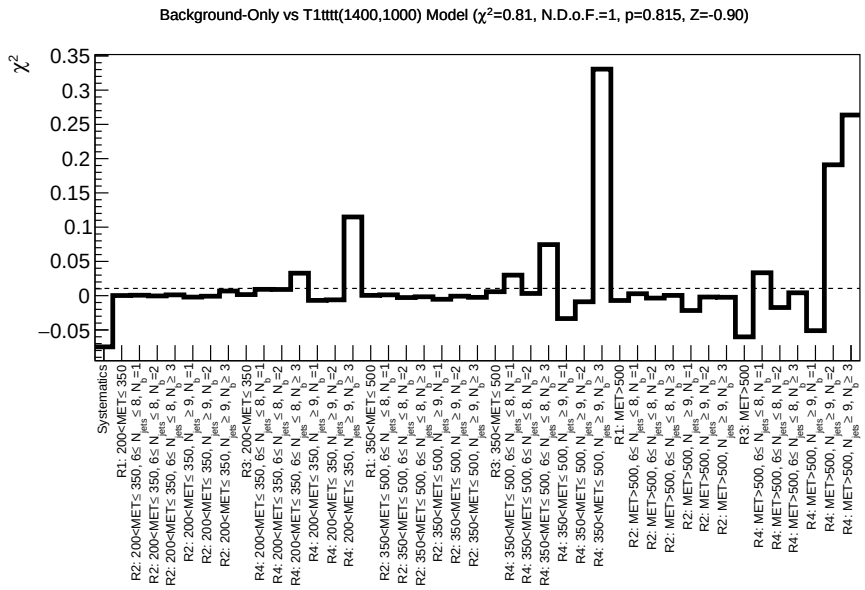

Figure 9.8: Contributions of the 42 bins (and one systematic uncertainty factor) to the approximately chi-square distributed test-statistic q from Equation (9.1). The null hypothesis is the usual background-only fit with fixed $r = 0$. The alternative hypothesis used for comparison has a floating r and uses T1tttt(1400,1000) for the signal shape.

statistic for each r being tested:

$$q_r = -2 \ln \left[\frac{\text{Pois}(N = N_{\text{obs}} | \mu = B + rS)}{\text{Pois}(N = N_{\text{obs}} | \mu = B + \hat{r}S)} \right]. \tag{9.2}$$

As usual, $\hat{r}$ is the maximum likelihood estimator of r. q_0 and q_1 represent test statistics for the background-only ($r = 0$) and signal hypotheses ($r = 1$). Both are shown as a function of the observed yield N_{obs} in Figure 9.10. Smaller values of q_r represent a better fit, while larger values represent a worse fit, with the minimum at $q_r = 0$ by construction. Note that q_0 grows for values of $N_{\text{obs}} < B$, and q_1 grows for values of $N_{\text{obs}} > B+S$. This is not desirable, as the background-only hypothesis is penalized for downward fluctuations and the signal hypothesis penalized for upward fluctuations.

The right plot in Figure 9.10 shows the distributions of the test statistic in the case of

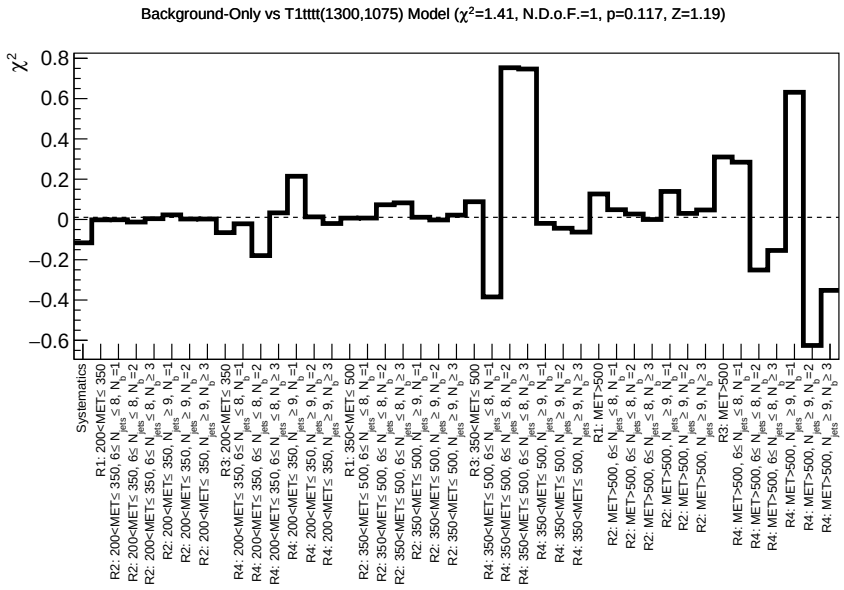

Figure 9.9: Contributions of the 42 bins (and one systematic uncertainty factor) to the approximately chi-square distributed test-statistic q from Equation (9.1). The null hypothesis is the usual background-only fit with fixed $r = 0$. The alternative hypothesis used for comparison has a floating r and uses T1tttt(1300,1075) for the signal shape.

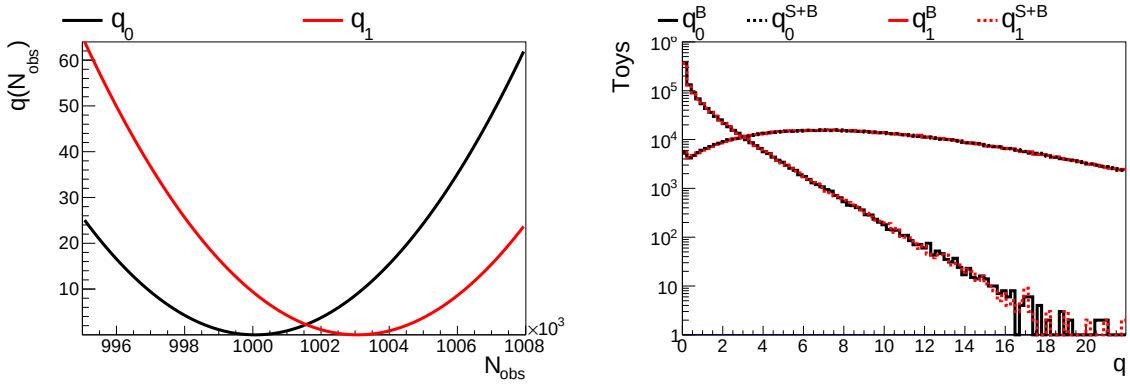

Figure 9.10: Left: The unbounded test statistic q_r from Equation (9.2) as a function of the observed yield N_{obs} for a single bin counting experiment model with a mean expected background yield of 10^6, a mean expected signal yield of 3×10^3, and no systematic uncertainties. The test statistic is shown for $r = 0$ and $r = 1$. Right: The distribution of the test statistics ($r = 0$ in black, $r = 1$ in red) for a background-only scenario (solid) and signal-plus-background scenario (dashed).

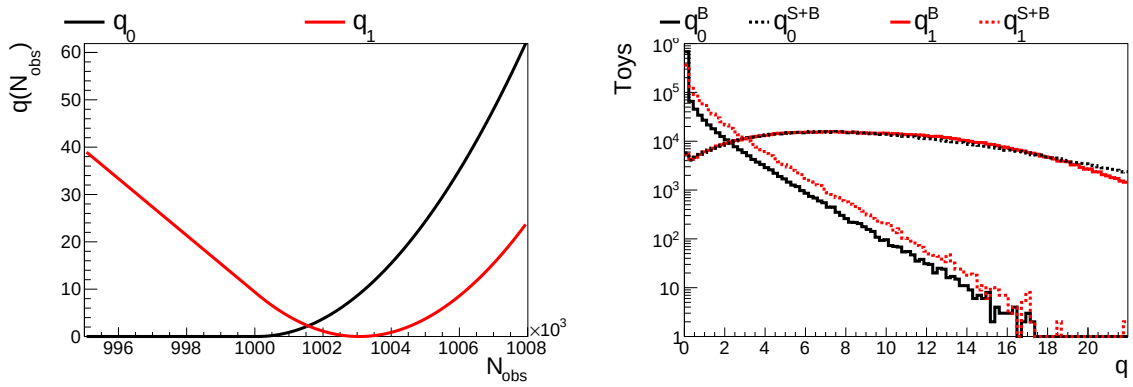

Figure 9.11: Left: The test statistic $q_{r,\text{sig}}$ from Equation (9.3) as a function of the observed yield N_{obs} for a single bin counting experiment model with a mean expected background yield of 10^6, a mean expected signal yield of 3×10^3, and no systematic uncertainties. The test statistic is shown for $r = 0$ and $r = 1$. Right: The distribution of the test statistics ($r = 0$ in black, $r = 1$ in red) for a background-only scenario (solid) and signal-plus-background scenario (dashed). The test statistic $q_{0,\text{sig}}$ has a known distribution in the absence of signal and is used to compute discovery significance.

a background only or signal-plus-background scenario. Note that the subscripts denote the hypothesized signal strengths and the superscripts the true signal strengths. When the hypothesized and true signal strengths are equal, the distribution of the test statistic is approximately chi-squared.

To prevent downward fluctuations from penalizing the background-only hypothesis, one can restrict $\hat{r}$ to non-negative values and obtain the modified test statistic

$$q_{r,\text{sig}} = -2 \ln \left[\frac{\text{Pois}(N = N_{\text{obs}} | \mu = B + rS)}{\text{Pois}(N = N_{\text{obs}} | \mu = B + \hat{r}S)} \right], \qquad \hat{r} \geq 0 \tag{9.3}$$

shown in Figure 9.11. In case of a downward fluctuation, the test statistic $q_{0,\text{sig}}$ is unchanged. While $q_{0,\text{sig}}$ is not chi-square distributed in the absence of signal, its asymptotic distribution still has a known analytic form [104, 105]. Since the p-value can be obtained quickly and easily from this asymptotic distribution, we use the test statistic $q_{0,\text{sig}}$ to evaluate discovery significance.

To prevent upward fluctuations from penalizing the signal hypothesis, one can further

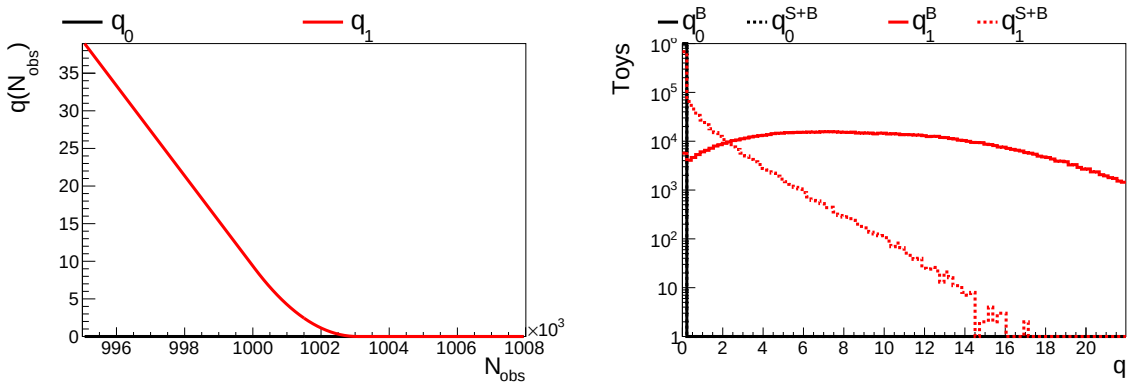

Figure 9.12: Left: The test statistic $q_{r,\text{lim}}$ from Equation (9.4) as a function of the observed yield N_{obs} for a single bin counting experiment model with a mean expected background yield of 10^6, a mean expected signal yield of 3×10^3, and no systematic uncertainties. The test statistic is shown for $r = 0$ and $r = 1$. Right: The distribution of the test statistics ($r = 0$ in black, $r = 1$ in red) for a background-only scenario (solid) and signal-plus-background scenario (dashed). The $q_{r,\text{lim}}$ are used to compute CL_s upper limits. Note that $q_{0,\text{lim}}$ is identically zero.

restrict the maximum likelihood signal strength $\hat{r}$ to values no greater than the tested r. This produces the test statistic

$$q_{r,\text{lim}} = -2 \ln \left[\frac{\text{Pois}(N = N_{\text{obs}} | \mu = B + rS)}{\text{Pois}(N = N_{\text{obs}} | \mu = B + \hat{r}S)} \right], \qquad 0 \leq \hat{r} \leq r \tag{9.4}$$

shown in Figure 9.12. The statistic $q_{0,\text{lim}} = 0$ is just a constant, but the distribution of $q_{1,\text{lim}}$ in the presence of signal has the same known asymptotic distribution as $q_{0,\text{sig}}$ in the absence of signal.

The statistics $q_{0,\text{sig}}$ and $q_{r,\text{lim}}$ are readily generalized to more complicated likelihood functions simply by using a fixed signal strength r in the likelihood for the numerator and the maximum likelihood estimator $\hat{r}$ in the denominator. All other nuisance parameters are profiled and set to their maximum likelihood values for the choice of r. The test statistic $q_{0,\text{sig}}$ is used to measure discovery significance and the statistics $q_{r,\text{lim}}$ is used to set limits via the CL_s method [106]. The procedure for finding CL_s upper limits on r at a 95% confidence level is as follows:

1. For some particular choice of r, compute the test statistic $q_{r,\mathrm{lim}}$.

2. Find the distribution of $q_{r,\mathrm{lim}}$ for a background only scenario and for a scenario where the true signal strength is equal to the selected r. This can be done either using asymptotic formulae or by generating "toys" or "pseudoexperiments," as explained below.

3. Using the distributions, compute the quantities CL_b and CL_{s+b}, the probabilities of obtaining a larger $q_{r,\mathrm{lim}}$ than the observed value. CL_b is computed using the background-only distribution and CL_{s+b} is computed using the distribution with signal at the hypothesized signal strength.

4. Compute the quantity $CL_s = CL_{s+b}/CL_b$.

5. Repeating the above, find the maximum r for which $CL_s \geq 0.05$ (or some other threshold if a different confidence level is preferred).

Note that the quantity CL_{s+b} is effectively a p-value for the the hypothesis that r has some particular value, with smaller values of CL_{s+b} indicating downward fluctuations that are less consistent with the presence of signal. Dividing by CL_b introduces deliberate over-coverage, which has two main advantages:

- confidence intervals for r always exist and always include $r = 0$, and

- a particular signal strength r will not be excluded if the background-only and signal-plus-background scenarios produce similar distributions of the test statistic and cannot be distinguished.

An illustration of how the CL_s method works is shown in Figure 9.13. The vertical green line represent an observed value of the test statistic corresponding to an observation that matches the background-only prediction. As mentioned above, there is a known

asymptotic distribution for the case where the hypothesized signal strength is equal to the true signal strength. This means that the dashed line distribution is relatively independent of r, except near $r \approx 0$ where the asymptotic assumptions break down. The vertical green line representing the observed test statistic moves relative to the dashed distribution, increasing CL_{s+b} as r is lowered. Changing r does not change CL_b (unless $r = 0$), so lower values of r produce larger CL_s. The center-right panel shows that $CL_s \approx 0.05$ when $r = 0.655$, meaning that $r > 0.665$ can be excluded at 95% confidence for this example.

Finally, it is sometimes desirable to determine the expected sensitivity of an analysis in either a background-only or signal-plus-background scenario. The most straightforward way to do this would be to simply use simulated data in place of the real data and compute the "observed" limits and significance as above. However, unless the simulation perfectly models the real data, then this approach may be biased. A more robust approach is to use the real data to produce "toys" or "pseudodata." The procedure for doing this is known as parametric bootstrapping and proceeds as follows:

1. Record the observed data.

2. Select a value of the signal strength parameter r. Taking $r = 0$, for example, will produce background-only toys, while $r = 1$ will generate toys with signal included at its nominal cross-section.

3. With r fixed, find the maximum likelihood values for all other parameters.

4. Translate the parameter values into Poisson mean parameters, as in Equations (6.14), (6.15), (6.16), and (6.17).

5. Using the Poisson means, generate random yields for each of the bins to obtain a toy dataset.

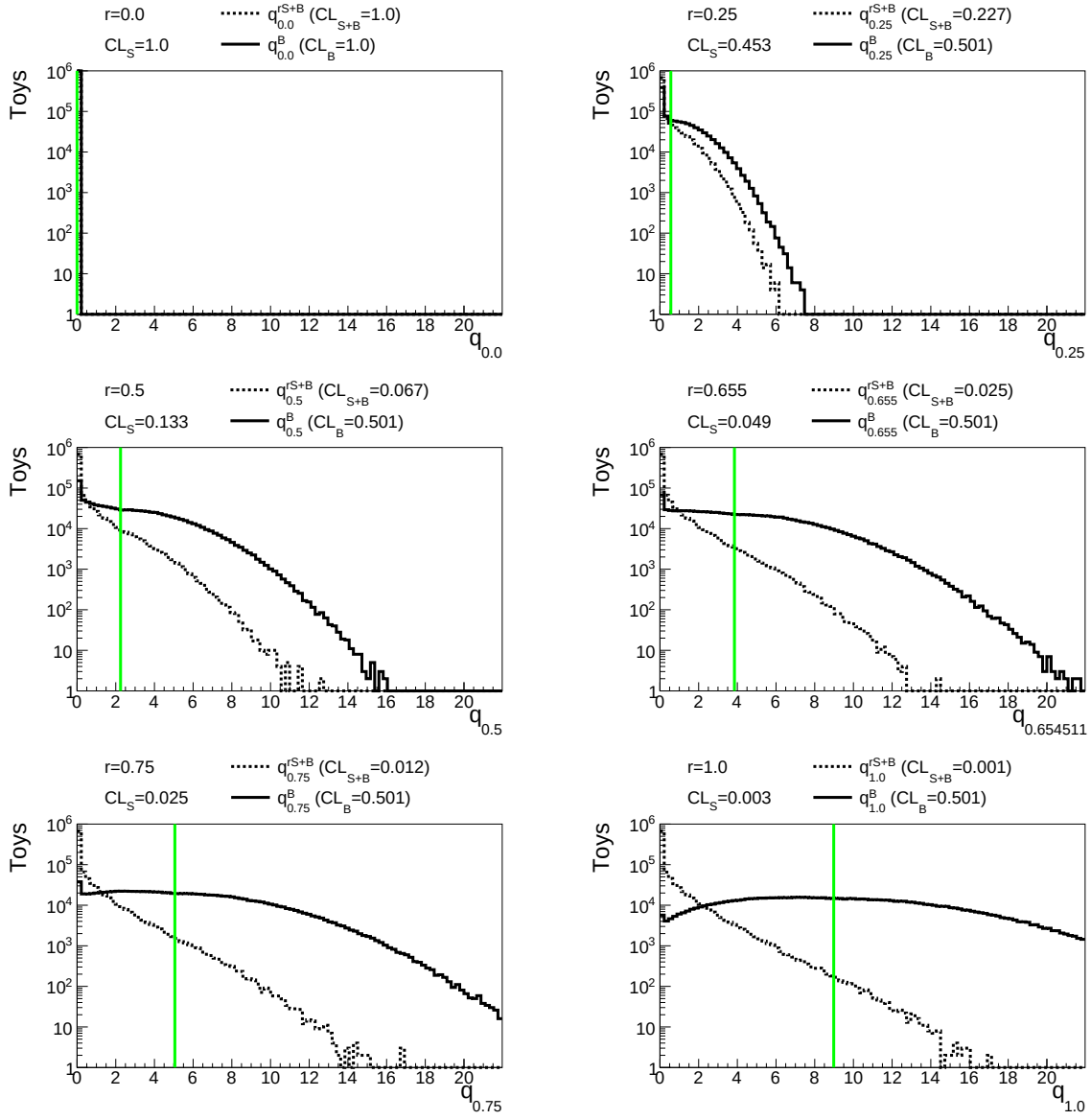

Figure 9.13: Illustration of how $q_{r,\mathrm{lim}}$ is used to compute CL_s upper limits on the signal strength parameter r for a single bin counting experiment model with a mean expected background yield of 10^6, a mean expected signal yield of 3×10^3, and no systematic uncertainties. The vertical line represents the observed $q_{r,\mathrm{lim}}$ when the observed yield is equal to the expected background. CL_b, the probability of obtaining a higher $q_{r,\mathrm{lim}}$ than the observed value given a background-only scenario (solid line), does not change with r. CL_{s+b}, the probability of obtaining a higher $q_{r,\mathrm{lim}}$ given a signal-plus-background scenario (dashed line) decreases with increasing r. The upper limit at 95% confidence corresponds to $r \approx 0.665$ where $CL_s = CL_{s+b}/CL_b = 0.05$ (center right panel).

6. Use the toy dataset to compute the test statistic (or other quantity of interest).

7. Repeat the above steps as many times as needed to determine the distribution of the test statistic to sufficient accuracy.

There is an alternative to producing toys. Instead, after obtaining the Poisson mean parameter for each bin, one can treat this mean as a (possibly non-integer) observed yield. This produces an "Asimov" dataset which can be used to find the median sensitivity [104, 105]. This has the advantage of being much faster, since one only needs to compute the maximum likelihood values of the fit parameters for a single representative dataset rather than for a large number of toys.

9.4 T1tttt and T5tttt Limits

Using the statistical tools detailed in Section 9.3, one can determine the significance of any excess and the cross section upper limits for any signal model. The discovery significances for the T1tttt and T5tttt models are shown in Figure 9.14. The significance has a Z-score of approximately -1 across the mass planes. The magnitude of the significance is computed from the p-value of the $q_{0,\text{sig}}$ statistic, and the sign of the significance set to match that of $\hat{r}$, so that downward fluctuations result in negative significance and vice versa. There is a small region of positive significance for models with the smallest mass splitting. This is caused by the few intermediate $E_{\text{T}}^{\text{miss}}$ bins with small excesses. It should be noted that Figure 9.14 shows local significance; since each point is testing a different hypothesis, computing a global p-value would require some means of accounting for the multiple comparisons problem, also known as the look-elsewhere effect.

Given the absence of any significant excess, the final step is to set limits on the T1tttt and T5tttt cross sections. Figure 9.15 shows 95% confidence level upper limits on the

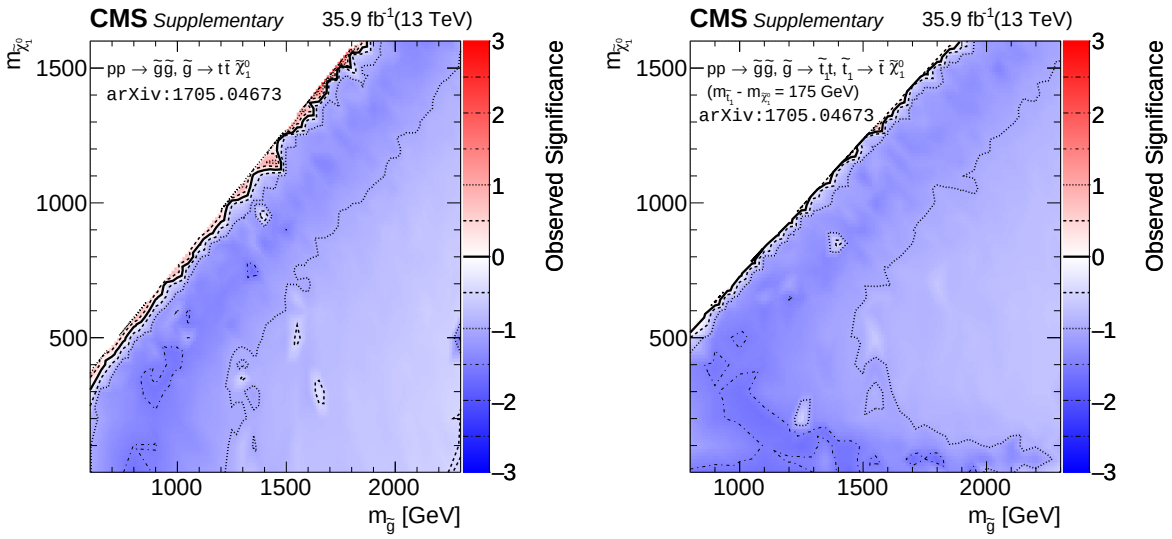

Figure 9.14: Observed significance in the T1tttt (left) and T5tttt (right) mass planes. Figure from supplementary material for Reference [11].

cross section of T1tttt and T5tttt. Limits are computed using the Higgs combination tool [107], which implements the CL_s method described in Section 9.3. For T1tttt, gluino masses up to approximately 1.9 TeV are excluded for neutralino masses below 1 TeV. Neutralino masses as large as 1175 GeV are excluded at a gluino mass of 1750 GeV. For large mass splitting, the cross section upper limit is approximately 1 fb. The observed limits are similar to or slightly better than the expected limits (computed from the Asimov dataset) throughout the mass plane.

The limits for T5tttt are similar except at low neutralino mass. A direct comparison of the T1tttt and T5tttt limits can be found in Figure 9.16. At low LSP mass, the sensitivity of this search decreases since the neutralino carries less momentum and reduces the average $E_{\mathrm{T}}^{\mathrm{miss}}$ of the signal events. Some sensitivity remains due to dilepton signal events with a lost lepton passing the event selection.

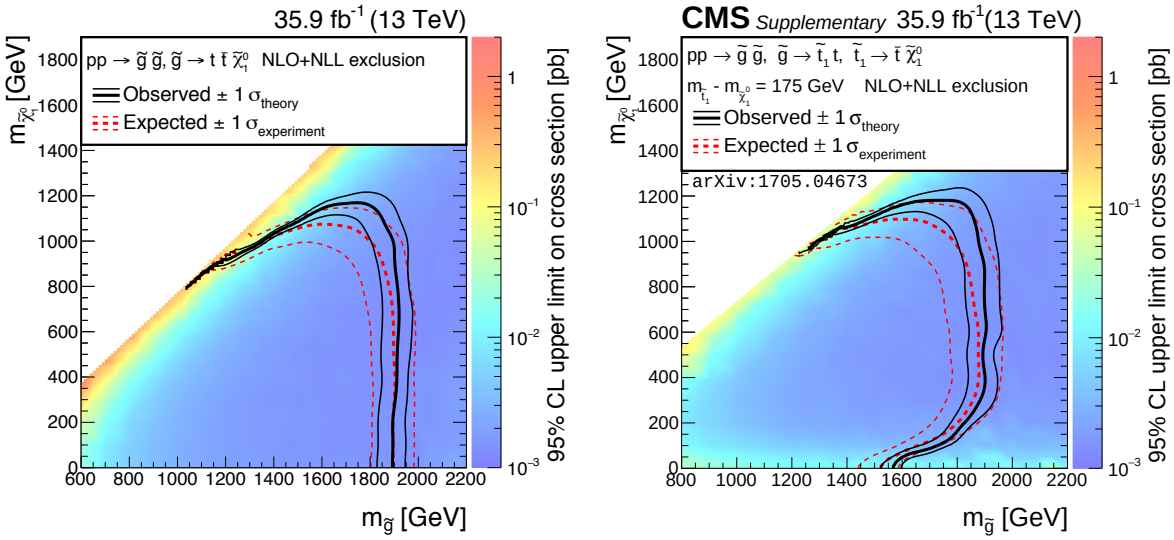

Figure 9.15: CL_s upper limits at a 95% confidence limit for T1tttt (left) and T5tttt (right). The color map shows the cross section upper limits. The black lines shows the excluded range of mass parameters (solid). The dashed black lines indicate uncertainty originating in the signal cross section. Points below and left of this line have a theoretical cross section above the excluded cross section. Similarly, the region of expected exclusion is shown by red lines, with the dashed red lines indicating experimental uncertainty. Left plot from Reference [13]. Right plot from supplementary material for Reference [11].

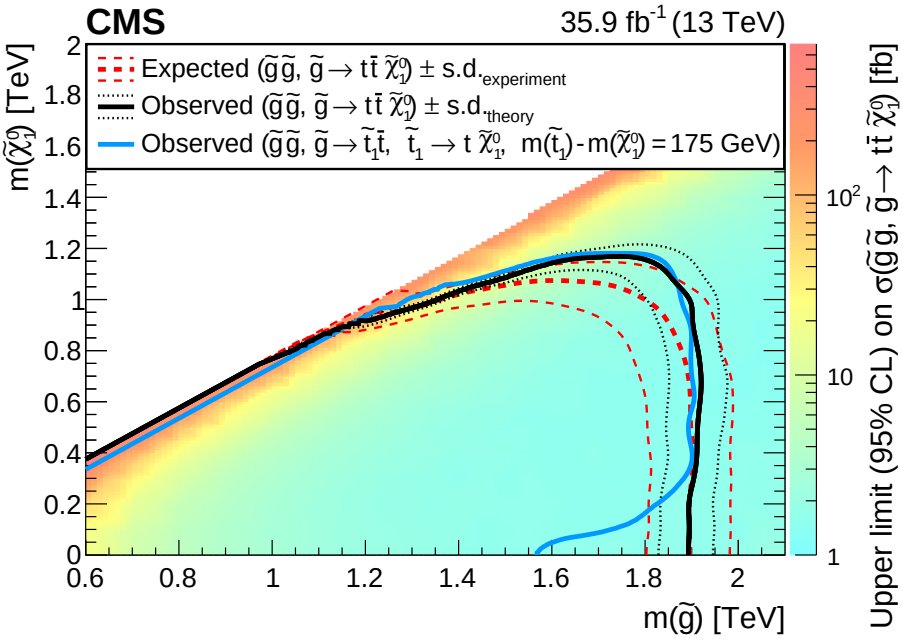

Figure 9.16: Comparison of the excluded regions for T1tttt and T5tttt models, showing their similarity. T5tttt limits are worse than T1tttt limits at low $\tilde{\chi}_1^0$mass because the $\tilde{\chi}_1^0$carries less momentum, reducing the average $E_{\mathrm{T}}^{\mathrm{miss}}$ of T5tttt events. Figure from Reference [11].

9.5 Aggregate Bins

Reinterpreting the results shown in Table 9.1 in terms of other signal models can be a rather tedious task. Theorists checking whether their latest models are consistent with the background estimates and observed yields would need to check 18 or 42 bins for the predictive and global fits, respectively. The simulated signal events must be correctly sorted into the appropriate bins and the estimated backgrounds and their correlations copied. The latter steps are simplified by providing digital copies of the results table and correlation matrices in the supplementary material for Reference [11], but this is still a significant amount of work for theorists to reproduce.

To simplify this process, we perform the background estimation using "aggregate bins." To create an aggregate bin result, we first choose a selection rule such as ($E_{\mathrm{T}}^{\mathrm{miss}} >$ 500 GeV, $N_{\mathrm{jets}} \geq 9$, $N_{\mathrm{b}} \geq 1$). An aggregate R1 (R3) bin is created by summing the

Table 9.2: Results from the background-only predictive fit in four aggregate bin options. The fit is independent of any signal model, but T1tttt yields from simulation are provided to give a sense of potential sensitivity. Note that each row is a separate fit, unlike in Table 9.1 where the rows are all produced by a single fit. Observed yields are consistent with the estimated backgrounds.

	Requirements			T1tttt			Background	
Name	$E_{\mathrm{T}}^{\mathrm{miss}}$ [GeV]	N_{jets}	N_{b}	(1800,100)	(1400,1000)	$\hat{\kappa}$	Pred. Fit	Obs.
High Mult.	> 200	≥ 9	≥ 3	3.4	6.9	1.4 ± 0.3	3.1 ± 0.8	2
Mixed	> 350	≥ 9	≥ 2	5.3	6.2	1.0 ± 0.4	2.7 ± 1.2	2
High $E_{\mathrm{T}}^{\mathrm{miss}}$	> 500	≥ 6	≥ 3	5.4	2.1	1.7 ± 0.6	0.5 ± 0.4	1
$N_{\mathrm{b}} = 1$	> 500	≥ 9	≥ 1	5.1	3.6	1.2 ± 0.4	0.4 ± 0.4	2

observed yields from all R1 (R3) bins satisfying the $E_{\mathrm{T}}^{\mathrm{miss}}$ requirement. Similarly, an aggregate R2 (R4) bin is created by summing the observed yields from the R2 (R4) bins satisfying the full requirement. This results in an ABCD plane with a single bin in each of the four analysis regions R1, R2, R3, and R4. Finally, we estimate the background yields in the aggregate R4 using a one-bin predictive fit.

We provide results for four aggregate bin options in Table 9.2. Note that the background estimate in each row in the table is produced by a separate fit. Unlike Table 9.1, in which the rows are meant to be considered simultaneously, only a single row should be considered for each signal model being tested.

The choice of aggregate bin depends on the properties of the signal model in question. The sensitivity of the four aggregate bin options to several selected signal models is provided in Table 9.3. T1tttt and T5tttt models with a large mass splitting typically benefit from a large $E_{\mathrm{T}}^{\mathrm{miss}}$ requirement, while those with a smaller mass splitting typically benefit from a large N_{jets} requirement. The option which requires only $N_{\mathrm{b}} \geq 1$ is not the best option for any of the T1tttt or T5tttt models, but allows for sensitivity to other models not considered here, which may not produce as many b-jets.

Choosing the best of the aggregate binning options allows for sensitivity within a few tens of percent of the fully binned result. Note that the systematic uncertainty in the

Table 9.3: Expected limits and significance for each of the four aggregate bin options and the full, finely binned analysis. The aggregate bin names correspond to those defined in Table 9.2. Note that the background systematic uncertainties are simply taken from the most similar bin in the full analysis rather than recomputing them from scratch. A 25% systematic uncertainty is assumed for the signal yield in all bins.

T1tttt Masses [GeV]		High Mult.	Mixed	High $E_{\mathrm{T}}^{\mathrm{miss}}$	$N_{\mathrm{b}} = 1$	Full Binning
1800,100	limit	1.43	0.89	0.59	0.71	0.59
	signif.	1.39	1.79	2.83	2.84	2.93
1600,1000	limit	0.84	0.77	0.98	1.05	0.67
	signif.	2.22	2.01	2.11	2.25	2.66
1400,1000	limit	0.75	0.81	1.65	1.05	0.76
	signif.	2.42	1.91	1.50	2.25	2.22
1300,1075	limit	34.62	11.41	5.20	4.27	3.83
	signif.	0.03	0.07	0.13	0.53	0.58

background yield is approximated for the aggregate bins in Table 9.3, and the systematic uncertainty in the signal yield assumed to be 25%. These approximations occasionally allow the aggregate bins to appear slightly better than the fully binned option when, in truth, the fully binned option would be more sensitive.

Chapter 10

Summary and Conclusions

This thesis has presented a search for supersymmetry in a $35.9\,\mathrm{fb}^{-1}$ dataset of proton-proton collisions with a center-of-momentum energy $\sqrt{s} = 13\,\mathrm{TeV}$ collected at the CMS detector in 2016. The search focuses on events with a final state containing a single lepton, high jet multiplicity, large missing transverse momentum $E_{\mathrm{T}}^{\mathrm{miss}}$, and one or more b-tagged jets. This final state provides sensitivity to the supersymmetry models T1tttt and T5tttt. Both of these models involve pair production of gluinos, with subsequent decay of the gluino to $\mathrm{t\bar{t}}\widetilde{\chi}_1^0$, where the neutralino $\widetilde{\chi}_1^0$ is the lightest supersymmetric particle, or LSP. In the case of T5tttt, this occurs via a sequential two-body decay chain with an intermediate on-shell stop squark, while in the case of T1tttt, the stop squark is off-shell and the gluino undergoes a three-body decay.

A distinguishing feature of the analysis is the use of the M_J variable, defined as the sum of "large-radius" jets produced by clustering the anti-k_{T}, $R = 0.4$ jets in an event. The transverse mass m_{T} of the lepton and $E_{\mathrm{T}}^{\mathrm{miss}}$ is approximately independent of M_J, allowing the use of an "ABCD" method to estimate the background. This method extrapolates the M_J spectrum in the signal-rich high-m_{T} region from a low-m_{T} control region. The $m_{\mathrm{T}} > 140\,\mathrm{GeV}$ requirement suppresses the single-lepton background, leaving

a background consisting mainly of dilepton $\mathrm{t\bar{t}}$+jets events at high m_{T}. On the other hand, the background in the low-m_{T} region contains primarily $\mathrm{t\bar{t}}$ + jets events with a single lepton. Despite the different compositions of the regions, jet multiplicity requirements ensure the presence of large amount of initial state radiation, or ISR, throughout. In the presence of significant ISR, the M_J spectra in the two samples converge.

Near-unity κ correction factors are derived from simulation and used to correct for any residual correlations between M_J and m_{T}. If the simulation modeled the real data perfectly, the corrections would result in a perfectly unbiased estimation of the background. The method is robust even in the presence of most realistic mismodeling scenarios because the double-ratio nature of κ causes uncorrelated errors in the M_J and m_{T} spectra to cancel out. Signal-depleted dilepton and $N_{\mathrm{jets}} = 5$ control samples are used to study the effects of any potential mismodeling, to confirm that there is no indication of mismodeling, and to assign systematic uncertainties in the κ factors.

To improve sensitivity, we estimate the background yield in 18 bins of $E_{\mathrm{T}}^{\mathrm{miss}}$, N_{jets}, and N_{b}. This binning improves the separation of signal and background events. Additionally, the kinematic properties of the signal events depend on the gluino and LSP masses, so binning provides added sensitivity to a broad range of masses.

The observed yields are consistent with the estimated background yields across all bins. Given the lack of any significant excess of events, we place limits on the T1tttt and T5tttt cross sections. For both T1tttt and T5tttt, we find an upper limit of approximately 1 fb on models with a large difference between the gluino and LSP masses. Gluinos masses up to 1.9 TeV are excluded for LSP masses below 1 TeV. Neutralino masses up to 1175 GeV are excluded at a gluino mass of 1750 GeV. Exclusion limits for T1tttt and T5tttt are similar, except at small LSP mass, where this search has reduced sensitivity to T5tttt because the neutralinos carry less momentum, reducing the average $E_{\mathrm{T}}^{\mathrm{miss}}$ of the signal events. Put another way, the limits are insensitive to the intermediate stop

squark mass. In all cases, limits are computed at a 95% confidence level using the CL_s method and assume a 100% branching fraction for the decay in question.

In a background-free, single bin search, the 95% confidence level upper limit on the signal cross section corresponds to the cross section needed to produce three signal events. This means that the upper limit is inversely proportional to the integrated luminosity. For the search described in this dissertation, many of the most sensitive bins are nearly background-free, and so we may expect the observed limits to also scale as the inverse of the integrated luminosity. Assuming that this is true, then a $3\,\text{ab}^{-1}$ dataset ought to produce cross section upper limits approximately 100 times lower than those we found with the current $35.9\,\text{fb}^{-1}$ data set. That is, with $3\,\text{ab}^{-1}$ of data we might expect to be able to exclude models with a cross section as low as 10 ab. This corresponds to an upper limit on the gluino mass of approximately 2.8 TeV. Extending the limits to 3 TeV and beyond will likely require a new collider.

As generic searches continue to exclude more models, targeted searches which attempt a more elaborate event reconstruction may become more important. Unfortunately, the high jet multiplicity, b-tagging, $E_{\text{T}}^{\text{miss}}$, and lepton requirements of this search may make it difficult to extend to models that do not have multiple top quarks in the final state.

Of course, the hope is not to continue excluding models, but for an eventual discovery. I wish the next generation of students luck and hope that their dissertations will describe the discovery of SUSY.

Bibliography

[1] A. Purcell, "Go on a particle quest at the first CERN webfest. Le premier webfest du CERN se lance à la conquête des particules", August, 2012.

[2] CMS Collaboration, "Summaries of CMS cross section measurements". Accessed: 2017 June 4.

[3] M. Papucci, J. T. Ruderman, and A. Weiler, "Natural SUSY Endures", *Journal of High Energy Physics* **2012** (2012), no. 9, 35, doi:10.1007/JHEP09(2012)035, arXiv:1110.6926.

[4] C. Borschensky et al., "Squark and gluino production cross sections in pp collisions at $\sqrt{s} = 13$, 14, 33, and 100 TeV", *The European Physical Journal C* **74** (2014), no. 12, 3174, doi:10.1140/epjc/s10052-014-3174-y, arXiv:1407.5066.

[5] C. De Melis, "The CERN accelerator complex. Complexe des accélérateurs du CERN", July, 2016. General Photo.

[6] CMS Collaboration, "CMS Luminosity – Public Results". Accessed: 2017 March 14.

[7] CMS Collaboration, "Detector Drawings", (March, 2012). CMS Collection.

[8] CMS Collaboration, S. R. Davis, "Interactive Slice of the CMS detector", August, 2016.

[9] CMS Collaboration, "The CMS experiment at the CERN LHC", *Journal of Instrumentation* **3** (2008), no. 08, S08004, doi:10.1088/1748-0221/3/08/S08004.

[10] M. Franco Sevilla and A. Dishaw, "Optical DAQ MotherBoard", April, 2015. Accessed 2017 June 7.

[11] CMS Collaboration, "Search for supersymmetry in pp collisions at $\sqrt{s} = 13\,\text{TeV}$ in the single-lepton final state using the sum of masses of large-radius jets", arXiv:1705.04673. Submitted to Physical Review Letters.

[12] CMS Collaboration, "CMS SUSY Results: Objects Efficiency", May, 2017. Accessed 2017 June 7.

[13] CMS Collaboration, "Search for supersymmetry in pp collisions at $\sqrt{s} = 13\,\text{TeV}$ in the single-lepton final state using the sum of masses of large radius jets", (June, 2016). Accessed 2017 June 7.

[14] CMS Collaboration, "Search for supersymmetry in pp collisions at $\sqrt{s} = 13\,\text{TeV}$ in the single-lepton final state using the sum of masses of large-radius jets", *Journal of High Energy Physics* **2016** (2016), no. 8, 122, doi:10.1007/JHEP08(2016)122, arXiv:1605.04608.

[15] D. Kovalskyi et al., "Fireworks: A physics event display for CMS", *Journal of Physics: Conference Series* **219** (2010), no. 3, 032014, doi:10.1088/1742-6596/219/3/032014.

[16] C. Patrignani and Particle Data Group, "Review of Particle Physics", *Chinese Physics C* **40** (2016), no. 10, 100001, doi:10.1088/1674-1137/40/10/100001.

[17] J. D. Richman, "Searches for New Physics at the Large Hadron Collider", pp. 239–284. Springer International Publishing, Cham, Switzerland, 2015. doi:10.1007/978-3-319-05362-2_7.

[18] D. Nisbet, "LHC Operation in 2016", in *LHC Performance Workshop 2017*. January, 2017.

[19] ATLAS Collaboration, "Observation of a new particle in the search for the Standard Model Higgs boson with the ATLAS detector at the LHC", *Physics Letters B* **716** (2012), no. 1, 1–29, doi:10.1016/j.physletb.2012.08.020, arXiv:1207.7214.

[20] CMS Collaboration, "Observation of a new boson at a mass of 125 GeV with the CMS experiment at the LHC", *Physics Letters B* **716** (2012), no. 1, 30–61, doi:10.1016/j.physletb.2012.08.021, arXiv:1207.7235.

[21] CMS Collaboration, "Observation of a new boson with mass near 125 GeV in pp collisions at $\sqrt{s} = 7$ and 8 TeV", *Journal of High Energy Physics* **2013** (2013), no. 6, 81, doi:10.1007/JHEP06(2013)081, arXiv:1303.4571.

[22] CMS Collaboration, "Precise determination of the mass of the Higgs boson and tests of compatibility of its couplings with the standard model predictions using proton collisions at 7 and 8 TeV", *The European Physical Journal C* **75** (2015), no. 5, 212, doi:10.1140/epjc/s10052-015-3351-7, arXiv:1412.8662.

[23] ATLAS Collaboration, "Measurement of the Higgs boson mass from the $H \to \gamma\gamma$ and $H \to ZZ^* \to 4\ell$ channels with the ATLAS detector using 25 fb^{-1} of pp collision data", *Physical Review D* **90** (September, 2014) 052004, doi:10.1103/PhysRevD.90.052004, arXiv:1406.3827.

[24] ATLAS and CMS Collaboration, "Combined Measurement of the Higgs Boson Mass in pp Collisions at $\sqrt{s} = 7$ and 8 TeV with the ATLAS and CMS Experiments", *Physical Review Letters* **114** (2015) 191803, doi:10.1103/PhysRevLett.114.191803, arXiv:1503.07589.

[25] CMS Collaboration, "Search for supersymmetry in pp collisions at $\sqrt{s} = 13$ TeV in the single-lepton final state using the sum of masses of large-radius jets", Technical Report CMS-PAS-SUS-16-037, CERN, Geneva, 2017.

[26] F. Zwicky, "Republication of: The redshift of extragalactic nebulae", *General Relativity and Gravitation* **41** (2009), no. 1, 207–224, doi:10.1007/s10714-008-0707-4.

[27] V. C. Rubin and W. K. Ford, Jr., "Rotation of the Andromeda Nebula from a Spectroscopic Survey of Emission Regions", *Astrophysical Journal* **159** (February, 1970) 379, doi:10.1086/150317.

[28] G. 't Hooft, "Naturalness, Chiral Symmetry, and Spontaneous Chiral Symmetry Breaking", volume 59 of *B*, pp. 135–157. Springer US, Boston, MA, 1980. doi:10.1007/978-1-4684-7571-5_9.

[29] E. Witten, "Dynamical breaking of supersymmetry", *Nuclear Physics B* **188** (1981), no. 3, 513–554, doi:10.1016/0550-3213(81)90006-7.

[30] M. Dine, W. Fischler, and M. Srednicki, "Supersymmetric technicolor", *Nuclear Physics B* **189** (1981), no. 3, 575–593, doi:10.1016/0550-3213(81)90582-4.

[31] S. Dimopoulos and S. Raby, "Supercolor", *Nuclear Physics B* **192** (1981), no. 2, 353–368, doi:10.1016/0550-3213(81)90430-2.

[32] S. Dimopoulos and H. Georgi, "Softly broken supersymmetry and SU(5)", *Nuclear Physics B* **193** (1981), no. 1, 150–162, doi:10.1016/0550-3213(81)90522-8.

[33] R. K. Kaul and P. Majumdar, "Cancellation of quadratically divergent mass corrections in globally supersymmetric spontaneously broken gauge theories", *Nuclear Physics B* **199** (1982), no. 1, 36–58, doi:10.1016/0550-3213(82)90565-X.

[34] P. Ramond, "Dual Theory for Free Fermions", *Physical Review D* **3** (May, 1971) 2415–2418, doi:10.1103/PhysRevD.3.2415.

[35] Y. A. Gol'fand and E. P. Likhtman, "Extension of the Algebra of Poincaré Group Generators and Violation of p Invariance", *Journal of Experimental and Theoretical Physics Letters* **13** (1971) 323–326. [Pis'ma v Zhurnal Eksperimental'noi i Teoreticheskoi Fiziki 13,452(1971)].

[36] A. Neveu and J. Schwarz, "Factorizable dual model of pions", *Nuclear Physics B* **31** (1971), no. 1, 86–112, doi:10.1016/0550-3213(71)90448-2.

[37] D. V. Volkov and V. P. Akulov, "Possible universal neutrino interaction", pp. 383–385. Springer Berlin Heidelberg, Berlin, Heidelberg, 1998. [Pis'ma v Zhurnal Eksperimental'noi i Teoreticheskoi Fiziki 16,621(1972)]. doi:10.1007/BFb0105270.

[38] J. Wess and B. Zumino, "A lagrangian model invariant under supergauge transformations", *Physics Letters B* **49** (1974), no. 1, 52–54, doi:10.1016/0370-2693(74)90578-4.

[39] J. Wess and B. Zumino, "Supergauge transformations in four dimensions", *Nuclear Physics B* **70** (1974), no. 1, 39–50, doi:10.1016/0550-3213(74)90355-1.

[40] P. Fayet, "Supergauge invariant extension of the Higgs mechanism and a model for the electron and its neutrino", *Nuclear Physics B* **90** (1975) 104–124, doi:10.1016/0550-3213(75)90636-7.

[41] H. Nilles, "Supersymmetry, supergravity and particle physics", *Physics Reports* **110** (1984), no. 1, 1–162, doi:10.1016/0370-1573(84)90008-5.

[42] S. P. Martin, "A Supersymmetry Primer", volume 21 of *Advanced Series on Directions in High Energy Physics*, ch. 1, pp. 1–153. World Scientific, April, 2010. arXiv:hep-ph/9709356. doi:10.1142/9789814307505_0001.

[43] J. L. Feng, "Naturalness and the Status of Supersymmetry", *Annual Review of Nuclear and Particle Science* **63** (2013) 351–382, doi:10.1146/annurev-nucl-102010-130447, arXiv:1302.6587.

[44] R. Barbieri and G. Giudice, "Upper bounds on supersymmetric particle masses", *Nuclear Physics B* **306** (1988), no. 1, 63–76, doi:10.1016/0550-3213(88)90171-X.

[45] S. Dimopoulos and G. Giudice, "Naturalness constraints in supersymmetric theories with non-universal soft terms", *Physics Letters B* **357** (1995), no. 4, 573–578, doi:10.1016/0370-2693(95)00961-J, arXiv:hep-ph/9507282.

[46] R. Barbieri and D. Pappadopulo, "S-particles at their naturalness limits", *Journal of High Energy Physics* **2009** (2009), no. 10, 061, doi:10.1088/1126-6708/2009/10/061, arXiv:0906.4546.

[47] G. R. Farrar and P. Fayet, "Phenomenology of the production, decay, and detection of new hadronic states associated with supersymmetry", *Physics Letters B* **76** (1978), no. 5, 575–579, doi:10.1016/0370-2693(78)90858-4.

[48] J. Alwall, P. C. Schuster, and N. Toro, "Simplified models for a first characterization of new physics at the LHC", *Physical Review D* **79** (April, 2009) 075020, doi:10.1103/PhysRevD.79.075020, arXiv:0810.3921.

[49] J. Alwall, M. Le, M. Lisanti, and J. G. Wacker, "Model-independent jets plus missing energy searches", *Physical Review D* **79** (January, 2009) 015005, doi:10.1103/PhysRevD.79.015005, arXiv:0809.3264.

[50] D. Alves et al., "Simplified models for LHC new physics searches", *Journal of Physics G: Nuclear and Particle Physics* **39** (2012), no. 10, 105005, doi:10.1088/0954-3899/39/10/105005, arXiv:1105.2838.

[51] CMS Collaboration, "Interpretation of searches for supersymmetry with simplified models", *Physical Review D* **88** (September, 2013) 052017, doi:10.1103/PhysRevD.88.052017, arXiv:1301.2175.

[52] ATLAS Collaboration, "Search for supersymmetry in final states with jets, missing transverse momentum and one isolated lepton in $\sqrt{s} = 7\,\text{TeV}$ pp collisions using $1\,\text{fb}^{-1}$ of ATLAS data", *Physical Review D* **85** (January, 2012) 012006, doi:10.1103/PhysRevD.85.012006, arXiv:1109.6606.

[53] ATLAS Collaboration, "Publisher's Note: Search for supersymmetry in final states with jets, missing transverse momentum and one isolated lepton in $\sqrt{s} = 7\,\text{TeV}$ pp collisions using $1\,\text{fb}^{-1}$ of ATLAS data [Phys. Rev. D 85, 012006 (2012)]", *Physical Review D* **87** (May, 2013) 099903, doi:10.1103/PhysRevD.87.099903, arXiv:1109.6606.

[54] CMS Collaboration, "Search for supersymmetry in pp collisions at $\sqrt{s} = 7\,\text{TeV}$ in events with a single lepton, jets, and missing transverse momentum", *Journal of High Energy Physics* **2011** (2011), no. 8, 156, doi:10.1007/JHEP08(2011)156, arXiv:1107.1870.

[55] ATLAS Collaboration, "Search for squarks and gluinos in events with isolated leptons, jets and missing transverse momentum at $\sqrt{s} = 8\,\text{TeV}$ with the ATLAS detector", *Journal of High Energy Physics* **2015** (2015), no. 4, 116, doi:10.1007/JHEP04(2015)116, arXiv:1501.03555.

[56] CMS Collaboration, "Search for supersymmetry in pp collisions at $\sqrt{s} = 8\,\text{TeV}$ in events with a single lepton, large jet multiplicity, and multiple b jets", *Physics Letters B* **733** (2014) 328–353, doi:10.1016/j.physletb.2014.04.023, arXiv:1311.4937.

[57] ATLAS Collaboration, "Search for gluinos in events with an isolated lepton, jets and missing transverse momentum at $\sqrt{s} = 13\,\text{TeV}$ with the ATLAS detector", *The European Physical Journal C* **76** (2016), no. 10, 565, doi:10.1140/epjc/s10052-016-4397-x, arXiv:1605.04285.

[58] CMS Collaboration, "Search for supersymmetry in events with one lepton and multiple jets in proton-proton collisions at $\sqrt{s} = 13\,\text{TeV}$", *Physical Review D* **95** (Jan, 2017) 012011, doi:10.1103/PhysRevD.95.012011, arXiv:1609.09386.

[59] L. Evans and P. Bryant, "LHC Machine", *Journal of Instrumentation* **3** (2008), no. 08, S08001, doi:10.1088/1748-0221/3/08/S08001.

[60] CMS Collaboration, "CMS Luminosity Measurements for the 2016 Data Taking Period", Technical Report CMS-PAS-LUM-17-001, CERN, Geneva, 2017.

[61] CMS Collaboration, "Precise mapping of the magnetic field in the CMS barrel yoke using cosmic rays", *Journal of Instrumentation* **5** (2010), no. 03, T03021, doi:10.1088/1748-0221/5/03/T03021, arXiv:0910.5530.

[62] CMS Collaboration, "The CMS trigger system", *Journal of Instrumentation* **12** (2017), no. 01, P01020, doi:10.1088/1748-0221/12/01/P01020, arXiv:1609.02366.

[63] CMS Collaboration, "Description and performance of track and primary-vertex reconstruction with the CMS tracker", *Journal of Instrumentation* **9** (May, 2014) P10009, doi:10.1088/1748-0221/9/10/P10009, arXiv:1405.6569.

[64] CMS Collaboration, "Particle–Flow Event Reconstruction in CMS and Performance for Jets, Taus, and MET", CMS Physics Analysis Summary CMS-PAS-PFT-09-001, CERN, April, 2009.

[65] CMS Collaboration, "Commissioning of the Particle–flow Event Reconstruction with the first LHC collisions recorded in the CMS detector", CMS Physics Analysis Summary CMS-PAS-PFT-10-001, CERN, 2010.

[66] W. Adam, R. Frühwirth, A. Strandlie, and T. Todorov, "Reconstruction of electrons with the Gaussian-sum filter in the CMS tracker at the LHC", *Journal of Physics G: Nuclear and Particle Physics* **31** (January, 2005) N9, doi:10.1088/0954-3899/31/9/N01, arXiv:physics/0306087.

[67] CMS Collaboration, "Performance of CMS muon reconstruction in pp collision events at $\sqrt{s} = 7$ TeV", *Journal of Instrumentation* **7** (2012), no. 10, P10002, doi:10.1088/1748-0221/7/10/P10002, arXiv:1206.4071.

[68] CMS Collaboration, "Performance of electron reconstruction and selection with the CMS detector in proton-proton collisions at $\sqrt{s} = 8$ TeV", *Journal of Instrumentation* **10** (2015), no. 06, P06005, doi:10.1088/1748-0221/10/06/P06005, arXiv:1502.02701.

[69] K. Rehermann and B. Tweedie, "Efficient Identification of Boosted Semileptonic Top Quarks at the LHC", *JHEP* **03** (2011) 059, doi:10.1007/JHEP03(2011)059, arXiv:1007.2221.

[70] A. Barr, C. Lester, and P. Stephens, "A variable for measuring masses at hadron colliders when missing energy is expected; m_{T2}: the truth behind the glamour", *Journal of Physics G: Nuclear and Particle Physics* **29** (2003), no. 10, 2343, doi:10.1088/0954-3899/29/10/304, arXiv:hep-ph/0304226.

[71] C. Lester and D. Summers, "Measuring masses of semi-invisibly decaying particle pairs produced at hadron colliders", *Physics Letters B* **463** (1999), no. 1, 99–103, doi:10.1016/S0370-2693(99)00945-4, arXiv:hep-ph/9906349.

[72] M. Cacciari, G. P. Salam, and G. Soyez, "FastJet user manual", *The European Physical Journal C* **72** (2012), no. 3, 1896, doi:10.1140/epjc/s10052-012-1896-2, arXiv:1111.6097.

[73] G. P. Salam, "Towards jetography", *The European Physical Journal C* **67** (2010), no. 3, 637–686, doi:10.1140/epjc/s10052-010-1314-6, arXiv:0906.1833.

[74] S. D. Ellis and D. E. Soper, "Successive combination jet algorithm for hadron collisions", *Physical Review D* **48** (October, 1993) 3160–3166, doi:10.1103/PhysRevD.48.3160, arXiv:hep-ph/9305266.

[75] Y. Dokshitzer, G. Leder, S. Moretti, and B. Webber, "Better Jet Clustering Algorithms", *Journal of High Energy Physics* **1997** (1997), no. 08, 001, doi:10.1088/1126-6708/1997/08/001, arXiv:hep-ph/9707323.

[76] M. Cacciari, G. P. Salam, and G. Soyez, "The anti-k_t jet clustering algorithm", *Journal of High Energy Physics* **2008** (2008), no. 04, 063, doi:10.1088/1126-6708/2008/04/063, arXiv:0802.1189.

[77] CMS Collaboration, "Determination of jet energy calibration and transverse momentum resolution in CMS", *Journal of Instrumentation* **6** (2011), no. 11, P11002, doi:10.1088/1748-0221/6/11/P11002, arXiv:1107.4277.

[78] M. Cacciari and G. P. Salam, "Pileup subtraction using jet areas", *Physics Letters B* **659** (2008), no. 12, 119–126, doi:10.1016/j.physletb.2007.09.077, arXiv:0707.1378.

[79] CMS Collaboration, "Identification of b-quark jets with the CMS experiment", *Journal of Instrumentation* **8** (2013), no. 04, P04013, doi:10.1088/1748-0221/8/04/P04013, arXiv:1211.4462.

[80] CMS Collaboration, "Identification of b quark jets at the CMS Experiment in the LHC Run 2", Technical Report CMS-PAS-BTV-15-001, CERN, Geneva, 2016.

[81] ATLAS Collaboration, "Search for direct pair production of the top squark in all-hadronic final states in proton-proton collisions at $\sqrt{s} = 8\,\text{TeV}$ with the ATLAS detector", *Journal of High Energy Physics* **2014** (2014), no. 9, 15, doi:10.1007/JHEP09(2014)015, arXiv:1406.1122.

[82] A. Hook, E. Izaguirre, M. Lisanti, and J. G. Wacker, "High multiplicity searches at the LHC using jet masses", *Physical Review D* **85** (Mar, 2012) 055029, doi:10.1103/PhysRevD.85.055029, arXiv:1202.0558.

[83] T. Cohen, E. Izaguirre, M. Lisanti, and H. K. Lou, "Jet substructure by accident", *Journal of High Energy Physics* **2013** (2013), no. 3, 161, doi:10.1007/JHEP03(2013)161, arXiv:1212.1456.

[84] S. El Hedri, A. Hook, M. Jankowiak, and J. G. Wacker, "Learning how to count: a high multiplicity search for the LHC", *Journal of High Energy Physics* **2013** (2013), no. 8, 136, doi:10.1007/JHEP08(2013)136, arXiv:1302.1870.

[85] CMS Collaboration, "Commissioning the performance of key observables used in SUSY searches with the first 13 TeV data", Technical Report CMS-DP-2015-035, CERN, Geneva, August, 2015.

[86] ATLAS Collaboration, "Search for massive supersymmetric particles decaying to many jets using the ATLAS detector in pp collisions at $\sqrt{s} = 8\,\text{TeV}$", *Physical Review D* **91** (June, 2015) 112016, doi:10.1103/PhysRevD.91.112016, arXiv:1502.05686.

[87] ATLAS Collaboration, "Erratum: Search for massive supersymmetric particles decaying to many jets using the ATLAS detector in pp collisions at $\sqrt{s} = 8\,\text{TeV}$", *Phys. Rev. D* **93** (Feb, 2016) 039901, doi:10.1103/PhysRevD.93.039901, arXiv:1502.05686.

[88] ATLAS Collaboration, "Search for new phenomena in final states with large jet multiplicities and missing transverse momentum at $\sqrt{s} = 8\,\text{TeV}$ proton-proton collisions using the ATLAS experiment", *Journal of High Energy Physics* **2013** (2013), no. 10, 130, doi:10.1007/JHEP10(2013)130, arXiv:1308.1841.

[89] ATLAS Collaboration, "Erratum: Search for new phenomena in final states with large jet multiplicities and missing transverse momentum at $\sqrt{s} = 8\,\text{TeV}$

proton-proton collisions using the ATLAS experiment", *Journal of High Energy Physics* **2014** (2014), no. 1, 109, doi:10.1007/JHEP01(2014)109, arXiv:1308.1841.

[90] J. Alwall et al., "The automated computation of tree-level and next-to-leading order differential cross sections, and their matching to parton shower simulations", *Journal of High Energy Physics* **2014** (2014), no. 7, 79, doi:10.1007/JHEP07(2014)079, arXiv:1405.0301.

[91] E. Re, "Single-top Wt-channel production matched with parton showers using the POWHEG method", *The European Physical Journal C* **71** (2011), no. 2, 1547, doi:10.1140/epjc/s10052-011-1547-z, arXiv:1009.2450.

[92] S. Alioli, P. Nason, C. Oleari, and E. Re, "NLO single-top production matched with shower in POWHEG: s- and t-channel contributions", *Journal of High Energy Physics* **2009** (2009), no. 09, 111, doi:10.1088/1126-6708/2009/09/111, arXiv:0907.4076.

[93] S. Alioli, P. Nason, C. Oleari, and E. Re, "Erratum: NLO single-top production matched with shower in POWHEG: s- and t-channel contributions", *Journal of High Energy Physics* **2010** (2010), no. 02, 11, doi:10.1007/JHEP02(2010)011, arXiv:0907.4076.

[94] R. D. Ball et al., "Parton distributions for the LHC run II", *Journal of High Energy Physics* **2015** (2015), no. 4, 40, doi:10.1007/JHEP04(2015)040, arXiv:1410.8849.

[95] M. Czakon, P. Fiedler, and A. Mitov, "Total Top-Quark Pair-Production Cross Section at Hadron Colliders Through $\mathcal{O}(\alpha_S^4)$", *Physical Review Letters* **110** (June, 2013) 252004, doi:10.1103/PhysRevLett.110.252004, arXiv:1303.6254.

[96] T. Sjöstrand et al., "An introduction to PYTHIA 8.2", *Computer Physics Communications* **191** (2015) 159–177, doi:10.1016/j.cpc.2015.01.024, arXiv:1410.3012.

[97] S. Agostinelli et al., "Geant4–a simulation toolkit", *Nuclear Instruments and Methods in Physics Research Section A: Accelerators, Spectrometers, Detectors and Associated Equipment* **506** (2003), no. 3, 250–303, doi:10.1016/S0168-9002(03)01368-8.

[98] CMS Collaboration, "The Fast Simulation of the CMS Detector at LHC", *Journal of Physics: Conference Series* **331** (2011), no. 3, 032049, doi:10.1088/1742-6596/331/3/032049.

[99] A. Ovcharova and M. Franco Sevilla, "Preliminary ISR reweighting and uncertainty recommendations for ICHEP", (July, 2016).

[100] A. Ovcharova and M. Franco Sevilla, "Preliminary ISR reweighting and uncertainty recommendations for Moriond'17", (December, 2016).

[101] CMS Collaboration, "Search for supersymmetry in multijet events with missing transverse momentum in proton-proton collisions at 13 TeV", Technical Report CMS-PAS-SUS-16-033, CERN, Geneva, 2017.

[102] G. P. Salam, "Elements of QCD for hadron colliders", in *High-energy physics. Proceedings, 17th European School, ESHEP 2009, Bautzen, Germany, June 14–27, 2009*, C. Grojean and M. Spiropulu, eds., p. 45, CERN. CERN, November, 2010. arXiv:1011.5131. doi:10.5170/CERN-2010-002.

[103] S. S. Wilks, "The Large-Sample Distribution of the Likelihood Ratio for Testing Composite Hypotheses", *The Annals of Mathematical Statistics* **9** (March, 1938) 60–62, doi:10.1214/aoms/1177732360.

[104] G. Cowan, K. Cranmer, E. Gross, and O. Vitells, "Asymptotic formulae for likelihood-based tests of new physics", *The European Physical Journal C* **71** (2011), no. 2, 1554, doi:10.1140/epjc/s10052-011-1554-0, arXiv:1007.1727.

[105] G. Cowan, K. Cranmer, E. Gross, and O. Vitells, "Erratum to: Asymptotic formulae for likelihood-based tests of new physics", *The European Physical Journal C* **73** (2013), no. 7, 2501, doi:10.1140/epjc/s10052-013-2501-z, arXiv:1007.1727.

[106] A. L. Read, "Presentation of search results: the CL_s technique", *Journal of Physics G: Nuclear and Particle Physics* **28** (2002), no. 10, 2693.

[107] ATLAS and CMS and LHC Higgs Combination Group Collaboration, "Procedure for the LHC Higgs boson search combination in Summer 2011", Technical Report CMS-NOTE-2011-005 and ATL-PHYS-PUB-2011-11, CERN, Geneva, August, 2011.